Physics with photons with the ATLAS run 2 data : calibration and identification, measurement of the Higgs boson mass and search for supersymmetry in di-photon final state

Stefano Manzoni

UNIVERSITÀ DEGLI STUDI DI MILANO

Scuola di Dottorato in Fisica, Astrofisica e Fisica Applicata

Ciclo XXX

UNIVERSITÉ PIERRE ET MARIE CURIE

École Doctorale Sciences de la Terre et Physique de l'Univers

Étalonnage en énergie et identification des photons, mesure de la masse du boson de Higgs et recherche de supersymétrie dans l'état final avec deux photons, avec les données du Run 2 de l'expérience ATLAS au LHC.

Par Stefano MANZONI

Thèse de doctorat de physique des particules

Dirigée par Leonardo CARMINATI et Giovanni MARCHIORI

Présentée et soutenue publiquement le 15 Décembre 2017

Devant un jury composé de:

M. Matteo CACCIARI
M. Leonardo CARMINATI
M. Mauro DONEGÀ
M. Fabrice HUBAUT
Mme. Lydia ICONOMIDOU-FAYARD
M. Giovanni MARCHIORI
M. Shahram RAHATLOU
M. Dan TOVEY

Contents

Introduction

The work presented in this manuscript is based on the proton-proton collision data from the Large Hadron Collider (LHC) (1) at a centre-of-mass energy of 13 TeV recorded by the ATLAS (2) detector in 2015 and 2016. The ATLAS detector is one of the general purpose experiments at the LHC. The research program of ATLAS ranges from the precise measurement of the parameters of the Standard Model (SM), which is the quantum field theory that as of today better describes the elementary particle interactions, to searches for signals of physics beyond the SM. Both these approaches are pursued in this thesis, which presents two different analyses. The first one is the precision measurement of the Higgs boson mass in the di-photon decay channel, and the second one is the search for the production of supersymmetric particles leading to a final state containing two photons and missing transverse momentum. Moreover, this manuscript describes in detail the photon (and electron) reconstruction, energy calibration and identification performance that are key points for both analyses. My main contributions are presented with major emphasis. In particular, the Monte Carlo multivariate calibration procedure of the electron and photon energy and the method developed to evaluate the probability that an electron is reconstructed as photon are extensively illustrated.

On July 4th, 2012, the ATLAS and CMS (3) collaborations announced the discovery of a new particle compatible with the Higgs boson predicted by the Standard Model, with a mass around 125 GeV (4; 5). The Higgs boson is a fundamental scalar particle whose existence is predicted by the Higgs mechanism proposed in 1964 by Higgs, Brout, Englert, Guralnik, Hagen and Kibble (6; 7; 8). The introduction of this mechanism in the Standard Model formulation is crucial to describe the mass terms of all massive elementary particles, without explicitly breaking the fundamental symmetry of the model. Measurements of the properties (mass, couplings, spin, parity) of this new particle were conducted by the ATLAS and CMS experiments exploiting the data collected during 2011 and 2012 (Run 1), in proton-proton collision at a centre-of-mass energies of 7 and 8 TeV, corresponding to an integrated luminosity of approximately 5 and 20 fb^{-1} respectively. Since the beginning of 2015 LHC has been accelerating protons to 6.5 TeV, allowing ATLAS to collect 36.1 fb^{-1} of data at $\sqrt{s} = 13$ TeV by the end of 2016. Thanks to the higher center-of-mass energy, which implies a higher Higgs boson production cross section ($\sigma^{SM}_{13\text{TeV}}/\sigma^{SM}_{8\text{TeV}} \sim 2.3$ for $m_H = 125$ GeV), and the larger amount of data collected, it has been possible to perform such measurements with a higher precision (9; 10). In particular, my work focused on the most recent measurement of the Higgs boson mass exploiting the di-photon decay channel that, together with the decay of the Higgs boson in four leptons final states (i.e. $H \to ZZ^* \to 4\ell$, with $\ell = e, \mu$), is the experimental signature characterized by the best invariant mass resolution. In this manuscript the full analysis procedure is described in detail as well as the combination of the results with the mass measurement in the four lepton final states. The measured value of the Higgs boson

mass in the di-photon channel is $m_H = 125.11 \pm 0.42$ GeV, while the value obtained from the combined measurement with the $H \to ZZ^* \to 4\ell$ analysis is $m_H = 124.98 \pm 0.28$ GeV. This measurement is in excellent agreement with, and has similar precision to, the value that was measured combining ATLAS and CMS Run 1 data (11).

The discovery of the Higgs boson completed the Standard Model of particle physics, which so far has been experimentally verified to an excellent level of accuracy. However, there are still some critical points that arise both from theoretical considerations and experimental results and may indicate that a more general theory is required to describe consistently the particle physics phenomenology. Supersymmetry (SUSY)(12; 13; 14; 15; 16; 17; 18) offers a possible solution to some of these open issues. The second analysis presented in this thesis is the search for production of supersymmetric particles (gluinos, squarks or winos) in a final state containing two photons and missing transverse momentum. This final state is predicted by a particular class of Supersymmetry models known as *Gauge-Mediated Supersymmetry Breaking* (19; 20; 21; 22; 23; 24; 25) (GMSB). The GMSB models predict a gravitino (the superpartner of the graviton) as the lightest supersymmetric particle (LSP), that leads to a final state signature containing high missing transverse momentum since the LSP escapes from the detector without interacting with it. In particular in the model considered in my work, the decay chain of the gluinos produced in proton-proton collisions decay to the production of pairs of next-to-lightest supersymmetric particles, the neutralinos. Each neutralino then decays to a gravitino and one or more SM particles, with a high probability of decay into a photon and a gravitino. This model has firstly been investigated with the data collected during 2015, corresponding to an integrated luminosity of 3.2 fb^{-1} (26). The search was updated using data collected in both 2015 and 2016. Due to the increased integrated luminosity, it was possible to obtain sensitivity to two extra models characterised by a lower cross section than the one mediated by the gluino pair production. In the first model the signal arises from the production, in the pp collisions, of a degenerate triplet of the $SU(2)$ gauge partner (wino), and in the second one the signal is due to squark pair production. Both the analysis of the 2015 data and the one of the combined 2015–2016 dataset are described in this manuscript. Since no significant excess is found over the SM expectation, lower limits of 2150 GeV, 1820 GeV and 1060 GeV are set on the mass of the gluino, squark and wino respectively. These limits improve the result obtained using Run 1 data (27) by ~ 750 GeV and ~ 400 GeV for the gluino and the wino mediated models, respectively.

Summary of the manuscript and personal contributions.

This manuscript is composed by nine Chapters. The first chapter (Chap. 1) summarizes the formulation of the Standard Model, focusing on the electro-weak symmetry breaking and the Higgs mechanism. This chapter includes also a review of the main measurements of the Higgs boson properties performed by the ATLAS and CMS collaborations with the data collected at $\sqrt{s} = 7$ and 8 TeV. The second chapter (Chap. 2) describes some of the limitations of the SM and introduces Supersymmetry (SUSY) as a possible extension of the SM that can overcome these problems. The main features of SUSY are summarized, in particular a detailed description of the Minimal supersymmetric Standard Model and of supersymmetry breaking mechanism is given. The chapter is concluded by a review of the results on the search for supersymmetry in the di-photon plus missing transverse momentum final state obtained by ATLAS and CMS using the Run 1 data.

Chap. 3 and Chap. 4 describe the LHC accelerator complex and the ATLAS detector. In Chapter four special emphasis is given to the Liquid Argon electromagnetic calorimeter,

which is the main sub-detector exploited by the measurements described in this thesis. During my doctorate I worked within the Liquid Argon ATLAS group covering different operational tasks. In particular, I have been one of the on-call experts for the system that delivers the high voltage to the calorimeter electrodes. My duties ranged from solving the issues happening during the data-taking to the hardware and software maintenance during "no-beam" periods.

Chap. 5 presents the algorithms used for the reconstruction of the physics object in the ATLAS detector, with a special attention to photons and electrons. This chapter describes also a new photon and electron reconstruction algorithm recently developed for the future analysis of Run 2 data (see Sec. 5.1.4). I was directly involved in the validation of this new release of the ATLAS software and my contribution is included in a public document soon to be released by the ATLAS collaboration.

Chap. 6 details the electron and photon energy calibration. The first step of the calibration procedure relies on a Monte Carlo based multivariate calibration (Sec. 6.1). This multivariate technique was already introduced at the end of the Run 1. I developed the framework to cope with the new data-format used by ATLAS in Run 2. Moreover, I have extracted the cluster energy calibration coefficients and checked the calibration performance for each of the several ATLAS software versions released during the last three years. I also extended the application of this calibration to online-objects used by the electron and photon triggers. My contributions are included in an ATLAS Public Note (28) and in a paper, which at the time of writing this manuscript is still in preparation, that summarizes the calibration procedure and performance with the 2015 and 2016 data. Chapter six proceeds through the description of all the other steps of the photon and electron calibration chain, reporting a detailed explanation of the systematic uncertainties that affect the energy measurement, which are the most relevant sources of uncertainty in the Higgs boson mass measurement reported in the eighth chapter.

The seventh chapter (Chap. 7) describes the two main techniques to discriminate prompt photons from background photons due to neutral meson decays: photon identification, based on the longitudinal and lateral shape of the reconstructed electromagnetic shower of the photon candidate and its leakage in the hadronic calorimeter, and "isolation" of the photon with respect to nearby hadronic activity detected either in the calorimeters or in the tracker. This chapter presents also the measurement of the probability that an electron is wrongly reconstructed as a photon, using a method that I have developed. The full procedure, the systematic uncertainty evaluation and the results using the 2015 and 2016 data are detailed in Sec. 7.3. A paper summarizing the ATLAS photon identification performance in 2015 and 2016, including the results of this study, is in preparation.

Chap. 8 presents the measurement of the Higgs boson mass in the di-photon decay channel and its combination with a similar analysis in the $H \to ZZ^* \to 4\ell$ decay channel. The results, reported in this chapter, are largely based on my own work. In particular, for this measurement I built a mass dependent paramentrization of the signal model (Sec. 8.4), I have estimated the expected systematic uncertainties on the mass measurement, (Sec. 8.4), and I have created the full likelihood model (see Sec. 8.7), and extracted the final results (see Sec. 8.9). Moreover, I have investigated different sets of event categories in order to optimize the statistical and systematic uncertainties (see Sec. 8.3.1) and to cross-check the reliability of the final measurement (see Sec. 8.10). For each set of categories, I have re-implemented the full analysis, updating the signal selection, the signal model parametrization, the background model definition and the systematic uncertainties evaluation. The results presented in this chapter are included in a public

conference note (10) presented at EPS 2017 and in a paper in preparation. The photon energy scale systematic uncertainty studies and the study of the effect of the variation of the Higgs boson mass on the Higgs boson coupling measurement are also ingredients of the measurement of the Higgs boson cross-section and coupling documented in a public conference note presented at EPS 2017 (9).

The final chapter (Chap. 9) describes the search for Supersymmetry in a final state with two photons and large missing transverse momentum. Two analyses are presented. The first one uses the data collected during only 2015, while the second one exploits the ten times larger dataset collected by ATLAS in 2015 and 2016. As one of the two main analyser I was involved in almost all the steps of the analysis. I have followed the generation and validation of the background MC samples. I have also implemented both the analysis framework on which the event selection relies, and the statistical framework exploited to define the optimal signal region requirements. I have evaluated the expected contribution of the electro-weak and irreducible background events in the SR. Finally, I have performed the statistical interpretation of the results in term of signal significance or upper limit on the parameters of the model under test. The result of this analysis are included in two public documents, a paper for the 2015 analysis (26) and a conference note for the 2015+2016 analysis (29), soon to be also sent to a journal for peer-review.

Some minor contributions to other publications of the ATLAS collaboration are not included in this manuscript, such as the study and the validation of a di-photon Monte Carlo sample generated at the Next-to-Leading-Order using the Sherpa generator. This sample describes the main background for di-photon resonance searches and it was planned to be used in the search for high-mass di-photon resonances, to have a better modelling of the irreducible background (30). I also performed checks of the photon energy calibration when a large di-photon excess was initially seen in 2015 data at a mass of 750 GeV (31).

I have also contributed to the search for high mass resonances decaying to a Z boson and a photon. I validated and generated the Monte Carlo sample that describes the SM $Z\gamma$ background and is used to optimize the background model exploited by the analysis (32).

Chapter 1

The Standard Model and the Higgs boson

In this chapter I introduce the theoretical model and the main experimental results that are the reference framework for the analysis conducted during my three years of doctorate.

In Sec. 1.1 the Standard Model (SM) of elementary particles and their interactions is introduced as the fundamental theoretical model for the search presented in this manuscript. Sec. 1.2 presents the Higgs boson mechanism as a consequence of the introduction of an additional scalar field in the theory. In Sec. 1.3 the phenomenology of the Higgs boson is discussed, in particular the main production modes at hadronic colliders and its decay channels. Finally Sec. 1.4 illustrates the experimental discovery of the Higgs boson and summarizes the main measurements conducted around this new particle using the Run 1 data.

1.1 Fundamental interactions in SM

The Standard Model (SM) is the quantum field theory that as of today better describes the elementary particle interactions at small distance and at high energy.

All the known forces can be described in terms of four fundamental interactions: *electromagnetic, weak, strong* and *gravitational*.

The Standard Model represents the best theory to describe experimental data on all fundamental particles and fundamental forces apart from gravitation. Figure 1.1 shows synthetically how the Standard Model is composed.

In the SM, matter is constituted of 12 fundamental fermions with spin $\frac{1}{2}$ and their anti-particles, with identical mass and opposite quantum numbers.

The fundamental fermions are divided in two subgroups, *quarks* and *leptons*, depending on which interactions they are subject to. Each of these subgroups is composed of three doublets of increasing mass. Leptons only interact through the electromagnetic and the weak forces, with corresponding quantum numbers that are the electric charge and the weak isospin, respectively. Quarks have an additional quantum number, color, related to the strong force.

Experimentally, the main difference between leptons and quarks is that leptons can be observed as isolated particles, while quarks are always bound together to form colorless particles with integer charge, called *hadrons*. Hadrons composed by three quarks are characterized by half-integer spin and are called *baryons*, while hadrons composed by a quark anti-quark pair are integer-spin particles called *mesons*.

Other fundamental particles are the *gauge bosons*, which play the role of mediators of the forces between the elementary fermions. The photon is the mediator of the electromagnetic interaction, the Z and W bosons mediate the weak force while the strong force is carried by gluons.

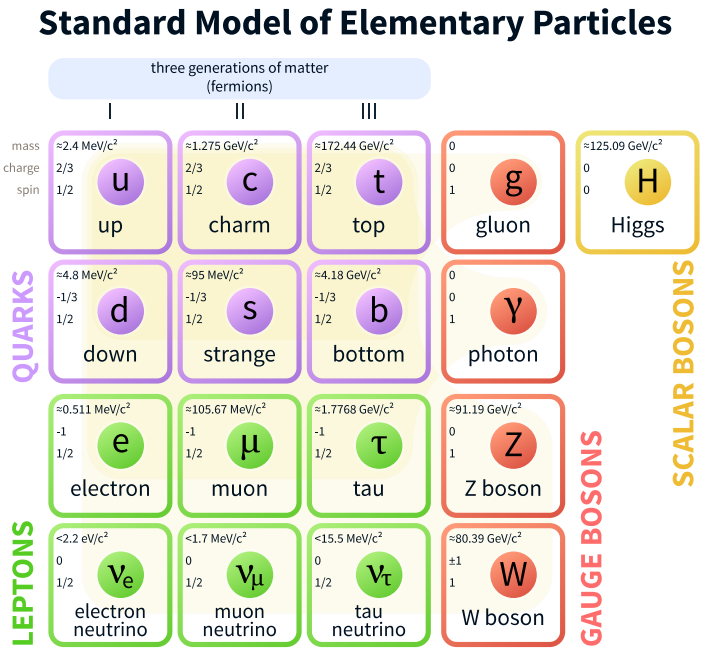

Figure 1.1: Standard Model fundamental particles (33).

Finally, the Higgs boson is a neutral fundamental scalar particle introduced in the Standard Model through the mechanism of mass generation of the gauge boson and all the other elementary particles considered in the theory.

The interactions in the mathematical formulation of the SM arise from the the invariance of the Lagrangian, which describes the kinematic of the matter fields, under local gauge symmetry transformation. These symmetries, from Noether's theorem, are associated with the conservation of some quantities (charge, color, etc.) at the point where the interaction occurs.

The requirement of invariance under local gauge symmetry makes necessary the introduction of some vector fields, called *gauge fields*, that couple to matter particles and mediate their interactions. The local gauge group symmetry chosen for the description of each interaction must have a number of generators, which corresponds to the number of vector fields added to the Lagrangian, equal to the number of mediators of the force.

1.1.1 Quantum Electrodynamics

Let us consider the Dirac Lagrangian, which describes a spinor field associated to a fermion of spin 1/2 and mass m.

$$L = i\bar{\psi}\gamma^{\mu}\partial_{\mu}\psi - m\bar{\psi}\psi. \tag{1.1}$$

This Lagrangian is invariant under global $U(1)$ transformation such as:

$$\psi \to e^{i\theta}\psi. \tag{1.2}$$

Let us consider now a local $U(1)$ gauge transformation defined as:

$$\psi \rightarrow e^{i\theta(x)}\psi, \tag{1.3}$$

where θ is a function of the time and space coordinates, denoted by x.

In order to make the Lagrangian (1.1) gauge invariant under (1.3), as required by the SM theory, it is necessary to introduce some extra terms. Such terms arise through a vector field A_μ that transforms as

$$A_\mu \rightarrow A_\mu + \frac{1}{q}\partial_\mu\theta(x), \tag{1.4}$$

where q is a free parameter that corresponds to the charge of the particle associated with the spinor field.

The Lagrangian for a free vector field A_μ, related to a spin 1 particle, is described by:

$$L = -\frac{1}{4}F^{\mu\nu}F_{\mu\nu}, \tag{1.5}$$

where $F^{\mu\nu} = (\partial^\mu A^\nu - \partial^\nu A^\mu)$ and a term $\frac{1}{2}m_A^2 A^\nu A_\nu$ is not considered because m_A is necessarily $m_A = 0$ to preserve the local gauge invariance.

After the introduction of the vector field, the new Lagrangian becomes:

$$L = -\frac{1}{4}F^{\mu\nu}F_{\mu\nu} + \bar{\psi}(i\not{D} - m)\psi, \tag{1.6}$$

where $\not{D} = \gamma^\mu D_\mu$ and D_μ is the covariant derivative defined as $D_\mu = \partial_\mu - iqA_\mu$. Expanding (1.6):

$$L = -\frac{1}{4}F^{\mu\nu}F_{\mu\nu} + [i\bar{\psi}\gamma^\mu\partial_\mu\psi - m\bar{\psi}\psi] + (q\bar{\psi}\gamma^\mu\psi)A_\mu. \tag{1.7}$$

This is the QED Lagrangian and the term $q\bar{\psi}\gamma^\mu\psi A_\mu$ describes the interactions between Dirac fields and the photon field (A_μ).

The coupling constant of the electromagnetic interactions is the fine structure constant:

$$\alpha = \frac{e^2}{4\pi\epsilon_0\hbar c} \cong \frac{1}{137}, \tag{1.8}$$

where $e = 1.602176 \times 10^{19}$ C is the electron charge, $\epsilon_0 = 8.854187 \times 10^{12}$ F·m^{-1} is the vacuum dielectric constant, $\hbar = \frac{h}{2\pi} = 1.054571 \times 10^{-34}$ J·s and h is the Planck constant, and $c = 299792458$ m·s^{-1} is the speed of light in vacuum (34).

Similarly to QED, a model that describes the strong interactions is obtained with local gauge transformations of a $SU(3)$ group, and the whole Standard Model is obtained from the gauge group $SU(3)_C \otimes SU(2)_L \otimes U(1)_Y$ as will be discussed in the following sections.

1.1.2 Quantum Chromodynamics

Strong interactions are mediated by 8 massless gluons. The gauge group that was identified as the responsible for these interactions is $SU(3)$ and the corresponding field theory is called Quantum Cromodynamics (QCD). Gluons interact not only with colored particles, i.e quarks, but also among themselves due to the non abelian structure of the $SU(3)_C$ group. It is therefore possible to have vertices with three or four gluons.

The Lagrangian of the strong interaction can be written as:

$$L_{QCD} = -\frac{1}{4}F^{i\mu\nu}F^{i}_{\mu\nu} + \sum_{r}\bar{q}_{r\alpha}i\not{D}^{\alpha}_{\beta}q^{\beta}_{r}, \tag{1.9}$$

where $q_{r\alpha}$ are the quark fields; the subscript r denotes the quark flavor (u,d,c,s,t,b) and the indices α and β run over the color quantum numbers (red, green, blue), and $F^{i}_{\mu\nu}$ is:

$$F^{i}_{\mu\nu} = \partial_{\mu}G^{i}_{\nu} - \partial_{\nu}G^{i}_{\mu} - g_{S}f_{ijk}G^{j}_{\mu}G^{k}_{\nu}. \tag{1.10}$$

f_{ijk} $(i,j,k$ =1,...,8) are the structure constants of the $SU(3)$ group and $F^{i}_{\mu\nu}$ is the field strength tensor for the gluon field G^{i}_{μ}, which depends on the QCD coupling constant.

The gauge invariance for L_{QCD} is obtained by defining the covariant derivative as:

$$D^{\alpha}_{\mu\beta} = \partial_{\mu}\delta^{\alpha}_{\beta} + ig_{S}G^{i}_{\mu}\lambda^{i\alpha}_{\beta}, \tag{1.11}$$

where the index α runs over the color quantum numbers for the gluon G^{i}_{μ} and λ^{i} are the Gell-Mann matrices that generates the $SU(3)$ symmetry.

The coupling constant for the strong interactions can be written as:

$$\alpha_{S}(\mu^{2}) = \frac{g_{S}}{4\pi} = \frac{12\pi}{(33-2n_{f})\ln\frac{\mu^{2}}{\Lambda^{2}_{QCD}}}, \tag{1.12}$$

where μ represents the energy transferred in the interaction, n_f is the number of quark flavors considered and Λ_{QCD} is the energy scale at which the perturbative QCD coupling diverges, $\Lambda_{QCD} \sim 200$ Mev/c. The pertubative expansion in QCD is valid only if $\alpha_S \ll 1$, i.e. when the energy scale of the process is much higher than Λ_{QCD}, $\mu^2 \gg \Lambda_{QCD}$.

The dependence of α_S on μ^2 is connected to a dependence on the distance between quarks. For a short distance (i.e for a large value of μ^2) the coupling between quarks goes to zero. In the limit situation where $\mu^2 \to \infty$ quarks behave as free particles. This regime is called *asymptotic freedom*. In the opposite situation of small μ^2, or large distance, the coupling between quarks becomes so strong that it is not possible to extract them from hadrons. This property is called *confinement* of quarks.

When attempting to extract a quark from a hadron, because of the increase of the potential energy due to the enlargement of the separation between quarks, new quark-antiquark pairs and gluons are produced. The process can then proceed with the creation of more pairs (*fragmentation*), since all the created quarks and antiquarks are bounded in colorless hadrons, in a process called *hadronization*.

1.1.3 Electro-Weak interaction

The modern theory of the weak interactions is rooted in the theory of β decay, which has been elaborated by Enrico Fermi in 1930. It is characterized by a Vector-Axial interaction that violates parity conservation. The charged weak current indeed affects only *left-handed* fermions and *right-handed* antifermions.

The weak charged-current interaction arises from a $SU(2)_L$ symmetry, where the subscript L means that only left-handed chirality states participate to these interaction; left-handed fermions are grouped into weak isospin doublets with $T = \frac{1}{2}$ and $T_3 = \pm\frac{1}{2}$ and right-handed fermions are classified in weak isospin singlets ($T = 0$, $T_3 = 0$). The mediators of this interaction are $W^{\pm}$ and Z bosons.

Today it is known that the weak and the electromagnetic interactions are different aspects of a common interaction, called electro-weak (EW), described by a larger gauge symmetry group. This group is: $SU(2)_L \times U(1)_Y$, where Y represents the weak hypercharge, that is related to the electric charge Q and the third component T_3 of weak isospin by the equation:

$$Q = T_3 + \frac{Y}{2}. \tag{1.13}$$

The generators of the $SU(2)_L \times U(1)_Y$ gauge symmetry group corresponds to four bosons: W^1, W^2, W^3 ($SU(2)_L$) and B ($U(1)_Y$).

The local gauge invariance is obtained by defining the covariant derivative D_μ as:

$$D_\mu = (\partial_\mu + igT_iW_\mu^i + \frac{ig'}{2}YB_\mu). \tag{1.14}$$

where T_i are the three components of the weak isospin and Y is the operator of the weak hypercharge. As a consequence, the interaction part of the electro-weak Lagrangian can be written as:

$$L_{EW}^{int} = -\frac{g'}{2}(\bar{\psi}\gamma^\mu\psi)B_\mu - g(\bar{\psi}_L\gamma^\mu T_i\psi_L)W_\mu^i, \tag{1.15}$$

The $U(1)_Y$ group can not be directly associated to electromagnetism because the B boson interacts in the same way with the two components of the left-handed doublet (e_L and ν_L), while the photon does not couple to neutrinos, which are neutral particles.

The electromagnetic interaction, mediated by the photon field A_μ, and the neutral weak current interaction, mediated by the Z boson field Z_μ, arises instead from a mixing of the W^3 and B field.

$$\begin{pmatrix} A_\mu \\ Z_\mu^0 \end{pmatrix} = \begin{pmatrix} \cos\theta_W & \sin\theta_W \\ -\sin\theta_W & \cos\theta_W \end{pmatrix} \cdot \begin{pmatrix} B_\mu \\ W_\mu^3 \end{pmatrix}, \tag{1.16}$$

where θ_W is the weak-mixing angle, also called Weinberg angle, with $\sin^2\theta_W = 0.23129 \pm 0.000022$ (34). Moreover, the $W^\pm$ bosons are a linear combination of W^1 and W^2:

$$W^\pm = \frac{1}{\sqrt{2}}(W^1 \mp iW^2). \tag{1.17}$$

The electric charge is related to the coupling constants of $SU(2)_L$ and $U(1)_Y$ by the equation:

$$g\sin\theta_W = g'\cos\theta_W = e. \tag{1.18}$$

The coupling constant for the weak neutral current, mediated by the Z boson, becomes:

$$g_Z = \frac{e}{\sin\theta_W\cos\theta_W}(T_3 - Q\sin^2\theta_W). \tag{1.19}$$

1.2 The Higgs mechanism

1.2.1 Spontaneous symmetry-breaking

The Standard Model Lagrangian, presented in the previous section, describes vector bosons and fermions that must be necessarily massless to preserve local gauge invariance, but the $W^\pm$ and Z^0 vector bosons that mediate weak interactions are massive, as

well as most of the fermions. The problem of introducing the masses in the Standard Model keeping local gauge invariance was solved by the Higgs mechanism proposed in 1964 by Higgs, Brout, Englert, Guralnik, Hagen and Kibble (6; 7; 8).

Here an example (35) is given to show how this mechanism works.

Consider a complex scalar field

$$\phi = \frac{1}{\sqrt{2}}(\phi_1 + i\phi_2) \tag{1.20}$$

coupled both to itself and to an electromagnetic field:

$$L = -\frac{1}{4}(F_{\mu\nu}F^{\mu\nu})^2 + |D_\mu\phi|^2 - V(\phi), \tag{1.21}$$

where $D_\mu = \partial_\mu + ieA_\mu$. This Lagrangian is invariant under the U(1) local transformation

$$\phi(x) \to e^{i\alpha(x)}\phi(x), A_\mu(x) \to A_\mu(x) - \frac{1}{e}\partial_\mu\alpha(x). \tag{1.22}$$

The potential $V(\phi)$ is defined as:

$$V(\phi) = \mu^2\phi^*\phi + \frac{\lambda}{2}(\phi^*\phi)^2. \tag{1.23}$$

For $\mu^2 > 0$ the potential has a minimum for $\phi_1 = \phi_2 = 0$, otherwise with $\mu^2 < 0$ the minimum occurs at

$$\langle\phi\rangle = \phi_0 = e^{i\theta}\left(\frac{-\mu^2}{\lambda}\right)^{\frac{1}{2}} \qquad 0 \le \theta \le 2\pi. \tag{1.24}$$

In this latter case there are infinite possible states of minimum potential, but the field

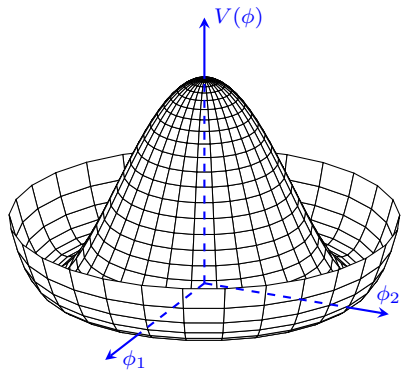

Figure 1.2: Shape of the "Mexican hat" potential in two dimensions as a function of the field components ϕ_1 and ϕ_2 .

ϕ acquires only a single vacuum expectation value and as a consequence the $U(1)$ local symmetry is *spontaneously broken*. For simplicity θ is taken equal to zero and $\phi(x)$ can be rewritten as:

$$\phi(x) = \phi_0 + \frac{1}{\sqrt{2}}(\phi_1(x) + i\phi_2(x)) \qquad \text{with} \quad \phi_0 = \left(\frac{-\mu^2}{\lambda}\right)^{\frac{1}{2}}, \tag{1.25}$$

where now ϕ_1 and ϕ_2 are the physical fields representing the excitations of the field ϕ around the minimum. The potential (1.23) becomes:

$$V(\phi) = +\frac{1}{2\lambda}\mu^4 + \frac{1}{2}(2\mu^2\phi_1^2) + \mathcal{O}(\phi_i^3), \tag{1.26}$$

so that the field ϕ_1 acquires the mass $m = \sqrt{-2\mu^2}$ and ϕ_2 is massless.

The latter field is a *Goldstone boson* (36) and it is generated in the spontaneous symmetry breaking. The Goldstone theorem states that given a Lagrangian that is invariant under a group of continuous transformation with N generators, if M of N generators are spontaneously broken, in the particle spectrum of the theory, developed around the vacuum expectation value, there will be M massless particles. Although the Goldstone boson is important in the spontaneously symmetry breaking, it does not appear as an independent physical particle. Using the local $U(1)$ gauge symmetry (1.22), it is possible to choose an $\alpha(x)$ in such a way that $\phi(x)$ becomes real for each value of x (*unitarity gauge*). Given (1.25), the field ϕ_2 is thus removed from the theory.

The kinetic energy $|D_\mu\phi|^2$ is described by:

$$|D_\mu\phi|^2 = \frac{1}{2}(\partial_\mu\phi)^2 + e^2\phi_0^2 A_\mu A^\mu + ..., \tag{1.27}$$

where cubic and quartic term in the fields A_μ, ϕ are omitted. The last term is the gauge boson A_μ mass term:

$$\frac{1}{2}m_A^2 A_\mu A^\mu \qquad m_A^2 = 2e^2\phi_0^2. \tag{1.28}$$

Finally the Lagrangian (1.21) becomes:

$$L = -\frac{1}{4}(F_{\mu\nu})^2 + (\partial_\mu\phi)^2 + e^2\phi^2 A_\mu A^\mu - V(\phi). \tag{1.29}$$

1.2.2 The Standard Model Higgs boson

The Higgs mechanism is used to introduce the mass terms in the Lagrangian of the Standard Model. Therefore the local gauge symmetry group to be considered is $SU(2) \times U(1)$ and the resulting theory, after spontaneous symmetry breaking, must still include QED with its unbroken $U(1)$ symmetry, since the photon must not acquire a mass. Hence the vacuum expectation value must be invariant under $U(1)$.

Only the electro-weak part of the SM is considered since the generator of SU(3) group are the gluons that are massless. Therefore the Lagrangian of the strong interaction can be factorized in the description of the mechanism of mass generation, since it does not contain mass related terms.

The Higgs mechanism introduces a complex doublet of scalar fields

$$\phi = \begin{pmatrix} \phi^+ \\ \phi^0 \end{pmatrix} = \frac{1}{\sqrt{2}} \begin{pmatrix} \phi_1 + i\phi_2 \\ \phi_3 + i\phi_4 \end{pmatrix}, \tag{1.30}$$

with the scalar Lagrangian L_ϕ

$$L_\phi = (D^\mu\phi)^\dagger(D^\mu\phi) - \mu^2\phi^\dagger\phi - \lambda(\phi^\dagger\phi)^2. \tag{1.31}$$

The canonical choice for the potential ground state (see Section 1.2.1) is given by

$$\phi_1 = \phi_2 = \phi_4 = 0, \qquad \phi_3 = \nu, \qquad \nu = \left(\frac{-\mu^2}{\lambda}\right)^{\frac{1}{2}}, \tag{1.32}$$

$$\phi_0 = \frac{1}{\sqrt{2}} \begin{pmatrix} 0 \\ \nu \end{pmatrix}. \tag{1.33}$$

Then it is possible to write the field ϕ as an expansion around the vacuum expectation value:

$$\phi_0 = \frac{1}{\sqrt{2}} \begin{pmatrix} 0 \\ \nu + H(x) \end{pmatrix}. \tag{1.34}$$

where, using the unitarity gauge, $H(x)$ is a scalar real field.

As shown in Section 1.1.3 the gauge fields $W_\mu^{1,2,3}$ and B_μ can be written as mass eigenstates for the $W^\pm$, Z^0 and A bosons. It is then possible to write the gauge Lagrangian $SU(2)_L \times U(1)_Y$ together with the scalar Lagrangian $\mathcal{L}_\phi$ as:

$$\begin{aligned} \mathcal{L}_\phi + \mathcal{L}_{gauge} \quad &= \tfrac{1}{2}\partial_\mu H \partial^\mu H + \mu^2 H^2 - \lambda\nu\sigma^3 - \tfrac{\lambda}{4}H^4 + \\ &+ \left(\tfrac{g\nu}{2}\right)^2 W_\mu^+ W^{-\mu} + \tfrac{1}{2}\left(\tfrac{g^2+g'^2}{4}\right)\nu^2 Z_\mu Z^\mu + \\ &+ \tfrac{1}{2}g^2\nu W_\mu^+ W^{-\mu} H + \tfrac{g^2\nu}{2}\tfrac{1}{2\cos(\theta_w)^2} Z_\mu Z^\mu H + \\ &+ \tfrac{g^2}{4} W_\mu^+ W^{-\mu} H^2 + \tfrac{g^2}{4}\tfrac{1}{2\cos(\theta_w)} Z_\mu Z^\mu \sigma^2 \end{aligned} \tag{1.35}$$

The first line describes the kinetic term and the self-coupling of the H scalar field, the second line the mass terms of the W and Z field, the third and fourth lines describe the coupling between the field H and the gauge bosons.

Thus the masses of the W and Z vector bosons can be written as:

- $m_W = \frac{g\nu}{2} = 81$ GeV
- $m_Z = \frac{\nu\sqrt{g^2+g'^2}}{2} = \frac{g\nu}{2\cos\theta_W} = \frac{m_W}{\cos\theta_W} = 91$ GeV.

and the field $H(x)$ is a scalar particle with mass

$$m_H = \sqrt{-2\mu^2} = \sqrt{2\lambda\nu^2}, \tag{1.36}$$

where ν is the Higgs vacuum expectation value, $\nu \sim 246$ GeV as measured via muon decay (37):

$$\nu = \sqrt{\frac{1}{\sqrt{2}G_F}}, \tag{1.37}$$

where G_F is the Fermi coupling constant, $G_F = 1.1663787 \times 10^{-5}\,\text{GeV}^{-2}$. Thus the scale of the Higgs mass is controlled by the vacuum expectation value of the field, but its precise theoretical value is unknown because of the new coupling constant λ. This result is important from a phenomenological point of view, because the theoretical model does not provide direct information about the mass range of the Higgs boson.

The coupling between the gauge bosons and the Higgs boson depends on the W and Z masses. Rewriting the coupling terms this behavior becomes explicit.

- $\frac{1}{2}g^2\nu W_\mu^+ W^{-\mu} H = 2\frac{m_W^2}{\nu}\, W_\mu^+ W^{-\mu} H$,

- $\frac{g^2\nu}{2}\frac{1}{2\cos(\theta_w)^2}Z_\mu Z^\mu H = \frac{m_Z^2}{\nu}Z_\mu Z^\mu H.$

Moreover, mass terms for the fermions that would have violated the gauge symmetry are now allowed by the scalar doublet and its charge conjugate.

Using the complex Higgs doublet it is possible to form the vertex

$$-\lambda_f \bar{\psi_L}\phi\psi_R, \tag{1.38}$$

that is invariant under $SU(2)_L \times U(1)_Y$.

In the Lagrangian of the Standard Model it is thus possible to include a a term that couples the Higgs doublet to a fermion mass as:

$$\mathcal{L}_{fermion-mass} = -\lambda_f[\bar{\psi}_L\phi\psi_R + \bar{\psi}_R\bar{\phi}\psi_L], \tag{1.39}$$

where λ_f is the Yukawa coupling constant for fermion f.

Considering for simplicity only the electronic flavor and the scalar field ϕ, expressed in the unitarity gauge as Eq. (1.34), Eq. (1.39) becomes:

$$\begin{aligned}
\mathcal{L}_e &= -\lambda_e\tfrac{1}{\sqrt{2}}\left[(\bar{\nu},\bar{e})_L\begin{pmatrix}0\\ \nu+H\end{pmatrix}e_R + \bar{e_R}(0,\nu+H)\begin{pmatrix}\nu\\ e\end{pmatrix}_L\right] \\
&= -\tfrac{\lambda_e(\nu+H)}{\sqrt{2}}[\bar{e}_L e_R + \bar{e}_R e_L] \\
&= -\tfrac{\lambda_e(\nu+H)}{\sqrt{2}}\bar{e}e \\
&= -\tfrac{\lambda_e\nu}{\sqrt{2}}\bar{e}e - \tfrac{\lambda_e}{\sqrt{2}}H\bar{e}e.
\end{aligned} \tag{1.40}$$

The first term is the mass term for the electron, where the mass is:

$$m_e = \frac{\lambda_e\nu}{\sqrt{2}}. \tag{1.41}$$

The second term describes the coupling of the electron to the Higgs field, which is proportional to the mass of the electron itself:

$$\frac{\lambda_e}{\sqrt{2}} = \frac{m_e}{\nu}. \tag{1.42}$$

In conclusion in the unitarity gauge, the mass term and the interaction with the Higgs boson for any quark or lepton is described by the Lagrangian term:

$$\mathcal{L}_f = -m_f\bar{f}f\left(1+\frac{H}{\nu}\right). \tag{1.43}$$

1.2.3 Theoretical constraints on the Higgs boson mass

The Higgs boson mass defined as $m_H = \sqrt{2\lambda\nu^2}$ in Eq. 1.36 is not predicted by the SM. Although ν is known ($\sim$ 246 GeV), λ is a free parameter of the theory and therefore also m_H is unconstrained. However, before the discovery of a new particle compatible with the SM Higgs boson was announced by the ATLAS (4) and CMS (5) collaborations in 2012, theoretical and experimental constraints were available to restrict the range of the allowed values of the Higgs boson mass. In particular the possibility to extend the Standard Model at higher energy regimes imposes different upper and lower limits on the Higgs boson mass (38).

- The *unitarity* requirement constrains the Higgs boson mass to be below ~ 700 GeV. In the Standard Model the Higgs boson plays an important role in the cancellation of high-energy divergences. The $W^+W^- \to W^+W^-$, vector boson scattering, for instance, without the introduction of the correction due to a Higgs boson lighter than around 700 GeV will diverge, growing proportionally to the center-of-mass energy. Therefore the unitarity of the theory is preserved if the Higgs boson mass is lower than approximately 700 GeV or if new physics is introduced at the scale of 1 TeV.

- The *renormalization* and *triviality* of the electro-weak theory set a stronger upper limit. From the renormalization, the Higgs boson quartic self-coupling is expected to increase with the energy of the interaction. In order to preserve the validity of the SM until any arbitrary scale, the SM should become a non-interacting (trivial) theory. Imagining the Standard Model as the low-energy limit, below a scale Λ, of a more complete theory, there is an upper limit on the possible values of m_H. If Λ is equal to the electro-weak scale ($\sim 1 \times 10^3$ GeV) the Higgs boson mass must be lower than 1 TeV. If the validity of the Standard Model extends up to the scale of the Grand Unification Theory (GUT), $\Lambda \sim 1 \times 10^{16}$ GeV, the Higgs boson could have mass up to $m_H = 200$ GeV (see Figure 1.3).

- The *vacuum stability* bound implies a lower limit on m_H. If the Higgs boson self-coupling is considered for a low-mass Higgs boson, loops with fermions and gauge bosons must be included in the radiative correction to the self coupling. The dominant correction is due to the top quark that contributes with a negative sign. If m_H is too low, the sign of the quartic term in the scalar potential is flipped and it is not possible to find a ground state about which the Lagrangian can be expanded. Therefore the Higgs boson mass is required to lie above a certain value depending on the cut-off Λ as shown in Figure 1.3.

1.3 The Higgs boson phenomenology at hadron colliders

1.3.1 The Higgs boson production modes at the LHC

In the proton-proton collisions at the LHC, the Higgs boson is expected to be produced mainly through the leading-order diagrams shown in Figures 1.4-1.7 (40): $gg \to H$ gluon-gluon fusion (ggF), vector boson fusion (VBF), associated production with a vector boson (WH and ZH, denoted together as VH), associated production with a top anti-top quark pair (ttH) or $b\bar{b}$ pair (bbH) and finally $t + H$ production. Figure 1.8 displays the most important Higgs production cross section at $\sqrt{s} = 13$ at the LHC, as a function of m_H (41).

For $m_H \lesssim 1$ TeV the dominant production cross-section is given by the gluon fusion process, mediated by the exchange of a heavy top quark (43). Since the Higgs boson couplings with quarks are described by Eq. (1.43) the contributions from lighter quarks are suppressed proportionally to $\frac{m_q^2}{m_t^2}$. A complete calculation of the $gg \to H$ cross section is available at the next-to-next-to-leading order (NNLO), and a next-to-next-to-next-to-leading order (N^3LO) calculation has been performed in the limit of $m_t \to \infty$ (44). The most updated value for the production cross-section of a Higgs boson with $m_H = 125$ GeV via gluon fusion process at the LHC at $\sqrt{s} = 13$ TeV is (41):

$$\sigma_{ggF} = 48.6 \text{ pb}^{+2.22 \text{ pb } (+4.56\%)}_{-3.27 \text{ pb } (-6.72\%)} \text{ (theory)} \pm 1.56 \text{ pb}(3.20\%)(\text{PDF} + \alpha_s), \tag{1.44}$$

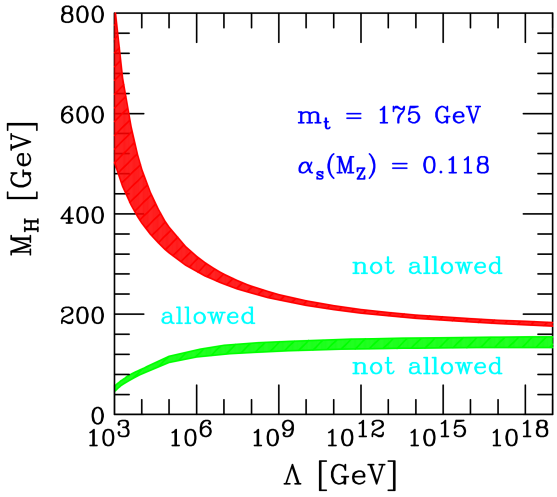

Figure 1.3: Theoretical constraints for the Higgs boson mass as a function of the energy scale Λ for the validity of the Standard Model. The upper red band corresponds to the triviality bound and its uncertainty, while the lower green band corresponds to the vacuum stability bound and its uncertainty (38; 39).

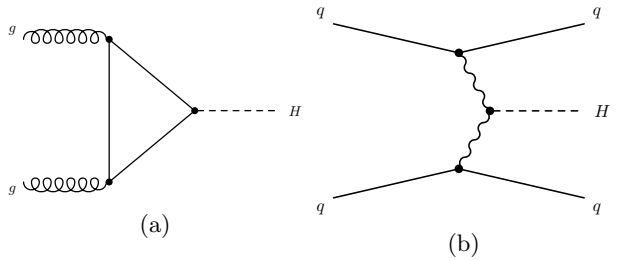

Figure 1.4: Examples of leading-order Feynman diagrams for Higgs boson production via the (a) ggF and (b) VBF production processes (40).

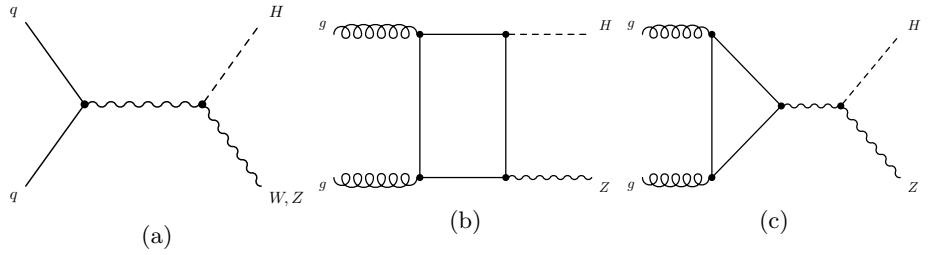

Figure 1.5: Examples of leading-order Feynman diagrams for Higgs boson production via the (a) $qq \to VH$ and (b, c) $gg \to ZH$ production processes (40).

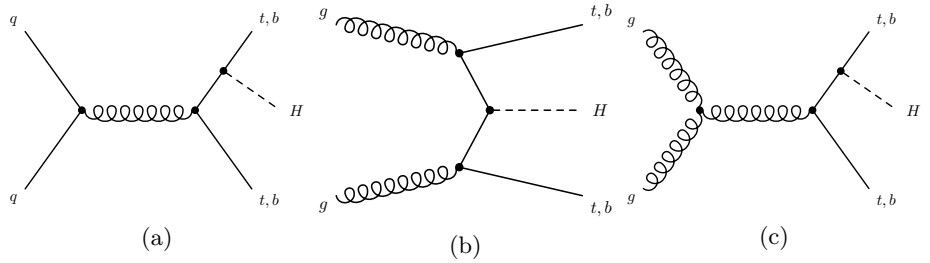

Figure 1.6: Examples of leading-order Feynman diagrams for Higgs boson production via the $qq/gg \to t\bar{t}H$ and $qq/gg \to b\bar{b}H$ processes (40).

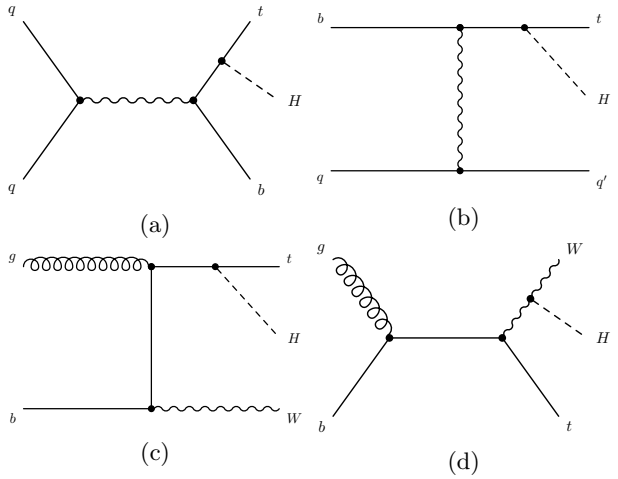

Figure 1.7: Examples of leading-order Feynman diagrams for Higgs boson production in association with a single top quark via the (a, b) tHq and (c, d) tHW production processes (40).

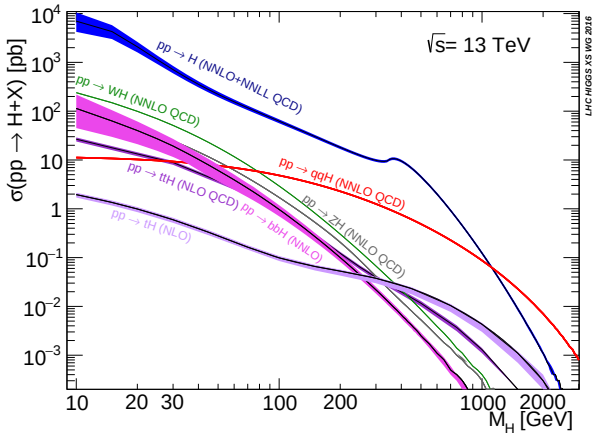

(a)

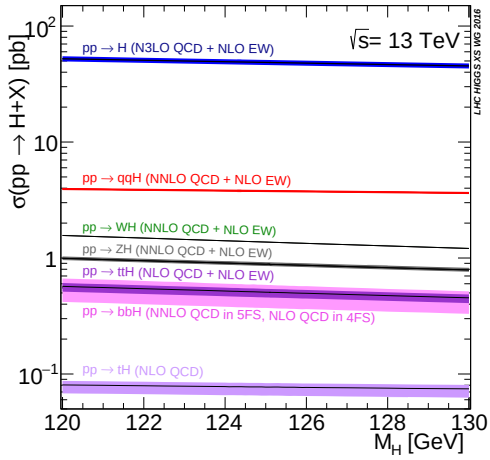

(b)

Figure 1.8: Standard Model Higgs boson production cross-section in $\sqrt{s} = 13$ TeV pp collisions as a function of the Higgs boson mass (42; 41), for a large range of masses (a) and for $m_H \in [120, 130]$ GeV (b), where the uncertainties are represented by the width of the colored line for each production mode displayed.

where the total uncertainty is less than 10%.

For 100 GeV $< m_H <$ 1000 GeV the SM Higgs production mode with the second-largest cross section at the LHC is VBF. It contributes up to $\sim$ 10% of the total production cross-section for $m_H = 125$ GeV. Vector boson fusion proceeds through the scattering of two incoming quarks mediated by the exchange of a W or a Z boson, which radiates the Higgs boson. The VBF has a clear experimental signature that consists in the presence of two jets, generated by the hadronization of the two quarks involved in the scattering process, in the forward region of the detector, close to the beam pipe, and little hadronic activity in the region between the 2 jets.

The next most relevant Higgs boson production mode at the LHC is the associated production with a W or Z vector boson. Most of the VH cross section is due to $q\bar{q}$ annihilation into an off-shell W or Z boson which then radiates a Higgs boson; for this reason, this process is also known as "Higgsstrahlung". For ZH production there are also gluon-gluon induced contributions that do not involve a virtual Z boson, but produce H and Z through a top quark loop. The $gg \to ZH$ production can be considered as a standalone process whose contribution starts at $O(\alpha_S^2)$, and it is described by the Feynman diagrams shown in Figures 1.5b and 1.5c.

Finally, the $b\bar{b}H$, $t\bar{t}H$ and tH production modes are characterized by the lowest cross sections and are particularly challenging to isolate from an experimental point of view; however, since the Higgs boson couples directly to quarks, the study of these productions modes can provide important information on the top-Higgs Yukawa coupling.

1.3.2 The Higgs boson decays

The Higgs boson is predicted to have no appreciable lifetime and to decay immediately into bosonic or fermionic final states.

The branching ratio of any single possible final state is defined as the ratio between the relative partial width for that final state over the total width, which is defined as the sum of the relative widths of all the possible Higgs boson decay modes:

$$BR(H \to X) = \frac{\Gamma(H \to X)}{\sum_i \Gamma(H \to X_i)} \tag{1.45}$$

Figure 1.9 shows the expected branching ratio for the decays of the SM Higgs boson as a function of its mass between 80 GeV and 1 TeV

Depending on m_H, different strategies are exploited to search for the Higgs boson.

- At very low mass ($m_H <$ 120 GeV), the Higgs boson decays mainly to a $b\bar{b}$ pair; however, due to the high cross-section of the QCD background processes with the same experimental signature, an inclusive search in the $b\bar{b}$ channel has very low sensitivity. To overcome this problem, the H$\to$ $b\bar{b}$ decay is only searched in the associated VH and $t\bar{t}H$ production modes.

- For 120 $< m_H <$ 130 GeV: the $H \to \gamma\gamma$ decay proceeds via loop diagram with main contributions from W boson and top quark loops. The leading-order Feynman diagrams for this process are shown in Figure 1.10 (40). Despite its small branching fraction ($\sim$ 0.23 % for $m_H = 125$ GeV), in the low mass range ($m_H \lesssim 125$ GeV) $H \to \gamma\gamma$ decay provides, togheter with the $H \to ZZ^*$ decay, the highest signal sensitivity to a SM Higgs boson signal, due to the excellent $\gamma\gamma$ invariant mass resolution ($\sim$1-2% (34)), which provides good discrimination of the irreducible continuous diphoton background.

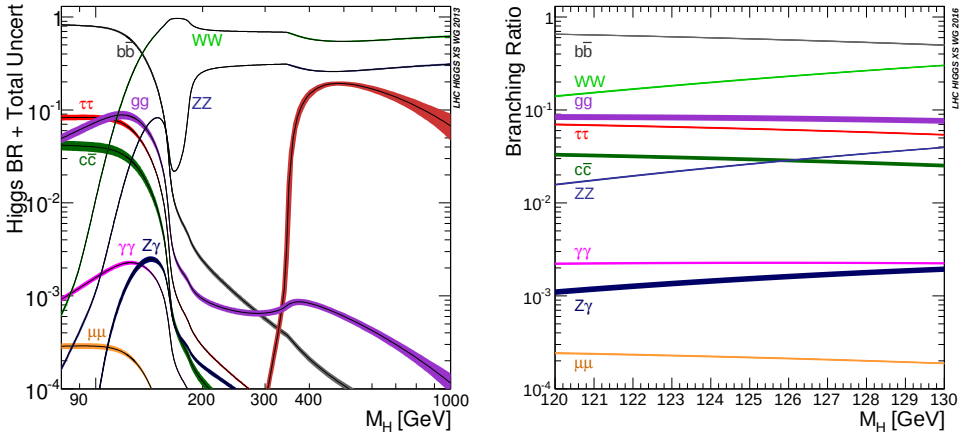

(a) (b)

Figure 1.9: Standard Model Higgs boson decay branching ratios as a function of the Higgs boson mass hypothesis (41; 42), for a large range of masses (a) and for $m_H \in [120, 130]$ GeV (b), where the uncertainties are rapresented by the width of the coloured line for each decay mode displayed.

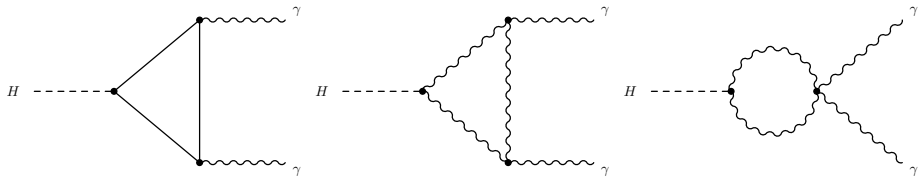

Figure 1.10: Examples of leading-order Feynman diagrams for Higgs boson decays to a pair of photons (40).

- For 130 GeV$< m_H$ the $H \to WW^{(*)} \to l\nu l\nu$ and $H \to ZZ$ decays become the channels with highest sensitivity. In particular $H \to ZZ^{(*)} \to 4l$ decay is considered the so-called *golden channel* because it has a good invariant mass resolution ($\sim$ 1-2% (34)), and, even if the total $H \to ZZ^{(*)} \to 4l$ production rate is extremely low, this channel has almost no background contributions.

Table 1.1 shows the branching ratios to various final states and the relative uncertainty for a SM Higgs boson with $m_H = 125$ GeV (42; 41; 34).

1.4 The Higgs boson discovery and property measurements at $\sqrt{s} = 7$ and 8 TeV

On July 4th, 2012, the ATLAS and CMS collaborations announced the discovery of a new particle compatible with the Higgs boson predicted by the Standard Model, with a mass around 125 GeV, with the significance shown in Figure 1.11. Moreover, the same results excluded a wider mass interval for other possible Higgs bosons with the properties predicted by the Standard Model. They allow only a light SM Higgs boson

Table 1.1: The branching ratios and the relative uncertainty for a SM Higgs boson with $m_H = 125$ GeV (34; 41; 42).

Decay channel	Branching ratio	Rel. uncertainty [%]
$H \to \gamma\gamma$	2.27×10^{-3}	$^{+5.0}_{-4.9}$
$H \to ZZ$	2.62×10^{-2}	$^{+4.3}_{-4.1}$
$H \to W^+W^-$	2.14×10^{-1}	$^{+4.3}_{-4.2}$
$H \to \tau^+\tau^-$	6.27×10^{-2}	$^{+5.7}_{-5.7}$
$H \to b\bar{b}$	5.84×10^{-1}	$^{+3.2}_{-3.3}$
$H \to Z\gamma$	1.53×10^{-3}	$^{+9.0}_{-8.9}$
$H \to \mu^+\mu-$	2.18×10^{-4}	$^{+6.0}_{-5.9}$

with $m_H \sim 125$ GeV (or very heavy one, with $m_H \gtrsim 500$ GeV) as it is shown in Figure 1.12.

After the discovery of this new particle the two collaborations focused on the determination of its properties and quantum numbers, and the verification of their compatibility with the SM predictions. The next paragraphs will summarize briefly the measurements performed by ATLAS and CMS on the mass, the main production and decay rates, and the spin and the parity of the new particle using the full Run 1 dataset corresponding to an integrated luminosity of approximately 5 fb^{-1} collected at $\sqrt{s} = 7$ TeV and 20 fb^{-1} collected at $\sqrt{s} = 8$ TeV.

1.4.1 The Higgs boson mass measurement

The $H \to \gamma\gamma$ and $H \to ZZ^* \to 4\ell$ decay channels allow the most precise measurement of the Higgs boson mass, since the energy and direction of the final state particles (i.e γ, e, μ) can be reconstructed with an excellent precision. As shown in Table 1.2, they are characterized by the best mass resolution among the main Higgs decay channels investigated at the LHC, ranging from 1.4 GeV to 2 GeV for ATLAS and from 1.0 GeV to 2.8 GeV for CMS (34). In these two channels the Higgs boson can be observed as a

Table 1.2: The five main decay channels to search for a SM Higgs boson with $m_H \sim 125$ GeV at the LHC and their invariant mass resolution in the ATLAS detector (34).

Decay channel	Mass resolution
$H \to \gamma\gamma$	1-2%
$H \to ZZ$	1-2%
$H \to W^+W^-$	20%
$H \to b\bar{b}$	15%
$H \to \tau^+\tau^-$	15%

narrow mass peak over a non resonant background. The background arises from prompt $\gamma\gamma$, γ+jet and di-jet processes for the $H \to \gamma\gamma$ channel; the $H \to ZZ^* \to 4\ell$ channel is characterized by a continuous background dominated by non-resonant ZZ^* production and with sub-dominant contributions from Z+jets and $t\bar{t}$ events.

In order to improve the accuracy of the mass measurement the selected events are separated in mutually exclusive categories that have different signal-to-background ratios, different invariant mass resolutions and different source of systematic uncertainties.

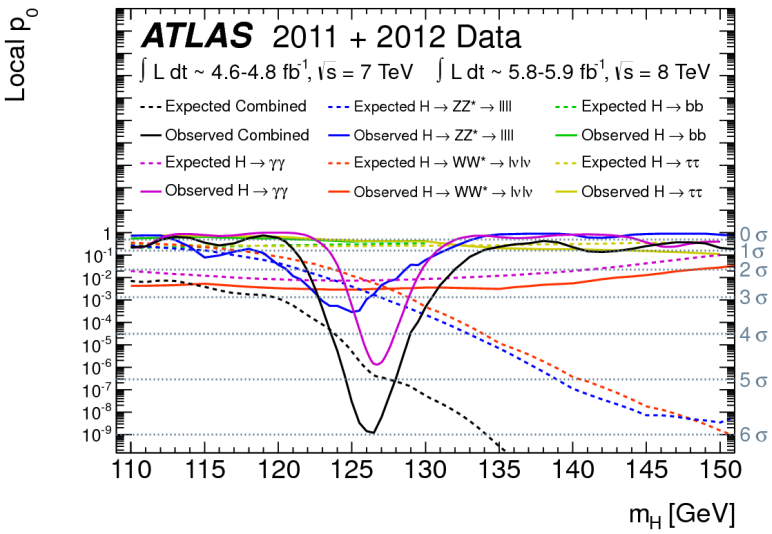

(a)

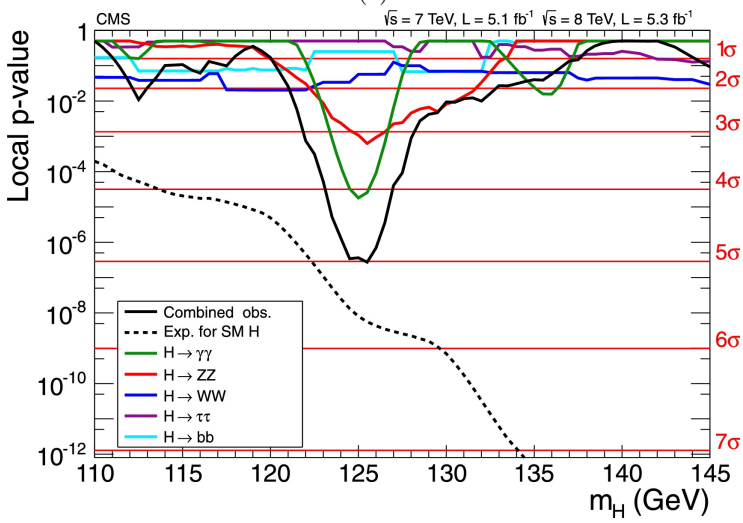

(b)

Figure 1.11: The local probability p_0 measured by ATLAS (4) (a) and CMS (5) (b) for a background-only experiment to be more signal-like than the observation, for individual channels and the combination in the low mass range of 110< $m_{\gamma\gamma}$ < 150 GeV (a) and 110< $m_{\gamma\gamma}$ < 145 GeV (b). The full curves give the observed individual and combined p_0. The dashed curves show the median expected value under the hypothesis of a SM Higgs boson signal at that mass. The horizontal lines indicate the p_0 corresponding to significances of 0σ to 6σ (a) and of 1σ to 7σ (b).

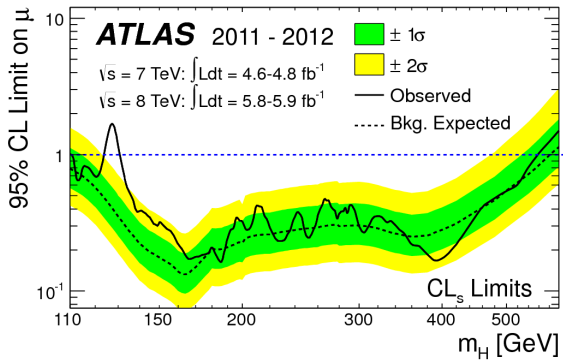

Figure 1.12: The observed (solid) 95% CL upper limit on the signal strength as a function of m_H and the expectation (dashed) under the background-only hypothesis. All the mass values, for which the solid curve lies below 1, are excluded (4).

For instance the ATLAS measurement in the di-photon channel is obtained using ten categories that are defined based on the photon type (unconverted/converted)and pseudorapidity, and the di-photon p_{Tt}, *i.e.* the component of the di-photon transverse momentum orthogonal to the di-photon thrust axis in the transverse plane (see Sec 8.3.2).

The Figures 1.13 and 1.14 show the invariant mass distributions of the $H \to \gamma\gamma$ and $H \to ZZ \to 4\ell$ channels obtained with the full Run 1 dataset (45; 46).

The results obtained from the individual channels and from their combination are summarized in Figure 1.15 (11).

The combined measurement of the Higgs boson mass in the $H \to \gamma\gamma$ (45; 47) and $H \to ZZ^* \to 4\ell$ (46; 48) channels with the ATLAS and CMS experiments gave as result (11):

$$m_H = 125.09 \pm 0.21(\text{stat.}) \pm 0.11(\text{syst.}) \text{ GeV}. \tag{1.46}$$

The main systematic uncertainty contribution arises from the energy scale of the photons.

In particular, the ATLAS measurement of the Higgs boson mass in the $H \to \gamma\gamma$ channel (45) is:

$$m_H = 126.02 \pm 0.43(\text{stat.}) \pm 0.27(\text{syst.}) \text{ GeV}. \tag{1.47}$$

1.4.2 The Higgs boson production and decay rate measurement

The ATLAS and CMS collaboration reported a combined measurement of the Higgs boson production and decay rates based on the Run 1 dataset (40). The main production modes considered are ggF, VBF, VH, ttH. The decay channels considered are those to bosons $H \to \gamma\gamma$ (49; 47), $H \to ZZ$ (46; 48), $H \to WW$ (50; 51; 52), and those to fermions $H \to \tau\tau$ (53; 54), and $H \to b\bar{b}$ (55; 56). Each decay mode is investigated by a dedicated analysis by each experiment.

The combination of the ATLAS and CMS results is performed through a global fit to over 600 categories, that are used in the individual analyses to improve the sensitivity and to discriminate among different production process. Typically each category covers mostly one decay mode, but possibly various production modes.

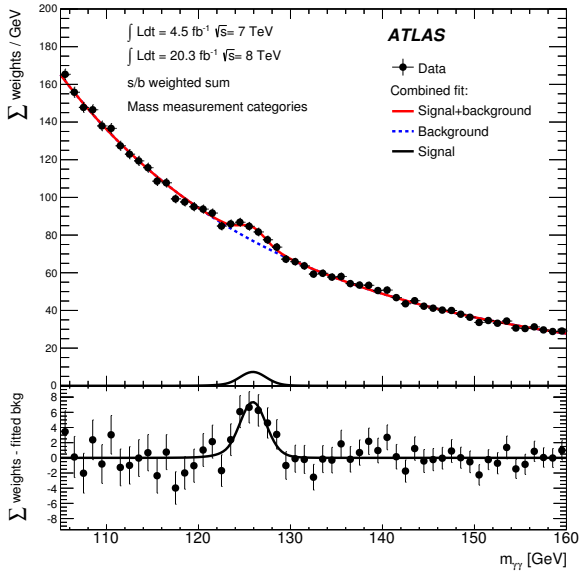

Figure 1.13: The di-photon invariant mass distribution in the $H \to \gamma\gamma$ analysis for selected data events (7 TeV and 8 TeV samples combined), showing weighted data points with errors, and the result of the simultaneous fit to all the categories. The fitted signal plus background is shown, along with the background-only component of this fit. The different categories are summed together with a weight given by the s/b ratio in each category. The bottom plot shows the difference between the summed weights and the background component of the fit (45).

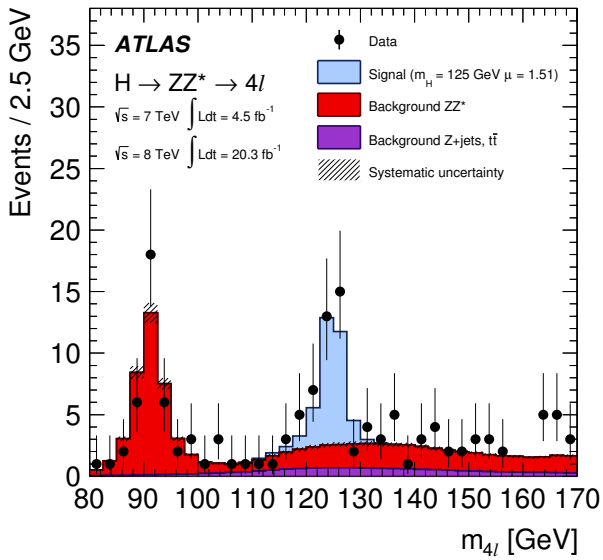

Figure 1.14: The distribution of the four-lepton invariant mass, $m_{4\ell}$, for the selected $H \to ZZ^* \to 4\ell$ candidates (filled circles) compared to the expected signal and background contributions (filled histograms) for the combined $\sqrt{s} = 7$ TeV and $\sqrt{s} = 8$ TeV data for the mass ranges $80 < m_{4\ell} < 170$ GeV. The signal expectation is shown for a mass hypothesis of $m_H = 125$ GeV and normalized to the beset fit value of the signal strenght $\mu = 1.51$ (*i.e.* the ratio of the measured Higgs boson yield to its SM expectation value). The expected backgrounds are shown separately for the ZZ^* (red histogram), Z+jets and $t\bar{t}$ components (violet histogram); the systematic uncertainty associated to the total background contribution is represented by the hatched areas (46).

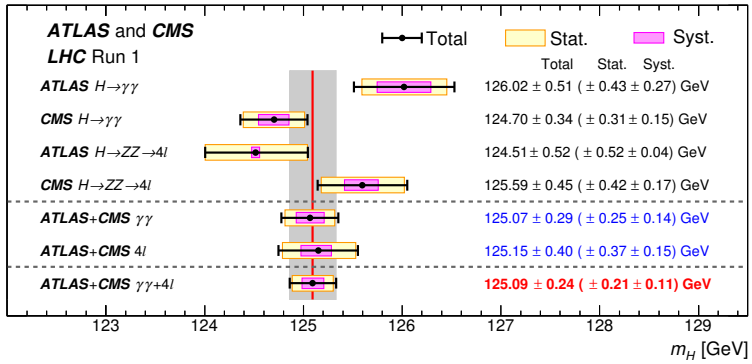

Figure 1.15: Summary of Higgs boson mass measurements from the individual Run 1 analyses of ATLAS and CMS and from their combination. The systematic (narrower, magenta-shaded bands), statistical (wider, yellow-shaded bands), and total (black error bars) uncertainties are indicated. The (red) vertical line and corresponding (gray) shaded column indicate the central value and the total uncertainty of the combined measurement, respectively (11).

The measurements are presented in terms of the signal-strength μ, defined as the ratio of the measured Higgs boson yield to its SM expectation value:

$$\mu = \frac{\sigma \times BR}{(\sigma \times BR)_{SM}}, \tag{1.48}$$

where σ is the total production cross-section of the Higgs boson. It is possible to define a signal strength for each production (i) and decay mode combination (f):

$$\mu_i^f = \frac{\sigma_i \times BR_f}{(\sigma_i \times BR_f)_{SM}} = \mu_i \times \mu_f, \tag{1.49}$$

with

$$\mu_i = \frac{\sigma_i}{(\sigma_i)_{SM}} \text{ and } \mu_f = \frac{BR_f}{(BR_f)_{SM}}, \tag{1.50}$$

where $i \in \{ggH, \text{VBF}, WH, ZH, t\bar{t}H\}$ and $f \in \{\gamma\gamma, ZZ, WW, \tau\tau, b\bar{b}\}$. By definition $\mu_i = 1$ and $\mu_f = 1$ in the SM hypothesis.

Given Eq. (1.50), the number of signal events (n_s^c) for each analysis category (c) is:

$$n_s^c = L \times \left(\sum_i \sum_f \mu_i \sigma_i^{SM} \times \mu_f BR_f^{SM} \times A_{if}^c \times \epsilon_{if}^c \right), \tag{1.51}$$

where A_{if}^c and ϵ_{if}^c are the detector acceptance and efficiency for the category c, given a combination of production i and decay mode f. This equation shows that the data do not allow to measure separately μ_i and μ_f without any further hypothesis in the fit, but only their products μ_i^f can be measured experimentally.

Given Eq. (1.51), the simplest measurement that can be performed is to assume that μ_i^f values are the same for all the i-f combination, so that in each category the SM predictions are scaled by a global signal strength μ (i.e. $\mu_i^f = \mu$). This parametrization provides the simplest test of compatibility between the data and the SM predictions. The best fit value obtained by ATLAS and CMS for $m_H = 125.09$ GeV is (40):

$$\mu = 1.09^{+0.11}_{-0.10} = 1.09^{+0.07}_{-0.07}\ (\text{stat.})\ ^{+0.04}_{-0.04}\ (\text{expt.})\ ^{+0.03}_{-0.03}\ (\text{thbdg.})\ ^{+0.07}_{-0.06}\ (\text{thsig.}), \tag{1.52}$$

where stat. is the statistical uncertainty, thsig. accounts for signal theory uncertainty, while thbdg. is the background theory uncertainty. Finally expt. collects the contributions of all the experimental systematic uncertainties.

This result is compatible within less than 1σ with the SM expectation $\mu = 1$, and the p-value of the compatibility between data and SM hypothesis is 40%.

It is also possible to evaluate the signal-strength of each individual production process (decay mode) requesting that $\forall f\ \mu_f = 1$ ($\forall i\ \mu_i = 1$), *i.e.* assuming all the five production cross sections (decay branching ratio) equal to the ones predicted by the SM, and simultaneously fitting the μ_i (μ_f) parameters. The results of these fits are shown in Figures 1.16 and 1.17 (40). All the production and decay signal strenghts are found to be in good agreement, within 1σ, with the SM prediction, except for $t\bar{t}H$ production signal strenghts that is measured to be $\mu_{ttH} = 2.3^{+0.7}_{-0.6}$ and differs by more than 2σ from 1.0. Table 1.3 shows the measured and expected significances for the observation of Higgs boson production processes and decay channels for the combination of ATLAS and CMS data (40).

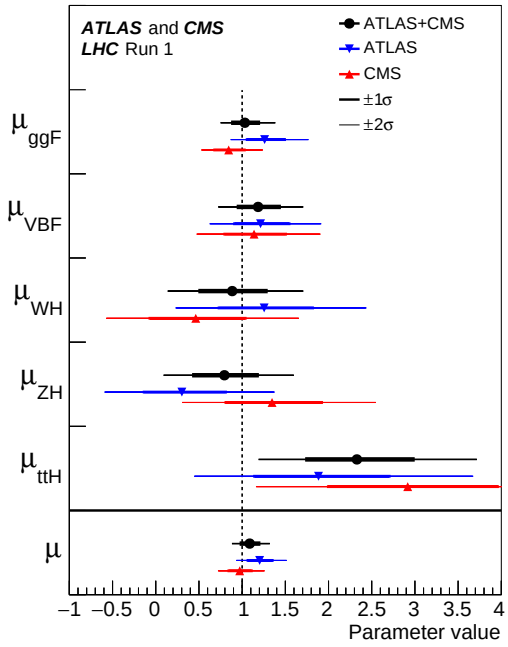

Figure 1.16: Best fit results for the production signal strengths for the combination of ATLAS and CMS data. Also shown are the results from each experiment. The error bars indicate the 1σ (thick lines) and 2σ (thin lines) intervals. The measurements of the global signal strength μ are also shown (40).

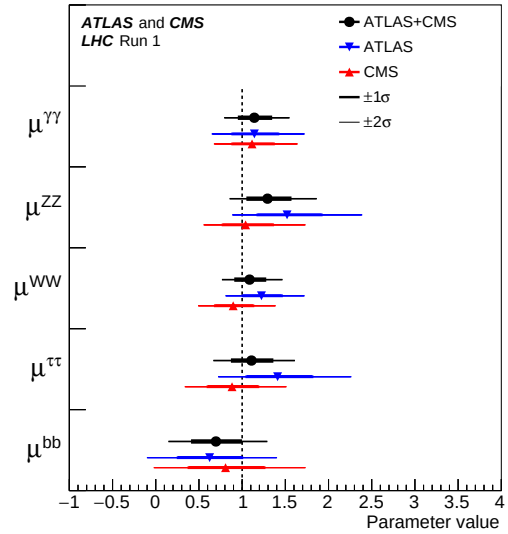

Figure 1.17: Best fit results for the decay signal strengths for the combination of ATLAS and CMS data. Also shown are the results from each experiment. The error bars indicate the 1σ (thick lines) and 2σ (thin lines) intervals (40).

Table 1.3: Measured and expected significances for the observation of Higgs boson production processes and decay channels for the combination of ATLAS and CMS with the full Run 1 dataset. The ggH production process, the $H \to ZZ$, $H \to WW$, and $H \to \gamma\gamma$ decay channels are not included since their significance is way higher than 5σ. All results are obtained constraining the decay branching fractions to their SM values when considering the production processes, and constraining the production cross sections to their SM values when studying the decays (40).

Production process	Measured significance [σ]	Expected significance [σ]
VBF	5.4	4.6
WH	2.4	2.7
ZH	2.3	2.9
VH	3.5	4.2
ttH	4.4	2.0
Decay channel		
$H \to \tau\tau$	5.5	5.0
$H \to bb$	2.6	3.7

Further insights on the Higgs couplings can be extracted measuring Higgs boson production modes that involve a coupling to fermions (ggH and ttH) or to vector bosons (VBF and VH). A new parametrization is built with two signal strength defined as:

$$\mu_F^f = \mu_{ggH+ttH}^f, \tag{1.53}$$

$$\mu_V^f = \mu_{VBF+VH}^f. \tag{1.54}$$

Two fits are performed. The first is a ten-parameter fit of μ_F^f and μ_V^f for each of the five decay modes. This is particularly powerful because the ratio μ_F^f/μ_V^f can be tested directly with no assumption on the Higgs branching ratios. Figure 1.18 shows the 68% CL 2D (μ_F^f, μ_V^f) contours obtained from this fit. The SM prediction (i.e. $\mu_F^f = 1$ and $\mu_V^f = 1$) lies inside each of this contours. The p-value of the compatibility between the SM expectation and the data is 90% (40). The second fit is a six-parameter fit of μ_F/μ_V and μ_V^f. The obtained best fit value is $\mu_F/\mu_V = 1.09^{+0.36}_{-0.28}$ and the p-value of the compatibility between the SM and the data is 75% (40).

1.4.3 The Higgs boson main quantum number measurement

In order to further investigate the characteristics of the newly discovered particle it is necessary to measure also its quantum numbers: the spin (J), the parity (P) and the charge conjugation (C), that for a SM Higgs boson are predicted to be $J^{PC} = 0^{++}$.

The $C = +1$ follows from the observation of the decay in the di-photon final state. Since the charge conjugation quantum number is multiplicative and given that photons are C-odd ($C = -1$) eigenstates, the observed neutral particle has to be C-even.

The observation of the $H \to \gamma\gamma$ decay gives also additional information about the spin of the Higgs boson. According to the Landau-Yang theorem (57; 58), which essentially states that a massive spin 1 particle can not decay in two photons, the possible spin values are restricted to 0 or 2.

The measurement of the spin-parity (J^P) quantum numbers is performed by ATLAS and CMS probing various alternative models against the SM. In particular three possible

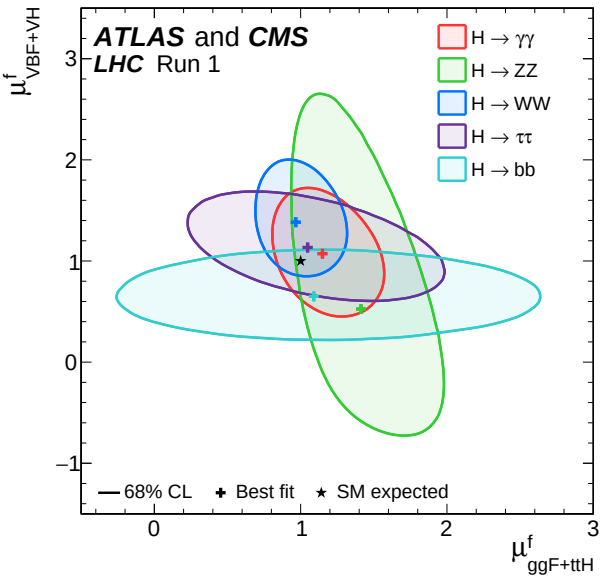

Figure 1.18: Negative log-likelihood contours at 68% CL in the $(\mu^f_{ggH+ttH}, \mu^f_{VBF+VH})$ plane for the combination of ATLAS and CMS, as obtained from the ten-parameter fit for each of the five decay channels $H \to ZZ$, $H \to WW$, $H \to \gamma\gamma$, $H \to \tau\tau$, and $H \to bb$. The best fit values obtained for each of the five decay channels are also shown, together with the SM expectation (40).

Beyond Standard Model (BSM) scenarios are considered: either the observed resonance is a spin-2 particle, or a pure BSM spin-0 CP-even, or CP-odd Higgs boson, or it is a mixture of the SM spin-0 state and a BSM spin-0 CP-even or CP-odd state.

In order to test these hypotheses the diboson decay modes are exploited: $H \to \gamma\gamma$, $H \to ZZ$ (59) and $H \to WW$ (60). In particular the di-photon channel can discriminate between the spin-0 and spin-2 hypothesis, while $H \to ZZ \to 4\ell$ can discriminate the 0^+ and 0^- hypotheses.

In the $H \to \gamma\gamma$ channel the analysis is performed using as discriminating variables the di-photon transverse momentum, $p_T^{\gamma\gamma}$ and the production angle of the two photons, measured in the Collins–Soper frame (61):

$$|\cos(\theta^*)| = \frac{|\sinh(\Delta\eta^{\gamma\gamma})|}{\sqrt{1+(p_T^{\gamma\gamma}/m_{\gamma\gamma})^2}} \frac{2p_T^{\gamma_1} p_T^{\gamma_2}}{m_{\gamma\gamma}^2}. \tag{1.55}$$

The expected distributions for these kinematic variables for both the SM and BSM hypotheses are shown in Figure 1.19 (59). The SM Higgs boson is expected to have a uniform $|\cos(\theta^*)|$ distribution except for a cutoff due to the p_T^{γ} selection requirement, while the spin-2 scenarios yield a distribution peaking at $|\cos(\theta^*)| = 1$.

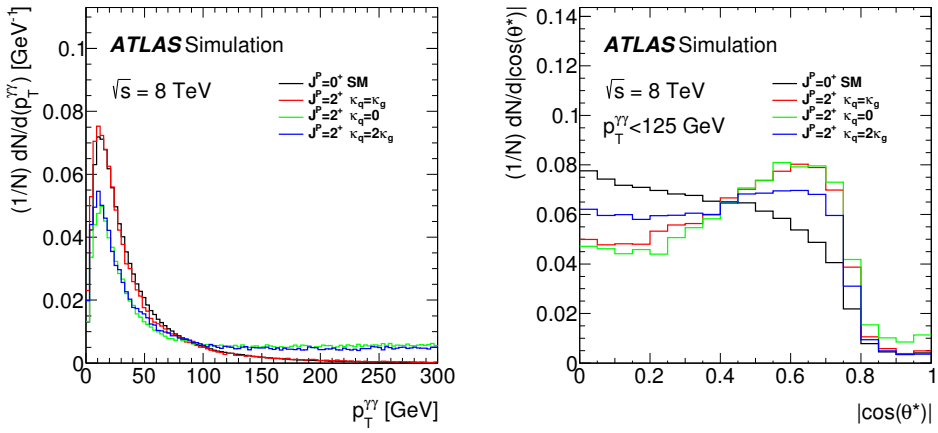

(a) (b)

Figure 1.19: Expected distributions of kinematic variables sensitive to the spin of the resonance considered in the $H \to \gamma\gamma$ analysis: (a) the transverse momentum of the $\gamma\gamma$ system $p_T^{\gamma\gamma}$ and (b) the production angle of the two photons in the Collins-Soper frame $|\cos(\theta^*)|$, for a SM Higgs boson (black) and for spin-2 particle models (red, green and blue). The three spin-2 models are characterized by different predicted couplings to quarks and gluons. In particular, the $k_q = 0$ case implies a negligible coupling to light quarks, whereas the $k_q = 2k_g$ case is an alternative scenario with an enhanced coupling to quarks (59).

The $H \to ZZ \to 4\ell$ analysis exploits two production angles θ^* and Φ_1, and three decay angles Φ, θ_1 and θ_2 in order to discriminate between the several J^P hypotheses. These angles are sketched in Figure 1.20 (59) and are defined as:

- θ_1 and θ_2 are the angles between final-state leptons with negative charge and the direction of flight of their respective Z boson mothers in the rest frame;

- Φ is defined as the angle between the decay planes of the four final state leptons expressed in the four lepton rest frame;
- Φ_1 is the angle between the decay plane of the leading lepton-pair and the plane defined by the Z_1 momentum (i.e. the Z boson associated with the leading lepton pair) in the rest-frame and the positive direction of the proton collision axis;
- θ^* is the Z_1 production angle with respect to the proton axis.

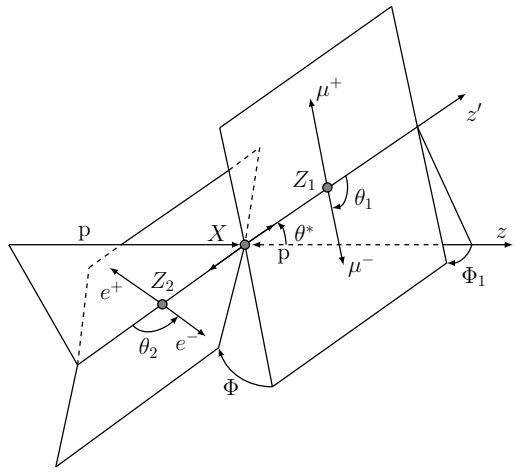

Figure 1.20: Definitions of the angular observables sensitive to the spin and parity of the resonance in the $H \to ZZ^* \to 4\ell$ decay (59).

For both ATLAS and CMS the data favor the $J^P = 0^+$ hypothesis, as summarised by the Figure 1.21, which shows the distribution of the test statistic for the SM Higgs boson and for the J^P alternative hypotheses obtained combining all the diboson decay channels. All tested alternative hypotheses are rejected at more than 99.9% confidence level (CL) in favour of the SM hypothesis (59; 62).

1.5 The Higgs boson studies at $\sqrt{s} = 13$ TeV

Since the beginning of 2015 LHC has been accelerating protons to 6.5 TeV, allowing ATLAS and CMS to collect data at $\sqrt{s} = 13$ TeV. The higher center of mass energy with respect to the Run 1 leads to an increase of the Higgs boson cross section, $\sigma^{13\text{TeV}}_{m_H=125}/\sigma^{8\text{TeV}}_{m_H=125} \sim 2.3$ in the SM.

The ATLAS and CMS collaboration have published new results based on the 36 fb^{-1} of *pp* collsions collected between 2015 and 2016, updating existing Run 1 results and looking for possible hints of BSM physics affecting the Higgs boson properties. Probably the most important new result is the first evidence of the $H \to b\bar{b}$ decay. Both ATLAS and CMS observed an excess over the expected background with a significance of of 3.5σ (63) and 3.3σ (64) respectively. The signal strength in this channel, obtained combining the Run 1 and the new data, is equal to $\mu = 0.90 \pm 0.18$ (stat.) $^{+0.21}_{-0.19}$ (syst.) (63) and $1.06^{+0.31}_{-0.29}$ (64), respectively. During the three years of my doctorate I contributed to some

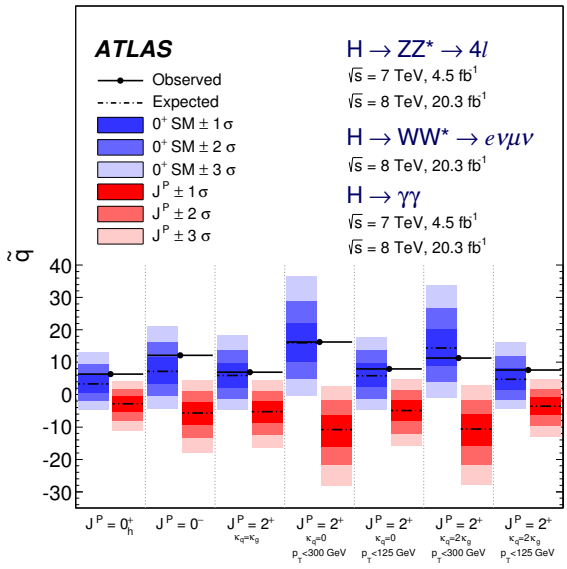

Figure 1.21: Distributions of the test statistic q for the SM Higgs boson and for the J^P alternative hypotheses. They are obtained by combining the $H \to ZZ^* \to 4\ell$, $H \to WW^* \to e\nu\mu\nu$ and $H \to \gamma\gamma$ decay channels. The expected median (black dashed line) and the ± 1, ± 2 and ± 3 σ regions for the SM Higgs boson (blue) and for the alternative J^P hypotheses (red) are shown for the signal strength fitted to data. The observed q values are indicated by the black points (59).

of these results (9; 10; 30; 31; 32). In particular the eighth chapter (Chap. 8) of this thesis reports in details the most recent measurement of the Higgs boson mass performed with the ATLAS detector.

Chapter 2

Supersymmetry

In this chapter, a particular Beyond Standard Model (BSM) theory, known as Supersymmetry (SUSY), is introduced. This model provides the principal motivation for the analysis described in Chapter 9, which looks for final states containing two photons and large missing transverse momentum (see Sec 5.4).

The first section of this chapter (2.1) briefly outlines some of the issues that affect the Standard Model and hint to the necessity of a theory extension. Sections 2.2–2.5 present the Supersymmetry theory which predicts for each particle of the SM a supersymmetric particle: a boson for each SM fermion and vice versa. In particular, these sections focus on the Minimal Supersymmetric Standard Model, which is the supersymmetric extension of the SM that requires the smallest number of additional particles. In Sec. 2.6 the production process of superymmetric particles at hadron collider is summarised. If SUSY is an exact symmetry of the nature, supersymmetric particles should have the same mass as Standard model particles, but since they have not yet been observed Supersymmetry must to be broken. Sec. 2.7 illustrates the Supersymmetry breaking models in particular focusing on the *Gauge-Mediated Supersymmetry Breaking* (GMSB) model and its phenomenological consequences. Finally, Sec. 2.8 summarises the experimental results obtained by the ATLAS and CMS collaborations in the searches of GMSB signals. For a complete description of Supersymmetry the reader is invited to refer to Refs. (65; 66).

2.1 The limitations of the Standard Model

The Standard Model presented in Chapter 1 is the theory that describes the interactions of the elementary particles. So far, it has been experimentally verified to an excellent level of accuracy. However, there are still some critical points that arise both from theoretical consideration and experimental results and may indicate that a more general theory is required to describe consistently particle physics phenomenology.

For example, several astronomical observations and cosmological measurements (67) have shown that the universe is composed by only $\sim 5\%$ of ordinary matter, which is described by the SM, while the remaining part is composed by *dark matter* ($\sim 27\%$), which has no electromagnetic interaction and has been inferred through its gravitational effects, and *dark energy* ($\sim 68\%$), which would lead to a repulsive force that tend to accelerate the expansion of the universe (68). There are no weakly interacting and stable particles in the SM that can be a good dark matter candidate,[1] and thus the Standard Model theory

[1] Dark matter is expected to be composed by relatively slow-moving particles compared to the speed of light (*Cold Dark Matter*, or CDM), and thus relativistic particle such as the neutrino cannot be a good dark matter candidate.

can not account for this 85%[2] dark fraction of the universe matter composition.

Moreover, an implementation of general relativity as a quantum theory is not yet available, and, therefore, the Standard Model does not include the description of the gravitational interactions. This is not a relevant issue for the description of the physical phenomena at the TeV energy scale, since at this energy the gravitational coupling is negligible if compared with the other fundamental forces. However, at the Planck energy scale, $M_P \sim 10^{18}$ GeV, gravitation quantum effects become important. The huge difference between the electro-weak scale ($M_W \sim 100$ GeV) and the Planck scale, and the corresponding difference between the weak force and the gravitational coupling, is considered a hint of the unnaturalness of the SM. This difference is also reflected in the expected fine-tuning cancellation in the Higgs mass calculation, also referred as the SM *hierarchy problem*.

The tree-level Higgs boson mass, m_H^2, receives quadratically divergent radiative corrections from the virtual effects of every SM particle. The resulting physical Higgs boson mass can be written as:

$$m^2_{H,\text{physical}} = m^2_{H,\text{bare}} - O(\lambda, g^2, h^2)\Lambda^2 + O(ln(\Lambda^2)), \tag{2.1}$$

where Λ is the scale where the Standard Model stops to be a valid theory and where new physics should appear. If the SM is valid up to the Planck scale, $\Lambda = M_P$, in order to have the measured Higgs mass $m_H \sim 125$ GeV there should be a fine tuned cancellation between the bare term and the radiative corrections of the order of $\frac{m_H^2}{m_P^2} = \frac{(10^2)^2}{(10^{18})^2}$. This seems very unnatural and it is considered as a strong hint of the presence of new physics at higher (intermediate) energy scale. In order to obtain a more natural theory, excluding the possibility that the Higgs boson field is not fundamental, it is necessary to introduce some cancellation mechanism between the various contribution to $\Delta m^2_{H,\text{physical,bare}}$. For example, the correction induced by the fermion loop, show in Figure 2.1a, to the Higgs boson mass can be written as:

$$\Delta m^2_{H,\text{physical,bare}} = -\frac{|\lambda_f|^2}{8\pi^2}\Lambda^2 + \dots\,, \tag{2.2}$$

where λ_f is the Yukawa coupling for the fermion f and the omitted terms grow at most logarithmically with Λ. The dominant term of the m_H^2 radiative corrections is due to the one-loop top radiative correction.

Considering a generic scalar S, depicted in Figure 2.1b, which couples to the Higgs field through the Lagrangian term $-\lambda_S|H|^2|S|^2$, leads to a $\Delta m^2_{H,\text{physical,bare}}$ term equal to:

$$\Delta m^2_{H,\text{physical,bare}} = +\frac{\lambda_s}{16\pi^2}\Lambda^2 + \dots\,. \tag{2.3}$$

Therefore if the Standard Model is extended with a symmetry that links each SM fermion with two complex scalars such that $\lambda_S = 2|\lambda_f|^2$, the quantum corrections to m_H are naturally canceled. The introduction of a boson-fermion symmetry is the basic idea from which the *Supersymmetry* theory is developed.

2.2 Supersymmetry

Supersymmetry (SUSY)(12; 13; 14; 15; 16; 17; 18) is a theory that postulates the existence of a symmetry between elementary bosons and fermions. This symmetry can be

[2]Since dark energy it is not referred as matter, 85% is given by the fraction of dark matter (27%) over the universe matter content (5%+27%).

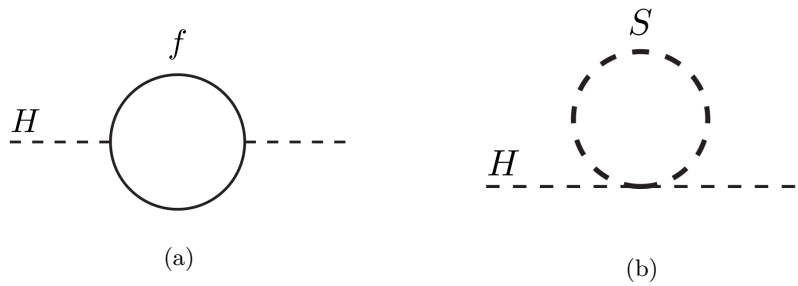

(a) (b)

Figure 2.1: One-loop quantum corrections to the Higgs squared mass parameter m_H^2, due to (a) a Dirac fermion f, and (b) a scalar S (65).

introduced using an operator Q that acts on the physical states in the following way:

$$Q|Boson\rangle = |Fermion\rangle \ , \qquad Q|Fermion\rangle = |Boson\rangle \ . \tag{2.4}$$

Since each time the symmetry is applied the spin of the considered state changes by $1/2$, Q must be a spinor carrying a $1/2$ spin. The generators Q, and their hermitian conjugate $Q^\dagger$, must satisfy an algebra defined by the Haag-Lopuszanski-Sohnius extension (69) of the Coleman-Mandula theorem (70), which is the only possible extension of the Poincaré algebra, and is defined by the relations:

$$\{Q, Q^\dagger\} = P^\mu \ , \tag{2.5}$$

$$\{Q, Q\} = \{Q^\dagger, Q^\dagger\} = 0 \ , \tag{2.6}$$

$$[P^\mu, Q] = \left[P^\mu, Q^\dagger\right] = 0 \ , \tag{2.7}$$

where P^μ is the four-momentum generator of the space-time translations.

The particles predicted are represented in the Q and $Q^\dagger$ algebra as *supermultiplets*. Each supermultiplet contains both the fermionic and bosonic states linked by the supersymmetry, that are usually called *superpartners*. The algebra generators commute with the generators of the gauge symmetries of the Standard Model, thus in every supermultiplet all the particles must have the same electric, isospin and color charge. Moreover, from Equation (2.7) is possible to deduce that also P^2 commutes with the Q and $Q^\dagger$ generators, therefore the particles belonging to the same supermultiplet have the same mass. As a consequence, every SM particle has its own superpartner.

It can be demonstrated that each supermultiplet has to contain an equal number of fermionic and bosonic degrees of freedom (65), *i.e.* $n_B = n_F$. To satisfy this condition, the simplest configuration is given by a supermultiplet composed by a Weyl fermion (with two spin helicity states, so $n_F = 2$) and two real scalars ($n_B = 1$ each). The two scalar fields can then be combined into a single complex scalar field. This combination of a complex scalar field and a two-component Weyl fermion is called *chiral* supermultiplet.

A supermultiplet can also contain a spin-1 vector boson. If the theory is renormalizable, this must be a massless boson, at least before the gauge symmetry is spontaneously broken. A massless spin-1 boson has two helicity states, thus $n_B = 2$. The supermultiplet can then be completed by a massless Weyl spin-1/2 fermion with $n_F = 2$. The superpartners of the gauge boson are called *gauginos*, and the combination of a gauge boson with a Weyl spin-1/2 fermion is called *gauge* supermultiplet.

Standard Model fermions can only be included in chiral supermultiplets, since their left-handed and right-handed parts transform differently under the SM gauge group.

2.3 The Minimal Supersymmetric Standard Model

Considering a supersymmetric extension of the Standard Model, each of the SM elementary particle has to be included in a chiral or gauge supermultiplet with a superpartner with a spin that differs by $\frac{1}{2}$. The simplest model, which requires the smallest number of additional particles, is called the Minimal Supersymmetric Standard Model (MSSM). The superpartners of the SM particles in the MSSM are the following:

- Sfermions are the SUSY partners of SM fermions, additionally classified in squarks and sleptons (the *s-* prefix stands for scalar). In particular, for each left-handed and right-handed component of the SM fermions there is one different sfermion. For example, the superpartner of the left-handed and right-handed components of the electron are $\widetilde{e}_{\mathrm{L}}$ and $\widetilde{e}_{\mathrm{R}}$, where, since $\widetilde{e}_{\mathrm{L,R}}$ are bosons, the labels refer only to the chirality of their SM partners.

- Gauginos are the fermionic partners of the SM gauge bosons. In the MSSM these are the winos ($\widetilde{W}^{\pm}$,$\widetilde{W}^{0}$), that are the superpartners of the SM $SU(2)$ generators, the bino ($\widetilde{B}^{0}$), which is the superpartner of the $U(1)$ generator, and the gluinos ($\widetilde{g}$), that are the superpartners of the gluons. After electro-weak symmetry breaking the W^0 and B^0 mix in the mass eigenstate Z^0 and γ, as well as $\widetilde{B}^0$ and $\widetilde{W}^0$ mix together forming the *Zino* ($\widetilde{Z}^0$) and the *photino* ($\widetilde{\gamma}$).

- Higgsino. They are the superpartners of the Higgs boson degrees of freedom. In the MSSM at least two Higgs doublet fields $H_u = (H_u^+, H_u^0)$ and $H_d = (H_d^0, H_d^-)$ are required, as shown later by Eq. (2.8).

Tables 2.1 and 2.2 summarize the composition of chiral and gauge supermultiplets that compose the MSSM.

Table 2.1: Chiral supermultiplets in the Minimal Supersymmetric Standard Model. The spin-0 fields are complex scalars and the spin-1/2 fields are left-handed two-component Weyl fermions.

Names		spin 0	spin 1/2	$SU(3)_C$, $SU(2)_L$, $U(1)_Y$
squarks, quarks	Q	$(\widetilde{u}_L \;\; \widetilde{d}_L)$	$(u_L \;\; d_L)$	$(\mathbf{3}, \mathbf{2}, \frac{1}{6})$
(×3 families)	$\bar{u}$	$\widetilde{u}_R^*$	$u_R^\dagger$	$(\overline{\mathbf{3}}, \mathbf{1}, -\frac{2}{3})$
	$\bar{d}$	$\widetilde{d}_R^*$	$d_R^\dagger$	$(\overline{\mathbf{3}}, \mathbf{1}, +\frac{1}{3})$
sleptons, leptons	L	$(\widetilde{\nu} \;\; \widetilde{e}_L)$	$(\nu \;\; e_L)$	$(\mathbf{1}, \mathbf{2}, -\frac{1}{2})$
(×3 families)	$\bar{e}$	$\widetilde{e}_R^*$	$e_R^\dagger$	$(\mathbf{1}, \mathbf{1}, +1)$
Higgs, higgsinos	H_u	$(H_u^+ \;\; H_u^0)$	$(\widetilde{H}_u^+ \;\; \widetilde{H}_u^0)$	$(\mathbf{1}, \mathbf{2}, +\frac{1}{2})$
	H_d	$(H_d^0 \;\; H_d^-)$	$(\widetilde{H}_d^0 \;\; \widetilde{H}_d^-)$	$(\mathbf{1}, \mathbf{2}, -\frac{1}{2})$

Table 2.2: Gauge supermultiplets in the Minimal Supersymmetric Standard Model.

Names	spin 1/2	spin 1	$SU(3)_C$, $SU(2)_L$, $U(1)_Y$
gluino, gluon	$\widetilde{g}$	g	(**8**, **1** , 0)
winos, W bosons	$\widetilde{W}^{\pm}$ $\widetilde{W}^{0}$	$W^{\pm}$ W^{0}	(**1**, **3** , 0)
bino, B boson	$\widetilde{B}^{0}$	B^{0}	(**1**, **1** , 0)

2.4 The MSSM superpotential and R-parity

The super-potential of the MSSM that describes the Yukawa couplings and Higgs mass term is taken to be:

$$W_{\rm MSSM} = \bar{u}\mathbf{Y}_u Q H_u - \bar{d}\mathbf{Y}_d Q H_d - \bar{e}\mathbf{Y}_e L H_d + \mu H_u H_d \ , \tag{2.8}$$

where H_u, H_d, Q, L, $\bar{u}$, $\bar{d}$, $\bar{e}$ are the chiral superfields corresponding to the supermultiplets in Table 2.1. μ has a dimension of the mass and thus provides a supersymmetric contribution to the mass of the Higgs boson and it is usually assumed to be real. Both the H_u and H_d are needed to describe the Yukawa coupling of the superfields $\bar{u}$ and $\bar{d}$, since the coupling of H and H^* exploited in the SM (see Eq. (1.39)) is forbidden by the SUSY theory. The dimensionless Yukawa coupling parameters $\mathbf{Y}_u$, $\mathbf{Y}_d$, $\mathbf{Y}_e$ are 3×3 matrices in the family space that, since the third generation leptons and quark are much heavier than others (*i.e.* $m_t \gg m_c, m_u$; $m_b \gg m_s, m_d$; $m_\tau \gg m_\mu, m_e$), can be approximated by:

$$\mathbf{Y}_u = \begin{pmatrix} 0 & 0 & 0 \\ 0 & 0 & 0 \\ 0 & 0 & y_t \end{pmatrix} \ , \ \mathbf{Y}_d = \begin{pmatrix} 0 & 0 & 0 \\ 0 & 0 & 0 \\ 0 & 0 & y_b \end{pmatrix} \ , \ \mathbf{Y}_e = \begin{pmatrix} 0 & 0 & 0 \\ 0 & 0 & 0 \\ 0 & 0 & y_\tau \end{pmatrix} \ . \tag{2.9}$$

In this approximation the superpotential becomes:

$$\begin{aligned} W_{\rm MSSM} \approx & y_t(t\bar{t}H_u^0 - \bar{t}bH_u^+) - y_b(\bar{b}tH_d^- - \bar{b}bH_d^0) \\ & - y_t(\bar{\tau}\nu_\tau H_d^- - \bar{\tau}\tau H_d^0) + \mu(H_u^+ H_d^- - H_u^0 H_d^0). \end{aligned} \tag{2.10}$$

Differently from the Standard Model, where given the $SU(3)_C \otimes SU(2)_L \otimes U(1)_Y$ gauge symmetry all the Lagrangian terms with dimension four or less conserve the baryonic (B) and leptonic (L) number, in the MSSM Lagrangian they are not conserved automatically. The superpotential can also include terms that violates B and L, as for instance:

$$W_{\Delta \rm L=1} = \alpha^{ijk} Q_i L_j \bar{d}_k + \beta^{ijk} L_i L_j \bar{e}_k + \gamma^i L^i H_u \ , \tag{2.11}$$

$$W_{\Delta \rm B=1} = \delta^{ijk} \bar{d}_i \bar{d}_j \bar{u}_k \ , \tag{2.12}$$

where i and j are gauge indices.

The violation of the baryonic and leptonic number leads potentially to proton decay, as shown in Figure 2.2, but this scenario is completely disfavoured by the experiment, since the measured limit on the decay time of the proton in a lepton-meson final state is $> 10^{34}$ years (71).

One solution to preserve the baryon and lepton number conservation is to introduce of an additional symmetry, know as R-parity in the model. R-parity is a multiplicatively

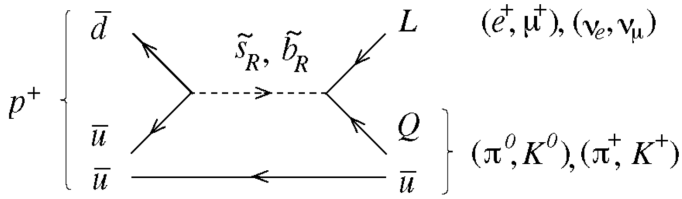

Figure 2.2: Feynman diagram for proton decay to an antilepton and a meson. In the diagram the δ vertex (from Eq (2.12)) on the left and the α vertex (from Eq 2.11) on the right (66).

conserved quantum number defined as:

$$P_R = (-1)^{3(\mathrm{B-L})+2S} \ , \tag{2.13}$$

where B is the baryon number, L is the lepton number, and S is the spin. Thus $R = +1$ is assigned to each SM particle and $R = -1$ to each supersymmetric partner.

In the MSSM R-parity is assumed to be conserved, then the sparticles and the particles can not be mixed, and every interaction vertex in the theory must contain an even number of $P_R = -1$ sparticles. This results in three important phenomenological consequences:

- the lightest supersymmetric particle (LSP) must be stable;
- each supersymmetric particle, except for the LSP, must decay into a state containing and odd number of LSP (generally one);
- in collider experiments supersymmetric particles can only be produced in even number.

The introduction in the theory of a stable LSP has some cosmological implication, since a neutral LSP can be a good candidate for the role of dark matter of the universe. From an experimental point of view, the presence in the theory of a LSP leads to a final state signature containing high missing transverse momentum since the LSP escapes from the detector without interacting with it.

2.5 The MSSM mass spectrum

In a theory with exact supersymmetry, fermions and their bosonic superpartners must be degenerate in mass, *i.e.* with the same mass value. However, since supersymmetric particles have not yet been observed, supersymmetry has to be broken. Given that no experimental evidence can justify the choice of a specific supersymmetry breaking mechanism, the SUSY breaking is modeled adding to the Lagrangian the most general SUSY-breaking terms. In particular, in order to preserve the capability of the SUSY theory to solve the hierarchy problem, the additional terms must not change the dimensionless SUSY terms in the Lagrangian in order to not introduce quadratic divergences. Terms with this features are called soft-breaking terms. These assumptions lead to an effective Lagrangian for the MSSM of the form:

$$L = L_{\mathrm{SUSY}} + L_{\mathrm{soft}}, \tag{2.14}$$

where $L_{\rm SUSY}$ contains all the gauge and Yukawa interactions, and dimensionless scalar couplings and preserve the exact invariance of the supersymmetry. On the contrary, $L_{\rm soft}$ violates SUSY and contains all allowed terms that do not introduce quadratic divergences in the theory and that are compatible with the $SU(3)_C \otimes SU(2)_L \otimes U(1)_Y$ gauge symmetry. The possible forms of the soft terms of $L_{\rm soft}$ are (72):

- soft gaugino masses: $\frac{1}{2} M_a \lambda^a \lambda^a$;
- soft bilinear scalar interactions: $\frac{1}{2} b_{ij} \phi_i \phi_j$;
- soft scalar mass-squares: $m_{ij}^2 \phi_i^\dagger \phi_j$;
- soft trilinear scalar interactions: $\frac{1}{2} \widetilde{A}_{ijk} \phi_i \phi_j \phi_k$.

In the expression above, a labels the gauge group. For the MSSM the more general and model independent soft Lagrangian is expressed by the following equation:

$$\begin{aligned} L_{\rm soft} = & -\frac{1}{2}(M_3 \widetilde{g}\widetilde{g} + M_2 \widetilde{W}\widetilde{W} + M_1 \widetilde{B}\widetilde{B}) + h.c. \\ & - (\widetilde{\bar{u}} \mathbf{A}_u \widetilde{\bar{Q}} H_u - \widetilde{\bar{d}} \mathbf{A}_d \widetilde{\bar{Q}} H_d - \widetilde{\bar{e}} \mathbf{A}_e \widetilde{\bar{L}} H_e) + h.c. \\ & - \widetilde{Q}^\dagger \mathbf{m}_Q^2 \widetilde{Q} - \widetilde{L}^\dagger \mathbf{m}_L^2 \widetilde{L} - \widetilde{\bar{u}}^\dagger \mathbf{m}_{\bar{u}}^2 \widetilde{\bar{u}} - \widetilde{\bar{d}}^\dagger \mathbf{m}_{\bar{d}}^2 \widetilde{\bar{d}} \\ & - m_{H_u}^2 H_u^* H_u - m_{H_d}^2 H_d^* H_d - (b H_u H_d + h.c.). \end{aligned} \tag{2.15}$$

where Q, $\bar{u}$, $\bar{d}$, L, $\bar{e}$, H_u, and H_d denote the $SU(2)$ weak doublets listed in Table 2.1 and summation over generations is implied. The first line of Equation (2.15) gives masses to the MSSM gauginos, the second line consist in trilinear scalar interactions, the third lines is composed by the squared mass terms for the squarks and the sleptons, and in the last line there are the Higgs boson squared mass terms, where b is the soft SUSY-breaking Higgs boson mass term.

These terms break supersymmetry because they contribute explicitly to the masses and the interactions of the SUSY sparticles but not to their SM superpartners. The underlying supersymmetry breaking is assumed to be spontaneous and take place in a hidden sector as explained in Sec 2.7.

All the terms introduced by $L_{\rm soft}$ lead to an abundance of free parameters that define the MSSM. In addition to the SM parameters, there are 105 masses, phases and mixing angles that can not be removed by the redefinition of the phases and flavor basis from the quark and lepton supermultiplets. However, thanks to experimental and phenomenological consideration, such as suppressing flavor changing neutral currents and excluding new sources of CP violation, they can be reduced down to 19 terms in the phenomenological MSSM model.

The soft parameters clearly have an impact on the MSSM mass spectrum and mixing. Indeed, in the MSSM the particles listed in Tables 2.1 and 2.2 are not necessarily mass eigenstates. After the electro-weak symmetry and the soft supersymmetry breaking, the particles with the same quantum number generally mix. In the following paragraph the resulting masses and mixing are presented. Table 2.3 summarizes the MSSM gauge eigenstates and their relative mass eigenstates.

2.5.1 Higgs sector

In the MSSM the Higgs boson scalar fields are composed by two complex doublets $H_u = (H_u^+, H_u^0)$ and $H_d = (H_d^0, H_d^-)$, with eight scalar degrees of freedom. After electro-weak symmetry breaking , three degrees of freedom become Nambu-Goldston bosons, that are not physically observed and are converted in the longitudinal polarization of the Z and $W^\pm$ bosons. The remaining five degrees of freedom produce 5 physical observable states, which constitutes the five Higgs bosons of the MSSM model:

- $H^\pm$, a charged Higgs boson pair;
- A^0, a neutral CP-odd Higgs boson;
- H^0 and h^0, two CP-even neutral Higgs boson, with the convention that $m_{h^0} < m_{H^0}$.

The $H^\pm$, A^0, H^0 could in principle have a mass much higher than the TeV scale, while h^0 is considered the Higgs boson observed by the ATLAS and CMS collaborations at $m_H \sim 125$ GeV (73).

2.5.2 Charginos and Neutralinos

Due to the effects of electro-weak symmetry breaking, the higgsinos and the electro-weak gauginos mix with each other. The combination of the neutral higgsinos (H_u^0, H_d^0) and the neutral gauginos ($\widetilde{B}^0$, $\widetilde{W}^0$) forms four $\frac{1}{2}$-spin particles called *neutralinos* ($\widetilde{\chi}_i^0$, with $i = 1, 2, 3, 4$). Using the gauge base $\psi_j^0 = \{\widetilde{B}^0, \widetilde{W}^0, H_u^0, H_d^0\}$ the neutralino mass Lagrangian is:

$$L_{m_{\tilde{\chi}^0}} = -\frac{1}{2}(\psi^0)^T \mathbf{M}_{\widetilde{N}} \psi^0 + h.c, \tag{2.16}$$

and $\mathbf{M}_{\widetilde{N}}$ is defined as:

$$\mathbf{M}_{\widetilde{N}} = \begin{pmatrix} M_1 & 0 & -\cos\beta \sin\theta_W m_Z & \sin\beta \sin\theta_W m_Z \\ 0 & M_2 & \cos\beta \cos\theta_W m_Z & -\sin\beta \cos\theta_W m_Z \\ -\cos\beta \sin\theta_W m_Z & \cos\beta \cos\theta_W m_Z & 0 & -\mu \\ \sin\beta \sin\theta_W m_Z & -\sin\beta \cos\theta_W m_Z & -\mu & 0 \end{pmatrix}. \tag{2.17}$$

Here M_1 and M_2 are defined from the MSSM soft Lagrangian, μ are the supersymmetric higgsino mass term and β is the angle defined by the relation $\tan\beta \equiv \nu_u/\nu_d$, where ν_u and ν_d are the vacuum expectation values of H_u^0 and H_d^0 respectively. The mass matrix $m_{\tilde{N}}$ can be diagonalized by a unitary matrix $\mathbf{N}$ in order to obtain the neutralino mass eigenstates:

$$\widetilde{\chi}_i^0 = \mathbf{N}_{ij} \psi_j^0, \tag{2.18}$$

where the indices i, j run over mass and gauge eigenstates, and $\mathbf{N}$ is such that

$$\mathbf{N}^* \mathbf{M}_{\widetilde{N}} \mathbf{N}^{-1} = \begin{pmatrix} m_{\tilde{\chi}_1^0} & 0 & 0 & 0 \\ 0 & m_{\tilde{\chi}_2^0} & 0 & 0 \\ 0 & 0 & m_{\tilde{\chi}_3^0} & 0 \\ 0 & 0 & 0 & m_{\tilde{\chi}_4^0} \end{pmatrix}. \tag{2.19}$$

$m_{\tilde{\chi}_i^0}$ are the real positive eigenstates of $\mathbf{M}_{\widetilde{N}}$, and by convention: $m_{\tilde{\chi}_1^0} < m_{\tilde{\chi}_2^0} < m_{\tilde{\chi}_3^0} < m_{\tilde{\chi}_4^0}$.

The composition of each neutralino mass eigenstate depends on the relative magnitude of the M_1, M_2, m_Z and μ parameters. Considering the region of the parameter space where:

$$m_Z \ll |\mu \pm M_1|, |\mu \pm M_2|, \tag{2.20}$$

the lightest neutralino is nearly a pure bino state $\widetilde{\chi}_1^0 = \widetilde{B}$ with mass $|M_1|$, while the other neutralino states are $\widetilde{W}^0$, $(\widetilde{H}_u^0 \pm \widetilde{H}_d^0)/\sqrt{2}$ with masses $|M_2|$ and μ respectively.

The mixing of the charged gauginos ($\widetilde{W}^+$) and of the charged higgsinos (H_u^+, H_d^-) leads to two $\frac{1}{2}$-spin mass eigenstates called *charginos* ($\widetilde{\chi}_i^\pm$, with $i = 1, 2$) with charge ± 1. The mixing is described by the matrix:

$$m_{\tilde{C}} = \begin{pmatrix} M_2 & \sqrt{2} m_W \sin\beta \\ \sqrt{2} m_W \cos\beta & \mu \end{pmatrix}. \tag{2.21}$$

By convention $m_{\widetilde{\chi}_1^\pm} < m_{\widetilde{\chi}_2^\pm}$.

2.5.3 Gluinos

The gluino is a color octet fermion, which cannot mix with any other MSSM particles (even if R-parity is violated). The gluino mass is directly defined by the soft lagrangian parameter M_3.

2.5.4 Squarks and sleptons

All the fermion scalar superpartners with the same quantum numbers (electric charge, R-parity and color quantum number) can mix both the left-handed and right-handed components leading to three 6×6 matrices for up-type, down-type squarks and charged sleptons, and an additional 3×3 matrix for the sneutrinos. However, since the mixing terms (*i.e.* off-diagonal terms) are expected to depends on the sfermion mass, the mixing is mainly relevant for slepton and squarks of the third generation (τ, t, b).

2.6 Supersymmetry particle production at hadron collider

At the LHC the supersymmetric particles can be produced in pairs (conserving the R-parity) through strong interactions (see Figures 2.3 and 2.4):

$$gg \rightarrow \widetilde{g}\widetilde{g},\ \widetilde{q}_i \widetilde{q}_j^{\,*}, \tag{2.22}$$
$$gq \rightarrow \widetilde{g}\widetilde{q}_i, \tag{2.23}$$
$$q\bar{q} \rightarrow \widetilde{g}\widetilde{g},\ \widetilde{q}_i \widetilde{q}_j^{\,*}, \tag{2.24}$$
$$q\bar{q} \rightarrow \widetilde{q}_i \widetilde{q}_j; \tag{2.25}$$
$$\tag{2.26}$$

and through electro-weak interaction (see Figure 2.5):

$$q\bar{q} \rightarrow \widetilde{\chi}^+\widetilde{\chi}^-,\ \widetilde{\chi}^0\widetilde{\chi}^0, \tag{2.27}$$
$$q\bar{q} \rightarrow \widetilde{\ell}^+\widetilde{\ell}^-,\ \widetilde{\nu}_\ell \widetilde{\nu}_\ell^{\,*}; \tag{2.28}$$
$$\tag{2.29}$$

Table 2.3: The gauge eigenstates and mass eigenstates of the particles in the Minimal Supersymmetric Standard Model (with sfermion mixing for the first two families assumed to be negligible).

Names	Spin	P	Gauge Eigenstates	Mass Eigenstates
Higgs boson	0	$+1$	$H_u^0\ H_d^0\ H_u^+\ H_d^-$	$h^0\ H^0\ A^0\ H^\pm$
squarks	0	-1	$\widetilde{u}_L\ \widetilde{u}_R\ \widetilde{d}_L\ \widetilde{d}_R$ $\widetilde{s}_L\ \widetilde{s}_R\ \widetilde{c}_L\ \widetilde{c}_R$ $\widetilde{t}_L\ \widetilde{t}_R\ \widetilde{b}_L\ \widetilde{b}_R$	(same) (same) $\widetilde{t}_1\ \widetilde{t}_2\ \widetilde{b}_1\ \widetilde{b}_2$
sleptons	0	-1	$\widetilde{e}_L\ \widetilde{e}_R\widetilde{\nu}_e$ $\widetilde{\mu}_L\ \widetilde{\mu}_R\widetilde{\nu}_\mu$ $\widetilde{\tau}_L\ \widetilde{\tau}_R\widetilde{\nu}_\tau$	(same) (same) $\widetilde{\tau}_1\ \widetilde{\tau}_2\widetilde{\nu}_\tau$
neutralinos	1/2	-1	$\widetilde{B}^0\ \widetilde{W}^0\ \widetilde{H}_u^0\ \widetilde{H}_d^0$	$\widetilde{\chi}_1^0\ \widetilde{\chi}_2^0\ \widetilde{\chi}_3^0\ \widetilde{\chi}_4^0$
charginos	1/2	-1	$\widetilde{W}^\pm\ \widetilde{H}_u^+\ \widetilde{H}_d^-$	$\widetilde{\chi}_1^\pm\ \widetilde{\chi}_2^\pm$
gluino	1/2	-1	$\widetilde{g}$	(same)

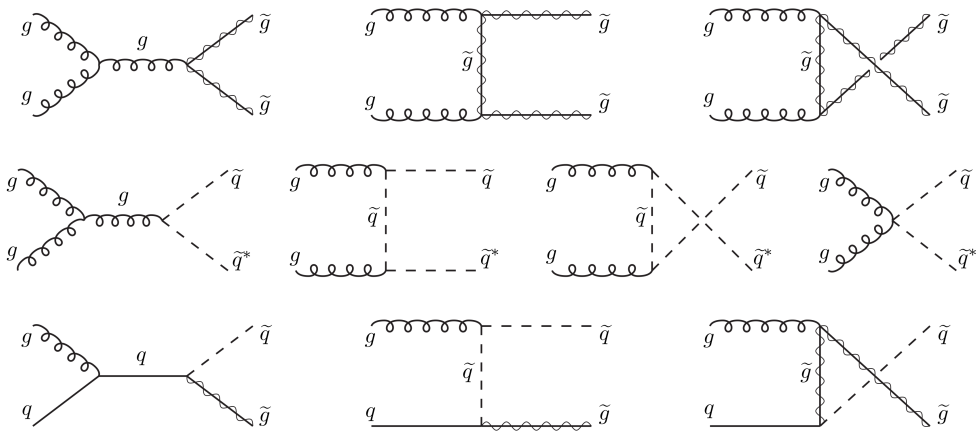

Figure 2.3: Feynman diagrams for gluino and squark production at hadron colliders from gluon-gluon and gluon-quark fusion (65).

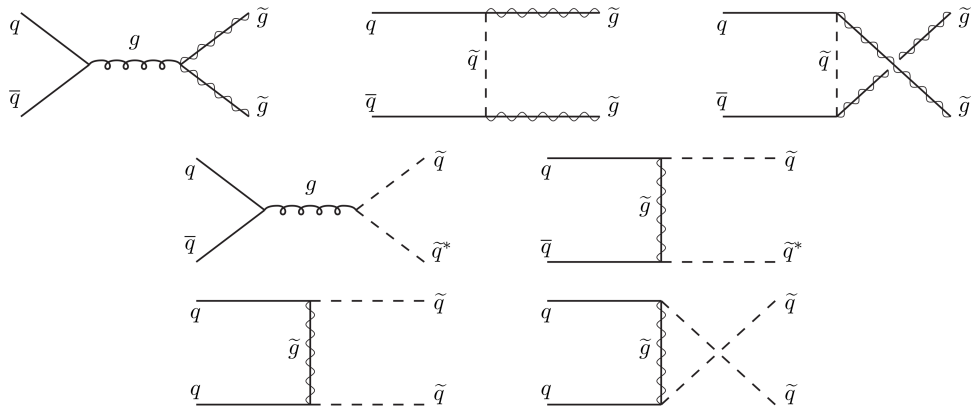

Figure 2.4: Feynman diagrams for gluino and squark production at hadron colliders from strong quark-antiquark annihilation and quark-quark scattering (65).

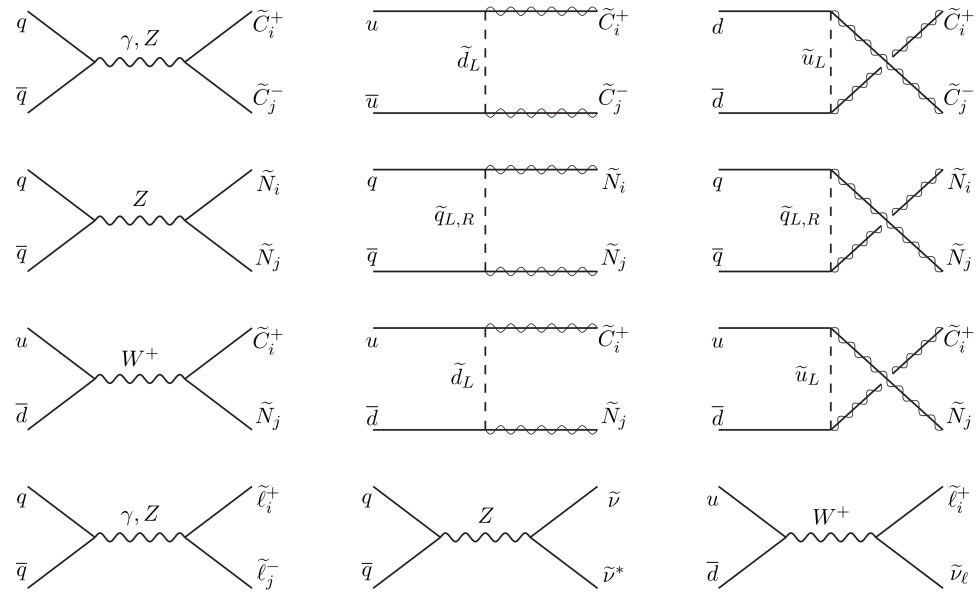

Figure 2.5: Feynman diagrams for electroweak production of sparticles at hadron colliders from quark-antiquark annihilation. The charginos ($\widetilde{C}_i^\pm = \widetilde{\chi}_i^\pm$) and neutralinos ($\widetilde{N}_i = \widetilde{\chi}_i^0$) in the t-channel diagrams only couple because of their gaugino content, for massless initial-state quarks, and so are drawn as wavy lines superimposed on solid (65).

Figure 2.6 shows the cross-section values at $\sqrt{s} = 8$ TeV for the different sparticle production modes. The dominant process at the LHC is the production of gluinos and squarks by gluon-gluon and gluon-quark fusion.

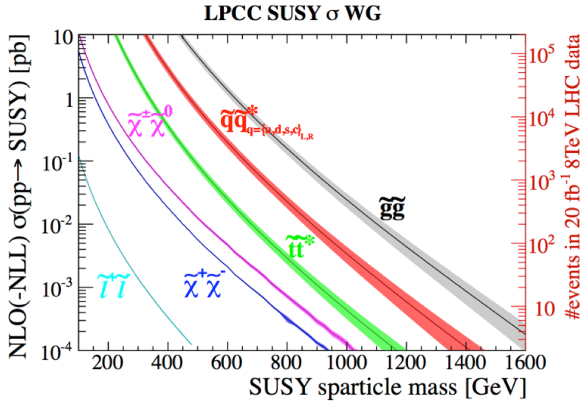

Figure 2.6: Cross section for the production of sparticles at LHC at 8 TeV center of mass energy as a function of the average mass of the pair produced (74).

2.7 Supersymmetry breaking

As mentioned in Sec 2.5, since the supersymmetric counterpart of the SM particles have not yet been observed, supersymmetry has to be broken. However, in order to include spontaneous symmetry breaking in the SUSY theory, it is necessary to further expand the model. Indeed, in case of supersymmetry breaking at tree-level, it is expected that at least some of the MSSM squarks and sleptons would be lighter than its ordinary partner, and thus should have been discovered already.

The SUSY breaking is expected to occur in a "hidden sector" of particles that have only very small direct couplings to the chiral supermultiplets of the "visible sector" MSSM, as depicted in Figure 2.7. The soft terms of the MSSM arise from the interaction of these two

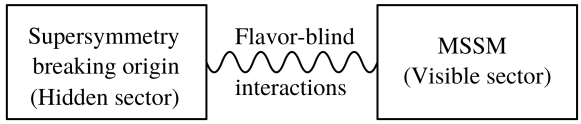

Figure 2.7: The presumed schematic structure for supersymmetry breaking (65).

sectors that mediates the supersymmetry breaking from the hidden sector to the visible one. The interaction are supposed to be flavor-blind, *i.e.* the messenger interactions do not violate flavor symmetries, in order to avoid large flavor changing neutral currents contributions in the soft Lagrangian term.

There are different scenarios that describe the interaction between the hidden and the visible MSSM sector. In the first scenario, the mediation is due to gravitational

interactions (*Planck-scale-mediated supersymmetry breaking*), which are relevant at the Planck scale (M_P). In this scenario, if supersymmetry is broken in an hidden sector by a vacuum expectation value $\langle F \rangle$, then the soft term in the observable sector should be

$$m_{\text{soft}} \sim \langle F \rangle / M_P, \tag{2.30}$$

where given a m_{soft} of the order of few hundreds of GeV, the energy scale of the supersymmetry breaking in the hidden sector should be $\sqrt{F} \sim 10^{10}$–10^{11} GeV.

The second possibility is that the mediating interactions are the ordinary electroweak and QCD gauge interactions. In this scenario where the supersymmetry breaking is mediated by gauge interactions (*Gauge-Mediated Supersymmetry Breaking* (19; 20; 21; 22; 23; 24; 25), or GMSB), the soft mass terms of the MSSM come from loop diagrams involving some *messenger* particles. These particles are additional chiral supermultiplets that couple to the source of supersymmetry breaking $\langle F \rangle$ and also couple through loop diagrams to the (s)quarks, (s)leptons and higgs(inos) of the MSSM through the ordinary $SU(3)_C \otimes SU(2)_L \otimes U(1)_Y$ gauge boson and gaugino interactions. Then the scale for the MSSM soft terms is:

$$m_{\text{soft}} \sim \frac{\alpha_{\text{a}}}{4\pi} \frac{\langle F \rangle}{M_{\text{mess}}}, \tag{2.31}$$

where $\alpha_{\text{a}}/4\pi$ is a loop factor for Feynman diagrams involving gauge interactions, and M_{mess} is the mass of the messengers. If $\sqrt{\langle F \rangle} \sim M_{\text{mess}}$ then the SUSY breaking scale can be as low as $\sqrt{\langle F \rangle} \sim 10^4$–$10^5$ GeV.

Including gravity, supersymmetry must be promoted to a local symmetry, called *supergravity*. In this context the local supersymmetry transformation are unified with the general relativity space-time symmetry. In this theory the gravitational interaction of the SM is mediated by the spin-2 *graviton*, that is embedded in a supermultiplet with its superpartner of spin $\frac{3}{2}$ called the *gravitino* ($\widetilde{G}$). Before the supersymmetry breaking, the graviton and the gravitino are massless particles with 2 helicity degrees of freedom, and interact with the MSSM particles only through gravitational interaction. Once SUSY is spontaneously broken in the hidden sector, as predicted by the Nambu-Goldstone theorem, a massless state arises, called the goldstino. In the same way described for the electro-weak symmetry breaking, the goldstino is absorbed by the gravitino and is converted in the gravitino longitudinal polarization. The gravitino acquires a mass, that is conventionally labeled as $m_{3/2}$:

$$m_{3/2} \sim \langle F \rangle / M_P. \tag{2.32}$$

The GMSB model predicts a gravitino much lighter than the other MSSM particles ($m_{\widetilde{G}} \ll 1$ keV), as long as $M_{\text{mess}} \ll M_P$. Therefore $\widetilde{G}$ is the LSP of the theory. It is important to notice that the gravitino inherits also the non gravitational interaction from the goldstino. This means that, since the gravitational coupling is weak, the interaction of the gravitino with the MSSM particles are mediated by its longitudinal polarization (*i.e.* the goldstino). In this framework all the MSSM sparticles are expected to decay promptly into the next-to-lightest supersymmetric particle (NLSP) which then decays into the gravitino, with couplings suppressed by $\langle F \rangle$. In principle, any of the MSSM superpartners could be the NLSP, but GMSB models usually consider either a neutralino or a charged lepton playing this role. Considering the neutralino case, since $\widetilde{\chi}_1^0$ is a mixture including the photino, it decays to a photon and in a gravitino with a partial width proportional to:

$$\Gamma(\widetilde{\chi}_1^0 \to \gamma \widetilde{G}) \propto k_{1\gamma} (m_{\widetilde{\chi}_1^0})^5 (\sqrt{\langle F \rangle})^{-4}. \tag{2.33}$$

Here $k_{1\gamma} \equiv |N_{11}\cos\theta_W + N_{12}\sin\theta_W|^2$ is the photino fraction of $\widetilde{\chi}_1^0$, and N_{ij} are defined by Eq. (2.19).

Since the neutralinos are a mixture of gaugino ($\widetilde{B}$, $\widetilde{W}^0$) and higgsino ($\widetilde{H}_u^0$, $\widetilde{H}_d^0$) eigenstates, the lightest neutralino can decay also to a Z boson or a Higgs boson (h^0) in association with the gravitino. If the $\tilde{\chi}_1^0$ is gaugino-like, it mainly decays as $\tilde{\chi}_1^0 \to \gamma/Z\tilde{G}$. If the $\tilde{\chi}_1^0$ is higgsino-like, it decays as $\tilde{\chi}_1^0 \to h\tilde{G}$. In addition, since the longitudinal component of the Z boson mixes with the Goldstone mode of the Higgs field, a higgsino-like neutralino can also decay as $\tilde{\chi}_1^0 \to Z\tilde{G}$. However, in this manuscript only the bino-like neutralino NLSPs are considered, resulting in a significant fraction of events for which both neutralinos decay as $\tilde{\chi}_1^0 \to \gamma\tilde{G}$, thus leading to the experimental signature of $\gamma\gamma + E_{\mathrm{T}}^{\mathrm{miss}}$. The $\tilde{\chi}_1^0$ branching fraction to $\gamma + \tilde{G}$ is 100% for $m_{\tilde{\chi}_1^0} \to 0$ and approaches $\cos^2\theta_W$ for $m_{\tilde{\chi}_1^0} \gg m_Z$, with the remaining part of the $\tilde{\chi}_1^0$ decaying to $Z + \tilde{G}$, as shown by Figure 2.8.

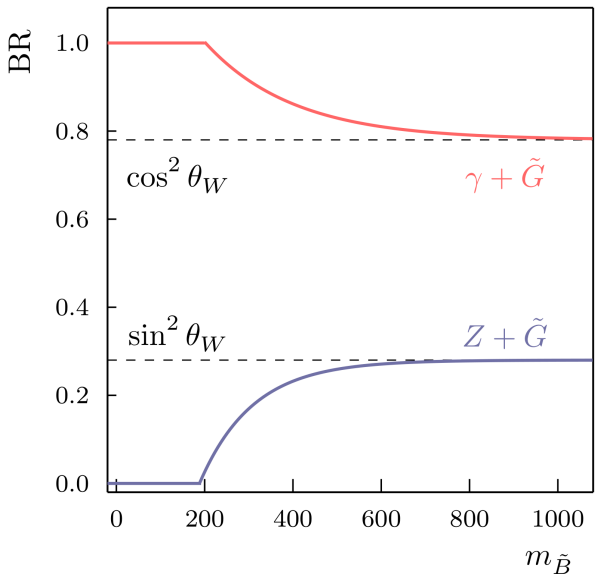

Figure 2.8: Branching ratio of the decay of the lightest neutralino, bino–like, to a gravitino and a photon or a Z boson as a function of the mass of the neutralino (75).

Finally, given Eq. (2.33), the mean decay length of $\widetilde{\chi}_1^0$ is proportional to $(\sqrt{\langle F\rangle})^4$. Three different regimes are therefore possible from the experimental point of view:

- $\sqrt{\langle F\rangle} \gtrsim 10^6\ GeV$: the neutralino decays outside the detector and resembles the stable neutralino case with missing transverse energy;

- $\sqrt{\langle F\rangle} \sim 10^6\ GeV$: the neutralino decays with a displaced vertex inside the detector (76);

- $\sqrt{\langle F\rangle} \lesssim 10^6\ GeV$: the neutralino NLSP decays promptly into a photon and a gravitino giving two photons plus missing energy in the final state, and this is the case considered for the analyses presented in Chap. 9.

2.8 Experimental GMSB searches at $\sqrt{s} = 8$ TeV in $\gamma\gamma + E_{\mathbf{T}}^{\mathbf{miss}}$ final state

The search for GMSB final states containing photons was performed by both the ATLAS and CMS collaborations using the data collected from pp collisions at $\sqrt{s} = 8$ TeV (27; 77). In particular, the two experiments looked for a final state containing two photons and missing transverse energy (due to the gravitino) produced through strong interaction as shown by Figure 2.9a.

The process proceeds through the creation of a couple of gluinos, that promplty into a NLSP neutralino (bino-like) and a quark–antiquark couple, and finally each neutralino decays promplty to a photon and a gravitino. Other SM objects (jets, leptons, photons) may be produced in these cascades. The ATLAS interpretation is based on the General Gauge Mediate (GGM) model that is based on a generalization of the GMSB, while the CMS analysis used a simplified model spectra scenario (78) which requires the branching ratio of the bino-like neutralino to the gravitino and the photon to be 100% excluding the contribution of the $Z + \widetilde{G}$ final state expected as explained in the previous section (see Figure 2.8).

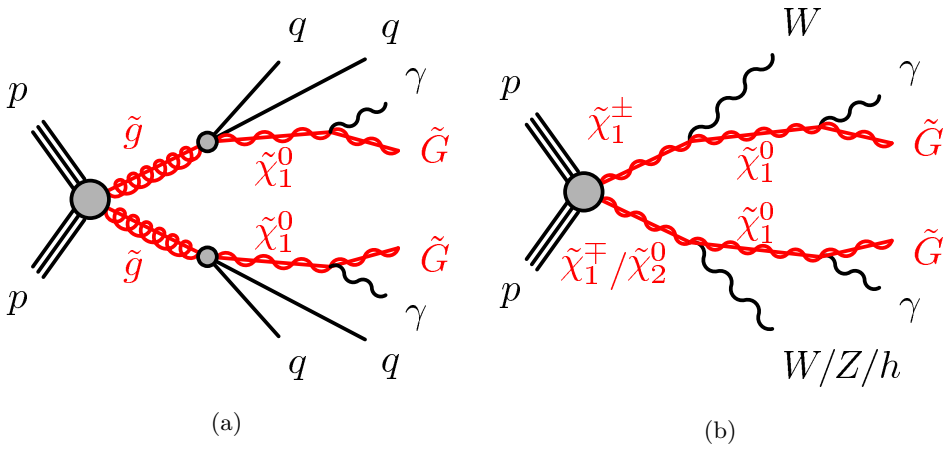

(a) (b)

Figure 2.9: Typical production and decay-chain processes for the strong production (a) and electro-weak production (b) instances of the GGM model for which the NLSP is a bino-like neutralino (27).

Neither analyses found any significant excess of events over the expected background produced by SM processes leading to a similar final state, therefore they set lower limits on the gluino mass. Exploiting an integrated luminosity $L \simeq 20$ fb^{-1} of $\sqrt{s} = 8$ TeV pp collisions the ATLAS collaboration excluded a gluino up to a mass of 1350 GeV and the lower limits from the CMS analysis range beyond 1.3 TeV for the gluino mass. The mass regions excluded in the $\widetilde{g}$–$\tilde{\chi}_1^0$ mass plane are shown in Figures 2.10 and 2.11 for the ATLAS and the CMS analyses respectively.

Additionally, the ATLAS analysis interpreted the result in term of the lower cross-section processes mediated by the electro-weak production as shown in Figure 2.9b. In this model the signal production proceeds through a degenerate triplet of wino states $\tilde{\chi}_2^0$ and $\tilde{\chi}_1^\pm$, and is dominated by the production of $\tilde{\chi}_1^+\tilde{\chi}_1^-$ and $\tilde{\chi}_2^0\tilde{\chi}_1^\pm$. Lower limits are then set on the mass of the wino across the $\tilde{\chi}_2^0$,$\tilde{\chi}_1^\pm$–$\tilde{\chi}_1^0$ mass plane. Wino are excluded up to a

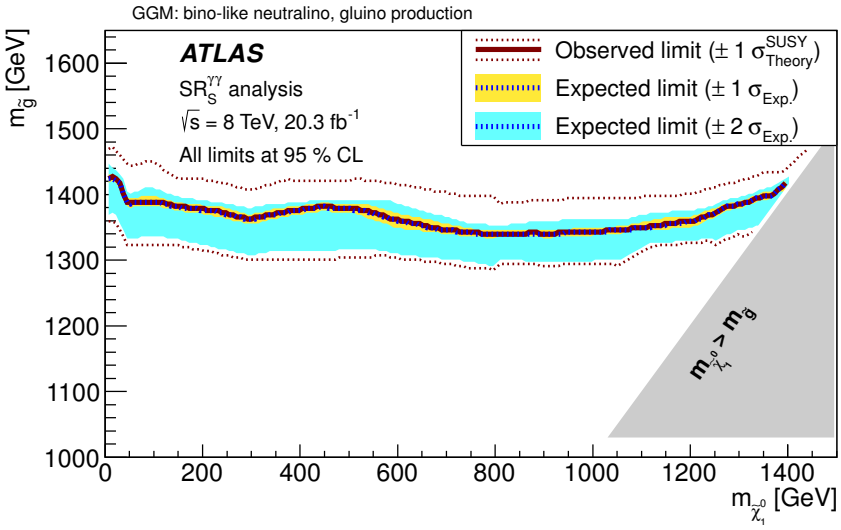

Figure 2.10: Exclusion limits in the gluino-bino mass plane of the ATLAS search performed with 8 TeV Run 1 data. Combinations of gluino and bino mass are excluded at 95% CL in the area below the unbroken curve. The observed limits are exhibited for the nominal SUSY model cross-section expectation, as well as for a SUSY cross section increased and decreased by one standard deviation of the cross-section systematic uncertainty. Also shown is the expected limit, as well as the ±1 and ±2 standard-deviation ranges of the expected limit (27).

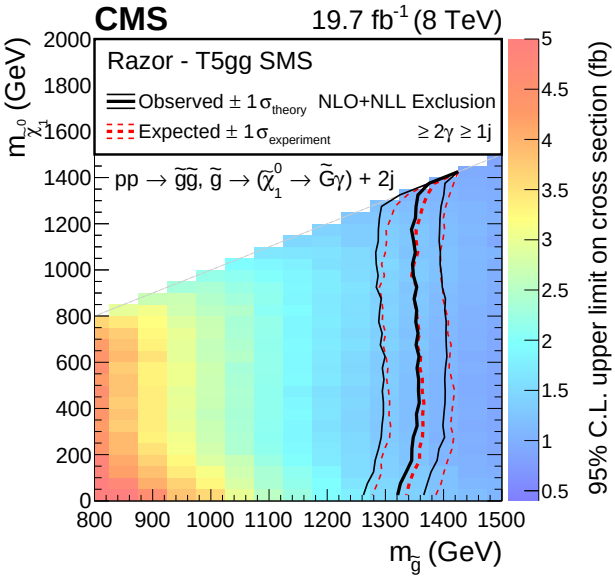

Figure 2.11: 95% C.L. observed upper limits on the signal cross section and exclusion contours in the gaugino-gluino mass plane for the T5gg simplified model spectra scenario for the CMS search perfomed with 8 TeV Run 1 data. The thick red dashed (black solid) line shows the expected (observed) limit. The thin dashed line and band show the 68% C.L. range about the expected limit. The solid line quantifies the impact of the theoretical uncertainty in the cross section on the observed limit. The color scale shows the excluded cross section for each set of mass values (77).

mass of ~ 600 GeV, as shown by Figure 2.12.

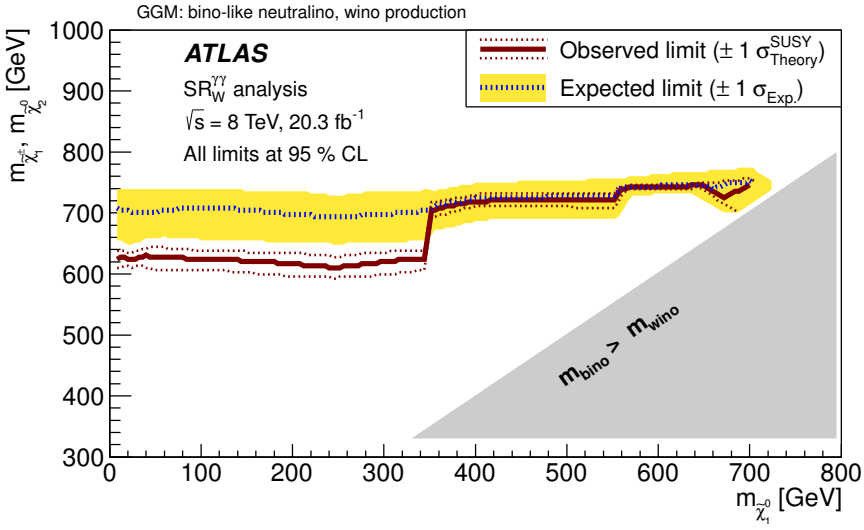

Figure 2.12: Exclusion limits in the wino-bino mass plane of the ATLAS search performed with 8 TeV Run 1 data. The vertical axis represents the wino mass while the horizontal axis represents the bino mass. The observed limits are exhibited for the nominal SUSY model cross-section expectation, as well as for a SUSY cross section increased and decreased by one standard deviation of the cross-section systematic uncertainty. Also shown is the expected limit, along with its ± 1 standard-deviation range. The discontinuity at $m_{\tilde{\chi}_1^0} = 350$ GeV is due to the switch between the use of two different signal regions in the analyses, the former of which exhibits a small excess of observed events relative to the expected SM background (27).

In Chapter 9 a similar search using the pp collision data collected at $\sqrt{s} = 13$ TeV by the ATLAS detector during the 2015 and the 2016 is presented. As shown by Figure 2.13 the gluino pair production cross-section at $\sqrt{s} = 13$ TeV is expected to increase by 40 times for $m_{\tilde{g}} = 1400$ GeV with respect to $\sqrt{s} = 8$ TeV. Therefore, a first analysis is performed using only the 3.2 fb^{-1} integrated luminosity collected during 2015, that is already sufficient to surpass the sensitivity on the gluino-pair mediated model, while the wino mediated process interpretation is considered only in the analysis exploiting the full 2015 and 2016 dataset.

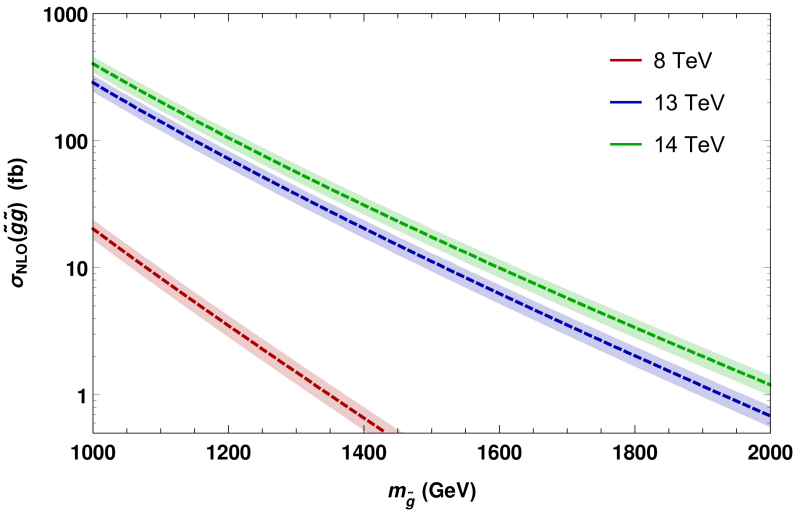

Figure 2.13: Gluino pair production cross-section at the LHC for $\sqrt{s} = 8$, 13, 14 TeV calculated at NLO with Prospino (79). Squarks are assumed to be heavy with mass $m_{\tilde{q}} = 5$ TeV. The shaded areas show the scale uncertainty.

Chapter 3

The Large Hadron Collider

The Large Hadron Collider (LHC) (1) is a proton and heavy ion accelerator and collider built at CERN, near Geneva. It is is located in a 27 km long underground tunnel at a depth of about 100 meters.

The project was approved by the CERN Council in December 1994. It was designed to overcome the performance, in term of center-of-mass energy and luminosity, of all existing and past accelerators such as the Tevatron $p\bar{p}$ collider at Fermilab and the LEP e^+e^- collider at CERN.

The LHC was designed to reach a proton-proton center-of-mass energy of 14 TeV and an instantaneous luminosity of $10^{34}\text{cm}^{-2}\text{s}^{-1}$ in proton-proton collision. Due to technical problems the center-of-mass energy was 7 TeV in 2010 and 2011, and 8 TeV in 2012. Since the beginning of 2015, after a technical shut-down of two years to consolidate the accelerator, the LHC has been accelerating protons up to 6.5 TeV, reaching a center-of-mass energy of 13 TeV, very close to the design value.

3.1 Interactions at hadron colliders

The LHC was projected as an hadron accelerator and collider, because accelerating electrons in a circular trajectory is very challenging and expensive, due to the huge radiative energy losses. Indeed a charged particle radially accelerated loses energy according to the relation (80):

$$\frac{dE}{dt} \propto \frac{E^4}{m^4}, \tag{3.1}$$

where E is the energy of the particle and m is its mass. Eq. (3.1) implies that in order to accelerate an electron (e) to the same energy of a proton (p), a synchrotron has to compensate for an energy loss that is $(m_p/m_e)^4 \sim 10^{13}$ higher.

However, the use of hadrons is not free from disadvantages. Protons are not elementary particles, they are composed of partons (quarks and gluons), which carry only a fraction of the total momentum of the proton. Collision events can be classified in two categories:

- *Soft Collisions.* In a LHC bunch crossing the most frequent interactions are originated by long distance collisions in which the protons behave as elementary particles. Usually such processes have low transferred momentum, therefore the particles in the final state are characterized by small transverse momentum. These events are called *minimum bias.*

- *Hard Collisions.* The hard collisions are rarer events and the most interesting ones from the experimental point of view. They are short distance collisions characterized by a high momentum exchange so that the production of particles at large angle, high transverse momentum and high mass is possible.

In hard collisions the composite structure of protons comes to light. Indeed, the collision can be considered as happening between two partons of the incoming protons. Therefore the center-of-mass energy depends on the fraction of momentum carried by the colliding gluons and quarks, and it is lower than the *pp* center-of-mass energy.

The parton center-of-mass energy $\sqrt{\hat{s}}$ is equal to

$$\sqrt{\hat{s}} = \sqrt{x_a x_b s}, \tag{3.2}$$

where $\sqrt{s}$ is the proton center-of-mass energy and x_a, x_b are the fractions of the proton momenta carried by the scattering partons. The cross section for a hard-scattering interaction is:

$$\sigma_{pp\to X} = \sum_{a,b} \int dx_a dx_b f_a(x_a, Q^2) f_b(x_b, Q^2) \hat{\sigma}_{ab\to X}(x_a, x_b), \tag{3.3}$$

where $\hat{\sigma}_{ab\to X}$ represents the cross section of the elementary interaction between two

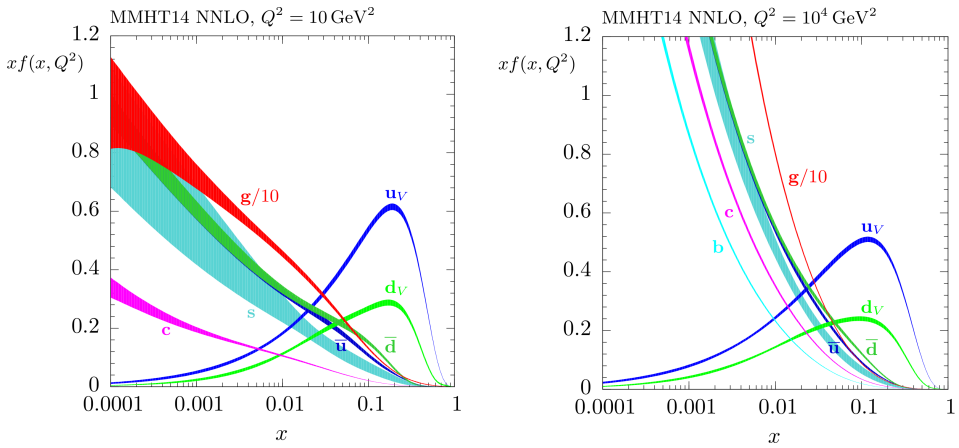

Figure 3.1: Parton Distribution Fucntions (PDFs) computed for $Q^2 = 10$ GeV^2 and $Q^2 = 10^4$ GeV^2 from MMHT 2014 PDFs (81).

partons and $f_a(x, \mu^2)$, $f_b(x, \mu^2)$ are the Parton Distribution Functions (PDFs), *i.e.* the probability that a partons carry a fraction x_a and x_b of the total proton momentum. Figure 3.1 shows the PDFs for the quarks in a proton, evaluated for $Q^2 = 2$ GeV^2.

In conclusion the experiments at hadron colliders have to cope with two main issues. The first is that the interesting hard collisions happen simultaneously with background arising from the minimum bias events and the *underlying event*, which is produced by the hadronization of many objects at low transverse momentum and small angle, which come from the rest of the colliding protons not involved in the hard interaction. The second issue is the fact that the center-of-mass energy is unknown and it is only quantifiable using the PDFsv nb, introducing additional uncertainty in the calculation of the theory cross-section prediction of the studied phenomena.

3.2 Luminosity and pileup

In a particle accelerator the rate of events of a process characterized by a cross-section σ_{event} is given by:

$$\frac{dN_{event}}{dt} = \mathcal{L}\sigma_{event}. \tag{3.4}$$

$\mathcal{L}$ is the instantaneous luminosity, when depends only on the beam parameters and can be written for Gaussian beams as:

$$\mathcal{L} = \frac{N_b^2 n_b f_{rev} \gamma_r}{4\pi\epsilon_n \beta^*} F \quad [\mathrm{cm}^{-2}\mathrm{s}^{-1}], \tag{3.5}$$

where:

- N_b is the number of particles per bunch;
- n_b is the number of bunches per beam;
- f_{rev} is the revolution frequency;
- γ_r is the relativistic gamma factor;
- ϵ_n is the transverse normalized beam emittance;
- β^* is the beta focusing function at the collision point;
- F is the geometric luminosity reduction factor due to the crossing angle at the interaction point; it can never be larger than 1.

Typical values for these quantities at the LHC are listed in Table 3.1.

Table 3.1: Typical proton running conditions at the LHC during *pp* collisons from 2010 to 2016, shown together with the design parameters (82).

Machine parameter	Design	2010	2011	2012	2015	2016
Beam energy [TeV]	7.0	3.5	3.5	4.0	6.5	6.5
N_b [10^{11} p]	1.15	1.0	1.3	1.5	1.0	1.1
n_b	2808	368	1380	1380	2244	2200
Bunch spacing [ns]	25	150	50	50	25	25
f_{rev} [kHz]			11.245			
ϵ_b [μm]	3.75	2.6	2.4	2.4	3.5	2.2
β^* [m]	0.55	3.5	1.0–1.5	0.6	0.8	0.4
Max. peak luminosity [10^{34} cm^{-2} s^{-1}]	1.0	0.021	0.35	0.77	0.47	1.45

The luminosity in the LHC is not constant but decreases with time due to the degradation of the intensity and of the emittance of the circulating beams. The time available (*i.e.* physics run) for data taking after the beam injection and acceleration in the LHC is optimized considering the beam luminosity degradation and the amount of time taken by

the accelerator chain to provide a new beam for data taking. The main cause of the luminosity decay at the LHC are the *pp* collision themselves in the LHC interaction points. The behavior of the luminosity as a function of time is:

$$\mathcal{L}(t) = \frac{\mathcal{L}_\prime}{(1 + t/\tau_{nuclear})^2}, \tag{3.6}$$

where

$$\tau_{nuclear} = \frac{N_{tot,0}}{\mathcal{L}_\prime \sigma_{tot} k}. \tag{3.7}$$

$N_{tot,0}$ is the initial beam intensity, $\mathcal{L}_\prime$ the initial luminosity, σ_{tot} the total *pp* cross section and k the number of interaction points (4).

The total number of collisions in a given period of time is proportional to the *integrated luminosity* $L = \int \mathcal{L} dt$. In particular, $N_{coll} = \sigma L$, where σ is the inelastic *pp* interaction cross-section. The results presented in this thesis are based on data collected by ATLAS at a center-of-mass energy $\sqrt{s} = 13$ TeV during 2015 and 2016, corresponding to an integrated luminosity of 3.9 fb^{-1} and 35.6 fb^{-1} respectively, before data quality requirements. Figure 3.2 shows the cumulative integrated luminosity delivered to and recorded by the ATLAS detector at 13 TeV center-of-mass energy in 2015 and 2016 together with the peak instantaneous luminosity delivered to ATLAS during stable beams as function of time.

Another important parameter, related to the instantaneous luminosity, is the mean number of inelastic interactions per bunch crossing, called *pileup* events. Pileup events, originated mainly from soft collisions, are not interesting for the physics program of ATLAS and are treated as a background. The pileup deteriorates the energy resolution in the object measurement (leptons, photons, jets, E_T^{miss}, etc.) and makes the identification of vertices and the reconstruction of tracks more difficult because it increases the number of hits in the tracker.

The pileup event rate and the instantaneous luminosity are related by:

$$\mathcal{L} = \frac{rate_{inelastic}}{\sigma_{inelastic}} = \frac{\mu n_b f_{rev}}{\sigma_{inelastic}}, \tag{3.8}$$

where μ is the number of inelastic interactions per bunch crossing, and n_b is the number of colliding bunches in the ring. The number of pileup interactions per bunch crossing μ is therefore proportional to $\frac{\mathcal{L}}{f}$ and it increases with the instantaneous luminosity.

During 2015 the mean number of inelastic interactions per bunch crossing was $\langle\mu\rangle = 13.7$. In the 2016 data taking it was $\langle\mu\rangle = 24.9$. Figure 3.3 shows the distribution of the mean number of interactions per bunch crossing for the 2015 and 2016 data.

3.2.1 The ATLAS luminosity measurement

A precise measurement of the delivered luminosity is a key component for precision physics measurements, in particular for the analyses aiming to evaluate the cross-section of a certain physics process.

In the ATLAS detector (2) the luminosity measurement (84) is provided by a Cherenkov detector named LUCID (LUminosity measurement using a Cherenkov Integrating Detector) (85). It is composed by two modules, composed by 20 photomultipliers (PMTs), surrounding the beam pipe on both forward ends of ATLAS, 17 m far from the interaction point, covering the pseudorapidity range $5.6 < |\eta| < 6.0$.

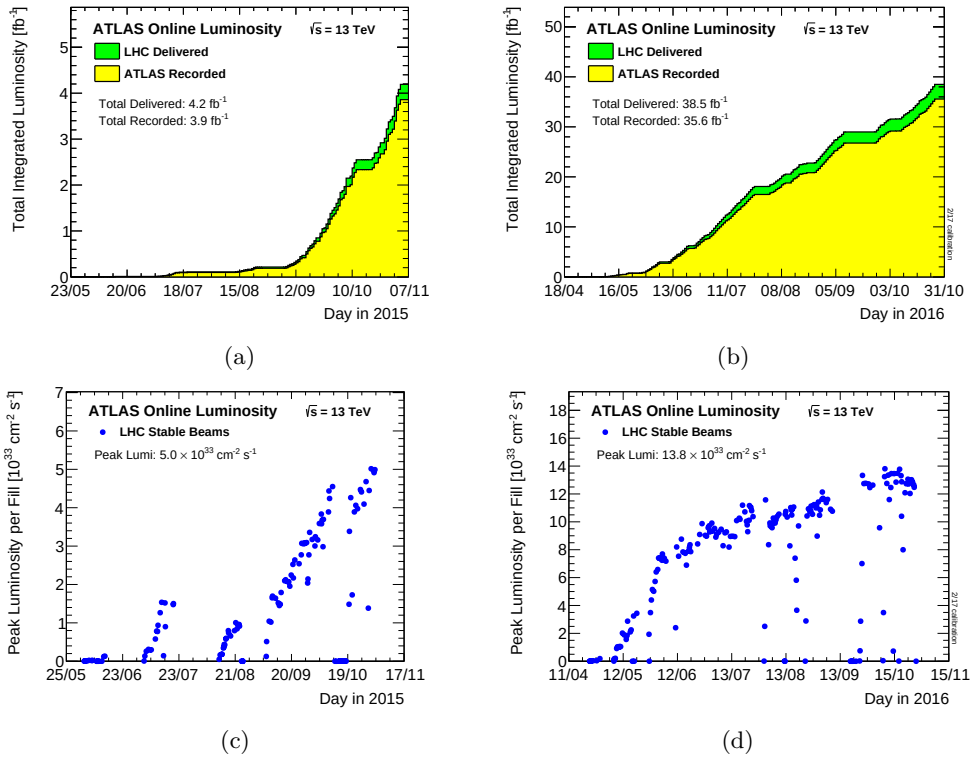

Figure 3.2: Top: Integrated luminosity versus time delivered by the LHC (green), recorded by ATLAS (yellow), during stable beam conditions for pp collisions at 13 TeV center-of-mass energy in 2015 (a) and 2016(b). Bottom: The peak instantaneous luminosity delivered to ATLAS during stable beams for pp collisions at 13 TeV centre-of-mass energy is shown for each LHC fill as a function of time in 2015 (c) and 2016 (d) (83).

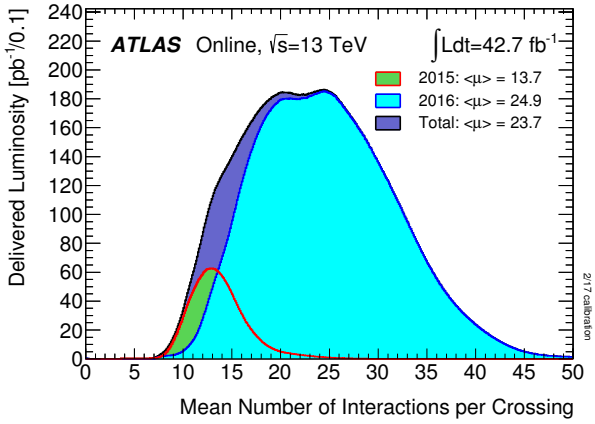

Figure 3.3: The luminosity-weighted distribution of the mean number of interactions per crossing for the 2015 and 2016 data. The mean number of interactions per bunch crossing corresponds to the mean of the poisson distribution on the number of interactions per crossing calculated for each bunch (83).

LUCID evaluates the luminosity $\mathcal{L}$ measuring the bunch luminosity $\mathcal{L}_b$ produced by each single pair of colliding bunches through a hit counting algorithm:

$$\mathcal{L}_b = \frac{\mu_b f_{rev}}{\sigma_{\text{inelastic}}} = \frac{\mu_{\text{visible}} f_{rev}}{\sigma_{\text{visible}}}, \tag{3.9}$$

where μ_b is the average number of inelastic interactions per bunch crossing and, given ϵ the product of the acceptance of the detector and the efficiency of the counting algorithm, $\mu_{\text{visible}} = \epsilon\mu$ and $\sigma_{\text{visible}} = \epsilon\sigma_{\text{inelastic}}$.

Since μ_{visible} is a directly measurable quantity, the calibration of the luminosity scale of LUCID amounts to determining the visible cross-section σ_{visible}. This is done using dedicated LHC fills called van der Meer scans (86) (vdM), where the size and shape of the interaction region is measured by recording the relative interaction rates as a function of the transverse beam separation, and thus deriving $\mathcal{L}_b$ from the geometrical configuration of the beam.

The LUCID luminosity is cross-checked with the measurement performed by other ATLAS subdetectors (see Chap. 4):

- the ATLAS Inner Detector provides a relative luminosity measurement by counting the numbers of the reconstructed charged-particle tracks;

- in the Tile Calorimeter (TileCal), the luminosity is measured from the the current drawn by each PMT, which is proportional to the number of particles interacting in a given TileCall cell;

- in the electromagnetic endcap (EMEC) and forward (FCal) calorimeters the luminosity is evaluated starting from the current that the High Voltage supplies inject into the LAr-filled cell gaps in order to maintain constant the electric field against the drops caused by the particle flux. This current is proportional to the particle flux and thus to the instantaneous luminosity.

The stability of the ATLAS luminometers is shown in Figure 3.4, in terms of percentage deviation of Inner Detector, TileCAL, EMEC measurements with respect to LUCID, showing a long-term stability better than 1%. This deviation, together with the uncertainty coming from the *vdM* calibration procedure (1.6%) and the calibration transfer factor (0.9 %) from the low-μ configuration of the *vdM* fills to the higher μ of physics runs, gives a final uncertainty of 2.1% and 3.2% for the luminosity collected in the 2015 and 2016 respectively (87).

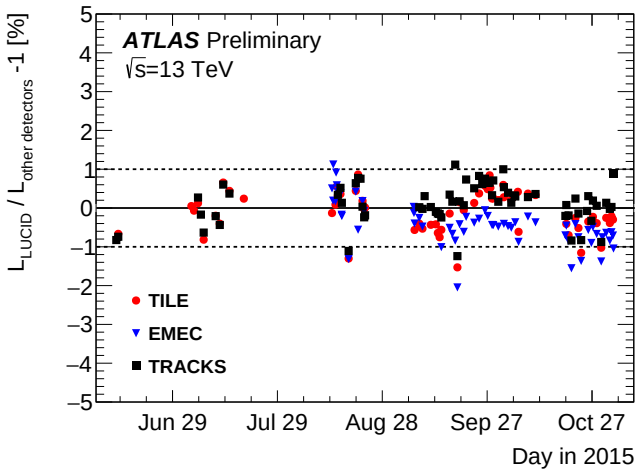

Figure 3.4: Run to run stability in 2015. The fractional difference with respect to LUCID is shown for the luminosity estimates provided by the Inner Detector (black dots), the Tile Calorimeter (red circles) and the electromagnetic calorimeters (blue triangles) (83).

3.3 Accelerator chain and LHC structure

As shown in Figure 3.5, a set of linear and circular accelerators are used to pre-accelerate protons and ions before their injection into the LHC. For protons, the accelerator chain is composed of:

- a linear accelerator (LINAC) that speeds up protons to 50 MeV;
- the Synchrotron Booster, that accelerates protons up to 1.4 GeV;
- the Proton Synchrotron (PS), where protons reach an energy of 25 GeV;
- the Super Proton Synchrotron (SPS), which accelerates protons up to 450 GeV and finally injects them into the LHC;

The protons are injected into LHC in clockwise and anticlockwise directions and they are accelerated up to the nominal energy $\sqrt{s}/2$. In order to bring the protons from 450 GeV to the nominal 7 TeV energy, superconducting Radio Frequency cavities (RF) (89) are used, each one capable of delivering 2 MV at 400 MHZ and operating at a temperature of 4.5 K. The LHC ramp to nominal energy per beam takes around 20 minutes.

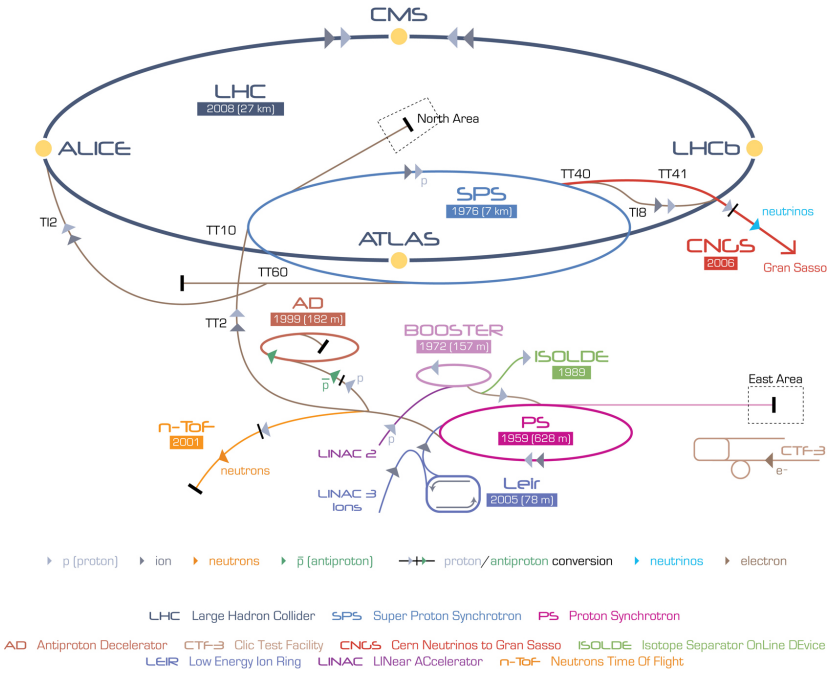

Figure 3.5: Accelerator complex at CERN (88).

The particle bending in the LHC relies on 1232 Niobium-Titanium superconducting deflecting dipole magnets which operate at the temperature of 1.9 K and produce a field of around 8.4 Tesla at a current of 11,700 A. The LHC lattice is then composed also by 392 quadrupole magnets, focusing the beam alternatively in the horizontal and in the vertical plane, depending on their polarity. The cross-sections of these two types of magnets are shown in Figure 3.6.

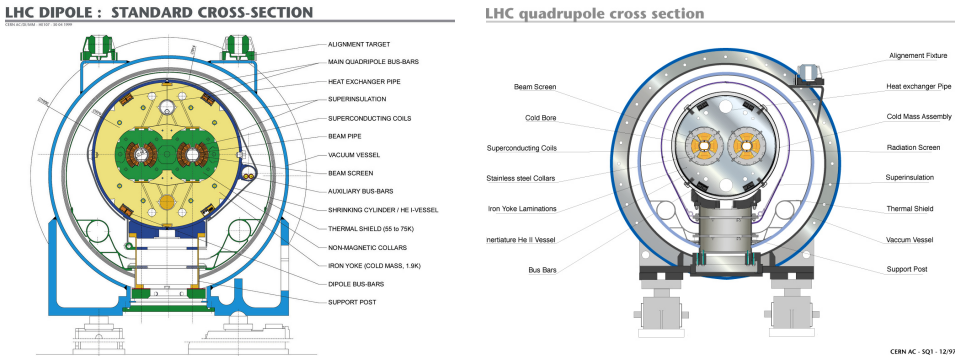

(a) (b)

Figure 3.6: Cross-section of the superconducting dipole (a) (90) and quadrupole (b) (91) magnets used in the LHC ring.

Figure 3.7 shows the schematic layout of a FODO cells in the LHC, which is composed

by six dipole magnets and two quadrupole magnets with opposite polarity. Higher order magnets such as sextupoles, octupoles and decapoles are installed at the end of the dipoles in order to correct field non uniformities and thus guarantee the stability of the beam.

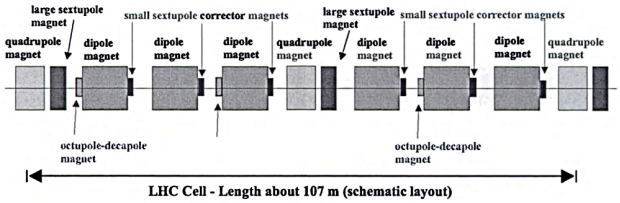

Figure 3.7: Schematic layout of one LHC cell with dipole, quadrupole and correction magnets (92).

3.4 The experiments at LHC

In the LHC ring the two proton beams collide in four points across the accelerator ring where the the four main experiments are placed. They are:

- **ATLAS** (A Toroidal LHC Apparatus) (2) and **CMS** (Compact Muon Solenoid) (3) are general purpose detectors, designed to cover the widest possible range of physics in the proton-proton and heavy ion collisions.

- **LHCb** (93) is focused on B hadron decays. The purpose of this detector is to study the properties of b quarks, and to measure the CKM matrix elements parameters that describe CP violation and rare b quark decays, for instance $B_S \rightarrow \mu^+\mu^-$, which are sensitive to new physics.

- **ALICE** (A Large Ion Collider Experiment) (94) is dedicated to heavy ion collisions to study the strong interactions of quarks–gluon plasma.

Two additional detectors, TOTEM and LHCf, are installed at the LHC near the CMS and ATLAS detectors, respectively. They study the beam soft collisions, which yield particles scattered in the forward region very close to the beam pipe.

- **TOTEM** (TOTal Elastic and diffractive cross section Measurement) (95) is optimized to measure the total pp cross section, to study the nuclear elastic pp cross section and to perform a comprehensive physics program on diffractive processes.

- **LHCf** (Large Hadron Collider forward) (96) is dedicated to the measurement of neutral particles emitted in the very forward region. Its measurements will be useful for interpreting and calibrating cosmic-ray experiments.

Chapter 4

The ATLAS detector

ATLAS (2) is one of the two general purpose experiments at the LHC.

The detector has a cylindrical shape with a radius of 12 meters and a length of 44 meters. It weights approximately 7000 tons.

The detector, shown in Figure 4.1, is composed by different nested sub-detectors, that from the closest one to the beam pipe to the outer one are:

- Inner Detector (ID), for charged particles tracking and reconstruction of interaction vertices;
- Electromagnetic Calorimeter (EM), for electron and photon energy reconstruction;
- Hadronic Calorimeter (HAD), for the detection of charged and neutral hadrons;
- Muon Spectrometer (MS), for the identification of muons.

The detector also includes a magnet system that produces the electromagnetic field needed for the measurement of charged particle momenta in the Inner Detector and in the Muon Spectrometer.

The ATLAS coordinate system is defined as follows. The z axis is defined by the beam direction and the x-y plane is the transverse plane perpendicular to the beam direction. The positive x direction points toward the center of the LHC ring and the y positive direction is up the x-z plane. All the transverse quantities (i.e. p_T, E_T, E_T^{miss}) are defined in the x-y plane.

The azimuthal angle is called ϕ and is measured around the beam direction, θ is the polar angle variable with respect to the z axis. To have a Lorentz invariant angular coordinate system around the interaction point the (η, ϕ) set of coordinates is used, where η is the pseudo-rapidity and is defined as:

$$\eta = -\ln\left[\tan\left(\frac{\theta}{2}\right)\right]. \tag{4.1}$$

The angular distance ΔR in the (η, ϕ) space is defined as:

$$\Delta R = \sqrt{(\Delta\eta)^2 + (\Delta\phi)^2}. \tag{4.2}$$

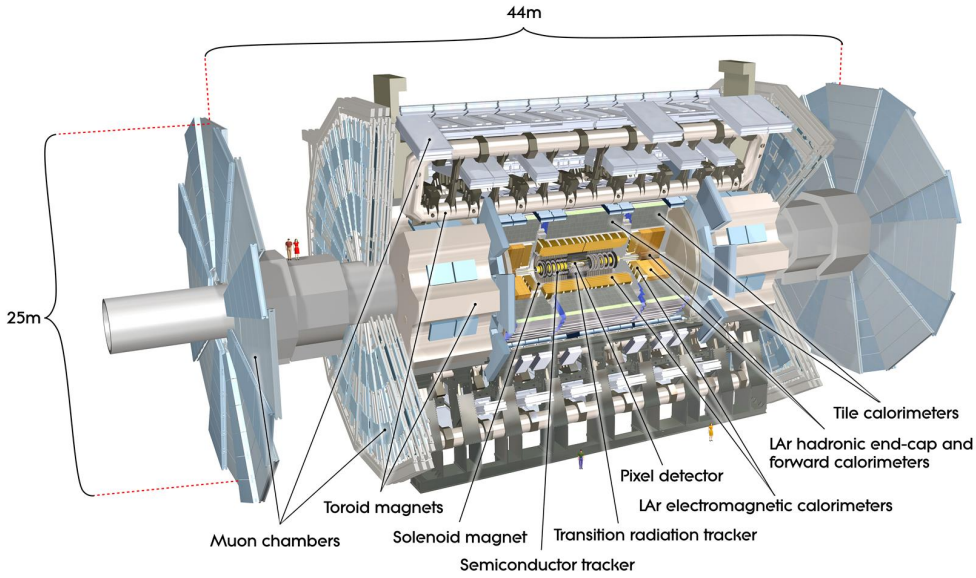

Figure 4.1: A schematic view of the ATLAS detector (97).

4.1 Magnet system

A superconducting magnet system provides a magnetic field over a volume of approximately 12,000 m^3. Differently from CMS, which uses a single solenoid magnet to provide a 4 T magnetic field, the ATLAS design includes two separate magnetic systems: a central solenoid (98), located between the ID and the EM calorimeter, which provides an axial magnetic field in the ID volume, a barrel toroid (99) and two end-cap toroids (100) that produce a toroidal magnetic field in the MS volume.

- **Solenoid**. The solenoidal magnet is a coil of superconducting material which provides a axial magnetic field of 2 T for the Inner Detector, generated by an 8 kA electric current, and it is cooled to a temperature of 4.5 K. It is 5.8 m long, with an inner radius of 1.23 m, and an outer one of 1.28 m, corresponding to 0.66 radiation lengths only. To optimize the material budget the coil is placed inside the calorimeter cryostat.

- **Toroids**. The ATLAS toroidal magnet system, shown in Figure 4.2, is composed of a barrel toroid, consisting of 8 separates coils with an electric current of 20 kA, and two end-caps toroids that provide a field of 0.5 T and 1 T in the central and end-cap regions respectively. The magnets are installed outside the calorimeters. The barrel has an inner diameter of 9.4 m, an outer diameter of 20.1 m, and it is 25.3 m long. The endcap toroids generate a magnetic field near the beam axis, in order to deflect the particles with small polar angles. Each of the toroids consists of eight superconducting coils inside an insulating vacuum vessel with a diameter of 10.7 m and is 5 m wide. Together with the barrel toroid they provide an almost complete geometric coverage of the magnetic field.

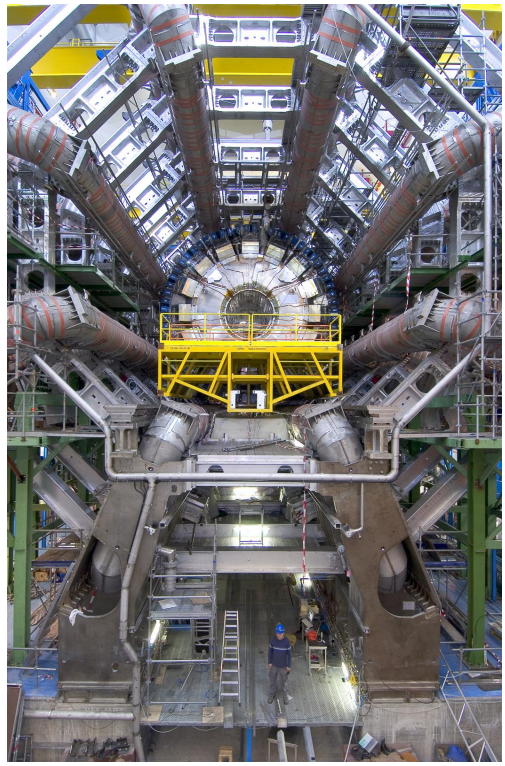

Figure 4.2: Photo of the 8 coils of the ATLAS detector barrel toroid during the installation (97).

4.2 Inner Detector

The ATLAS Inner Detector (101), shown in Figure 4.3, is the closest ATLAS sub-detector to the beam pipe. It is designed to provide hermetic and robust pattern recognition and excellent momentum resolution of charged particles and both primary and secondary vertex reconstruction capability.

Due to the proximity to the interaction point, the ID design requires a high resistance to radiation for all the sensors, on-detector electronics, mechanical structures and services.

The ID is composed of a barrel and of two end-caps to extend the pseudorapidity coverage to $|\eta| = 2.5$. It is immersed in a 2 T solenoidal magnetic field and it is constituted of layers of high resolution silicon detectors at inner radii and of gaseous tracking detectors at higher radii. Given the high number of tracks per events, high granularity detectors are needed to perform high precision track parameter measurements and the event vertex reconstruction.

The inner detector is made of three sub-detectors that exploit different technologies: silicon pixels (Pixel detector), silicon microstrips (Semi-Conductor Tracker, or SCT) and straw-tubes (Transition Radiation Tracker TRT). The sub-detector structure is shown in a virtual section of the ID in Figure 4.4.

- The Pixel detector (102) is the first detector that is crossed by the particles produced by the beam interactions and it has the best spatial resolution performance of all

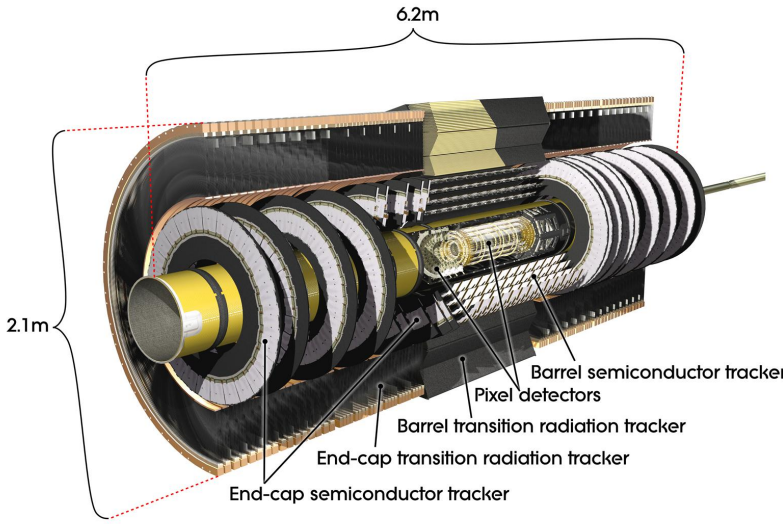

Figure 4.3: The ATLAS Inner Detector (97).

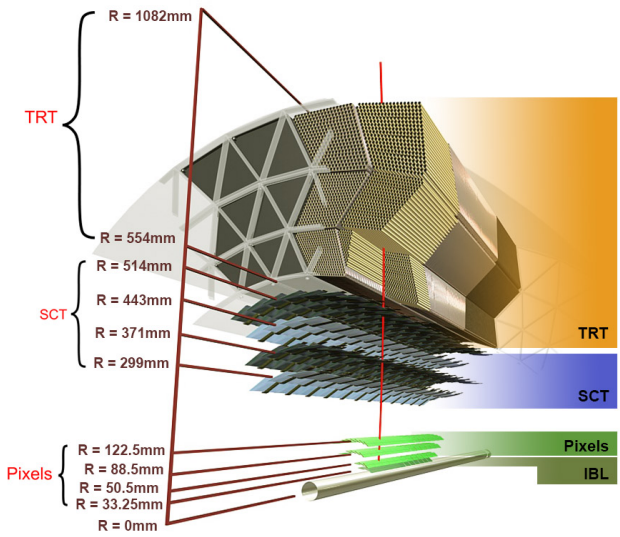

Figure 4.4: Virtual section of Inner Detector in the barrel region (97).

sub-detectors. It is placed close to the beam pipe at radii going from 31 mm to 123 mm and covers a pseudorapidity region of $|\eta| < 2.5$. It is made of silicon pixel detectors arranged in four cylindrical layers in the barrel area, positioned at radial distances of 31 mm, 50.5 mm, 88.5 mm and 122.5 mm from the beam line. In the two end-caps it is composed of three disks, arranged at radial distances of 49.5 mm, 58.0 mm and 65.0 mm. The pixel sensors are segmented in R-ϕ and z and they are characterized by an intrinsic hit position resolution of ~ 12 μm along R-ϕ and a resolution along the z direction of ~ 72 μm in the first layer and ~ 115 μm for the

other three layers. The pixels provide generally 4 points for each track crossing the detector.

The innermost pixel layer in the barrel, called the Insertable B-Layer (103) (IBL), was installed between, Run 1 and Run 2, between a new smaller beam pipe and the first layer of the original Pixel detector. The additional room needed for the installation of the IBL was obtained with a new beryllium beam pipe with a reduced inner diameter (47 mm instead of 59 mm) to fit inside the IBL. This new detector allows to restore in Run 2 the tracking and b-tagging efficiency of the Pixel detector that have been deteriorated due to radiation damage and hardware failure and inefficiencies. Moreover the Run 1 configuration of the Pixel detector was designed for a peak luminosity of $1 \times 10^{34}\,\mathrm{cm}^2\mathrm{s}^{-1}$ which has been exceeded during the LHC Run 2 (see Table 3.1). Finally, being very close to the interaction point, the IBL allows to improve the accuracy of the vertex and track impact parameter. Figure 4.5 shows the improvement of resolution on the transverse impact parameter (the distance d_0 in the xy plane between the track closest point to the z axis and the z axis itself) and on the longitudinal impact parameter (the z coordinate z_0 of the closest point of approach to the z axis) determination as a function of p_T due to the additional IBL pixel layer (104).

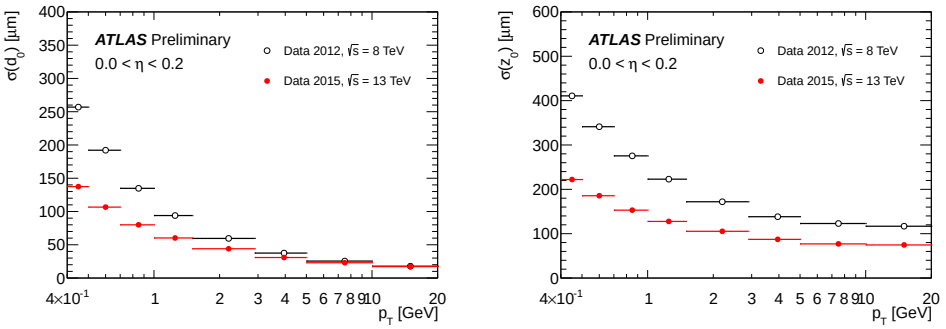

(a) $\sigma(d_0)$ (b) $\sigma(z_0)$

Figure 4.5: Transverse impact parameter (a) and longitudinal impact parameter (b) resolution measured with data taken in 2015, at $\sqrt{s} = 13$ TeV, with the Inner Detector including the IBL, as a function of p_T, for values of $0.0 < |\eta| < 0.2$, compared to that measured with 2012 data, at $\sqrt{s} = 8$ TeV (104).

- The Semi-Conductor Tracker (105; 106) completes the precision tracking of the Pixel detector. It is placed at medium radii (299 mm$< r <$ 514 mm) of the ID volume and it is composed of eight layers of silicon microstrips in the barrel region and nine layers in the end-caps. The barrel layers are organized in 4 cylinders made of two layers of sensors glued back-to-back with a 40 mrad stereo angle. They are placed at approximate radial distances of 30, 37, 44 and 51 cm from the interaction point, and provide 4 additional space points for each tracks. The intrinsic hit resolution of the strips is ~ 16 μm along R-ϕ and ~ 580 μm along the z axis .

- At larger radii (554 mm$< r <$ 1082 mm), the Transition Radiation Tracker (107; 108) is the outer part of the inner detector and provides up to 36 additional points though with a worse intrinsic single hit spatial resolution ($\sim 130\,\mu$m in $r - \phi$).

The TRT works both as a drift chamber measuring the charge drift time and as transition radiation detector for electron identification. It is composed of straw-tubes filled with a Xenon gas mixture, with a diameter of 4 mm and long up to 150 cm. Starting in 2012 a gradually increasing number of Xe leaks were detected in the TRT. Because of the high cost of Xenon gas some TRT modules were filled with a significantly less expensive Argon-based gas mixture. In the barrel region there are 50000 tubes parallel to the beam line and 320000 tubes in end-cap regions disposed radially in wheels. The spaces between the straws are filled with polymer fibres (barrel) and foils (endcaps) to create transition radiation. Transition radiation (TR) is emitted when a highly relativistic charged particle with a Lorentz factor $\gamma \gtrsim 10^3$ traverses boundaries between materials of different dielectric constants. TR photons are absorbed by the Xe and Ar atoms, depositing additional energy in the gas and leading to significantly higher readout signals with an amplitude that can exceed the 6 keV high threshold (HT). This functionality provides substantial discriminating power between electrons and pions over the energy range between 1 and 200 GeV and is a key component of the electron identification selection criteria (see Sec. 5.1.2). The probability for electrons and pions to exceed the HT as a function of the Lorentz-γ factor is shown in Figure 4.7a, only the most energetic pions have large enough γ-factor to emit TR. Figure 4.7b shows the pion misidentification probability for HT fraction criteria that give 90% electron efficiency selection.

The overall ID momentum resolution (achieved in Run 1, so before the IBL insertion) is

$$\frac{\sigma_{p_\mathrm{T}}}{p_\mathrm{T}} = 0.05\% \cdot p_\mathrm{T} \oplus 1\%. \tag{4.3}$$

The amount of material in the ID to achieve high granularity and including readout and cooling system is quite sizeable and it is shown in Figure 4.7 in terms of radiation length X_0 and nuclear interaction length λ (see Sec. 4.3.1). It varies from 0.5 to 2.5 X_0 depending on η (109). As a consequence the photons may convert into electron-positron pairs before reaching the electromagnetic calorimeter and electrons loose part of their energy through bremsstrahlung emissions affecting the resolution of the energy measured by the calorimeter system.

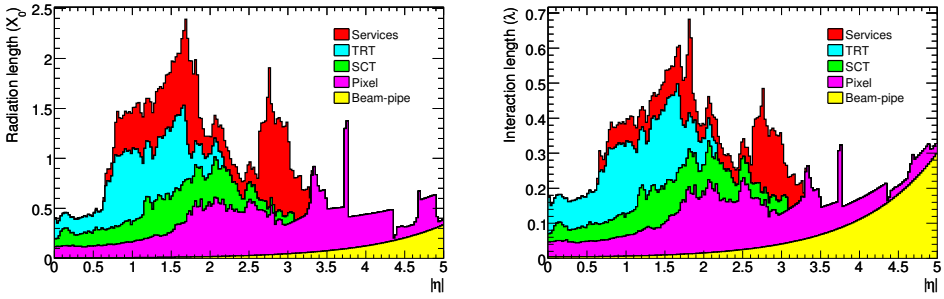

(a) X_0 (b) λ

Figure 4.6: Material distribution (X_0, λ) at the exit of the ID envelope, including the services and thermal enclosures. The distribution is shown as a function of $|\eta|$ and averaged over ϕ (109).

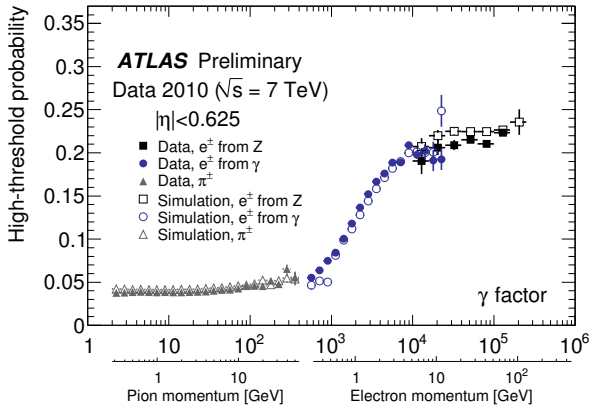

(a)

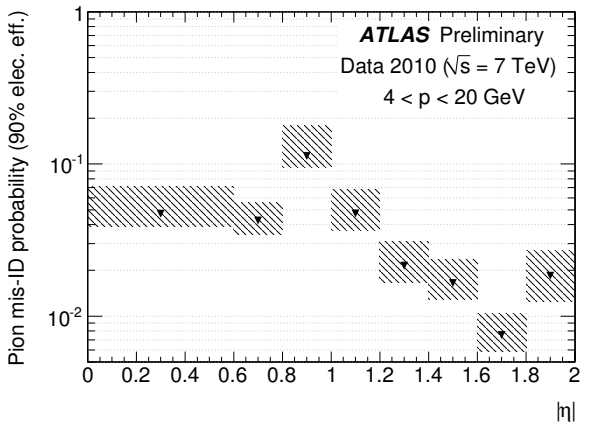

(b)

Figure 4.7: (a) Probability of a TRT high-threshold (HT) hit as a function of the Lorentz factor γ for the TRT ($|\eta| < 0.625$). (b) Pion misidentification probability for HT fraction criteria that give 90% electron efficiency, determined separately in different η bins (110).

4.3 Calorimeters

The ATLAS calorimetric system, shown in Figure 4.8, consists of three calorimeters: the Electromagnetic Calorimeter (EM) that covers the pseudorapidity region $|\eta| < 3.2$, the Hadronic Calorimeter (Had) which covers the pseudorapidity region $|\eta| < 3.9$ and the Forward Calorimeter (FCal) which covers the pseudorapidity region $3.1 < |\eta| < 4.9$. The calorimeters have the main purpose of measuring the energy and direction of incident hadrons, electrons and photons and they also give a fundamental contribution in the measurement of the missing transverse energy.

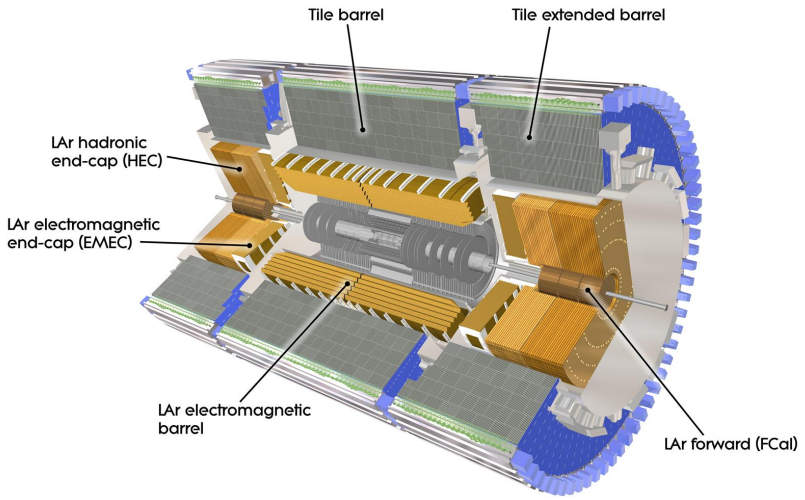

Figure 4.8: Calorimeters in ATLAS (97).

4.3.1 Introduction to calorimetry

In this sub-section some basic information about calorimetry are briefly presented. A special emphasis is put on this technique of particle detection in this manuscript since the EM calorimeter has a key role in the measurements presented in this thesis.

The measurement of the energy deposited by a particle entering a calorimeter is based on the collection of the energy of the particles produced in the interaction of the incident particle with the dense matter which constitutes the detector.

The secondary particle cascade generated in this interaction is called the “shower”. The incident particle interacts with the detector producing multiple new particles, that in turn interact with the detector producing other particles. This process keeps going on until the particles of the shower have low energy and are absorbed by the matter of the detector.

The energy of all the secondary particles is usually collected by detecting the light produced in a scintillating material, or the charge produced through ionization in a gas or in a liquid.

The calorimeters can be classified in two typologies depending on the construction.

- *Sampling* calorimeters, where the "passive" material which degrades the particle energy and the "active" material that provides a measurable signal are different and alternated. This is the case of all the ATLAS calorimeters, which use Liquid Argon (LAr) or polystyrene scintillator as active material and lead (Pb), copper, or iron as passive material.

- *Homogeneous* calorimeters, that are constituted by a material which has the properties needed both to contain the shower and to detect the deposited energy. The CMS electromagnetic calorimeter is a homogeneous calorimeter made of $PbWO_4$ crystals. The main advantage of the homogeneous calorimeters is that the whole energy deposited in the calorimeter can be collected, while for sampling calorimeter the energy deposited in the passive material is lost. Thus the homogeneous calorimeters are usually characterized by a better energy resolution than the sampling calorimeters, as discussed below.

The size and the geometrical configuration of a calorimeter depends on the particle type and energy range of interest. In the next sections the main parameters characterizing the interaction of high energy electrons, photons and hadrons with the detectors are defined.

Electromagnetic showers

At high energy, photons interact with matter primarily via pair production, while high energy electrons interact with matter through bremsstrahlung and emit secondary photons. These two processes continue until the secondary photon energy fall below the pair production threshold or when the energy of the secondary electrons reaches the range at which the energy loss by ionization and by bremsstrahlung are equivalent. This threshold is called the critical energy E_c, and is parametrized (for liquid and solid materials) as:

$$E_c = \frac{610 \text{ MeV}}{Z + 1.24}, \tag{4.4}$$

where Z is the atomic number of the material.

The parameters that characterize the development of the electromagnetic shower are its depth and its width. The shower depth quantifies the material thickness needed to contain 95% of the longitudinal energy profile of the shower energy. It can be parametrized as:

$$L(95\%) \approx t_{max} + 0.08Z + 9.6 = \left[\ln\left(\frac{E_0}{E_c}\right) + C_j\right] + 0.08Z + 9.6 \text{ [X}_0\text{]}, \tag{4.5}$$

where E_0 is the energy of the incident particle and C_j is a parameter which can be -0.5 or +0.5 depending on the incident particle being an electron or a photon respectively. $L(95\%)$ is described in units of radiation length X_0, which is defined as:

$$X_0 = \frac{716.4 \text{ [g cm}^{-2}\text{]} \times A}{Z(Z+1)\ln\left(287/\sqrt{Z}\right)}, \tag{4.6}$$

that represents the amount of material which causes an electron beam reduce its energy by a factor of e. For instance, for Liquid Argon (LAr) and Lead (Pb), we obtain:

$$E_c^{\text{LAr}} = 32.84 \text{ MeV}, \; X_0^{\text{LAr}} = 14 \text{ cm}; \tag{4.7}$$

$$E_c^{\text{Pb}} = 7.43 \text{ MeV}, \; X_0^{\text{Pb}} = 0.56 \text{ cm}. \tag{4.8}$$

Thus considering an electron with an initial energy $E = 100$ GeV, the shower depth in LAr and Pb result :

$$L^{\mathrm{LAr}}(95\%) \approx 260 \text{ cm}; \tag{4.9}$$

$$L^{\mathrm{Pb}}(95\%) \approx 15 \text{ cm}. \tag{4.10}$$

The other important parameter for electron and photon showers is the *Molière radius* (R_M). 95% of an electromagnetic shower is enclosed in twice the R_M, which characterizes the lateral development of the shower. It is defined as:

$$R_M = \frac{21\mathrm{MeV}}{E_c} X_0. \tag{4.11}$$

It should be noticed that the width of the electromagnetic shower depends only on the calorimeter material property and not on the energy of the incoming particle.

Hadronic showers

The physics processes that make a high energy hadron interacting producing a shower of secondary particles are considerable different to the processes leading to electromagnetic showers. Hadron showers consist of two distinctly different components:

- an electromagnetic component (30%–60% of the total energy) from the decays into photons of π^0s and ηs generated in the absorption process;
- an hadronic component which combines every other process, such as slow neutrons production or spallation protons. The main difference between the two components is that some fraction of energy of the hadronic component does not contribute to the signals. This *invisible energy* is mainly due to the binding energy of nucleons released in the nuclear reactions and represents up to 40% of the total non-EM energy.

The parameter which describes the hadronic shower is the nuclear interaction length λ, which can be approximated by:

$$\lambda \approx 35A^{1/3} \text{ g cm}^{-2}. \tag{4.12}$$

95% of the longitudinal energy deposit profile of the hadronic shower is contained in:

$$t_{95\%} = t_{max} + 2\lambda E^{0.13}, \tag{4.13}$$

where t_{max} is

$$t_{max} = 0.2 \ln(E/1\mathrm{GeV}) + 0.7 \ [\lambda]. \tag{4.14}$$

Considering LAr and Pb and an incident pion of energy equal to 100 GeV, we obtain:

$$\lambda_{LAr} = 85.77 \text{ cm and } t_{95\%}^{LAr} \approx 450 \text{ cm}, \tag{4.15}$$

$$\lambda_{Pb} = 17.59 \text{ cm and } t_{95\%}^{Pb} \approx 90 \text{ cm}. \tag{4.16}$$

λ is much larger than X_0, and thus the longitudinal containment of a 100 GeV pion needs a layer of Lead almost 6 time more thick than the one requested to contain a 100 GeV electron shower. Therefore, in the experiments design the electromagnetic calorimeter is fit inside the hadronic calorimeter.

The calorimeter resolution

Another important quantity that defines the performance of the calorimeter is its energy resolution $\sigma(E)/E$, which is given by:

$$\frac{\sigma}{E} = \frac{a}{\sqrt{E}} \oplus \frac{b}{E} \oplus c, \tag{4.17}$$

where a is called the *stochastic term*; b includes the contribution arising from the electronic noise and it is usually negligible at the range of energy studied by the ATLAS detector; finally c is the *constant term* that depends on detector non uniformity, alignment and electronic calibration uncertainties. The constant term limits the resolution at high energy.

The stochastic term a describes the contributions to the resolution given by the statistical fluctuation of the shower development. Indeed, if we consider an ideal homogeneous calorimeter of infinite size and without any response deterioration due to instrumental effects, its intrinsic resolution is determined mainly by the fluctuation of the total tracks length T_0, defined as the sum of all ionization tracks due to all charged secondary particles that compose the shower. T_0 is given by:

$$T_0 \propto X_0 \frac{E_0}{E_c}, \tag{4.18}$$

where E_0/E_c is equal to the number of particles in the shower. The resolution is thus given by:

$$\sigma(E) \propto \sigma(T_0) = \sqrt{T_0}, \tag{4.19}$$

and

$$\frac{\sigma(E)}{E} \propto \frac{1}{\sqrt{T_0}} \propto \frac{1}{\sqrt{E}}. \tag{4.20}$$

In homogeneous calorimeters intrinsic fluctuations are small and typical stochastic terms of homogeneous electromagnetic calorimeters are at the level of a few percent in units of $1/\sqrt{E(\mathrm{GeV})}$.

For a sampling calorimeter the energy deposited in the active medium fluctuates event by event because the active layers are interleaved with absorber layers. The resolution in sampling calorimeter is then limited by the number of particles N_{ch} that cross the active material layers. This number is proportional to

$$N_{ch} \propto \frac{E}{d}, \tag{4.21}$$

where d is the thickness of the layer of the passive material. Considering the particle interactions with the active material statistically independent we obtain :

$$\frac{\sigma}{E} \propto \frac{1}{\sqrt{N_{ch}}} = \sqrt{\frac{d}{E_0}}. \tag{4.22}$$

Another factor which contributes to the stochastic term for sampling calorimeter is the *sampling fraction*, which is defined as:

$$f_{samp} = \frac{E_{mip}(active)}{E_{mip}(active) + E_{mip}(passive)}, \tag{4.23}$$

where $E_{mip}(active)$ and $E_{mip}(passive)$ are the energy deposited from a minimum ionizing particle in the active and passive material. Considering f_{samp}, the resolution can be described as:

$$\frac{\sigma(E)}{E} \propto \sqrt{\frac{d}{f_{samp}}} \frac{1}{\sqrt{E}}. \tag{4.24}$$

The typical energy resolution of sampling electromagnetic calorimeters is in the range 5–20%/$\sqrt{E(\text{GeV})}$.

4.3.2 The ATLAS Electromagnetic Calorimeter

The ATLAS Electromagnetic Calorimeter (111; 112) (EM) is 6.65 meters long and has an outer radius of 2.25 meters. It is composed of a central barrel region, which covers $|\eta| < 1.4$, and two end-caps, that cover $1.4 < |\eta| < 3.2$. The EM calorimeter is a sampling calorimeter made of 2 mm layers of Liquid Argon as active medium, interleaved with copper electrodes, which collect the ionization charge generated by the EM shower, and with lead absorbers plates, with a thickness of 1.5 mm (for $|\eta| < 0.8$) or 1.13 mm (for $|\eta| > 0.8$) and glued to a stainless-steel sheet 0.2 mm thick, in order to improve their mechanical strength.

Electrodes and absorbers are arranged in an accordion geometry to provide a full coverage in ϕ and avoid cracks due to the outgoing readout system.

In order to contain completely the electromagnetic shower, the EM calorimeter has a thickness of more than 22 radiation lengths (X_0) in the barrel and more than 24 X_0 in the end-caps.

The Electromagnetic Calorimeter is segmented in 190000 cells along η and ϕ and is composed of 4 longitudinal layers to be able to record precisely the longitudinal development of the electromagnetic shower. The four layers are:

- *Presampler* (PS). This is a very thin module, with a thickness of 1.1 cm, which is placed inside the solenoid. It is exploited to reconstruct the energy lost by a particle before reaching the calorimeter and covers the $|\eta| < 1.8$ region.
- *Layer 1* (L1). This accounts for up to 6 X_0 (including material in front). This layer has the finest segmentation along η, $\Delta\eta = 0.0031$ (see Table 4.1) in order to discriminate between prompt photons and π^0 decaying in two almost collinear photons.
- *Layer 2* (L2). It extends up to 22 X_0 and it is segmented in cells of size $\Delta\eta \times \Delta\phi = 0.025 \times 0.025$. The second layer contains most of the energy of the showers originated by photons and electrons with energy up to 50 GeV.
- *Layer 3* (L3). It has a thickness of about 2 additional X_0 and it is used to estimate the energy leaked in the hadronic calorimeter.

The complete segmentation description of the EM calorimeter is summarized in Table 4.1 and shown in Figure 4.9.

The nominal Electromagnetic Calorimeter resolution is:

$$\frac{\sigma(E)}{E} \approx \frac{(10\% \div 17\%)}{\sqrt{E}} \oplus 0.7\%, \tag{4.25}$$

where E is expressed in GeV and the stochastic term depends on η. The noise term is negligible and it is expected to contribute above ~ 0.5 GeV.

Table 4.1: Electromagnetic Calorimeter segmentation.

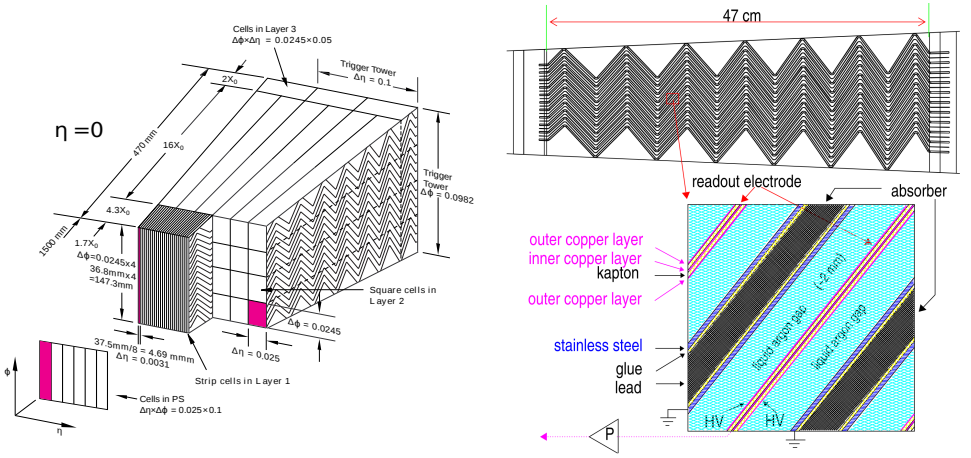

Figure 4.9: Electromagnetic Calorimeter accordion structure and barrel granularity, with a detailed description of the active and passive material layer composition (113).

Energy reconstruction in the electromagnetic calorimeter

Photons and electrons entering the EM calorimeter interact with the lead absorbers and originate the electromagnetic showers. The secondary particles ionise the LAr that fills the gaps between the absorbers. The ionisation electrons drift to the copper electrodes that are powered by a High Voltage (HV) system that guarantees a constant electric field between the electrodes and the absorbers that are grounded (see Fig. 4.9). In particular, in the barrel the cell gaps are ~ 2 mm wide and the nominal potential of 2 kV leads to a typical charge collection time of 400 ns (113), that is longer than the interval between two consecutive LHC bunch crossing (25 ns). The ionization current has a triangular shape and is proportional to the energy deposited in the active volume and it is approximately 3 μA/GeV for the EM barrel. The signal is brought to the Front End Boards (FEBs), where it is pre-amplified and then it is shaped by a multi-gain bipolar filter. The properties of the CR-RC^2 are optimized in order to minimize the sum of the electronic and pileup noise at high luminosity. The resulting signal, as showed in Figure 4.10a, is characterized by a typical rise time of ~ 45 ns. Three different amplification levels are provided by the shaper in order to accommodate the full range of particle energies produced in the collisions: Low Gain (LG), Medium Gain (MG), and High Gain (HG).

The shaped signal is then sampled at the 40 MHz LHC bunch crossing frequency and stored in analog pipelines while waiting the online trigger decision (L1, see Sec. 4.5). In the case the event passes a trigger selection the sample corresponding to the peak in medium gain is digitized by a 12-bit analog-to-digital converter (ADC). Based on this sample, the most suited gain is chosen and the relative sample is digitized and sent to the read-out through optical fibres.

The conversion of the measured amplitude A of the electric signal to the cell deposited

energy (E) in MeV is performed using the relation (114):

$$E_{cell} = F_{\mu\mathrm{A}\to\mathrm{MeV}} \times F_{\mathrm{DAC}\to\mu\mathrm{A}} \times \frac{1}{\frac{M_{\mathrm{phys}}}{M_{\mathrm{cali}}}} \times G \times \sum_{j=1}^{\mathrm{N_{samples}}} A_j(s_j - p_j), \tag{4.26}$$

where

- s_j are the samples of the shaped ionization signal, converted in digital information by the ADC in the selected gain, measured for the first $\mathrm{N_{samples}}$ time slices ($\mathrm{N_{samples}} = 5$ in Run 1 while in Run 2 is reduced to 4). Using multiple samples around the peak reduces the noise level, and therefore improves the precision of the energy reconstruction. Figure 4.10b shows the typical noise levels as a function of the number of samples used to calculate the energy deposit. The amplitude s_j is corrected for the pedestal value p_j, that is obtained in calibration runs without any input signal present in the cell. The coefficients A_j is calculated according to an optimal filtering algorithm (115) that optimizes the resultant energy and timing resolution. it is derived from the predicted shape of the ionization pulse and the noise autocorrelation, accounting for both the electronic and the pileup components.

- $F_{\mu\mathrm{A}\to\mathrm{MeV}}$ converts the ionization current to the total deposited energy at the calorimeter scale and is determined from test-beam data and validated with a detailed detector simulation.

- $F_{\mathrm{DAC}\to\mu\mathrm{A}}$ converts the Digital-to-Analog Converter (DAC) setting of the calibration board to the injected current, and is determined from known parameters of the calibration boards and injection resistors.

- G is the cell gain, evaluated by injecting a well known calibration signal and reconstructing the corresponding cell response during special calibration run.

- $\frac{M_{\mathrm{phys}}}{M_{\mathrm{cali}}}$ is the factor which corrects the G parameter quantifying the ratio of response to a calibration pulse and an ionization pulse corresponding to the same input current.

4.3.3 The Hadronic Calorimeter

The Hadronic Calorimeter is 6.10 meters long and has an external radius of 4.25 meters and covers the pseudorapidity region $|\eta| < 3.9$. The central barrel region for $|\eta| < 1.7$ consists in a sampling calorimeter using iron as absorber and scintillators as active medium and is divided in cells of size $\Delta\eta \times \Delta\phi = 0.1 \times 0.1$ (116; 117). Figure 4.11 shows the components in a module of the tile calorimeter. In the end-cap section of the hadronic calorimeter (HEC), Liquid Argon is used as the active medium and copper and tungsten plates are used as absorbers (118). The HEC cells have a granularity of $\Delta\eta\times\Delta\phi = 0.1\times0.1$ or 0.2×0.2 depending on η.

The overall thickness of the hadronic calorimeter is 11 λ (nuclear interaction length) for $\eta = 0$. The nominal energy resolution for hadronic jets (combined with the electromagnetic calorimeter) is:

$$\frac{\sigma(E)}{E} \approx \frac{50\%}{\sqrt{E}} \oplus 3\%. \tag{4.27}$$

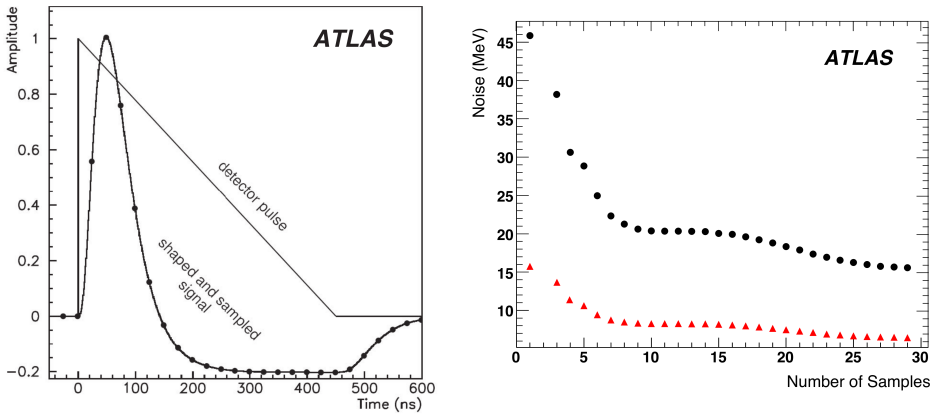

(a) (b)

Figure 4.10: (a): shapes of the LAr calorimeter current pulse in the detector and of the signal output from the shaper chip. The dots indicate an ideal position of samples separated by 25 ns . (b): typical noise levels for the EM barrel first (triangles) and second (circles) layers as a function of the number of samples used to calculate the deposited energy (114).

4.3.4 The Forward Calorimeter

The Forward Calorimeter (119) (FCal) is placed at 4.7 m from the interaction point and provides a measurement of both electromagnetic and hadronic showers. In particular the electromagnetic part is made with copper as passive material and LAr as sensitive medium, while the hadronic parts use tungsten as absorber material and LAr as the active material.

The typical energy resolution of the FCal is:

$$\frac{\sigma(E)}{E} \approx \frac{100\%}{\sqrt{E}} \oplus 10\%. \tag{4.28}$$

4.4 The Muon Spectrometer

Except for muons and neutrinos, all other particles produced in the beam collisions are absorbed by the calorimeters. For this reason the muon spectrometer (120) is the outer part of ATLAS. The purpose of this detector is the measurement with high precision of the muon momentum, using the trajectory deviation caused by the toroidal magnetic field. The MS is composed by three parts, one central barrel and two end-caps, and it covers the pseudorapidity region $|\eta| < 2.7$, apart for a little gap for $|\eta| < 0.1$ needed by the services for the inner detectors. The MS structure is shown in Figure 4.12.

The magnetic field bends a muon trajectory in the (R, z) plane, where hits for track reconstruction are measured by two different systems: Monitored Drift Tubes (MDTs) in the barrel and Cathode Strip Chambers (CSCs) in the forward region. MDTs cover the region $|\eta| < 2.7$ while CSCs cover $2.0 < |\eta| < 2.7$. Each chamber of the MDTs is made of 3-8 layers of drift tubes with an average resolution of 80 μm per tube and 35 μm per chamber. CSCs are multiwire chambers optimized to have the wires oriented in the radial

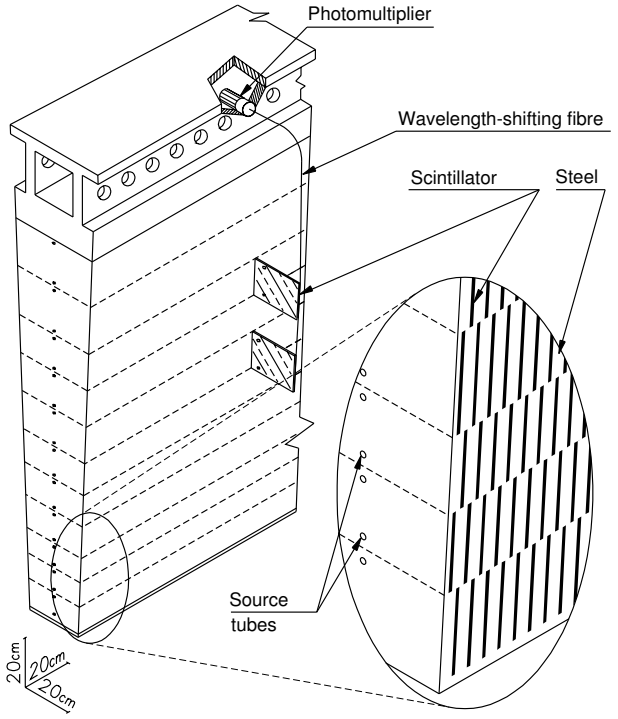

Figure 4.11: Illustration of the components in a module of the tile calorimeter (116).

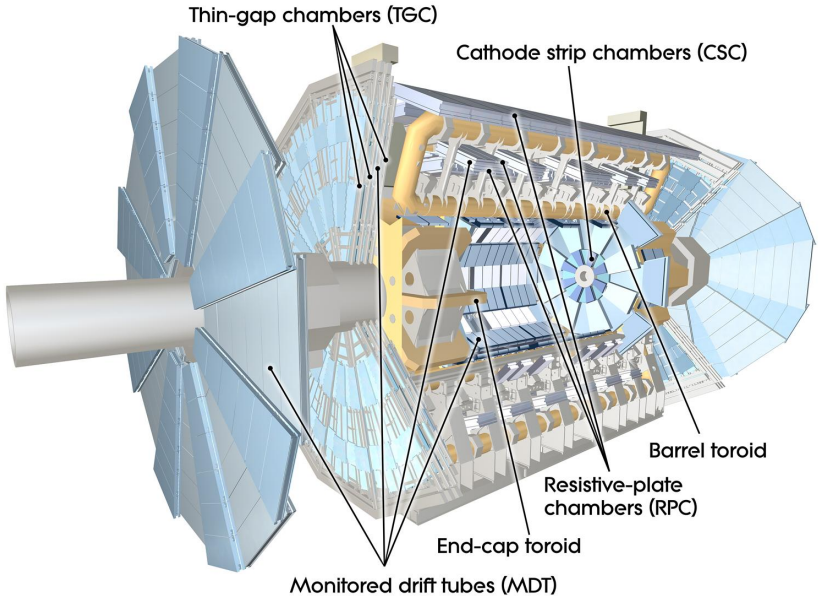

Figure 4.12: Cut view of the muon system structure (97).

direction. This design provides a resolution of 60 μm in the bending plane and 4 mm in the transverse plane. Drift tubes measure the position of the passing muon from the time interval between the trigger signal and the signal in the drift chambers.

In order to provide a fast muon trigger the muon spectrometer is equipped, in addition to the aforementioned precision chambers, with fast trigger chambers which can record and deliver track information within 15-25 ns. The muon trigger system is composed of resistive plate chambers (RPCs) for $|\eta| < 1.05$ and thin gap chambers (TGCs) in the end-cap region ($1.05 < |\eta| < 2.4$).

For a track of $p_T \sim 1$ TeV the typical sagitta is approximately 500 μm. The ATLAS muon system, in particular the MDTs, provides a momentum resolution between 2-3% and $\sim 10\%$ in a p_T range between 10 GeV and 1 TeV.

4.5 Trigger system

Given the huge number of collisions and the impossibility to save all of this information, ATLAS is equipped with an online two-level trigger system. At the instantaneous luminosity of LHC during the Run 2 data taking, the ATLAS detector is exposed to one bunch crossing every 25 ns with an average of 25 proton-proton collision per bunch crossing. The trigger system has to decrease the event rate from the nominal bunch crossing rate of 40 MHz to a rate of about 1 KHz, that is the maximum rate at which data can be processed.

The Level one trigger (121) (L1) is a hardware trigger implemented in custom-built electronics. It uses coarse-granularity information from the muon chambers, calorimeters and forward detectors. The L1 trigger searches for objects with high transverse momentum: muons, electrons, photons and jets, as well as large missing and total transverse energy. For each event, the L1 trigger defines one or more Regions-of-Interest (RoI); these are the regions of the detector where the selection process has identified interesting features. The L1 decision is characterized by an overall latency of less than 2.5 μs reducing the event rate to about 100 kHz.

The High Level Trigger (122) (HLT) is a software-based trigger. It uses all the information available within the RoIs, identified by the L1 trigger, exploiting the full detector granularity and offline-like algorithms. The HLT reduces the output rate to approximately 1 kHz with a nominal processing time of about 4 s.

Figure 4.13 shows an example of L1 and HLT trigger rates grouped by trigger signature in a typical run taken in 2016 (123).

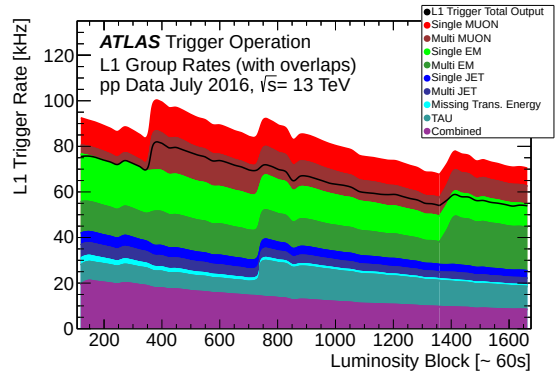

(a)

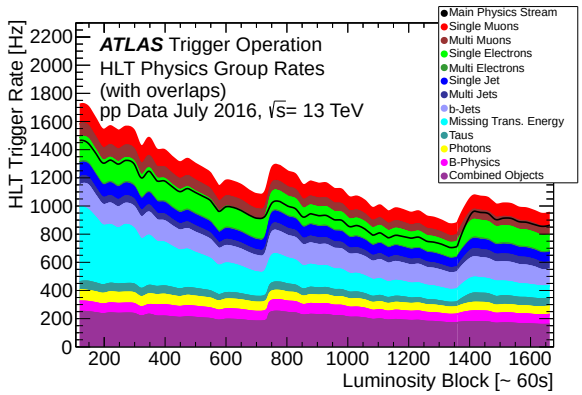

(b)

Figure 4.13: (a) L1 and (b) HLT trigger rates grouped by trigger as a function of the number of luminosity blocks which correspond to on average 60 s per luminosity block in a fill taken in July 2016 with a peak luminosity of $L = 1.02 \times 10^{34}$ cm^{-2}s^{-1} and an average pile up of $\mu = 24.2$. Black lines show the (a) L1 total rate and (b) HLT main physics stream rate (123; 124).

Chapter 5

Physics objects reconstruction with the ATLAS detector

5.1 Electron and Photon reconstruction

The electron and photon recostruction (125; 126) is based on the tracks reconstructed in the Inner Detector and on the clusters of energy deposits in the electromagnetic calorimeter. The reconstruction is designed to separate electrons, unconverted photons and photon conversions in the detector material to electron-positron pairs. The clusters are matched to tracks extrapolated to the second layer of the calorimeter or to conversion vertex candidates. Clusters without any matching track or matching conversion vertex are classified as unconverted photon candidates. Clusters with a matching secondary vertex reconstructed from one or two tracks are considered as converted photon candidates. An electron candidate is created if a matched track is found and no matched conversion is flagged.

5.1.1 Energy cluster in the EM calorimeter

In the central region of the ATLAS detector ($|\eta| < 2.47$) the electron and photon reconstruction process starts from energy deposits in the EM calorimeter. A preliminary set of EM clusters is created by a *sliding-windows* algorithm (127). The η-ϕ space of the EM calorimeter is divided into a grid of $N_\eta \times N_\phi = 200 \times 256$ elements ("towers") of size $\Delta\eta^{\text{tower}} \times \Delta\phi^{\text{tower}} = 0.025 \times 0.025$, corresponding to the granularity of the second layer of the EM calorimeter. Inside each element of the grid the energy of all the cells in all longitudinal layers are summed to obtain the "tower energy". A fixed size window of 3×5 in units of 0.025×0.025 in $\eta \times \phi$ moves across each element of the tower grid; when the energy measured in the window, which is the sum of the transverse energy covered by the window, is identified as a local maximum with energy above 2.5 GeV, a seed cluster is formed. The cluster is then built around the seed position by taking all cells within a rectangle of size $N_\eta^{\text{cluster}} \times N_\phi^{\text{cluster}}$ centered on a layer-dependent barycenter position: the L2 layer uses as energy-weighted η and ϕ barycentre the pre-cluster barycentre; once the clustering of L2 is done adding all the cells in the $N_\eta^{\text{cluster}} \times N_\phi^{\text{cluster}}$ window, a new L2 barycentre is evaluated and is used as seed for the clustering of the first strip layer and for the third layer, finally the PS uses as barycentre the one calculated from the L1 energy distribution.

The dimension of the cluster should be large enough in order to contain most of the energy deposit profile of an electromagnetic shower, on the other hand including more cells means including more electronic and mainly pileup noise. In Run 2 the cluster size of the electrons and photons is $N_\eta^{\text{cluster}} \times N_\phi^{\text{cluster}} = 3 \times 7$ (5×5) in unit of 0.025×0.025 in the barrel (endcap). The clusters are larger along ϕ axis in order to cope with material

effects, such as bremsstrahlung and photon conversion, that broadens the EM showers along the ϕ direction due to the bending of the solenoidal magnetic field.

The efficiency of the cluster search varies from 95% at $E_{\mathrm{T}} = 7$ GeV to more than 99% for $E_{\mathrm{T}} > 15$ GeV.

5.1.2 Electron reconstruction

An electron candidate, in the region $|\eta| < 2.47$, is defined by the existence of one or more reconstructed tracks matched to a seed cluster (128; 129). Once seed clusters are defined, a search for tracks reconstructed in the ID that are loosely matched to the seed cluster is performed. The match is based on the extrapolation of the tracks to the second layer of the EM calorimeter. A track is considered loosely matched to a cluster if the difference in (η,ϕ) coordinates with the seed cluster barycentre is below 0.05 along η and either within 0.2 (0.1, for TRT-only tracks) along ϕ in the direction of the bending of the tracks in the magnetic field or within 0.05 in the opposite direction. In 2012 the track fitting and extrapolation algorithm was improved with a dedicated correction for bremsstrahlung energy losses. The GSF (Gaussian Sum Filter) algorithm (130) refits all the loosely matched tracks. The re-fitted tracks are then used to compute the final matching with the seed cluster and to compute the electron four-momentum. The GSF algorithm is particularly beneficial in case of low-p_{T} electrons where the contribution to the resolution of the four-momentum of the track parameter is dominant and bremsstrahlung effects are stronger. The previous matching requirements are applied except for a tighter request on the ϕ difference in the direction of the bending of the tracks, $\Delta\phi < 0.1$.

If more than one track points to the same seed cluster, the track with the smallest ΔR between the impact point on the EM calorimeter and the seed cluster is chosen, unless the difference between the ΔR of the tracks is less than 0.01. In the latter case, the track with more pixel hits is preferred, giving extra weight to a hit in the innermost layer. All the seed clusters with their matching tracks are treated as electron candidates and rebuilt using 3×7 (5×5) cells in $\eta \times \phi$ in the barrel (endcaps) of the EM accordion calorimeter as explained in the previous section. Finally, the four-momentum of the electron candidate is computed using information from both the final cluster and the best matched track to the initial seed cluster. The energy is given by the cluster energy, while the ϕ and η directions are taken from the corresponding track parameters, except for tracks reconstructed using only the TRT detector, for which the position of the barycentre of the cluster is used instead. Figure 5.1 shows the measured electron reconstruction efficiency as a function of E_{T} for the 2015 dataset. A full descripition of the electron reconstruction process can be found in Ref (129).

In order to reduce the background from photon conversions and from other secondary particles, electrons are requested to be compatible with the hard collision interaction vertex. Electrons have to pass the selection requirements $d_0/\sigma_{d_0} < 5$, where σ_{d_0} is the uncertainty on the d_0 parameter, and $\Delta z_0 \sin\theta < 0.5$ mm, where Δz_0 is the z_0 difference between the primary vertex and the track.

To determine whether the reconstructed electron candidates are prompt objects not originating from hadron decays, algorithms for electron identification are applied. In Run 2, likelihood based electron identification algorithm are used. This method exploits the discriminating power of the variables listed in Table 5.1 and assigns to a given object the probability to be a electron-like or background-like candidate. The probability density function are determined from $Z \to ee$, $J/\psi \to ee$ and di-jet simulated events. Three operating points are provided – *loose*, *medium*, *tight* – with an increasing background

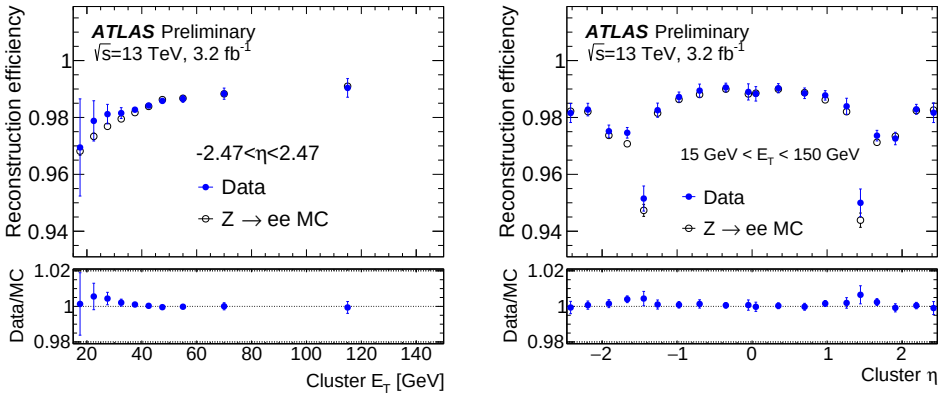

(a) (b)

Figure 5.1: Reconstruction efficiencies in data and MC as a function of E_{T} integrated over the full pseudorapidity range (a) and as a function of η for 15 GeV $< E_{\mathrm{T}} <$ 150 GeV (b), for the 2015 dataset (129).

rejection power. Figure 5.2 shows the efficiency to identify electrons from $Z \to ee$ decays and the background di-jet events for the three identification working points.

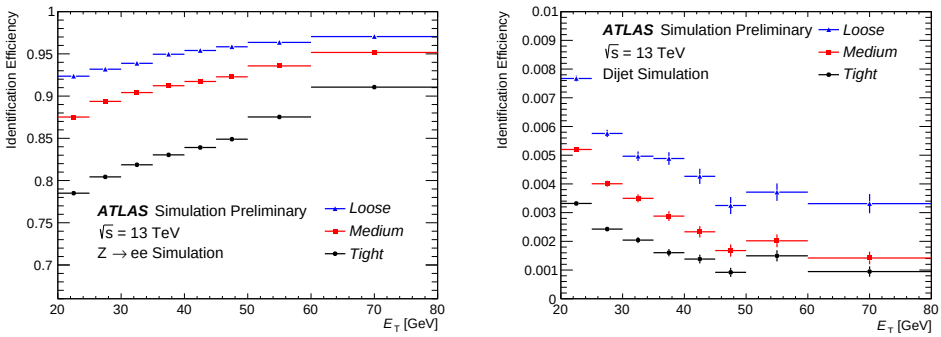

(a) (b)

Figure 5.2: The efficiency to identify electrons from $Z \to ee$ decays (a) and the efficiency to identify hadrons as electrons (b). The efficiencies are obtained using Monte Carlo simulations, and are measured with respect to reconstructed electron candidates. The candidates are matched to true electrons for $Z \to ee$ events (129).

Table 5.1: Definition of electron discriminating variables used for electron identification (129).

Type	Description	Name
Hadronic leakage	Ratio of E_{T} in the first layer of the hadronic calorimeter to E_{T} of the EM cluster (used over the range $\lvert\eta\rvert < 0.8$ or $\lvert\eta\rvert > 1.37$)	R_{Had1}
	Ratio of E_{T} in the hadronic calorimeter to E_{T} of the EM cluster (used over the range $0.8 < \lvert\eta\rvert < 1.37$)	R_{Had}
3^{rd} layer of EM calorimeter	Ratio of the energy in the 3^{rd} layer to the total energy in the EM accordion calorimeter. This variable is only used below 100 GeV because it is know to be inefficient at high energies.	f_3
2^{nd} layer of EM calorimeter	Lateral shower width, $\sqrt{(\Sigma E_i \eta_i^2)/(\Sigma E_i) - ((\Sigma E_i \eta_i)/(\Sigma E_i))^2}$, where E_i is the energy and η_i is the pseudorapidity of cell i and the sum is calculated within a window of 3×5 cells	$w_{\eta 2}$
	Ratio of the energy in 3×3 cells over the energy in 3×7 cells centered at the electron cluster position	R_η
	Ratio of the energy in 3×7 cells over the energy in 7×7 cells centered at the electron cluster position	R_ϕ
1^{st} layer of EM calorimeter	Shower width, $\sqrt{(\Sigma E_i (i - i_{\mathrm{max}})^2)/(\Sigma E_i)}$, where i runs over all strips in a window of $\Delta\eta \times \Delta\phi \approx 0.0625 \times 0.2$, corresponding typically to 20 strips in η, and i_{max} is the index of the highest-energy strip	$w_{s\,\mathrm{tot}}$
	Ratio of the energy difference between the largest and second largest energy deposits in the cluster over the sum of these energies	E_{ratio}
	Ratio of the energy in the strip layer to the total energy in the EM accordion calorimeter	f_1
Track condition	Number of hits in the innermost pixel layer; it discriminates against photon conversions	n_{Blayer}
	Number of hits in the pixel detector	n_{Pixel}
	Number of total hits in the pixel and SCT detectors	n_{Si}
	Transverse impact parameter with respect to the beam line	d_0
	Significance of transverse impact parameter defined as the ratio of d_0 and its uncertainty	d_0/σ_{d_0}
	Momentum lost by the track between the perigee and the last measurement point divided by the original momentum	$\Delta p/p$
TRT	Likelihood probability based on transition radiation in the TRT	eProbabilityHT
Track-cluster matching	$\Delta\eta$ between the cluster position in the 1^{st} layer and the extrapolated track	$\Delta\eta_1$
	$\Delta\phi$ between the cluster position in the 2^{nd} layer and the track extrapolated from the perigee	$\Delta\phi_2$
	Defined as $\Delta\phi$, but the track momentum is rescaled to the cluster energy before extrapolating the track from the perigee to the middle layer of the calorimeter	$\Delta\phi_{res}$
	Ratio of the cluster energy to the track momentum	E/p

5.1.3 Photon reconstruction

The reconstruction of photons follows that of electrons, with some complications. A complete description of the photon reconstruction procedure can be found in Ref. (131).

Once seed clusters are reconstructed, a search for tracks consistent with originating from a secondary vertex is performed.

"Double-track" conversion vertices are reconstructed from pairs of oppositely charged tracks, consistently with the electron hypothesis defined by the TRT high-threshold hits requirements. Geometric requirements are used to select the track pairs exploiting the angle between the two tracks, their separation distance at the point of their closest approach, and the separation of the tracks at the reconstructed vertex. Track pairs compatible with originating from a secondary vertex are then classified in three categories: Si-Si if both tracks have hits in the silicon detectors, Si-TRT and TRT-TRT if only one or none of the tracks has hits in the silicon detectors. The efficiency of the reconstruction of the double-track conversion vertices decreases significantly for conversions taking place at higher radii. This is manly due to asymmetric photon conversions, where one of the two electrons is very soft, and to high-energy photon conversions without sufficient separation between the two outgoing tracks, so that they can not be resolved by the TRT detector. In order to reduce the conversion-finding inefficiency, conversion vertices with a single outgoing track are also considered.

"Single-track" conversion vertices are reconstructed from tracks without hits in the first layer of the pixel detector, in order to exclude prompt-electron contributions. In this case the conversion vertex is defined by the first measurement of the track.

Once the double-track conversion vertices have been identified, they are extrapolated to the seed cluster. In case the tracks momenta differ by less than a factor four, both the tracks are extrapolated to the L2 of the EM calorimeter; in the opposite case a straight line from the conversion vertex is used. For single-track conversion vertex the extrapolation to the second layer of the calorimeter is done from the last measurement of the related track. A conversion vertex is successfully matched to the seed cluster if the distance in ϕ and in η between extrapolated tracks and the cluster barycentre is less than 0.05. If the tracks are not reconstructed in the silicon detector the requirements become: $\Delta\phi < 0.02$ (0.03) in the direction of (opposite to) the bending, and $\Delta\eta < 0.35$ (0.2) in the barrel (endcap). The last selection is significantly looser since the TRT does not provide pseudorapidity measurement.

Figure 5.3 shows the fraction of photon candidates reconstructed as unconverted or converted photons as a function of the candidate transverse momentum and pseudorapidity.

The EM clusters can be reconstructed at the same time as electrons and photons. The final arbitration between the unconverted photon, converted photon and electron hypotheses is performed in the following way:

- Photon: a candidate particle is reconstructed as a photon if there are no tracks with at least four hits in the silicon detector matched to the calorimeter cluster; if a double-silicon conversion vertex is found and a candidate electron track with no hits in the pixel detector is part of the vertex, the candidate is flagged as a photon.

- Electron: a candidate particle is reconstructed as an electron if no conversion vertex is matched with its track and the track is reconstructed with at least two hits in the pixel detector and four hits in the silicon detector. In the case the track is part of a conversion vertex, the particle is reconstructed as electron if the vertex is not

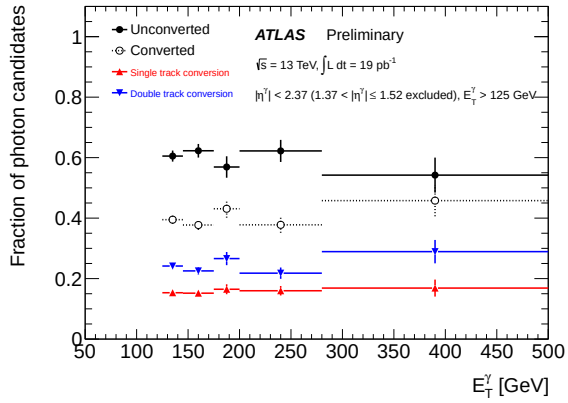

(a)

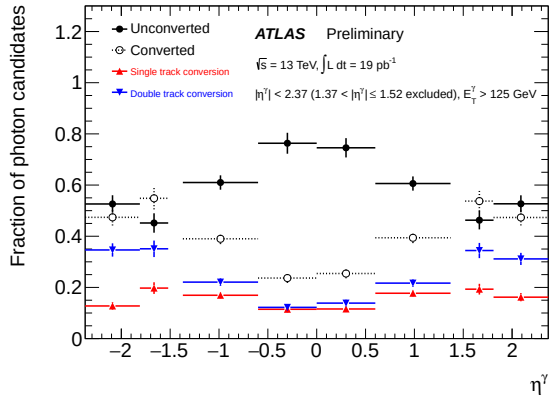

(b)

Figure 5.3: Fraction of photon candidates reconstructed as unconverted or converted photons as a function of (a) the candidate transverse momentum or (b) the candidate psudorapidity, in pp collisions at $\sqrt{s} = 13$ TeV. The photon candidates are required to pass the photon identification based on the shapes of the associated electromagnetic cluster and to be isolated (see Chap. 7). Converted photon candidates are also split into single-track and double-track conversions (132).

a double-silicon tracks vertex, or, if this is the case, only one of the tracks matched to the vertex has innermost pixel hits.

- The candidate particle is reconstructed both as an electron and a photon if it does not fulfill the previous requirements, or if $E_{\text{cluster}}/p_{\text{track}} > 10$ GeV, or the track transverse momentum is smaller than 2 GeV.

5.1.4 Dynamical and topological cell clustering-based approach

A new approach to reconstruct energy deposits in the ATLAS EM calorimeter is employed to reconstruct electron and photons in the 2017 data-taking. This new method is based on a dynamical, topological cell-based approach (*topo-cluster*) (133) for cluster building instead of relying on the sliding window algorithm illustrated in Sec. 5.1.1. This new technique allows for improved measurements of electron and photon energies, particularly in situations where an electron radiates a bremsstrahlung photon, or a photon converts to an electron-positron pair.

Differently from the sliding window algorithm, topo-clusters are formed following signal-significance patterns. In particular, the variable that determines the seeding and the growth of a topo-cluster is the cell significance, $\zeta_{\text{cell}}^{\text{EM}}$, which is defined as:

$$\zeta_{\text{cell}}^{\text{EM}} = |\frac{E_{\text{cell}}^{\text{EM}}}{\sigma_{\text{noise}}^{\text{EM}}}|, \tag{5.1}$$

where $E_{\text{cell}}^{\text{EM}}$ is the absolute cell energy at the EM scale and $\sigma_{\text{noise}}^{\text{EM}}$ is the expected cell noise. The topo-cluster reconstruction follows the "4-2-0" scheme: the process begins identifying cells with a $\zeta_{\text{cell}}^{\text{EM}} \geq 4$, then around these seeds-clusters neighboring cells with $\zeta_{\text{cell}}^{\text{EM}} \geq 2$ are collected. If two clusters contain the same cell with absolute energy 2σ above the noise, they are merged in a unique one. Finally, when all the nearby cells with $\zeta_{\text{cell}}^{\text{EM}} \geq 2$ are collected a set of neighboring cells with $\zeta_{\text{cell}}^{\text{EM}} \geq 0$ is added to the topo-cluster. This same topo-cluster algorithm is used in ATLAS to reconstruct other objects (jets, τ, etc.), therefore not only cells from LAr calorimeter are initially included in the cluster, but also hadronic calorimeter cells. In order to identify the clusters that are originated from electromagnetic showers, a selection is applied requiring that the EM fraction of the cluster f_{EM} is greater than 0.5, and hadronic calorimeter cells are then removed from the selected clusters. f_{EM} is defined as:

$$f_{\text{EM}} = \frac{E_{\text{L1}} + E_{\text{L2}} + E_{\text{L3}}}{E_{\text{clus}}}, \tag{5.2}$$

where $E_{\text{L}x}$ is the sum of the energy of the cluster cells in the layer x. From the list of all the reconstructed topo-cluster with $E_{\text{T}} > 400$ MeV, seed topo-cluster candidates are selected.

A candidate electron seed topo-cluster is required to have a $E_{\text{T}} > 1$ GeV and has to be matched with a track with at least four hits in the silicon tracker. For photons, since no track match is required, seed topo-clusters with transverse energy $E_{\text{T}} > 1.5$ GeV are used.

Once a seed topo-cluster has been found, the algorithm starts looking for satellite clusters among all the remaining topo-clusters with lower E_{T} in a window $\Delta\eta \times \Delta\phi = 0.075 \times 0.125$ around the seed cluster barycentre. Moreover, for converted photons a topo-cluster is selected as a satellite if it is matched to the same conversion vertex of the

seed cluster or if it is matched to one of the tracks associated to the conversion vertex of the seed cluster. For electrons, satellite clusters are selected between the topo-clusters that are within a $\Delta\eta \times \Delta\phi = 0.125 \times 0.3$ window around the seed topo-cluster barycentre and that are at least matched to one track with hits in the silicon detector, such that the best-matched track for both the satellite and the seed topo-cluster is the same. The diagram in Figure 5.4 summarizes this procedure.

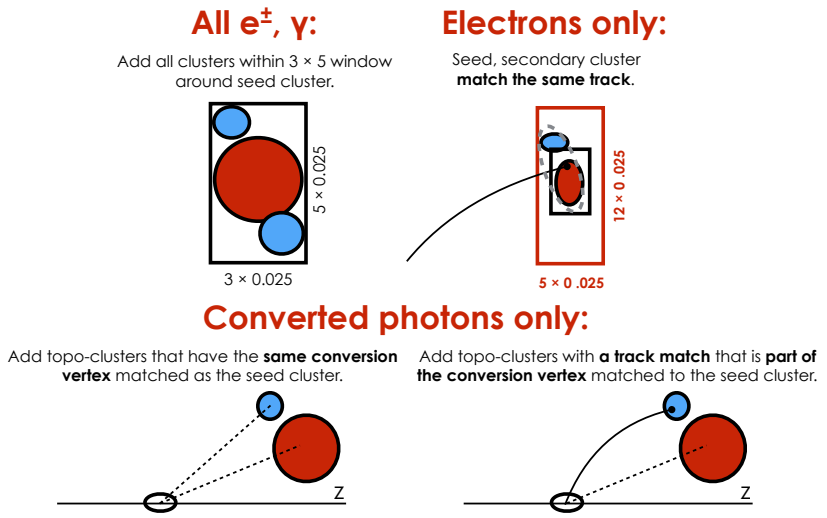

Figure 5.4: Diagram of the superclustering algorithm common for electrons and photons.

When the seed cluster and satellite clusters are selected, a "super-cluster" is formed combining the list of all the cells associated to each individual cluster. Finally, since inside the current calibration procedure (see Chap. 6) it is expected to have a smaller systematic uncertainty on the energy scale if the lateral leakage, *i.e.* the fraction of the lateral energy profile of the EM shower exceeding the cluster size, is constant with respect to the particle energy, the superclusters are restricted to 3 (5) cells in the barrel (endcap) along the η direction. This restriction does not widely affect the improvement in the energy description obtained by the super-cluster approach, since the material effects, such as bremsstrahlung, broaden the EM showers along the ϕ direction.

Figure 5.5 shows the cluster shape in the second layer of the calorimeter cells η-ϕ plane between the sliding window and the super-cluster for an electron generated with an energy of 17.59 GeV. Thanks to the contribution of the satellite clusters from photon bremsstrahlung the raw energy (*i.e* before the calibration) collected inside the super-cluster is the 96% of the generated energy, instead of the 77% collected by the sliding window approach. Figures 5.6 and 5.7 compare the uncalibrated response of electron and converted photons reconstructed using the super-cluster and sliding window algorithm. The two figures show the fitted Gaussian peak on $E_{\text{raw}}/E_{\text{true}}$ distribution in different region of $E_{\text{T}}^{\text{true}}$ and $|\eta|$. Moreover, supercluster reconstruction algorithm results in an improvement of the resolution both for electrons and converted photons. Figures 5.8 and 5.9 compare the calibrated expected resolution (see Chap. 6) of electron and converted photons reconstructed using the super-cluster and sliding window algorithm, showing the interquartile range (IQE) of $E_{\text{calib}}/E_{\text{true}}$ (see Sec. 6.1.5) in different region of $E_{\text{T}}^{\text{true}}$ and

$|\eta|$. An improvements in resolution of up to 20-30% is found in some bins in the end-cap region of the detector for simulated events without pileup.

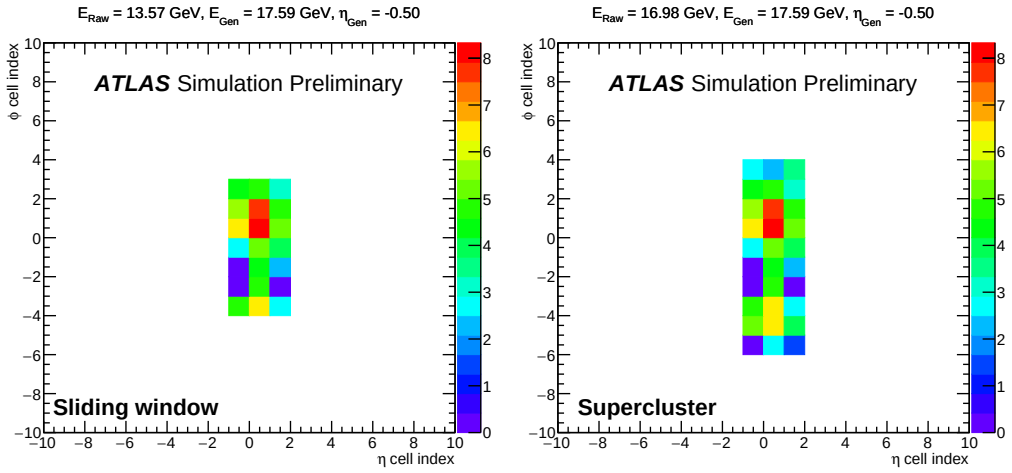

Figure 5.5: An example of an electron cluster is shown for the sliding window (left) and supercluster (right) algorithms. The raw energy E_{raw} is defined as the sum of the energies in the cluster cells before the Monte Carlo-based calibration (see Chap. 6). The z-axis of this distribution is the natural logarithm of the raw cell energy.

The performance of the supercluster algorithm has been evaluated also using Monte Carlo simulations, reconstructed with an average interaction rate of $15 < \langle\mu\rangle < 40$, of several relevant physics topologies. Using supercluster-based reconstruction an improvement of $\sim 8\%$ is observed in the core Gaussian width of the m_{ee} distribution of $J/\Psi \to e^+e^-$ events. A $\sim 6\%$ improvement in the ratio of resolution to mean is also observed for the m_{ee} distribution of $Z \to e^+e^-$ events. Finally, considering the $H \to \gamma\gamma$ events the resolution improves by 5% with respect sliding-window reconstructed events. A larger improvement of $\sim 9\%$ can be observed selecting only diphoton events with two double-track Si conversion.

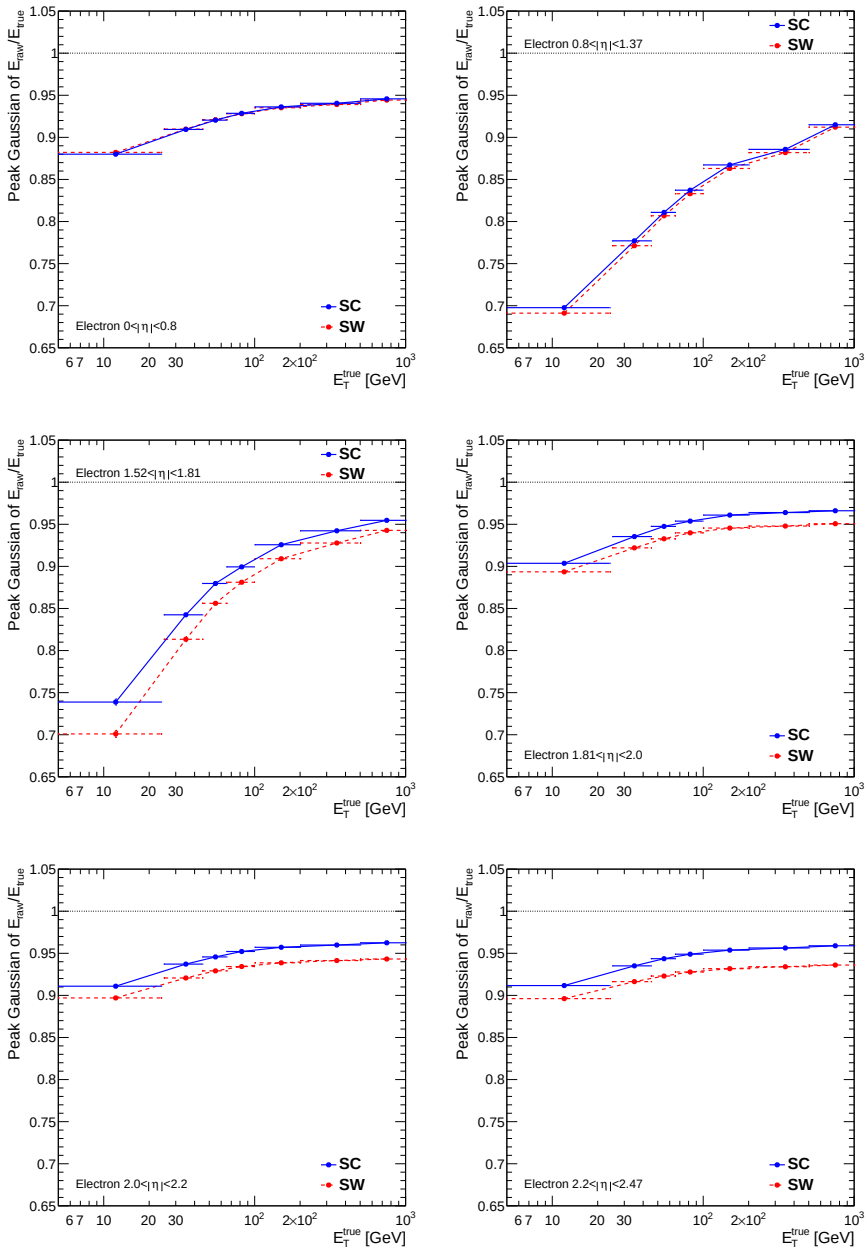

Figure 5.6: Uncalibrated peak position of the energy response, calculated using a Gaussian fit to the core of the response distribution, for simulated electrons without pileup. Sliding window-based response is shown in red, while the supercluster-based response is shown in blue.

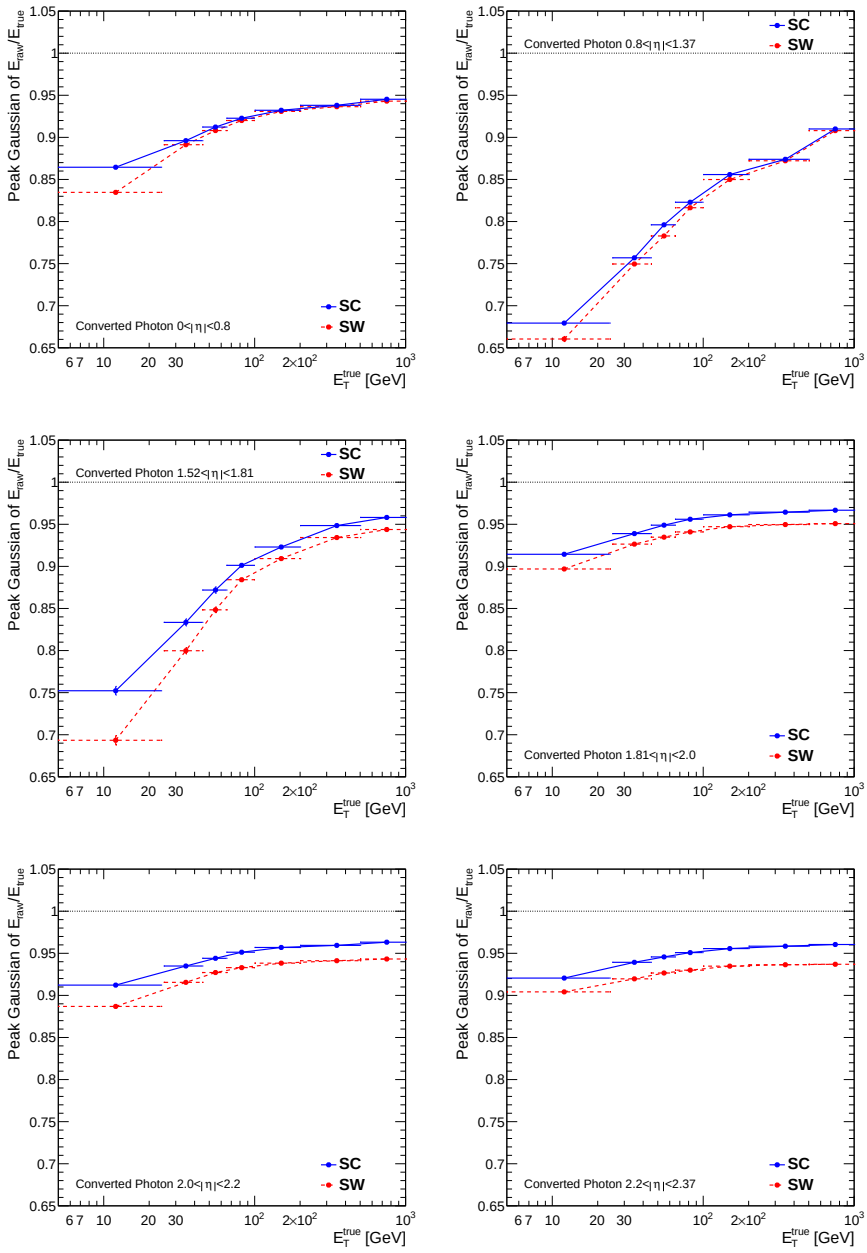

Figure 5.7: Uncalibrated peak position of the energy response, calculated using a Gaussian fit to the core of the response distribution, for simulated converted photons without pileup. Sliding window-based response is shown in red, while the supercluster-based response is shown in blue.

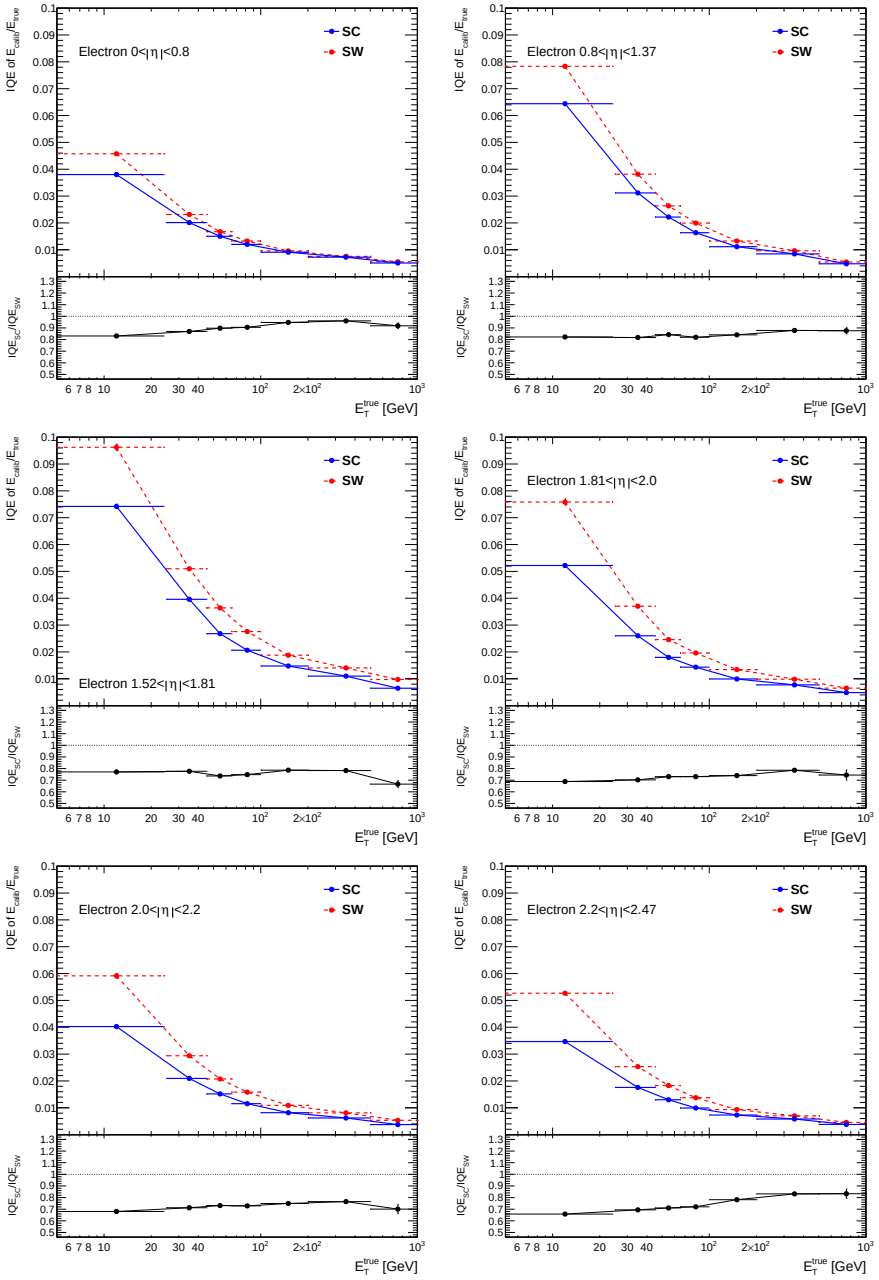

Figure 5.8: Calibrated energy response resolution, expressed in terms of IQE, for simulated electrons without pileup. Sliding window-based response is shown in red, while the supercluster-based response is shown in blue.

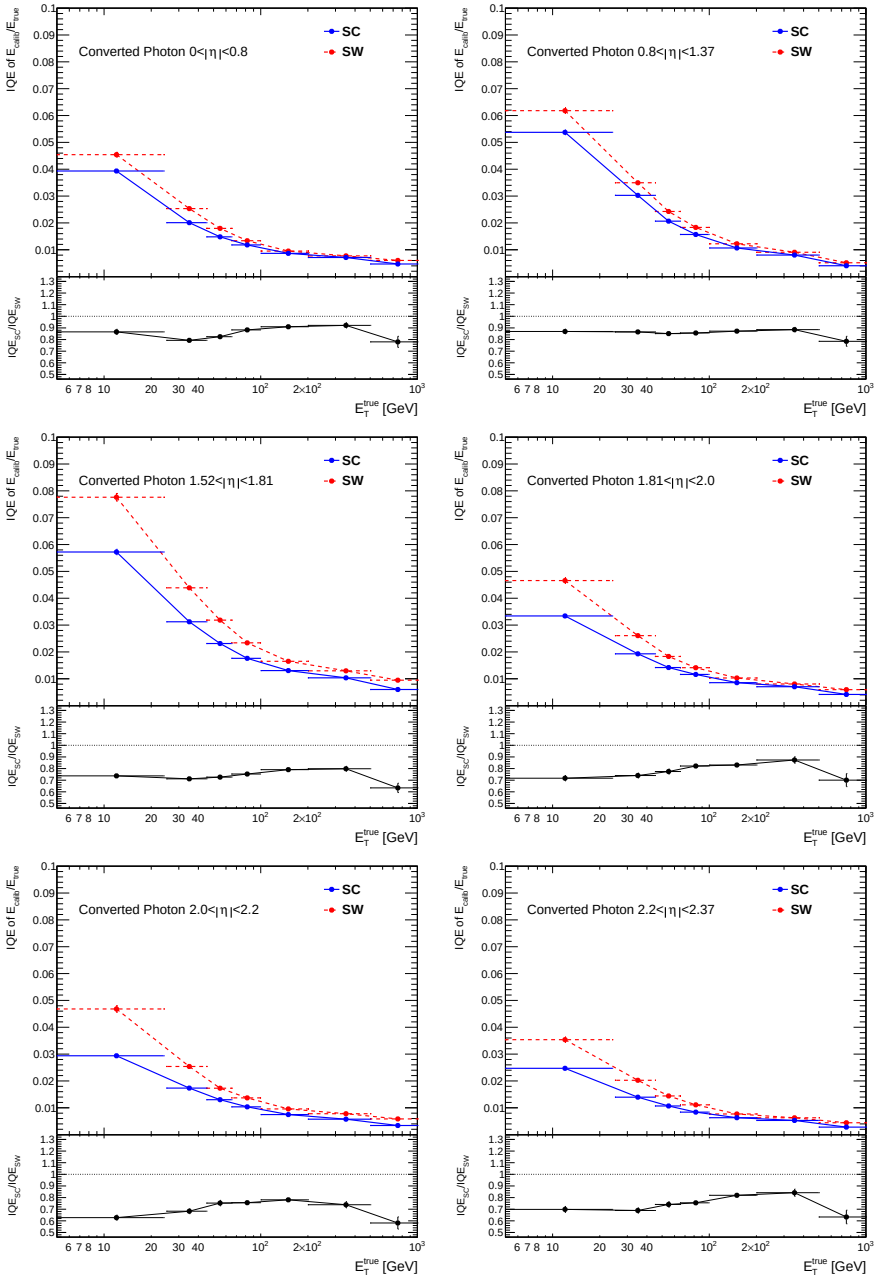

Figure 5.9: Calibrated energy response resolution, expressed in terms of IQE, for simulated converted photons without pileup. Sliding window-based response is shown in red, while the supercluster-based response is shown in blue.

5.2 Muon reconstruction

Muon reconstruction (134) is performed independently in the Inner Detector (covering $|\eta| < 2.5$), the Muon Spectrometer (covering $|\eta| < 2.7$), and the calorimeters. The information from each sub-detector are then combined to form the muon tracks used at analysis level. The combination of the ID and the MS information increases the purity of the reconstructed muon sample and provides a good momentum resolution over a large p_{T} range. Four muon types are defined depending on which sub-detector is used in the reconstruction.

- Combined (CB) muon: track reconstruction is performed independently in the ID and MS, and a combined track is formed with a global refit that uses the hits from both the ID and MS sub-detectors.

- Segmented-tagged (ST) muon: a track in the ID is classified as a muon if, once extrapolated to the MS, it is associated with at least one local track segment in the MDT or CSC chambers.

- Calorimeter-tagged (CT) muon: a track in the ID is identified as a muon if it can be matched to an energy deposit in the calorimeter compatible with a minimum-ionizing particle. This algorithm recovers the acceptance in the region where the MS is only partially instrumented for allowing cabling and services to the calorimeters and trackers ($|\eta| < 0.1$).

- Extrapolated (ME) muon: the muon trajectory is reconstructed based only on the MS track and a loose requirement on the probability of originating from the interaction point based on the track impact parameter.

When two muon types share the same ID track, preference is given to CB muons, then to ST, and finally to CT muons. The overlap with ME muon in the muon spectrometer is resolved comparing the fit quality and the number of hits of the tracks.

Muon identification is performed by applying quality requirements that suppress background, mainly from pion and kaon decays, while selecting prompt muons with high efficiency and/or guaranteeing a robust momentum measurement. It is expected that the fit quality of the muon candidates originating from in-flight decays of charged hadrons will be poor and that their momentum measured in the ID and MS will be significantly different. The muon identification algorithm is based on three variables:

- q/p *significance*, defined as the absolute value of the difference between the ratio of the charge and momentum of the muons measured in the ID and MS divided by the sum in quadrature of the corresponding uncertainties;

- ρ', defined as the absolute value of the difference between the transverse momentum measurements in the ID and MS divided by the p_{T} of the combined track;

- the normalized χ^2 of the combined track fit.

Additionally, to guarantee a robust momentum measurement, requirements on the number of track hits in the ID and MS are applied.

Four muon identification selections (*Medium, Loose, Tight*, and $High - p_{\mathrm{T}}$) are provided to address the specific needs of different physics analyses. The reconstruction efficiency for Medium muon selection is shown by Figure 5.10.

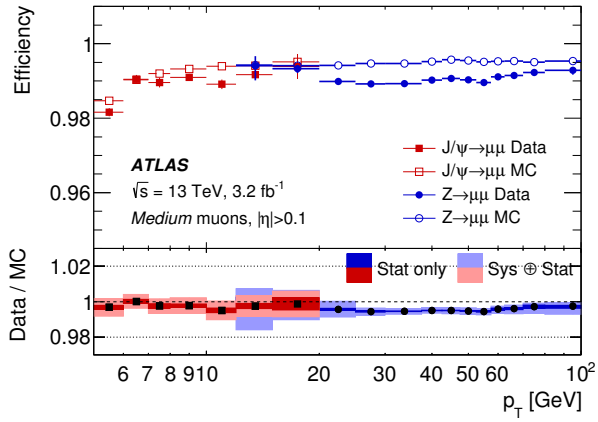

Figure 5.10: Reconstruction efficiency for the Medium muon selection as a function of the p_{T} of the muon, in the region $0.1 < |\eta| < 2.5$, as obtained with $Z \to \mu\mu$ and $J/\psi \to \mu\mu$ events. The error bars on the efficiencies indicate the statistical uncertainty. The panel at the bottom shows the ratio of the measured to predicted efficiencies, with statistical and systematic uncertainties (134).

5.3 Jet reconstruction

Quarks and gluos hadronise immediately after their production (see Sec. 1.1.2), producing in the detector sprays of hadrons, called "jets". Hadronic jets are reconstructed in the ATLAS detector by the *anti-k_t* algorithm (135), starting from three-dimensional energy clusters of calorimeter cells. The response of the calorimeter to the reconstructed jets is calibrated using a p_{T} and η dependent factor evaluated from simulation (136). A correction dependent on the jet area (137) is also applied to remove the contribution due to in-time and out-of-time pileup. Finally, a residual correction (Jet Energy Scale, or JES) is applied to the jet p_{T} in data using a well calibrated reference object. The JES is validated for central jets ($|\eta| < 0.8$) with $20 < p_{\mathrm{T}} < 950$ GeV using a photon or Z boson as reference object, based on transverse momentum balance in Z+jet and γ+jet events. Then, topologies with three or more jets are used to balance a high-p_{T} jet against a recoil system composed of several lower-p_{T} jets, that have an energy in the range of the $Z/\gamma + jet$ calibrations and are therefore already calibrated. This allows extending the calibrations to a p_{T} of 2 TeV (138).

Once the jets are reconstructed, different requirements (*jet cleaning criteria*) are applied in order to reduce the background arising from non-collision background and instrumental effects. Additionally a requirement on the *Jet Vertex Fraction* (JVF) (139) can be applied. JVF is defined as the sum of the scalar transverse momentum of the tracks that are associated with the jet and originated from the hard-scatter vertex, divided by the scalar p_{T} sum of all the tracks associated to the jet.

$$\mathrm{JVF} = \frac{\sum_k p_{\mathrm{T}}^{\mathrm{trk}_k}(\mathrm{PV}_0)}{\sum_l p_{\mathrm{T}}^{\mathrm{trk}_l}(\mathrm{PV}_0) + \sum_{n\geq 1} sum_l p_{\mathrm{T}}^{\mathrm{trk}_l}(\mathrm{PV}_n)}, \tag{5.3}$$

where PV_0 is the hard scatter vertex and PV_n, $n \geq 1$ corresponds to primary vertices due to pileup interactions in the same bunch crossing.

Imposing a lower limit on this variable rejects the majority of pileup jets, but the background rejection of the JVF selection is affected by a strong dependence on the number of primary vertex present in the event (N_{Vtx}). A multivariate combination of JVF and N_{Vtx} called the *Jet Vertex Tagger* (JVT) is built in such a way that the resulting jet background rejection efficiency is stable as a function of N_{Vtx} to further reduce the pileup contribution and improve the purity of the jet reconstructed from the hard interaction. Figure 5.11 shows the dependence of the pileup jet fake rate on the number of primary vertices when imposing cuts on JVT and JVF.

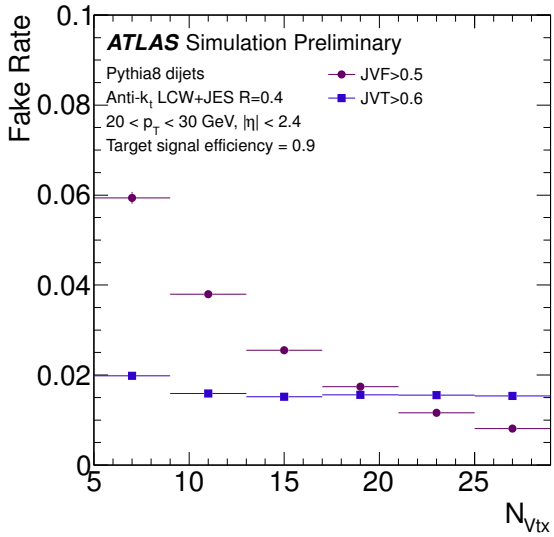

Figure 5.11: $\mathrm{N_{Vtx}}$ dependence of the pileup jet fake rate when imposing cuts on JVT (blue) and JVF (violet) such that the inclusive hard-scatter jet efficiency is 90% (139).

5.4 Missing transverse energy

The missing transverse energy ($E_{\mathrm{T}}^{\mathrm{miss}}$) (140; 141) is the quantity which is exploited to identify final states with particles that only weakly interact with the detector material, such as the neutrinos or other particles predicted by BSM theories. The $E_{\mathrm{T}}^{\mathrm{miss}}$ quantifies the momentum imbalance along the transverse plane with respect to all the momenta of the objects reconstructed in a given event. The $E_{x(y)}^{\mathrm{miss}}$ components are calculated as:

$$E_{x(y)}^{\mathrm{miss}} = E_{x(y)}^{\mathrm{miss,e}} + E_{x(y)}^{\mathrm{miss},\gamma} + E_{x(y)}^{\mathrm{miss},\tau} + E_{x(y)}^{\mathrm{miss,jets}} + E_{x(y)}^{\mathrm{miss},\mu} + E_{x(y)}^{\mathrm{miss,soft}}, \tag{5.4}$$

where each term is given by the negative vectorial sum of the momenta of the respective calibrated objects:

$$E_x^{\mathrm{miss,term}} = -\sum_i^{N_{\mathrm{cell}}^{\mathrm{term}}} E_i \sin\theta_i \cos\phi_i, E_y^{\mathrm{miss,term}} = -\sum_i^{N_{\mathrm{cell}}^{\mathrm{term}}} E_i \sin\theta_i \sin\phi_i, \tag{5.5}$$

- $E_{x(y)}^{\text{miss,e}}$ is reconstructed from the calibrated energies of the clusters associated to electrons with $p_{\text{T}} > 10$ GeV in the pseudorapidity regions $0 < |\eta| < 1.37$ and $1.52 < |\eta| < 2.47$;

- $E_{x(y)}^{\text{miss},\gamma}$ is reconstructed from the calibrated energies of the clusters associated to photons with $p_{\text{T}} > 25$ GeV in the pseudorapidity regions $0 < |\eta| < 1.37$ and $1.52 < |\eta| < 2.47$;

- $E_{x(y)}^{\text{miss},\tau}$ is given by the contribution of hadronically-decay τ leptons with $p_{\text{T}} > 20$ GeV in the pseudorapidity regions $0 < |\eta| < 1.37$ and $1.52 < |\eta| < 2.47$;

- $E_{x(y)}^{\text{miss},\mu}$ is given by the contribution of muons with $p_{\text{T}} > 10$ GeV in the pseudorapidity region $|\eta| < 2.7$;

- $E_{x(y)}^{\text{miss,jets}}$ is obtained by the calorimetric jets, reconstructed by the anti-k_{t} algorithm with radius parameter $R = 0.4$, with a $p_{\text{T}} > 20$ GeV. In order to remove jets originating from pileup, a requirement on the jet vertex tagger variable (JVT > 0.64) is applied to jets with $|\eta| < 2.47$ and $p_{\text{T}} < 50$ GeV. The tracks associated to jets that fail this requirement are included in the $E_{x(y)}^{\text{miss,soft}}$ term;

- $E_{x(y)}^{\text{miss,soft}}$, the soft term is reconstructed from signal tracks not associated with any object passing the previous selection cuts. It is built from tracks with $p_{\text{T}} > 0.4$ GeV and $|\eta| < 2.5$ and not matched to any selected objects. Only tracks compatible with the primary vertex are included.

From the $E_{x(y)}^{\text{miss}}$, $E_{\text{T}}^{\text{miss}}$ is calculated as:

$$E_{\text{T}}^{\text{miss}} = \sqrt{(E_x^{\text{miss,term}})^2 + (E_y^{\text{miss,term}})^2}. \tag{5.6}$$

Chapter 6

Electron and photon energy calibration

The precise reconstruction of the energy of electrons and photons is a key ingredient for many physics measurement, such as the accurate determination of the Higgs and W boson masses.

The photon and electron energy measurement by the EM calorimeter is limited by several effects. In particular the finite dimension of the cluster and the presence of inactive material upstream of and inside the calorimeter worsen the energy reconstruction performance. Figure 6.1 illustrates the four main components that affect the linearity and the resolution of the final energy measurement, which are:

- the energy loss due to the amount of material between the interaction point and the first layer of the calorimeter as shown in Figure 6.20 ("front" component);
- the energy loss due to inactive material inside the calorimeter ("sampling" component);
- the lateral (i.e in the η-ϕ plane) energy loss outside the reconstructed cluster ("out-of-cluster" component);
- the energy loss behind the calorimeter in the longitudinal direction ("leakage" component).

Due to such energy losses without a calibration procedure the simple sum of the energy in the cells of the EM cluster is biased with respect to the true energy carried by the incident particle, as shown by Figure 6.2.

In ATLAS the photon and electron energy calibration procedure (143; 28) can be summarized in three main steps:

- the electronic signal read out by each LAr calorimeter cell inside the cluster is converted into a raw value of the energy deposited by the incident particle (144; 145), see Sec. 4.3.2;
- a Monte Carlo based calibration, exploiting different variables of the reconstructed particle, converts the raw energy E_{raw} of the cluster to the calibrated photon and electron energy. This calibration is applied both to data and Monte Carlo samples;
- the data-driven measurement of the intercalibration factor between the different regions of the detector and the in-situ measurement, mainly using $Z \to ee$ events, of the different energy scale and resolution in data and MC , are used to correct the energy scale in data and smear the energy resolution in the simulation.

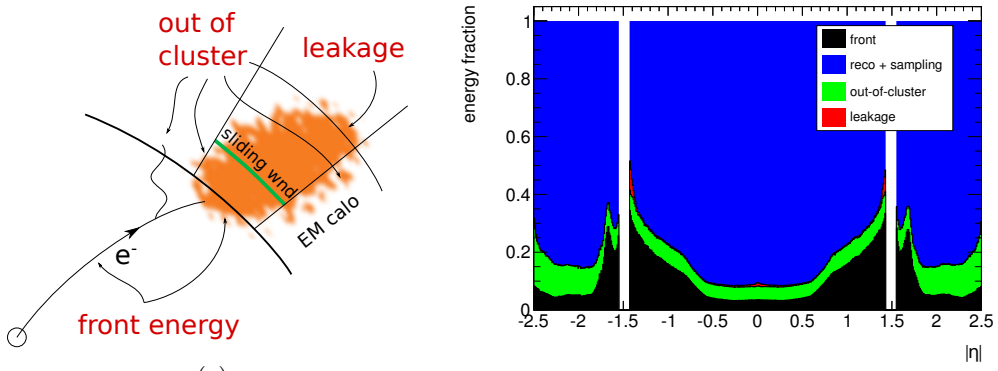

(a) (b)

Figure 6.1: (a) Sketch of the various component of the energy loss affecting the linearity and the resolution of the final energy measurement.(b) Energy decomposition in the various component of the energy loss for 50 GeV electrons (142).

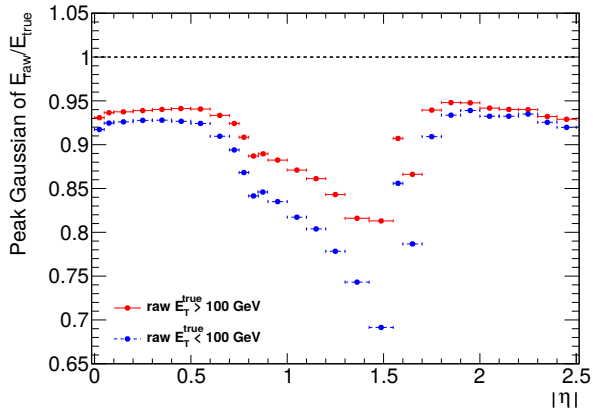

Figure 6.2: Gaussian peak position of the distribution of the ratio of the raw energy reconstructed in the accordion over the true energy versus the pseudorapidity, for electrons with $E_{\mathrm{T}}^{\mathrm{true}} > 100$ GeV (red dots) or $E_{\mathrm{T}}^{\mathrm{true}} < 100$ GeV (blue dots).

The different steps of the full procedure to calibrate the electron and photon energy response are shown in Figure 6.3 (143). My contribution focuses on the first step of the calibration chain training, maintaining and optimizing the multivariate Monte Carlo-based calibration. In particular, I adapted the training framework in order to cope with the new data format which has been used by ATLAS since 2015, and I have updated the calibration each time a major change in the reconstruction algorithm was released or new simulation was available.

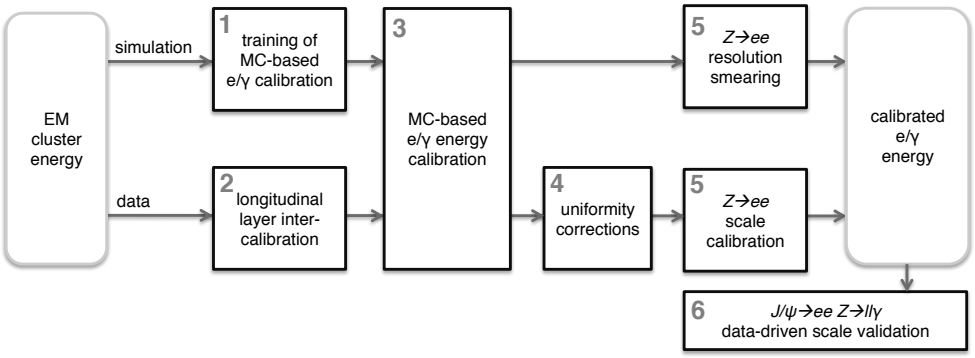

Figure 6.3: Schematic overview of the procedure used to calibrate the energy response of electrons and photons in ATLAS (143).

6.1 Multivariate Monte Carlo energy calibration

The Monte Carlo based calibration is the first step of the electron and photon energy calibration chain implemented in ATLAS. It relies on a multivariate regression technique based on boosted decision trees (BDT) with gradient boosting training (146; 147). Its optimization is performed separately for electrons, converted and unconverted photons using single particle simulations without any additional inelastic *pp* collisions and underlying event overlaid.

The calibration is implemented using the Toolkit for Multivariate Analysis (TMVA) framework (148). This framework provides a ROOT-integrated machine learning environment for the processing and parallel evaluation of multivariate classification and regression techniques. In particular, the energy calibration is a pure regression problem where, given a set of input variables, the algorithm tries to minimize the root mean square of the defined target.

The choice of using an MVA tool presents several advantages. First of all, thanks to the multivariate nature of the algorithms, it is possible to take into account the correlation between all the input variables, leading to a better resolution and a better linerity, defined as the most probable value of the ratio between the calibrated and the truth energy of the particle, $E_{\text{calib}}/E_{\text{true}}$) . Figure 6.4 shows the improvement given by the introduction of the MVA calibration in Run 1 compared to the previous calibration technique adopted by ATLAS, using a Monte Carlo simulation of $H \to \gamma\gamma$ and $J/\psi \to ee$ events. The peak of the MVA calibrated di-photon and di-electron invariant mass distributions is closer to the Higgs boson and J/ψ simulated mass value. Moreover, using the MVA calibration, the resolution of converted (unconverted) photons improves by up to 15% (20%), leading

to a 10% narrower di-photon invariant mass distribution. No significant improvements have been observed for electrons, except at $1.52 < |\eta| < 1.8$ where they vary from 10% to 30% depending on E_{T} (143).

Finally, the use of an MVA tool allows updating the calibration factors when an improved simulation is available, since the work is done internally by TMVA and the user acts only on the configuration file; for the same reason it is also straightforward to modify the configuration to introduce new input variables in the calibration process.

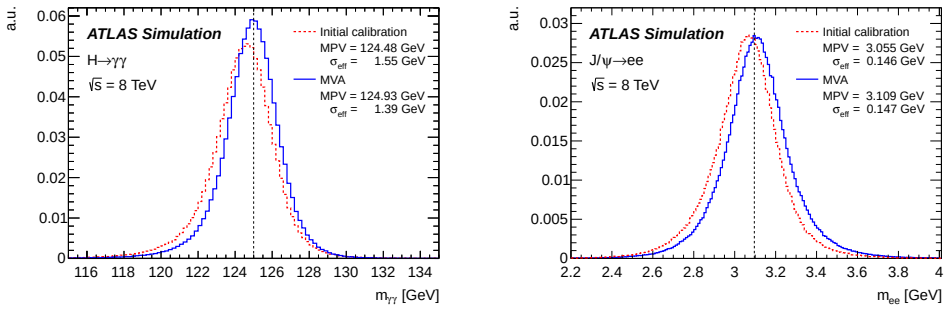

(a) $H \to \gamma\gamma$ (b) $J/\psi \to ee$

Figure 6.4: Comparison of the diphoton invariant mass distributions, $m_{\gamma\gamma}$, for a simulated Standard Model Higgs boson with a mass of 125 GeV, obtained with the initial Run 1 calibration and with the MVA calibration (left). A similar comparison is shown for the dielectron invariant mass distributions, m_{ee}, for simulated $J/\psi \to ee$ decays (right). The dashed black lines indicate the simulated particle masses (143).

6.1.1 Samples and selection

The training of the MVA energy calibration is performed on simulated samples of single particle events in the ATLAS interaction point. The single particles are generated using the GEANT-based PARTICLE GUN generator and passed through a detailed GEANT4 simulation of the ATLAS detector (149; 150). The samples contain 40M of single photon events and 40M of single electron events.

The true transverse energy of the particles is distributed according to Figure 6.5. The E_{T} spectrum was designed to provide candidates up to 3 TeV without discontinuities and maximizing their number in the region between 7 and 200 GeV.

The photons and electrons to be used in the training have to fulfill the loose identification requirements (see Sec. 7.1). This request is not applied for the η bins 1.37-1.4, 1.4-1.46, 1.46-1.52 and 2.47-2.5(Sec. 6.1.3), because the efficiency of the loose identification in these regions is suboptimal and removes too many objects from the training sample.

6.1.2 Target and input variables

The goal of the calibration is to estimate the true energy of the particles from the quantities measured by the detector. The MVA target must be either the energy or a quantity from which it is possible to compute this energy. The target considered for the training is the correction to the total raw cluster energy measured in the accordion: $E_{\mathrm{true}}/E_{\mathrm{acc}}$.

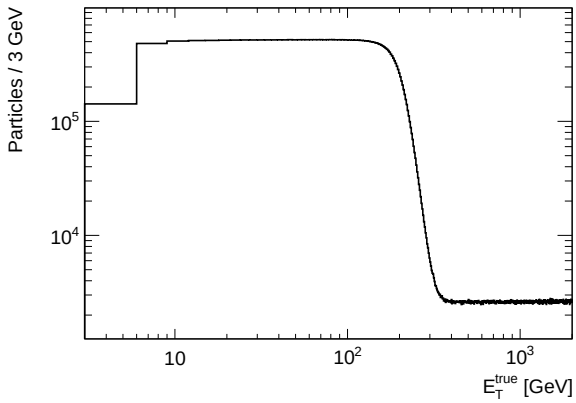

Figure 6.5: Input E_T distributions of the particles at truth level used to generate the MC samples for the MVA calibration.

The MVA uses several input variables in order to evaluate this correction. The variables are chosen for their correlation with the target distributions. Another important factor related to the choice of variables is how well that distributions are modeled in the simulation. For example, the variables that describe the shape of the electromagnetic shower in the EM calorimeter are not yet used because of some not completely understood data-MC differences, in particular for photons.

The quantities used both for electrons and photons are:

- **Total raw cluster energy in the accordion**: $E_{\text{acc}} = E_{s1}^{\text{raw}} + E_{s2}^{\text{raw}} + E_{s3}^{\text{raw}}$, defined as the sum of the uncalibrated energies of the three accordion layers.

- **Ratio of the energy in the presampler to the energy in the accordion**: $E_{s0}^{\text{raw}}/E_{\text{acc}}$, used only for clusters in the acceptance of the presampler ($|\eta| < 1.8$).

- **Ratio of the energy in the first accordion layer to the second one**: $E_{s1}^{\text{raw}}/E_{s2}^{\text{raw}}$.

- **Pseudorapidity in the ATLAS frame**: η, i.e. taking into account the misalignment of the detector, in order to correct for the variation of the material in front of the accordion, among other effects.

- **Cell index**: an integer number between 0 an 99 which identifies the cell in the second layer of the calorimeter and is defined as the integer part of the division $\eta_{\text{calo}}/\Delta\eta$, where η_{calo} is pseudorapidity of the cluster in the calorimeter frame and $\Delta\eta = 0.025$ is the size of one cell in the second layer.

- η **with respect to the cell edge**: η_{calo} modulo $\Delta\eta = 0.025$. This variable allows correcting for the variation of the lateral energy leakage due to the finite cluster size, which is larger for particles that hit the cell close to the edges.

- ϕ **with respect to the lead absorbers**: ϕ_{calo} modulo $2\pi/1024$ ($2\pi/768$) in the barrel (endcap), corresponding to the periodicity of lead sheets in each region. This variable allows correcting for the slight variations of the sampling fraction seen by a particle as a function of ϕ.

Some additional quantities are used only for the energy calibration of the photons that convert inside the volume of the inner detector (0 <R< 800 mm). They are:

- **Radius of the conversion**: used only if $p_{\mathrm{T}}^{\mathrm{conv}} > 3$ GeV, where $p_{\mathrm{T}}^{\mathrm{conv}}$ is the sum of the transverse momentum of the conversion tracks.
- **Ratio of the E_{T} in the accordion to the conversion $p_{\mathrm{T}}^{\mathrm{conv}}$**: $E_{\mathrm{T}}^{\mathrm{acc}}/p_{\mathrm{T}}$, where $E_{\mathrm{T}}^{\mathrm{acc}} = E^{\mathrm{acc}}/\cosh(\eta)$.
- **Fraction of the $p_{\mathrm{T}}^{\mathrm{conv}}$ carried by the highest-p_{T} track**.

Transition region

In the transition region ($1.4 < |\eta| < 1.6$) between the barrel and the endcap electromagnetic calorimeter, the amount of material traversed by the particles before reaching the first active layer of the calorimeter ranges from 5 to almost 10 radiation lengths. To mitigate the impact of this inactive material on the reconstructed energy dedicate scintillators (E4) are installed in the transition region. E4 scintillators are part of the Intermediate Tile Calorimenter (ITC). The ITC is located in the gap region, in between the long and the extended barrels of the tile calorimeter, and it has been designed to correct the energy lost in the passive material that fills the gap region. ITC is composed by two standard tile cell groups and four groups (E1, E2, E3, and E4) of cells, highlighted in yellow in Figure 6.6, with active material consisting of only one scintillator. Each of these four groups of cells covers the entire azimuthal plane with a granularity $\Delta\phi \sim 0.1$. In particular, E4 scintillators cover the pseudorapidity region $1.4 < |\eta| < 1.6$ and contributes for 0.026 X_0.

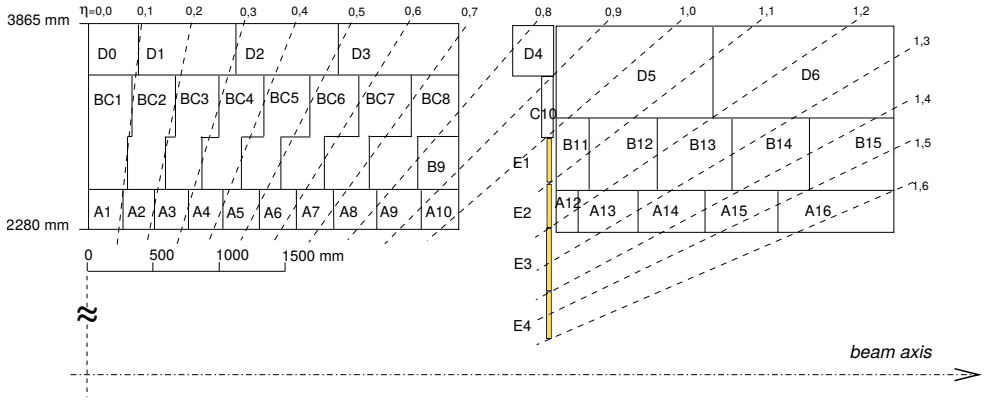

Figure 6.6: Schematic showing the TileCal cell and scintillator structure, including the so-called "E-cells" (E1-E4) which are highlighted in yellow.

Electrons and photons in the gap region deposit energy in the electromagnetic barrel and endcap calorimeter and in the E4 scintillators as well. Variable accounting for the energy deposited in the E4 scintillators has been added to the training of the Monte Carlo based calibration. For the $|\eta|$ intervals 1.4-1.46, 1.46-1.52, 1.52-1.6 the additional variables included in the MVA regression are:

- **Energy in three consecutive E4 scintillators over the energy in EM accordion**: $E_{3\times E4}/E_{\mathrm{acc}}$. The electron shower width is wider than one E4 scintillator,

thus for each electron the sum of the energies from three consecutive E4 scintillators along ϕ ($E_{3\times E4}$) is considered.

- **Difference in ϕ between angle of the electron cluster barycenter and the position of the E4 scintillator**: $\Delta\phi = \phi_{\text{cluster}} - \phi_{E4}$.

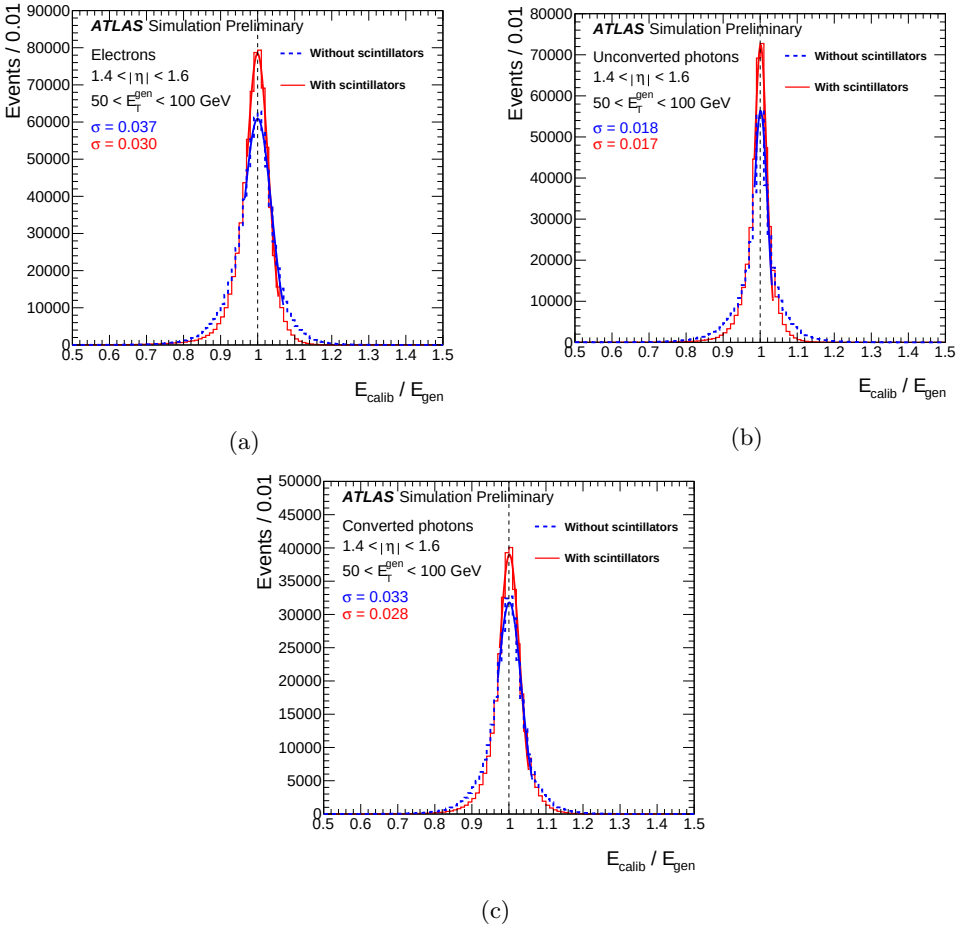

Figure 6.7: Distributions of the calibrated energy, E_{calib}, divided by the generated energy, E_{gen}, for (a) electrons , (b) unconverted photons , and (c) converted photons, generated with $1.4 < |\eta| < 1.6$ and $50 < E_T^{\text{gen}} < 100$ GeV. The blue dashed (red solid) histogram shows the results based on the energy calibration without (with) the scintillator information. The curves represent Gaussian fits to the cores of the distributions, between [-1, +2] standard deviations (σ) (28).

Figure 6.7 shows the improvement in the energy calibration in the region $1.4 < |\eta| < 1.6$ for electrons, converted and unconverted photons with generated energy between 50 and 100 GeV, evaluated using single particle simulations without pileup. The width of the distribution of the ratio of the calibrated energy E_{calib} to the generated energy of the particle E_{true} has been estimated using a Gaussian fit of the core of the distribution and

using the interquartile range (i.e IQE, see Sec. 6.1.5). In the first case the improvement in the energy resolution is about 20% for electrons, 15% for converted and 8% for unconverted photons when comparing to a similar calibration without using the information from the scintillators, and 22%, 20% and 29% respectively in the second case (28).

6.1.3 Binning

In order to help the MVA to adjust the response as a function of many variables which have different behaviors in different regions of the phase space, the sample was divided into bins in pseudorapidity ($|\eta|$), transverse energy in the accordion (E_T^{acc}) and particle type (electron, converted photon and unconverted photon). A rectangular mesh of 10×9 bins in $|\eta| \times E_T^{\text{acc}}$ was defined, plus an additional 3×6 "special bins" for the regions close to the edges of the two half-barrel modules ($\eta \sim 0$), and 3×1 for the transition region bins ($1.4 < |\eta| < 1.6$). The total number of bins used for the training is 111. The bin edges are the following:

- bins in $|\eta|$:
  - "normal": 0, 0.05, 0.65, 0.8, 1.0, 1.2, 1.37 and 1.6, 1.74, 1.82, 2.0, 2.2, 2.47, 2.5;
  - "special": 0-0.05, 1.37-1.4, 2.47-2.5;
  - "transition region": 1.4, 1.46, 1.52, 1.6;
- bins in $E_{\text{T}}^{\text{acc}}$:
  - "normal": 0, 10, 20, 40, 60, 80, 120, 500, 1000 and 50000 GeV;
  - "special": 0, 25, 50, 100, 500, 1000 and 50000 GeV;
  - "transition region": 0, 10000 GeV.

An independent optimization is performed for each of the $|\eta| \times E_{\text{T}}^{\text{acc}}$ bin separately for electrons, converted and unconverted photons, for a grand total of 333 bins. Even if the algorithms used are relatively slow, the training code was developed to run in parallel on batch queues (e.g CONDOR (151)) over hundreds of nodes. Thus the whole training takes only a few hours to run all the 333 sub-processes.

6.1.4 Energy Shifts

Multivariate regression algorithms normally aim at minimizing the root mean square (RMS) of the distribution of the target quantity. Since the target distribution $E_{\text{true}}/E_{\text{acc}}$ is not perfectly Gaussian, in particular for particles with low E_{T}, this leads to an optimization in which the mean value of the output energy E_{calib} is close to the true energy E_{true}, but not necessarily equal to it. A set of shifts are computed and applied on top of the MVA output such that the peak of the distribution of $E_{\text{calib}}/E_{\text{true}}$ is centered at 1. The mean value of the smallest interval containing 10% of the events in each bin (defined below) was chosen to estimate the peak position.

Single shifts per bin in $|\eta| \times E_{\text{T}}^{\text{acc}}$ were found to vary considerably in adjacent transverse energy bins, due to the change in the shape of the distributions as a function of energy. Moreover the shifting procedure is more relevant for objects with low transverse energy, and therefore a finer binning with respect to the training is used at low E_{T}. The $E_{\text{T}}^{\text{acc}}$ bins are:

- 0, 5, 7, 10, 15, 30, 50, 80, 3000 GeV for $0 < |\eta| < 1.4$ and $1.6 < |\eta| < 2.5$;
- 0, 15, 45, 160, 1000 GeV for $1.4 < |\eta| < 1.46$;
- 0, 17, 25, 500 GeV for $1.46 < |\eta| < 1.52$;
- 0, 100, 350, 100 GeV for $1.52 < |\eta| < 1.6$.

A linear interpolation was used to produce a continuous energy dependence, connecting the barycenter of adjacent transverse energy bins. Figure 6.8 shows the distribution of $E_{\text{calib}}/E_{\text{true}}$ in a very asymmetric case, considering low-E_{T} electrons ($10 < E_{\text{T}} < 15$ GeV), and a more symmetric case, considering intermediate-E_{T} electrons ($70 < E_{\text{T}} < 75$ GeV), before and after the shift correction.

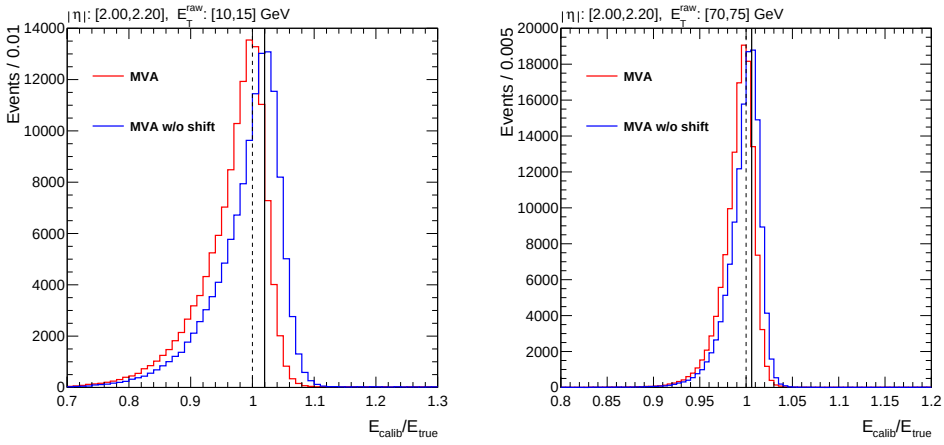

(a) $10 < E_{\text{T}} < 15$ GeV (b) $70 < E_{\text{T}} < 75$ GeV

Figure 6.8: Example of the shift effect for electrons. The distributions of $E_{\text{calib}}/E_{\text{true}}$ are compared before and after the shift, indicated by the solid vertical line.

6.1.5 Performance

The performance of the calibration based on the MVA optimization is evaluated in terms of linearity, energy resolution, and dependence of the response on the MVA calibration input quantities, in order to verify that the calibration has been correctly trained and that it is not affected by residual dependencies on the input variables.

The linearity is quantified by the peak position of $E_{\text{calib}}/E_{\text{true}}$ as a function of E_T^{true}, estimated by the mean value of a Gaussian function fitted to the core of the distribution in each (E_T^{true}, $|\eta|$) bin. The fits are restricted to the range [-1, +2] standard deviations to avoid biases from the tails.

The resolution is defined as the interquartile range of $E_{\text{calib}}/E_{\text{true}}$, i.e. the distance between the first and the last quartiles of the data in each bin, scaled in order to mimic the standard deviation in case of a normal distribution. It is defined as:

$$\text{IQE} = \frac{Q_3 - Q_1}{2\phi^{-1}(0.75)}, \tag{6.1}$$

where Q_1 and Q_3 are the first and the third quartile of the distribution and ϕ^{-1} represents the inverse of the cumulative distribution function of the Normal distribution. Therefore, an observation of IQE = 1 implies that the IQE of the energy response is equivalent to that of a unit-width Gaussian function. An example of the quartiles of a Normal distribution is shown in Figure 6.9, where the area between two quartiles encompasses 25% of the full distribution, such that the area enclosed by Q_1 and Q_3 contains the middle 50% of the distribution. The IQE is chosen as the resolution estimator since it is one of the most commonly used dispersion statistic estimator and one of the least affected by outliers.

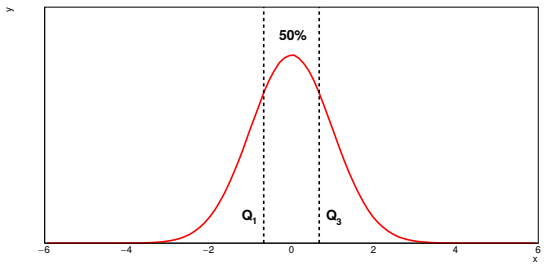

Figure 6.9: Diagram showing the range of the interquartile range (IQR) of a Normal distribution, where Q_1 and Q_3 are the first and third quartiles of the distribution.

Figure 6.10 shows the $E_{\text{calib}}/E_{\text{true}}$ Gaussian peak position as a function of $p_{\text{T}}^{\text{truth}}$ ($|\eta_{cl}|$) for electrons, unconverted and converted photons training, considering different $|\eta|$ ($p_{\text{T}}^{\text{truth}}$) sub-samples. The distributions are steadily close to one except for low E_{T} objects, for which they are shifted from 1 by less then 1%.

Figure 6.11 shows the $E_{\text{calib}}/E_{\text{true}}$ interquartile as a function of $p_{\text{T}}^{\text{truth}}$ ($|\eta|$) for electrons, unconverted and converted photons, considering different $|\eta_{cl}|$ ($p_{\text{T}}^{\text{truth}}$) sub-samples. The photon and electron energy resolution, as described by the equation (4.17), decreases as a function of the energy. The resolution dependence on $|\eta|$, as shown by the left column plots, is mainly due to the amount of material in front of the first layer of the calorimeter that is not homogeneous with respect to the pseudorapidity (see Fig. 4.7).

The behaviour of the calibrated energy as a function of the input variables and several other variables has also been investigated. Figure 6.12 shows the peak position of the ratio between the calibrated energy (the raw energy) and the true particle energy distribution as a function of the fraction of the energy deposited in the different layers of the calorimeter. After the calibration no residual correlation is observed between the $E_{\text{calib}}/E_{\text{true}}$ and the energy collected in the presampler and in the three layers of the EM calorimeter.

Figures 6.13 and 6.14 show the peak position of the ratio between the calibrated energy (the raw energy) ratio and the true particle energy distribution as a function of the η position with respect to the cell edge and the ϕ coordinate with respect to the lead absorbers for unconverted photons after (before) the calibration. The multivariate training can reabsorb completely the modulation effect, giving a flat response of the calibrated energy with respect to these variables.

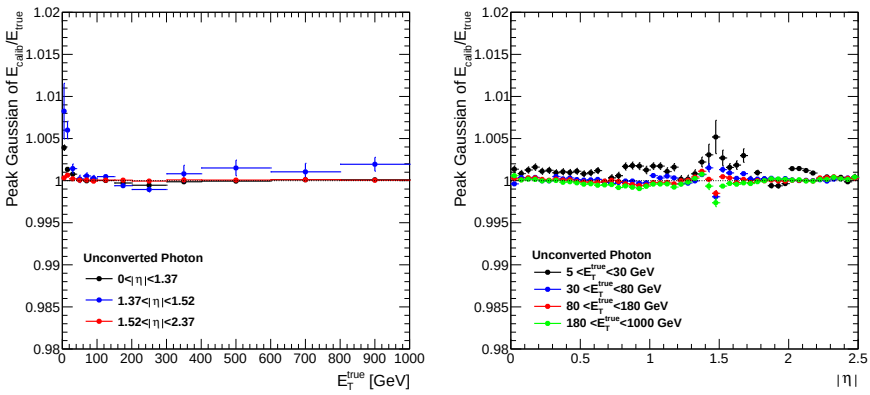

(a) Unconverted photons

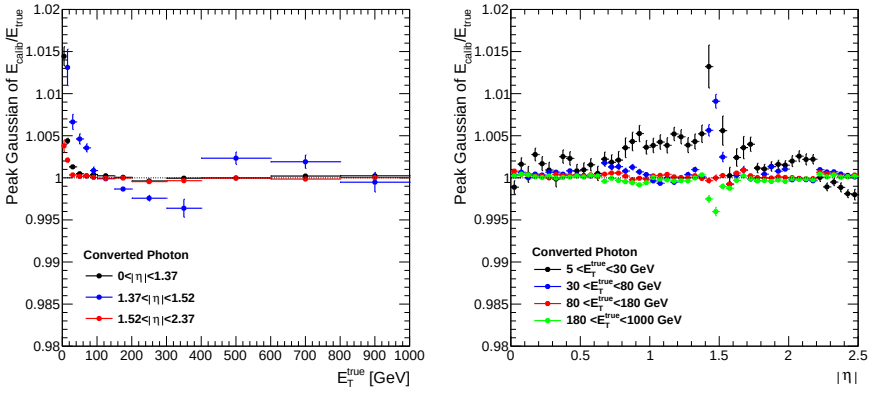

(b) Converted photons

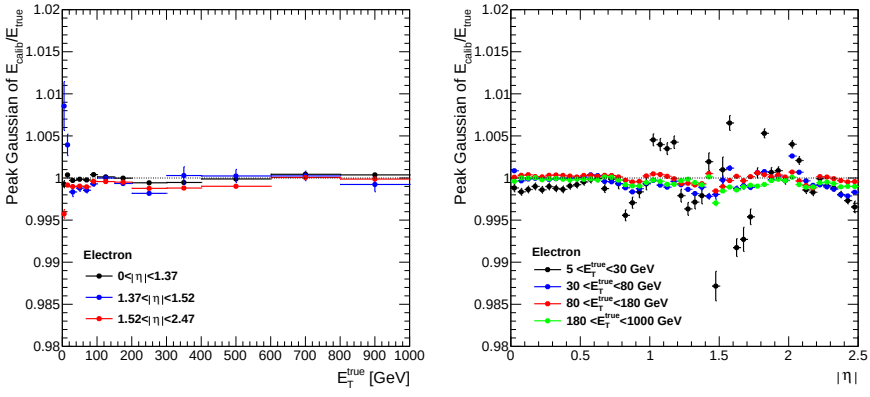

(c) Electrons

Figure 6.10: Calibrated peak position of the energy response, calculated using a Gaussian fit to the core of the response distribution as function of E_{T}^{true} and $|\eta|$ for (a) unconverted photons, (b) converted photons and (c) electrons.

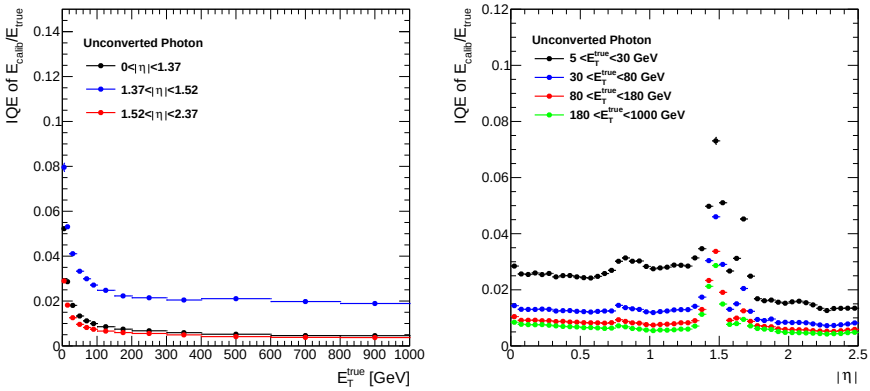

(a) Unconverted photons

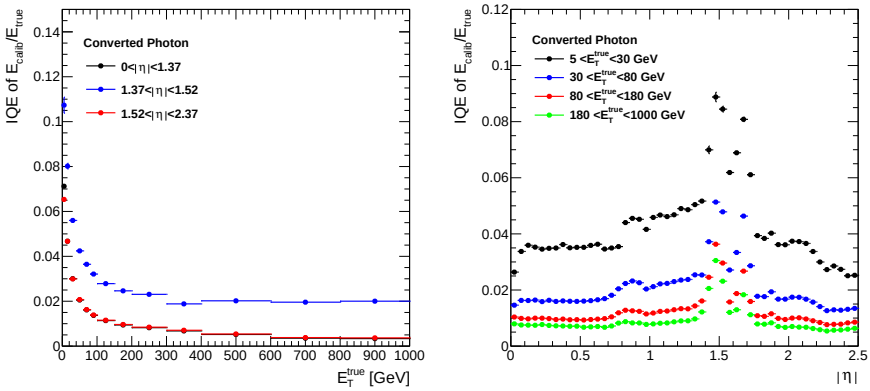

(b) Converted photons

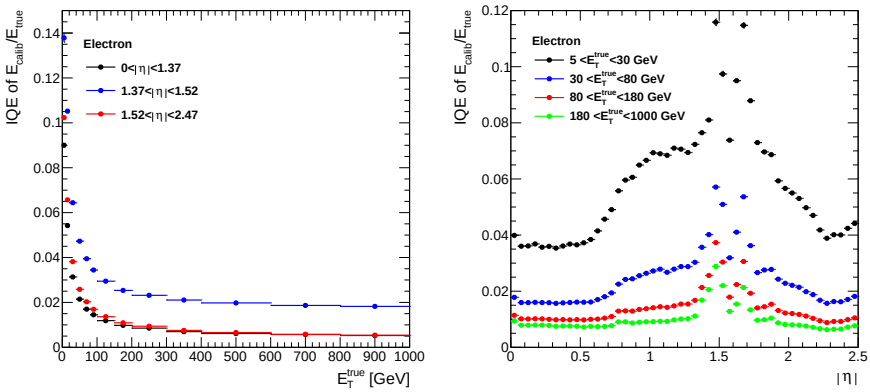

(c) Electrons

Figure 6.11: Calibrated energy response resolution, expressed in terms of IQE, as function of E_{T}^{true} and $|\eta|$ for (a) unconverted photons, (b) converted photons and (c) electrons.

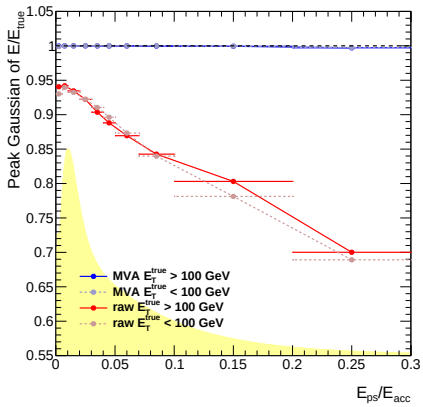

(a) Presampler fraction

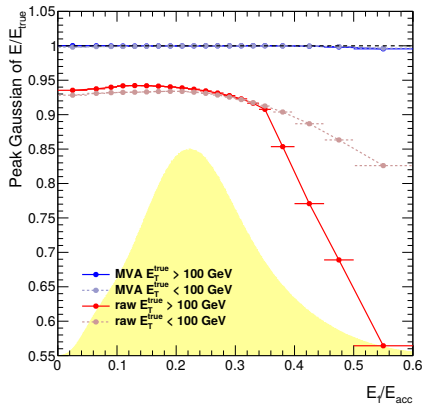

(b) E_1 fraction

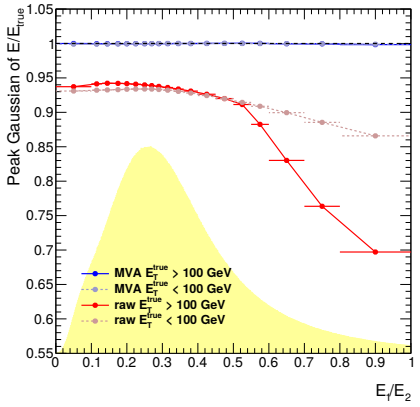

(c) E_1/E_2 fraction

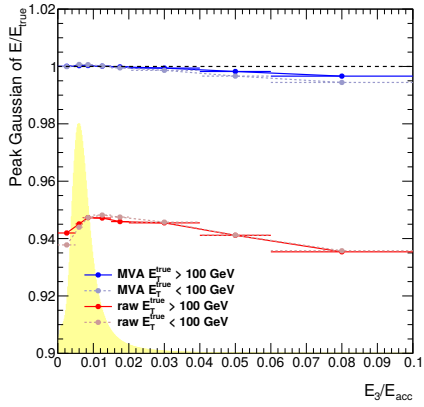

(d) E_3 fraction

Figure 6.12: Peak position of E/E_{true} as a function of the presampler fraction, E1 fraction, E1/E2 and E3 fraction for electrons comparing MVA calibration (blue) and raw energy (red). For the presampler fraction the distribution is only for $|\eta| < 1.8$. Each histogram (in yellow) illustrates the distribution of the corresponding variable.

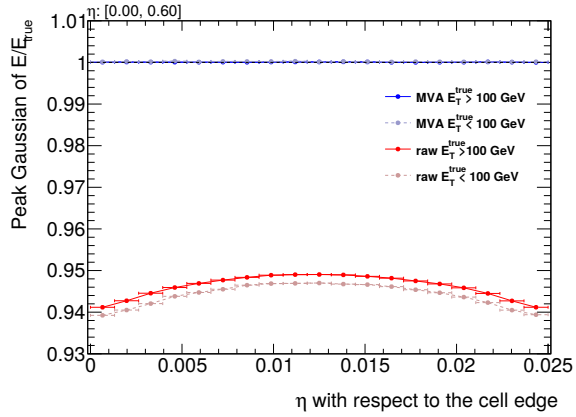

(a) $0 < |\eta| < 0.6$

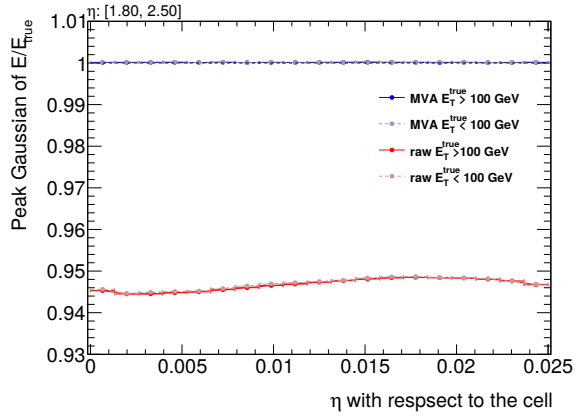

(b) $1.8 < |\eta| < 2.5$

Figure 6.13: Peak position of E/E_{true} as a function of η_{calo} with respect to the cell edge for unconverted photons comparing MVA calibration (blue) and raw energy (red).

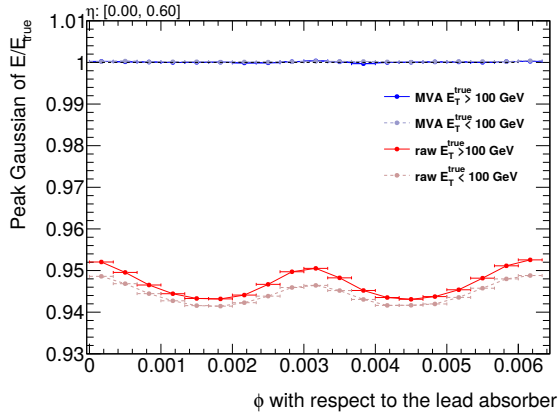

(a) $0 < |\eta| < 0.6$

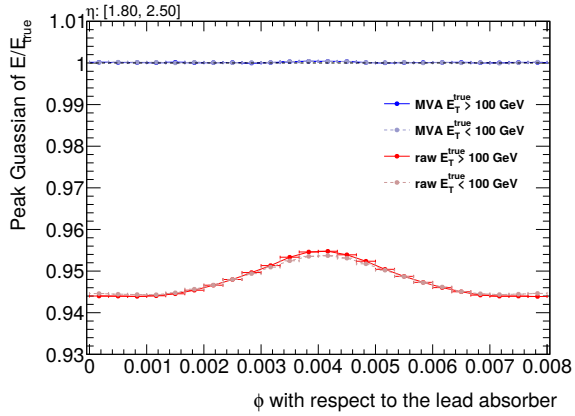

(b) $1.8 < |\eta| < 2.5$

Figure 6.14: Peak position of E/E_{true} as a function of ϕ with respect to the lead absorber for unconverted photons comparing MVA calibration (blue) and raw energy (red).

Pileup dependency

The MVA energy calibration is trained on Monte Carlo samples reconstructed without additional pileup events, but the *pp* collisions produced during 2015 and 2016 are characterized by an average inelastic interaction rate per bunch crossing equal to $\langle\mu\rangle = 13.7$ and $\langle\mu\rangle = 24.9$ respectively (see Sec. 3.2). Figure 6.15 shows the linearity and resolution of the photon and electron energy calibration as a function of μ evaluated using MC single particle samples. A little dependency on pileup is found. The largest effects are measured for low energy objects. In particular for electrons with 0 GeV $< E_{\mathrm{T}}^{\mathrm{true}} <$ 30 GeV, a shift of $\sim 0.7\%$ of the $E_{\mathrm{calib}}/E_{\mathrm{true}}$ peak position is measured and the resolution worsened by $\sim 10\%$ for $\mu = 25$. This as well as other possible differences between the MC based calibration and the data distributions are absorbed by the scale energy and resolution corrections applied at the end of the calibration procedure (see Sec. 6.4).

6.2 Layer intercalibration

In order to compare the data with the simulated events it is necessary to evaluate the energy scale factor that reduces the energy measured in the data to the one simulated in the Monte Carlo. Moreover, since the EM calorimeter is longitudinally segmented, the response of the different layers has to be calibrated. In the ATLAS calibration scheme three procedures are exploited to determine the final calorimeter energy scale in data. They consist of the measurement of the energy scale of the presampler, the measurement of the intercalibration scale between the first and the second layer of the accordion, and finally a global scale factor exploiting the in-situ measurement of electrons decaying from Z boson decays.

In this section the relative calibration of the first and second layer of the accordion together with the calibration of the energy response of the presampler are presented (143).

The data-MC intercalibration factor between the first (L1) and the second layer (L2) is defined as

$$\alpha_{1/2} = \frac{\langle E_{1/2}^{\mathrm{data}} \rangle}{\langle E_{1/2}^{\mathrm{MC}} \rangle}, \tag{6.2}$$

where $\langle E_{1/2} \rangle$ is the ratio of the most probable values (MPV) of the energy deposited by a particle in the first and the second layer of the EM calorimeter. In particular, this measurement is performed using $Z \to \mu\mu$ events, since the muon energy deposits in the calorimeter are insensitive to the amount of passive material in front of it. Figure 6.16 shows $\alpha_{1/2}$ as a function of $|\eta|$, measured using the data collected in Run 1 at $\sqrt{s} = 8$ TeV. The total uncertainty varies between 1% to 1.5% in the barrel region and is 1.5% in the endcap. These values are in agreement with those evaluated using 2015 and 2016 data, therefore they are retained as the nominal L1-L2 intercalibration factor also in Run 2. The L1/L2 calibration bias is then removed from the data by applying an $|\eta|$ dependent correction such that $E_2^{\mathrm{corr}} = E_2 \times \alpha_{1/2}$.

After the intercalibration of L1 and L2, the presampler energy scale α_{PS} is determined from the ratio of the energy measured in the PS (E_0) in data and in MC for electrons coming from Z boson decays. In order to interpret correctly this ratio in terms of an energy calibration factor, the effects of a possible mis-modelling of the passive material upstream of the presampler have to be taken into account. Indeed they affect the showering of the electromagnetic particle and therefore the energy collected in the PS. This correction exploits the strong correlation between $E_{1/2}$ and the upstream material. A

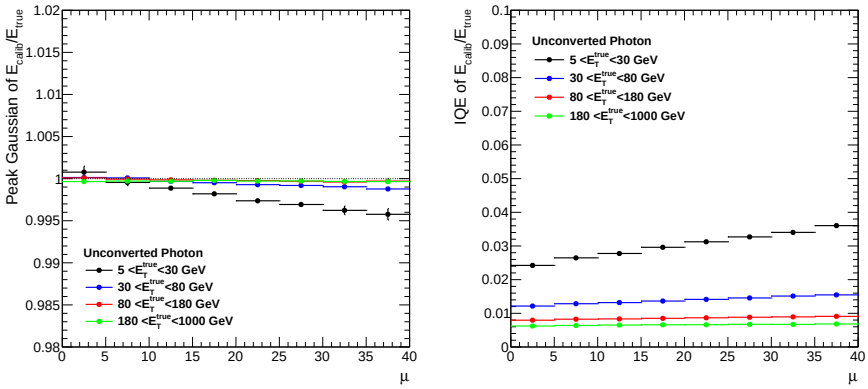

(a) Unconverted photons

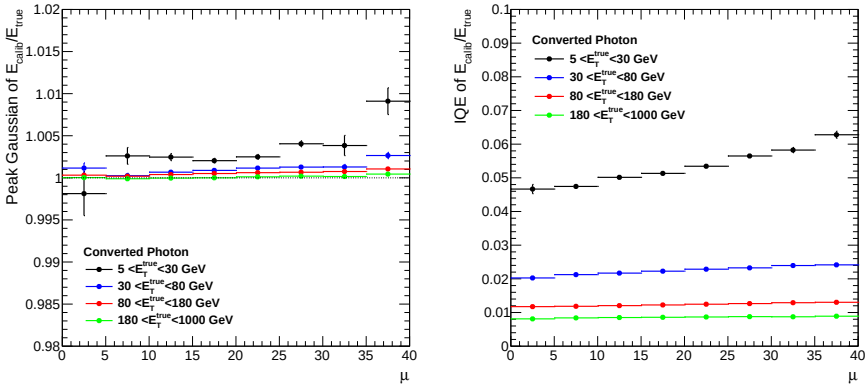

(b) Converted photons

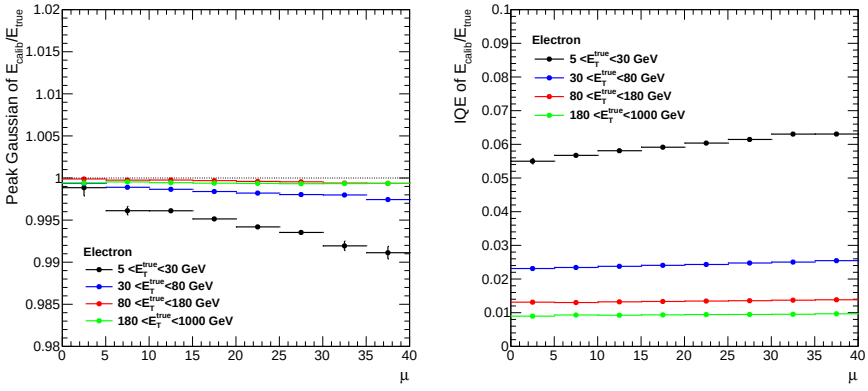

(c) Electrons

Figure 6.15: Calibrated energy linearity and resolution as a function of the number of inelastic interaction per bunch crossing, μ, for (a) unconverted photons, (b) converted photons and (c) electrons.

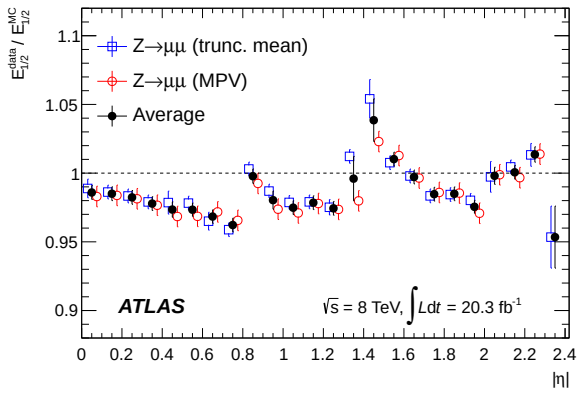

Figure 6.16: Ratio $\langle E_{1/2}^{\text{data}}\rangle/\langle E_{1/2}^{\text{MC}}\rangle$ as a function of $|\eta|$, as obtained from the peak position (MPV) of the muon energy deposits in L1 and L2, and from the mean of these energy deposits computed in an interval containing 90% of the distribution (trunc. mean). The error bars represent the total uncertainty of the $Z \to \mu\mu$ analysis (143).

linear correlation factor ($A(\eta)$) between the variation of E^{PS} and $E_{1/2}$ due to the material amount variation is evaluated using alternative MC samples with different amount of passive material upstream of the calorimeter. In addition, a second parameter ($b_{1/2}$) is needed to correct $E_{1/2}$ for the mis-modeled material between the presampler and the first layer of the EM calorimeter, to which the PS energy measurement is not sensitive.

$b_{1/2}$ is defined as $b_{1/2} \equiv E_{1/2}^{\text{data}}/E_{1/2}^{\text{MC}}$, and, assuming a correct L1/L2 intercalibration and in absence of material bias, should be equal to 1. It is probed using a sample of unconverted photons from $Z \to \ell\ell\gamma$ events, with a veto on the raw PS energy in order to limit the probability that a conversion occurred between the end of ID and the PS, since photons that reach the PS without converting are not sensitive to the inner detector material. It is verified using simulation that the requirement of $E_0 < 500$ MeV minimizes the sensitivity of the unconverted photon sample to the material variation upstream of the PS.

Finally, α_{PS} is evaluated as:

$$\alpha_{\text{PS}} = \frac{E_0^{\text{data}}}{E_0^{\text{corr}}}, \tag{6.3}$$

where E_0^{corr} is the PS energy in the MC after the correction for the material mismodeling:

$$E_0^{\text{corr}} = \left[1 + A(\eta)\left(\frac{E_{1/2}^{\text{data}}(\eta)}{E_{1/2}^{\text{MC}}(\eta) b_{1/2}(\eta)} - 1\right)\right] E_0^{\text{MC}}. \tag{6.4}$$

Figure 6.17 shows the ratio of the average PS energies, $E_0^{\text{data}}/E_0^{\text{MC}}$, as a function of $|\eta|$. The energy scale α_{PS} is then evaluated averaging $E_0^{\text{data}}/E_0^{\text{corr}}$ over intervals corresponding to the pre-sampler module size (i.e $\Delta\eta = 0.2$ in the barrel and $\Delta\eta = 0.3$ in the endcap). The measurement is accurate to the 2-3% level, depending on pseudorapidity.

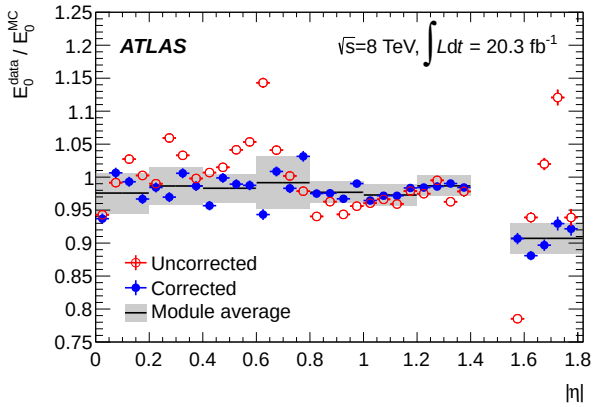

Figure 6.17: Ratio of the average PS energies, $E_0^{\text{data}}/E_0^{\text{MC}}$, for electrons in data and simulation as a function of $|\eta|$, before and after corrections for $b_{1/2}$ and material upstream of the PS. The full lines with shaded bands represent the PS energy scale as a function of $|\eta|$, $\alpha_{\text{PS}}(\eta)$, and its uncertainty (143).

6.3 Uniformity correction

A set of corrections is implemented in the data to account for response variations not included in the simulation due to the non nominal setup of the LAr high voltage system, geometric effects such as the intermodule widening induced by gravity (*i.e.* the gap between the barrel EM modules are widened due to a gravity-induced sagging effect that is not included in the simulation), and bias introduced by the LAr hardware electronic calibration (143).

In particular, a new study of the impact of the non linearity of the gain of the read-out electronics has been performed using special runs in 2015 and in 2017. As described in Sec 4.3.2, in order to adapt to the wide range of expected energies the electronic signals of the EM calorimeter cells are reconstructed with three different gain settings. The electrons coming from a Z boson usually have their cell energies recorded using the High Gain (HG) while for example 1/3 of the H$\rightarrow \gamma\gamma$ events have a photon reconstructed with at least one cell in Medium Gain (MG). In order to estimate the relative intercalibration of the MG and HG, special runs have been performed requesting a significantly lower threshold to switch between HG and MG, so that almost all the electrons from Z boson decays have at least one L2 cell recorded using MG. Then the relative energy scale between the MG and HG configurations can be derived using $Z \rightarrow ee$ events from standard and special runs. The relative energy scale difference between standard and special runs is consistent with 0 except in the region $0.8 < |\eta| < 1.37$, where a significant difference is observed. This difference is not completely understood at the moment, thus no correction is applied to data and the deviation from 1 is taken as uncertainty. Propagating the uncertainty of the gain intercalibration to the reconstructed particle energies results in a typical uncertainty of $\approx$ 0.10-0.15% in the barrel and $\approx$ 0.3-0.5% in the endcap for unconverted photons with $E_{\text{T}} = 60$ GeV.

6.4 Energy scale and resolution

After the application of the intercalibration layer scale factors, the simulation-based calibration, and the corrections for the non-uniformity of the detector response, a residual disagreement in the energy scale and resolution is still present between data and simulation. The energy mis-calibration is quantified as the difference in response between data and simulation, and is parametrized as:

$$E_i^{\text{data}} = E_i^{\text{MC}}(1+\alpha_i), \tag{6.5}$$

where E_i^{data} and E_i^{MC} are the electron energy in data and simulation, and α_i represents the deviation from the unbiased calibration in a given pseudorapidity region labeled i. The difference in energy resolution between data and simulation can be modeled by an effective constant term (c_i'):

$$\left(\frac{\sigma(E)}{E}\right)_i^{\text{data}} = \left(\frac{\sigma(E)}{E}\right)_i^{\text{MC}} \oplus c_i'. \tag{6.6}$$

The c_i' term arises from the detector non uniformity, alignment and electronic calibration uncertainties that are not perfectly taken into account in the ATLAS simulation.

Energy scale corrections (α_i) and additional constant terms for the energy resolution (c_i') have been evaluated using a pure control sample of $Z \to ee$ events selected in the 2015 and 2016 data.

For $Z \to ee$ events the effect of the electron energy mis-calibration on the di-electron invariant mass is:

$$m_{ij}^{\text{data}} = \sqrt{E_i(1+\alpha_i)E_j(1+\alpha_j)\cos\theta_{ij}} = m_{ij}^{\text{MC}}\sqrt{(1+\alpha_i)(1+\alpha_j)} \sim m_{ij}^{\text{MC}}(1+\alpha_{ij}), \tag{6.7}$$

where

$$\alpha_{ij} \sim \frac{(\alpha_i+\alpha_j)}{2}, \tag{6.8}$$

and the electron pair is reconstructed in the i and j intervals of pseudorapidity. The effective constant term of the energy resolution in data leads to a wider di-electron invariant mass resolution, given by:

$$\left(\frac{\sigma(m)}{m}\right)_{ij}^{\text{data}} = \frac{1}{2}\left[\left(\frac{\sigma(E)}{E}\right)_i^{\text{MC}} \oplus c_i' \oplus \left(\frac{\sigma(E)}{E}\right)_j^{\text{MC}} \oplus c_j'\right] = \left(\frac{\sigma(m)}{m}\right)_{ij}^{\text{MC}} \oplus c_{ij}', \tag{6.9}$$

where

$$c_{ij}' = \frac{(c_i' \oplus c_j')}{2}. \tag{6.10}$$

The quantities α_{ij} and c_{ij}' are evaluated independently for each (η_i, η_j) configuration of the two electrons. Invariant mass histograms, called templates, are generated for various values of α_{ij} and c_{ij}' from the simulation, modified by a known injected energy scale and resolution perturbation factor. The templates are then compared to the data distribution and the optimal values of the energy scale and resolution correction (α_i and c_i') are obtained through a χ^2 minimization. The method is applied to a sample of $Z \to ee$ decays, selecting events with two electrons in the final state with $p_{\text{T}} > 27$ GeV and $|\eta| < 2.47$. The results are shown in Figure 6.18, where the energy scale and the effective

constant term are shown as a function of the pseudorapidity. The energy scale correction factors are typically of the order of 1-2%, with an uncertainty ranging from 0.01% to 0.1%. The constant term varies between 0.7% and 2% for $|\eta| < 2.4$, with an uncertainty of 0.1%–0.2%. Some of the sources of systematic uncertainty for this procedure are listed in the following. The uncertainties quoted are the averages over the full η spectrum.

- *Event selection.* These uncertainties are obtained varying the identification requirement and the isolation requirement for the candidate electrons, and varying the invariant mass window used to define the MC templates. They give a square total uncertainty equal to $\delta\alpha = 6 \times 10^{-4}$ and $\delta c' = 1 \times 10^{-3}$.

- *Background impact.* The electroweak background events ($Z \to \tau\tau$, $t\bar{t}$ and WW, ZZ, WZ diboson events) impact is evaluated measuring the energy scale factors using MC templates that include also the contribution from background events while in the nominal case they are not included. This source of uncertainty accounts for $\delta\alpha = 0.2 \times 10^{-4}$ and $\delta c' = 0.2 \times 10^{-4}$.

- *Method.* The nominal results are compared with the ones obtained by an alternative method which relies on a likelihood fit to the energies scales and a relative different of $\delta\alpha = 1 \times 10^{-4}$ and $\delta c' = 5 \times 10^{-4}$ is found.

- *Closure.* The intrinsic accuracy of the template method is tested by injecting a known energy scale and an additional effective constant factor into a Monte Carlo sample. The corresponding α and c' are then derived and compared to the injected values in order to quantify the possible bias induced by the method. The quoted uncertainties are $\delta\alpha = 0.6 \times 10^{-4}$ and $\delta c' = 1.1 \times 10^{-3}$.

- *Material mismodeling between data and MC.* The energy and resolution scale factor are measured only on a sub-sample of signal electrons that have lost up to 50% of their energy throughout bremsstrahlung photon emission. These electrons are selected requesting that their momentum measured at the outer radius of the ID ($(q/p)^{\mathrm{out}}$) is at least grater than the half of the momentum measured at the interaction point ($(q/p)^{\mathrm{IP}}$) ($f_{brem} = 1 - (q/p)^{\mathrm{IP}}/(q/p)^{\mathrm{out}} < 0.5$). This additional section modifies the energy and resolution scale factors by $\delta\alpha = 4 \times 10^{-4}$ and $\delta c' = 4 \times 10^{-4}$.

6.5 Systematic uncertainties

In addition to the uncertainties discussed in the previous section for the in-situ corrections, many additional sources of uncertainty on the energy scale and resolution for electrons and photons are considered: beam configuration, detector description, procedures and statistics of the samples used for data-driven corrections. The main sources of uncertainty on the energy scale are shown in Figure 6.19[1] for $|\eta| < 0.6$ and 5 GeV $< E_{\mathrm{T}} <$ 1 TeV for electrons, unconverted and converted photons and listed below (28).

- *Layer intercalibration*: the impact of the PS and L1/L2 layer intercalibration on the reconstructed particle energy is propagated studying the induced bias on the

[1]The values represented in Figure 6.19 are not yet updated to the last uptodate recommendation released by the ATLAS e/γ performance working group which have been used for the measurement of the Higgs boson mass reported in Chapter 8.

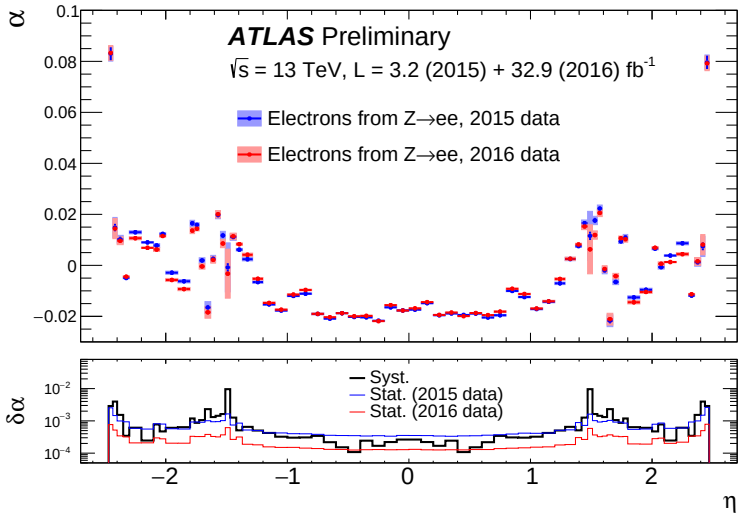

(a)

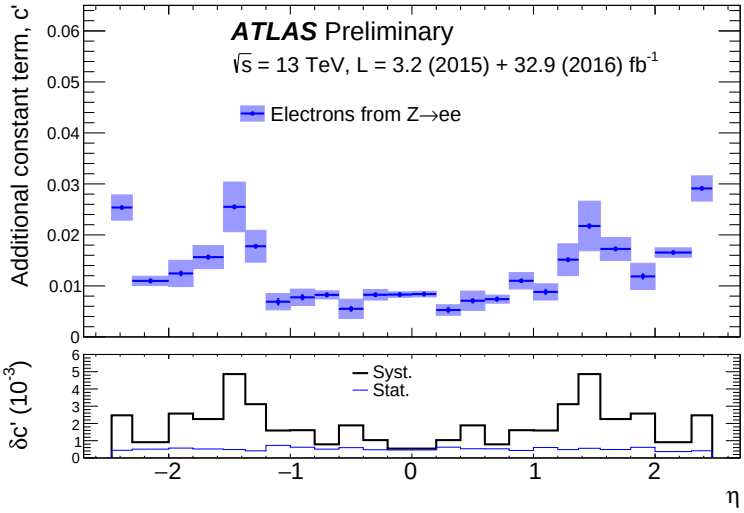

(b)

Figure 6.18: (a) Energy scale correction factor α from $Z \to ee$ events as a function of η, applied to match data to the MC. Electrons or positrons are required to have $p_T > 27$ GeV and $|\eta| < 2.47$. The total systematic uncertainty on this quantity is represented by the red and blue bands on the top plot and by the thick black line on the bottom plot. In the bottom inset, the thin blue (resp. red) line represents the 2015 (resp. 2016) statistical uncertainty. The differences (within $\pm 0.2\%$) between the 2015 and 2016 data energy scale correction factors are mostly related to small changes in detector conditions (LAr temperature) as well as to the higher luminosity of the 2016 data compared to 2015. (b) Additional constant term c' as a function of η, applied to the simulation to match the data resolution. The total systematic uncertainty on this quantity is represented by the blue band (resp. thick black line) on the top plot (resp. bottom inset). In the bottom inset, the thin blue line represents the 2015 + 2016 statistical uncertainty. The 2015 and 2016 energy resolutions are similar (40).

final energy for a given variation in E_0 or E_1/E_2. Fo The scale factors $\alpha_{1/2}$ used to intercalibrate the first two layers of the electromagnetic calorimeter as a function of η have been determined using the 2015 and 2016 data, and found to be in agreement with the measurement using the 2012 data. An additional systematic uncertainty equal to the maximum observed discrepancy between the two measurement ($\sim$ 1.5–2.5%) has been included in the uncertainty model.

- *Layer 2 gain*: the uncertainty of the gain intercalibration to the reconstructed particle energies resulting in a typical uncertainties of $\approx$ 0.10-0.15% in the barrel and $\approx$ 0.3-0.5% in the endcap for uncovered photons with $E_{\mathrm{T}} = 60$ GeV.

- *Material*: the ID, Cryostat and calorimeter material uncertainties are obtained by comparing the energy response in Monte Carlo samples simulated with nominal and modified detector geometry. The difference in the energy response are scaled comparing the material variation of the corresponding distorted simulated sample with the actual material measurement uncertainties, yielding to the energy scale uncertainties. The values of the uncertainties relative to the description of the material before the calorimeter for $|\eta| < 2.5$ have been retained from the data driven studies of Run 1. An additional source of uncertainty for the mis-modeling in the simulation of the IBL material and of the modified inner-detector patch panel (PP0) inserted during the shutdown between Run 1 and Run 2 has been considered for Run 2. Figure 6.20 and 6.21 show the simulation amount of material and the measured difference in material up to the first layer of the EM calorimeter (L1) in data and Monte Carlo as function of η, compared to the systematic uncertainty bands on such quantities from Run 1 and Run 2.

- *In-situ calibration ($Z \to ee$)*: the uncertainty on the energy scale and additional constant term of the energy resolution have been evaluated as described in Sec. 6.4.

- *Pedestal*: in 2012 data, residual small baseline shifts ($\pm$10 MeV) were observed in data, and an effect coming from the pedestal determination in electronics calibration data has been corrected as a function of the bunch train position. Nevertheless, residual effects from pileup-induced shifts can be present after the correction, and given the higher expected luminosity in Run 2, this systematic uncertainty has been estimated to be $\pm$20 MeV.

- *Uncertainties related to the scintillators for* $1.4 < |\eta| < 1.6$: four independent sources of uncertainty on the response of the scintillators have been considered:

    - data-simulation difference, evaluated as the difference in the mean of the energy in the scintillators in $Z \to ee$events: it ranges between 1% and 4.3%, depending on η. This is mainly due to the modelling of the light attenuation inside the scintillators;
    - uncertainty on the electromagnetic scale calibration factor that converts the Tile Calorimeter signals to the energy deposited by electrons. From studies of the Tile Calorimeter in test-beam (153), this factor has a spread of 2.4%, which has been taken as an uncertainty;
    - initial intercalibration using the Minimum Bias (MB) system: 1%;
    - uncertainty of the calibration using laser over the whole year: 4%.

The last two sources of uncertainty correspond to the time-dependent calibration of the responses of the E4 scintillators. The monitoring and calibration of E4 scintillators response are performed by two different calibration systems: a Laser system (117) that provides the calibration of the photomultipliers gain and the MB system (154) that is capable to monitor and calibrate the E4 scintillator responses based on the integrated currents from minimum bias events over time during data-taking. An initial intercalibration of all the E4 scintillators in the first 25 ns collision run was performed by the MB system with 1% uncertainty; later, during data-taking only the laser was used. Those systematic effects are considered independent, and added in quadrature in the *scintillators* uncertainty.

- *Photon-specific uncertainties*: since the in-situ calibration obtained with the $Z \to ee$ events is applied also to photons, additional photon-specific systematic uncertainties arise from this extrapolation. In particular, two additional source of mismodeling between MC samples and data are specifically evaluated for photons. The first one is the difference in conversion rate between simulated samples and data, which is originated by an imperfect description in the simulation of the efficiency of the reconstruction of the tracks originated from a photon conversion and the efficiency of matching the tracks to the cluster. Moreover, the conversion rate mismodeling can be also induced by a different description in data and MC of the probability to wrongly associate pileup induced tracks or fake tracks with an EM energy cluster that leads to a fake conversion. If the misclassification rate is different between data and simulated samples, this can create a bias in the energy scale and in the energy resolution, since the MVA calibration is separately trained for unconverted and converted photons. The second systematic uncertainty source is the imperfect modelling of the lateral shower development in the simulation, that induces a wrong lateral leakage description in the MC. If this mismodeling is different for photons and electrons, it can bias the photon energy estimation, because the in-situ energy scale factor can absorb this MC-data difference only for electrons, but not for photons.

In conclusion, the global calibration uncertainty model accounts for 77 independent systematic variations for the energy scale and 9 independent systematic variations for the effective constant term. A simplified model has also been developed, considering all the effects to be fully correlated across η, and summing the effects of all the sources of systematic uncertainty in quadrature to form a single systematic variation. This systematic uncertainty model is usually pessimistic and is used only by analyses not very sensitive to the energy scale uncertainties of electrons and photons. A similar simplification for the uncertainties on the resolution is provided. The total calibration uncertainty for photons with E_{T} around 60 GeV is 0.4% in the barrel and 0.8% in the endcap. In the case of electrons with E_{T} around 40 (10) GeV the total uncertainty is 0.02% (0.5%) in the barrel and 0.1% (0.8%) in the endcap.

Systematic uncertainties in the calorimeter energy resolution arise from uncertainties in the modelling of the sampling term and on the measurement of the constant term in Z boson decays, in the amount of material in front of the calorimeter, which affect electrons and photons differently, and in the modelling of the small contribution to the resolution from fluctuations in the pileup from other proton-proton interactions in the same or neighboring bunch crossings. The uncertainty on the calorimeter energy resolution is typically 10–20% for photons from Higgs boson decays, and varies from 5% to 10% for electrons in the E_{T} range from 10 GeV to 45 GeV.

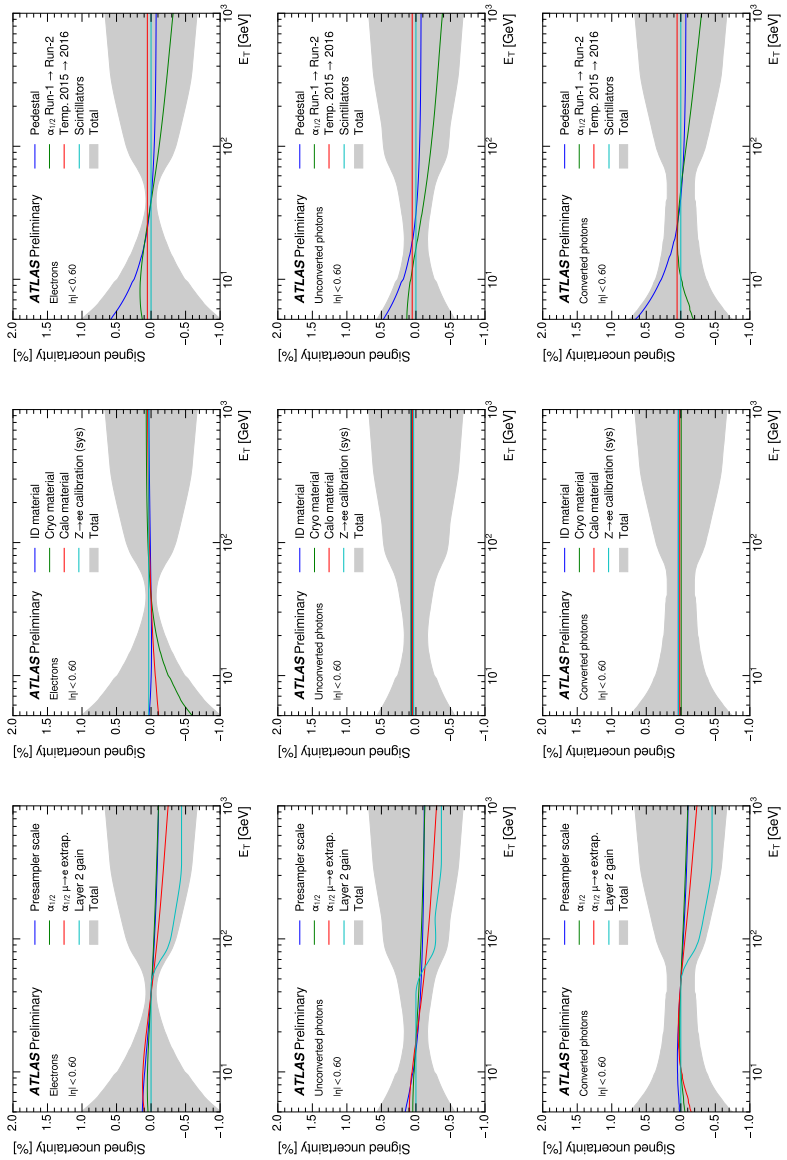

Figure 6.19: Main contributions to the systematic uncertainty on the energy scale after calibration corrections, shown as a function of E_{T} and for $|\eta| < 0.6$, in the case of electrons (top row), unconverted photons (middle row), and converted photons (bottom row). The total uncertainty bands represent the quadratic sum of all systematic uncertainty sources described in the text and represented in the various columns. The last column in particular shows the additional systematic uncertainties introduced from Run 1 to Run 2 and the temperature uncertainty added when comparing 2015 data to 2016 data (28).

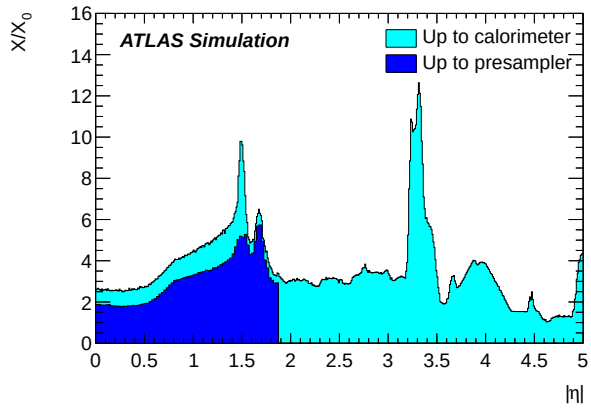

Figure 6.20: Amount of material traversed by a particle (IBL not yet included), X/X_0, as a function of $|\eta|$, in the improved simulation up to the PS and the EM calorimeter (143).

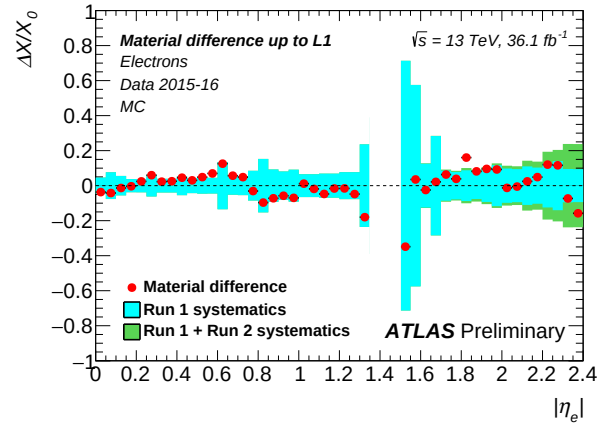

Figure 6.21: Measurement of the difference in material up to the first layer of the EM calorimeter (L1) in data and Monte Carlo. The material difference is estimated from the longitudinal shower profile (E_1/E_2) of electron candidates and is given here in number of radiation lengths X_0. The difference is plotted against systematic uncertainty bands from Run 1 and Run 2. The blue band summarizes the set of correlated and data-driven noncorrelated material uncertainties determined in Run 1 calibration studies. The simulation of the inner detector service material in the gap between the barrel and endcap cryostats ($|\eta| = 1.55$-1.70) has been modified to yield a better agreement with Run 1 data, so the blue band overestimates the expected material difference in this region. The green band includes additional uncertainties that are related to the introduction of new material to the detector for Run 2. In particular, the uncertainties cover potential simulation mismodelling of the IBL tracking detector and a modified inner-detector patch panel (PP0). At high $|\eta|$, these uncertainties are dominated by a 50% uncertainty in the PP0 simulation material (152).

6.6 Energy calibration cross-checks

After applying all the corrections, *i.e.* the energy scale factors in data and the effective constant term of the energy resolution in the simulation, the $Z \to ee$ invariant mass distributions in data and simulation for $80 < m_{ee} < 100$ GeV agree at the level of 1-2%, rising up to 5% toward the borders of the interval, as shown by Figure 6.22 (10).

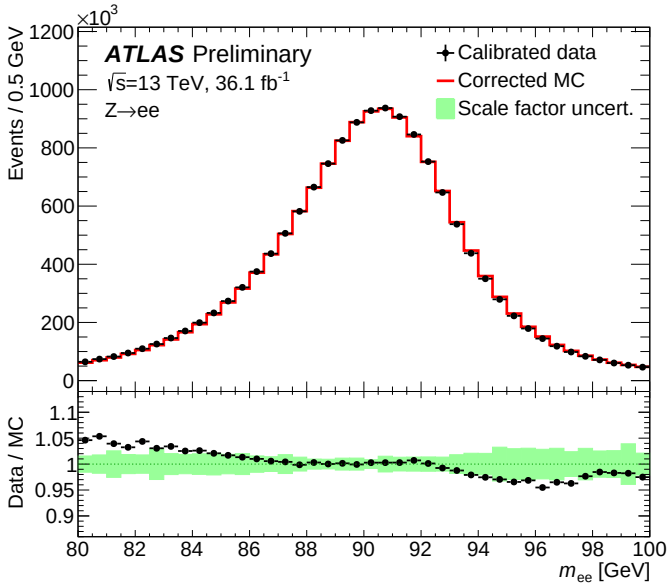

Figure 6.22: Inclusive dielectron invariant mass distribution from $Z \to ee$ decays in data compared to MC after applying the full calibration. No subtraction of the background (expected to be at the level of 0.5% and with a non-peaking m_{ee} distribution) is applied, and the simulation is normalised to data. The lower panel shows the data to simulation ratio, together with the total scale factor uncertainty (10)

The global calorimeter energy scale is verified using $J/\psi \to e^+e^-$ and $Z \to \ell^+\ell^-\gamma$ events.

$J/\psi \to e^+e^-$ events are a good probe to verify the extrapolation of the scale factor to the low E_{T} regime. The energy scale corrections are extracted independently as a function of the electron pseudorapidity through a fit of the invariant mass distribution of the dielectron system, after applying the corrections extracted from the $Z \to ee$ samples. The residual electron response corrections are computed with a precision of 10^{-2}-10^{-3} using the 36 fb^{-1} of pp collision at $\sqrt{s}$ collected in 2015 and 2016, which, due to the highly prescaled $J/\psi \to ee$ triggers, correspond to an effective luminosity of 0.7 fb^{-1} and sixtythousand selected events. The residual corrections are found to be compatible with zero within the uncertainties, as shown in Figure 6.23 (10).

A similar check is performed by computing residual corrections for photons in a sample of radiative Z boson decays, $Z \to \ell\ell\gamma$, in order to verify the assumption that the scale factors extracted for electrons as shown in Sec. 6.4 are valid also for photons. A fit to

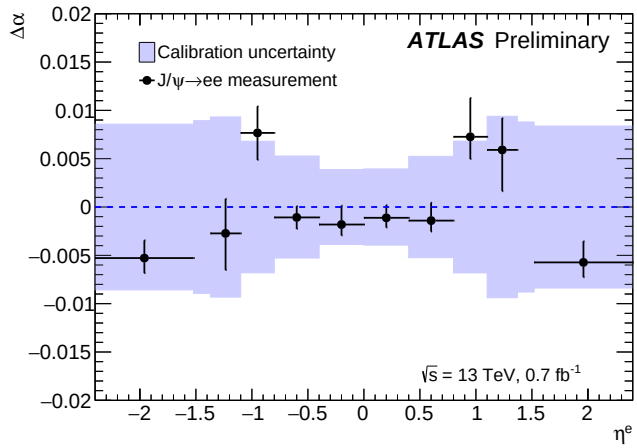

Figure 6.23: Energy calibration scale factors $\Delta\alpha$ obtained from $J/\psi \to e^+e^-$ samples after having applied the Z-based calibration, as a function of the electron pseudorapidity in the reference frame of the calorimeter. The error bars on the data points represent the total uncertainty specific to the $J/\psi \to e^+e^-$ analysis and include both statistical and systematic uncertainties. The band represents the calibration systematic uncertainty extrapolated from $Z \to e^+e^-$ events. The luminosity is the sum of the prescaled luminosities collected by the J/ψ triggers in 2015 and 2016. The corresponding unprescaled luminosity is 36.1 fb^{-1} (10).

the $\ell\ell\gamma$ invariant mass distribution is performed to measure the reconstructed mass peak position. The residual scale factor is quantified, after applying the corrections extracted for electrons, using a double ratio method:

$$R(\alpha_i) = \frac{\langle m(\ell\ell\gamma(\alpha_i))_{\text{data}}\rangle / \langle m(\ell\ell)_{\text{data}}\rangle}{\langle m(\ell\ell\gamma)_{\text{MC}}\rangle / \langle m(\ell\ell)_{\text{MC}}\rangle}, \tag{6.11}$$

where $\langle m(\ell\ell\gamma)\rangle$ and $\langle m(\ell\ell)\rangle$ are the average three body and two body invariant masses of the $Z \to \ell\ell\gamma$ and $Z \to \ell\ell$ candidates. The value of α_i that yields $R(\alpha_i) = 1$ is defined as the residual photon energy scale factor. By normalizing the $m(\ell\ell\gamma)_{\text{data}}/m(\ell\ell\gamma)_{\text{MC}}$ ratio to $m(\ell\ell)_{\text{data}}/m(\ell\ell)_{\text{MC}}$ one, the electron energy scale uncertainty contribution is suppressed in this measurement. The residual corrections for photons are computed using both the 2015 and 2016 data with uncertainties varying between 2% and 4%, and they are found to be compatible with zero, as shown in Figure 6.24 (10).

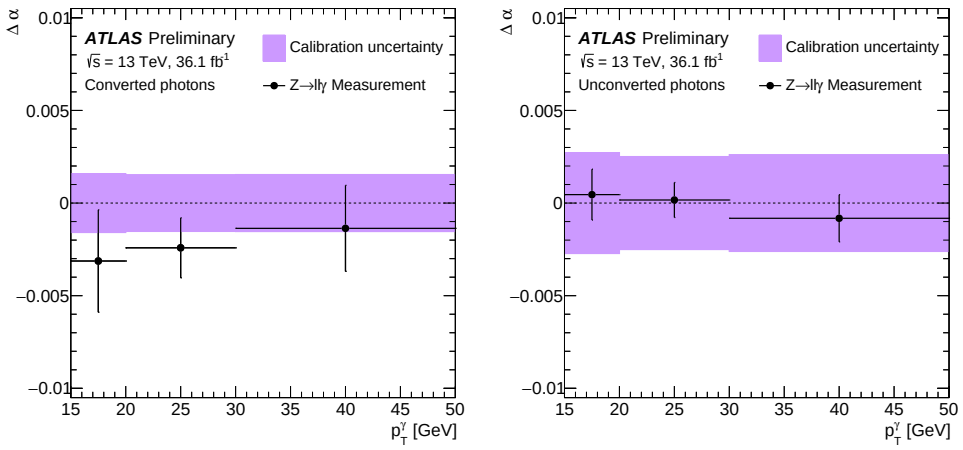

(a) (b)

Figure 6.24: Energy calibration scale factors $\Delta\alpha$ for (a) photons converted to e^+e^- and (b) unconverted photons, computed with a double ratio method using $Z \to ee\gamma$ and $Z \to \mu\mu\gamma$ events, after having applied the Z-based calibration, as a function of the photon transverse momentum. The error bars on the data points represent the total uncertainty specific to the $Z \to \ell\ell\gamma$ measurement and include both statistical and systematic uncertainties. The purple band represents the calibration systematic uncertainty extrapolated from $Z \to e^+e^-$ events (10).

Chapter 7

Photon identification and isolation

Several physics processes in proton-proton collisions result in the production of final states with *prompt photons*, which are photons not originating from the decays of hadrons. The processes with the largest cross sections are the production of photons in association with jets ($qg, q\bar{q} \to \gamma + X$) and the production of photons pairs ($gg, q\bar{q} \to \gamma\gamma$). Prompt photons are also produced in rare events, such as di-photon decays of the Higgs boson or even predicted by BSM models such as the supersymmetry model investigated in Chap. 9.

This chapter describes the strategy used in ATLAS to distinguish prompt photons from *background photons*, which are usually real photons originating from hadron decays. In particular, Sec. 7.1 summarizes the photon identification procedure based on the quantities that are sensitive to the shape of the photon energy deposit in the calorimeter. Sec. 7.2 describes another observable called *isolation*, which quantifies the presence of additional hadrons around a photon candidate and allows improving further the jet-background rejection of the photon selection. Finally, Sec. 7.3 reports the methods used to evaluate the residual background contamination after the identification and isolation selection. In particular, I measured the fraction of electrons wrongly reconstructed and identified as photons, which is an important ingredient for the background estimation in the analysis described in Chap. 9.

7.1 Photon identification

The photon identification algorithm (131) in ATLAS relies on independent requirements applied to calorimetric variables (*shower shapes*) which deliver good separation between prompt photons and background photons from QCD jets. These variables can be grouped in three main categories: hadronic leakage variables, that rely on the information coming from the hadronic calorimeter, variables using the second longitudinal compartment of electromagnetic calorimeter, and variables using the first layer of the EM calorimeter.

- **Hadronic leakage**:
  - $R_{had} = \frac{E_T^{\rm had}}{E_{\rm T}}$ is the ratio of the transverse energy $E_{\rm T}^{\rm had}$ deposited in the cells of the hadronic calorimeter in a window $\Delta\eta \times \Delta\phi = 0.24 \times 0.24$ behind the photon EM calorimeter cluster over the total transverse energy $E_{\rm T}$ of the photon candidate;
  - $R_{had1} = \frac{E_{\rm T}^{\rm had,1}}{E_{\rm T}}$, where $E_{\rm T}^{\rm had,1}$ is the energy deposited only in the first layer of the hadronic calorimeter;
- **EM Second layer**:

- $R_\eta = \frac{E^{S2}_{3\times7}}{E^{S2}_{7\times7}}$ is the ratio between the energy deposited in 3×7 and 7×7 cells in the second layer of the EM calorimeter and centered around the cluster seed;
- $R_\phi = \frac{E^{S2}_{3\times3}}{E^{S2}_{3\times7}}$ is the ratio between the energy deposited in 3×3 and 3×7 cells of the second layer of the EM calorimeter. The distribution of R_ϕ is very different for unconverted and converted photons, since the electron pairs produced in the conversion are bent in different directions in ϕ by the solenoid magnetic field. Converted photons are thus characterized by a wider shower in the ϕ direction than unconverted photons;
- $\omega_{\eta 2}$ describes the lateral width along η of the shower in the second layer of the calorimeter and is defined as $\omega_{\eta 2} = \sqrt{\frac{\sum_i E_i \eta_i^2}{\sum_i E_i} - \left(\frac{\sum_i E_i \eta_i}{\sum_i E_i}\right)^2}$, where E_i is the energy deposited in each cell of the cluster and η_i is the pseudorapidity position of the cell;

- **EM First layer**:

  - $F_{side} = \frac{E(\pm3)-E(\pm1)}{E(\pm1)}$, where $E(\pm n)$ is the energy deposited in the $\pm n$ strips along η around the maximum in the first layer of the EM calorimeter. F_{side} represents the fraction of energy outside the three strips around the maximum but within seven strips;
  - ω_{s3} is the width along η of the shower for three strips around the maximum and is defined as: $\omega_{s3} = \sqrt{\frac{\sum_i xE_i(i-i_{max})^2}{\sum_i E_i}}$, where i is the strip identification number and E_i is the energy deposited in each strip cell;
  - ω_{tot} is evaluated as ω_{s3} but using all the strips of the cluster in a window $\Delta\eta\times\Delta\phi = 0.0625\times0.196$, corresponding to 20×3 cells;
  - $\Delta E = E^{S1}_{2^{nd}max} - E^{S1}_{2^{nd}min}$, is the difference between the energy associated with the second maximum in the strip ($E^{S1}_{2^{nd}max}$) and the minimum reconstructed energy in the strip between the first and the second maxima ($E^{S1}_{2^{nd}min}$);
  - E_{ratio} describes the relative difference of the energies of the largest and second largest energy deposits, evaluated as $E_{ratio} = \frac{E^{S1}_{1^{st}max} - E^{S1}_{2^{nd}max}}{E^{S1}_{1^{st}max} + E^{S1}_{2^{nd}max}}$.

Two selections are defined: a *loose* selection and a *tight* selection. The *loose* selection exploits only the information from the EM calorimeter second layer and from the hadronic calorimeter. This selection is optimized to provide a high photon identification efficiency which varies from 97% for photon with $E_{\mathrm{T}} = 20$ GeV to above 99% for $E_{\mathrm{T}} > 40$ GeV, with a corresponding background rejection factor (*i.e.* the ratio of the number of initial jets to the number of reconstructed background photon which fulfil the identification requests) equal to 1000 (155). The *loose* selection is normally used in several trigger signatures and as preliminary selection in photon analyses to define samples and control regions enriched of background events.

The *tight* selection is based on all the variable at the beginning of this section. The additional EM calorimeter first layer variables provide a good rejection against hadronic jets in which a neutral meson carries most of the jet energy. The fine granularity of the strips layer allows the reconstruction of the two energy separated maxima of the photons

originated from a π^0 decay. The *tight* criteria are optimized separately for converted and unconverted photon candidates, in order to take into account the fact that the electromagnetic deposits for converted photons are wider due to the bending in opposite directions in ϕ of the electron and positron which are originated in the conversion. The *tight* selection provides a photon identification efficiency of 85% for photon with $E_{\mathrm{T}} > 40$ GeV and a corresponding background rejection factor equal to 5000 (155). Table 7.1 summarizes the definition of the identification variables and the shower shapes exploited by each menu.

Table 7.1: Discriminating variables used for *loose* and *tight* photon identification.

Category	Description	Name	*loose*	*tight*
Acceptance	$\|\eta\| < 2.37$, with $1.37 < \|\eta\| < 1.52$ excluded	–	•	•
Hadronic leakage	Ratio of E_{T} in the first sampling layer of the hadronic calorimeter to E_{T} of the EM cluster (used over the range $\|\eta\| < 0.8$ or $\|\eta\| > 1.37$)	R_{had_1}	•	•
	Ratio of E_{T} in the hadronic calorimeter to E_{T} of the EM cluster (used over the range $0.8 < \|\eta\| < 1.37$)	R_{had}	•	•
EM 2^{nd} layer	Ratio of 3×7 to 7×7 $\eta \times \phi$ cell energies	R_η	•	•
	Lateral width of the shower	w_{η_2}	•	•
	Ratio of 3×3 to 3×7 $\eta \times \phi$ cell energies	R_ϕ		•
EM 1^{st} layer	Shower width calculated from three strips around the strip with the maximum energy deposit	$w_{s\,3}$		•
	Total lateral shower width	$w_{s\,\mathrm{tot}}$		•
	Energy outside the core of the three central strips but within seven strips divided by the energy within the three central strips	F_{side}		•
	Difference between the energy associated with the second maximum in the strip layer and the energy reconstructed in the strip with the minimum value found between the first and second maxima	ΔE		•
	Ratio of the energy difference associated with the largest and second largest energy deposits to the sum of these energies	E_{ratio}		•

The selection optimization is performed using Monte Carlo samples and is evaluated independently in seven intervals of photons pseudorapidity (0-0.6, 0.6-0.8, 0.8-1.15, 1.15-1.37, 1.52-1.81, 1.81-2.01, 2.01-2.37) in order to take into account the calorimeter geometry and the material upstream of the calorimeters that affects the shower shapes and is highly dependent on η.

The distributions of the shower shape variables (e.g. R_η, ω_{s3}, F_{side}) in the ATLAS MC simulation do not perfectly agree with the ones observed in data. Indeed, even if the shapes of these distributions in the simulation are in good agreement with the data, a small systematic shift between data and MC has been observed. This issue is not observed for shower shapes sensitive to the longitudinal shower development.

The values of the shower shapes in the Monte Carlo samples are corrected by a constant shift in bins of η and p_{T}, in order to match the distributions in the data. The shifts are calculated minimizing the χ^2 between the data and the shifted MC distributions of photon candidates which have passed the *tight* identification and isolation selection criteria (see Sec 7.2). These corrections are evaluated in several bins of pseudorapidity and transverse momentum. Figure 7.1 shows the comparison between the data and the MC distribution of R_η and ω_{s3} before and after the correction.

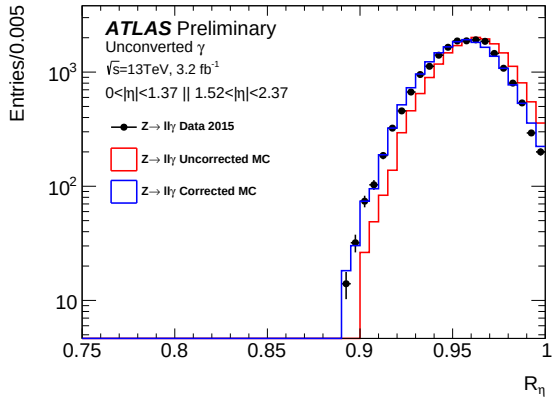

(a) R_η

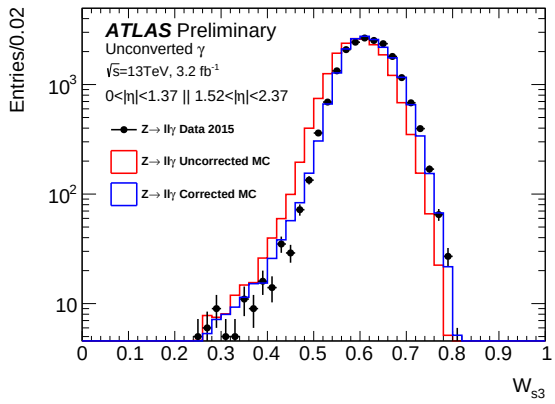

(b) ω_{s3}

Figure 7.1: Two examples of shower-shape variables, R_η (a) and ω_{s3} (b), for unconverted photons: the black points are for the photons from $Z \to \ell^+\ell^-\gamma$ events in data, the red histogram for the photons from $Z \to \ell^+\ell^-\gamma$ events in the simulation before applying the shift, and the blue histogram after applying the shift (156).

The efficiency of the *tight* photon identification criteria (ϵ_{ID}) is measured as the number of isolated photons passing the *tight* identification selection over the total number of isolated photons, exploiting three different techniques:

- a first method relies on a pure sample of photon selected from leptonic radiative decay of the Z boson, $Z \to \ell^+\ell^-\gamma$, $\ell = e, \mu$, and allows a precise measurement of

ϵ_{ID} in the low E_{T} region (10 GeV$\lesssim E_{\mathrm{T}} \lesssim$ 80 GeV);

- a second method, know as "electron extrapolation", uses an electron sample selected from $Z \to e^+e^-$ decays in order to obtain a pure sample of electromagnetic shower shapes from data. The electron shower shape distributions are then corrected for the difference observed in Monte Carlo between photon and electron shower shape distributions. This method covers and intermediate E_{T} region (30 GeV$\lesssim E_{\mathrm{T}} \lesssim$ 100 GeV) due to the kinematic of the Z boson decay;

- a third method uses a matrix method to determine the number of prompt photons in control sample before and after applying the *tight* identification criteria. In order to discriminate between the prompt photons and the background the track isolation (see next section) is used. This method allows coverage of a very large range in E_{T} (20 GeV$\lesssim E_{\mathrm{T}} \lesssim$ 1.5 TeV).

Figures 7.2 and 7.3 show the *tight* photon identification efficiency evaluated with the three different data-driven methods in four $|\eta|$ bins (0-0.6, 0.6-1.37, 1.52-1.81, 1.81-2.37) for unconverted and converted photons respectively.

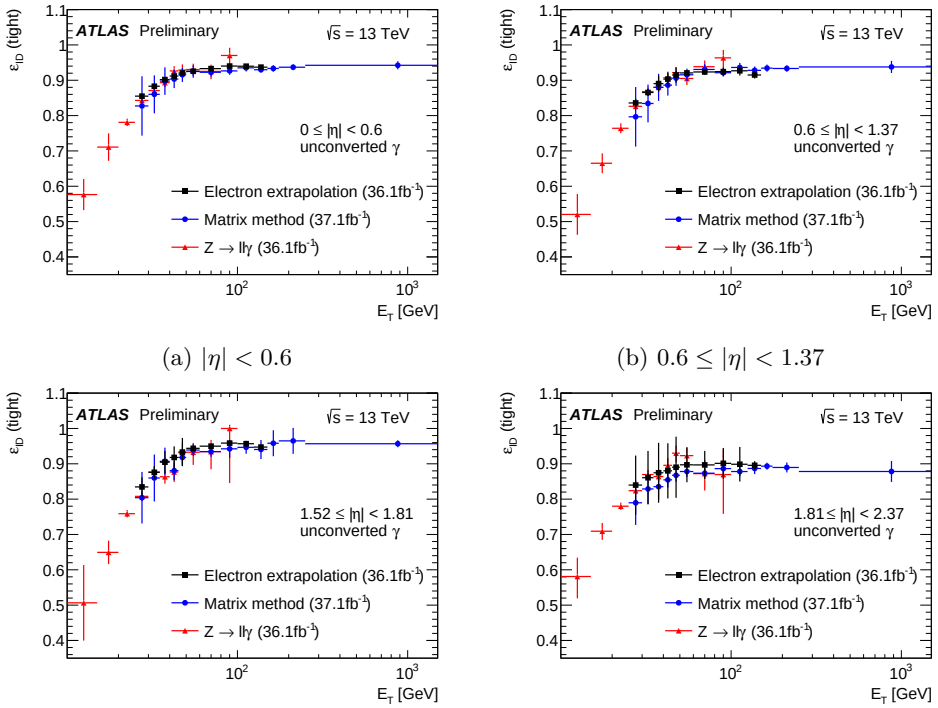

(a) $|\eta| < 0.6$ (b) $0.6 \leq |\eta| < 1.37$

(c) $1.52 \leq |\eta| < 1.81$ (d) $1.81 \leq |\eta| < 2.37$

Figure 7.2: Comparison of the data-driven measurements of the identification efficiency for unconverted photons as a function of E_{T} in the region 20 GeV$< E_{\mathrm{T}} <$ 1500 GeV, for the four pseudorapidity intervals (a) $|\eta| < 0.6$, (b) $0.6 \leq |\eta| < 1.37$, (c) $1.52 \leq |\eta| < 1.81$, and (d) $1.81 \leq |\eta| < 2.37$. The error bars represent the sum in quadrature of the statistical and systematic uncertainties estimated in each method (156).

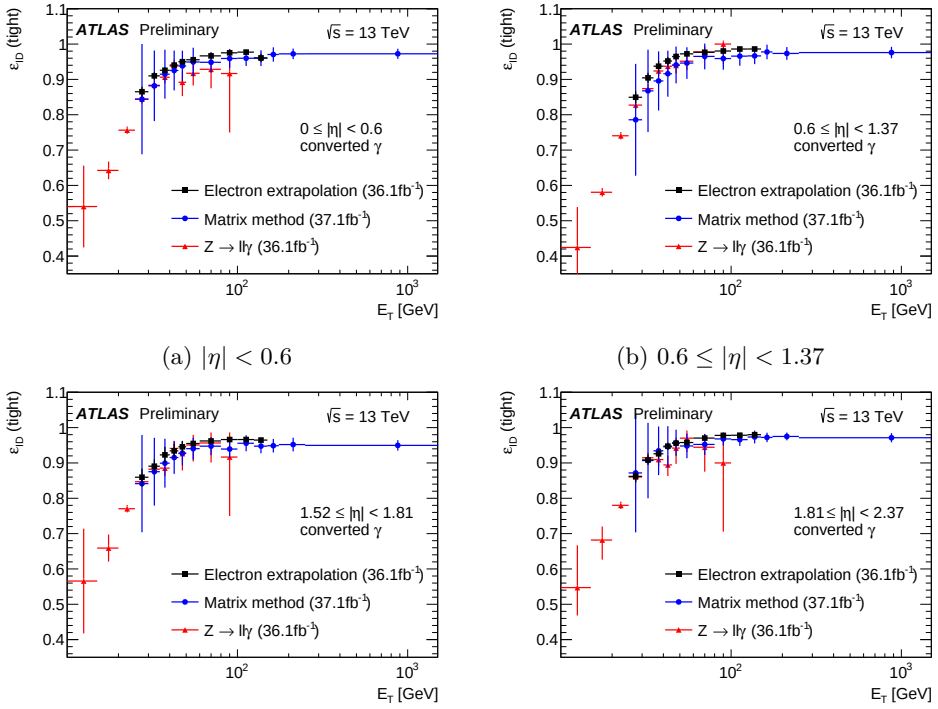

(a) $|\eta| < 0.6$ (b) $0.6 \leq |\eta| < 1.37$

(c) $1.52 \leq |\eta| < 1.81$ (d) $1.81 \leq |\eta| < 2.37$

Figure 7.3: Comparison of the data-driven measurements of the identification efficiency for converted photons as a function of E_{T} in the region 20 GeV$< E_{\mathrm{T}} <$ 1500 GeV, for the four pseudorapidity intervals (a) $|\eta| < 0.6$, (b) $0.6 \leq |\eta| < 1.37$, (c) $1.52 \leq |\eta| < 1.81$, and (d) $1.81 \leq |\eta| < 2.37$. The error bars represent the sum in quadrature of the statistical and systematic uncertainties estimated in each method (156).

7.2 Photon isolation

An experimental isolation requirement, based on the transverse energy deposited in the calorimeter in a cone around the photon candidate, is applied in order to further reduce the main background from high-p_{T} π^0 inside a jet. The transverse isolation energy $E_{\mathrm{T}}^{\mathrm{iso}}$ is evaluated from the energy deposited in both the electromagnetic and hadronic calorimenters in a cone of radius 0.4 (or 0.3, 0.2) in the η-ϕ plane (sec. 7.2.1). Moreover the activity around the photon candidate can also be measured exploiting the tracks reconstructed in the Inner Detector (sec. 7.2.2).

7.2.1 Calorimeter isolation

The calorimetric isolation $E_{\mathrm{T}}^{\mathrm{iso}}$ is defined as the scalar sum of the energy in all calorimeter cells (EM and HAD) within a cone of some radius (typically $\Delta R = 0.4$) around the photon (or electron). This quantity is computed from three-dimensional topological clusters of calorimeter cells (see Sec 5.1.4) whose barycenter is inside the isolation cone. A rectangular core of cells (5×7 in $\eta \times \phi$) around the photon barycenter is excluded from the sum, in order not to include the photon energy. Given that the Molière radius (sec. 4.3.1) of the ATLAS EM calorimeter is $R_M = 4.8$ cm, that corresponds to 1.3 cells in the EM barrel, 5×7 cells should contain more than 95% of the photon energy. For high E_{T} photons the residual lateral energy leakage outside the 5×7 cell window dominates the profile of the isolation. A correction is applied to take into account the fraction of the photon $E_{\mathrm{T}}^{\mathrm{iso}}$ (typically 2-5% depending on η), which leaks out the 5×7 cell window. After this correction $E_{\mathrm{T}}^{\mathrm{iso}}$ is nominally independent of the photon transverse energy.

Moreover, $E_{\mathrm{T}}^{\mathrm{iso}}$ is corrected to remove the pileup and underlying event contribution. The correction procedure evaluates the ambient transverse energy density on an event-by-event basis, where the ambient energy density is given by the median of the transverse jet energies divided by the jet area. In particular, jets are reconstructed with the *anti-k_T* algorithm (135) with a radius parameter of 0.5, without any p_{T} threshold. An area is associated to each jet via a Voronoi tessellation of the η-ϕ space. The transverse energy density for each jet is evaluated as the ratio between the transverse momentum of the jet and the corresponding area. Finally the correction to $E_{\mathrm{T}}^{\mathrm{iso}}$ is evaluated multiplying the median jet transverse energy for the area of the isolation cone.

7.2.2 Track isolation

The track isolation $p_{\mathrm{T}}^{\mathrm{iso}}$ is computed by summing the transverse momenta of all the tracks with $p_{\mathrm{T}} > 1$ GeV reconstructed in the ID inside a cone of certain radius ($\Delta R = 0.2,\ 0.3,\ 0.4$) centered around the photon direction. Tracks are required to be compatible with originating from the primary vertex of the main interaction, in order to minimize the pile-up contribution. In order to subtract the contribution of the candidate photon and of secondary electrons from photon conversion, the tracks associated to the photon and also all the tracks that extrapolated to the L2 fall into a window 0.05×0.1 in $\Delta\eta \times \Delta\phi$ around the photon cluster position are subtracted from $p_{\mathrm{T}}^{\mathrm{iso}}$.

7.3 The electron-to-photon fake rate

After the application of the identification and isolation requirement a small fraction of non prompt photon still contaminates the final sample of signal photos. These background

photon candidates are mainly jets that are mis-identified as photons, but there is also a small contribution from electrons that are reconstructed as photons. Background photon candidates from electrons are particularly relevant for the analysis illustrated in Chap. 9 but also for search of di-photon resonances with masses close to that of the Z boson.

Prompt electrons and photons leave a very similar signature in the detector, with a large, narrow energy deposit in the electromagnetic calorimeter and small leakage in the hadronic calorimeter behind it. Electrons are characterized by tracks from the primary vertex pointing to an electromagnetic calorimeter cluster; the same, however, can occur for photons converting early in the detector. Although photon and electron reconstruction algorithms are designed to reduce the mis-identification of electrons as photons, a residual small fraction of electrons can still be reconstructed as photons and pass the photon identification requirements. Since the reconstruction efficiency of the electromagnetic cluster is almost equal to 100%, the fraction of electrons wrongly reconstructed (and identified) as photons is mainly due to tracking inefficiency or bad matching of the track with the energy cluster reconstructed in the calorimeter. The next paragraphs show how the probability that an electron is reconstructed as a photon, the so called *electron-to-photon fake rate*, is measured.

The most intuitive definition of the electron to photon fake rate is:

$$\rho = \frac{N(e^{\text{truth}} \to \gamma^{\text{reco}})}{N_e^{truth}}, \tag{7.1}$$

where $N(e^{\text{truth}} \to \gamma^{\text{reco}})$ is the number of reconstructed photons originating from N_e^{truth} true electrons.

In data what can be measured is the number of reconstructed and identified photons in a pure sample of reconstructed electrons. The electron-to-photon fake rate probability can be defined as:

$$F_{e\to\gamma} \equiv \frac{\epsilon(e^{\text{truth}} \to \gamma^{\text{reco}})\epsilon_\gamma}{\epsilon(e^{\text{truth}} \to e^{\text{reco}})\epsilon_e} = \frac{(N(e^{\text{truth}} \to \gamma^{\text{reco}})/N_e^{\text{truth}})\epsilon_\gamma}{(N(e^{\text{truth}} \to e^{\text{reco}})/N_e^{\text{truth}})\epsilon_e} \overset{(7.1)}{=} \frac{\rho}{1-\rho}\frac{\epsilon_\gamma}{\epsilon_e}, \tag{7.2}$$

which corresponds to the ratio between the probability to (wrongly) reconstruct and identify an electron as a photon over the probability to (correctly) reconstruct an electron.

Using the data the truth information is not directly accessible, so the fake rate is defined as the ratio between the probability to (wrongly) reconstruct and identify an electron as a photon over the probability to (correctly) reconstruct an electron as such, *i.e.* we measure the following quantity:

$$F_{e\to\gamma} \equiv \frac{N(e^{\text{truth}} \to \gamma^{\text{reco}})\epsilon_\gamma}{N(e^{\text{truth}} \to e^{\text{reco}})\epsilon_e}, \tag{7.3}$$

where ϵ_γ and ϵ_e are respectively the identification efficiency for the photon and the electron-[1]

Analyses with photons in the final state can thus estimate the background from prompt electrons faking photons in their signal region by selecting a control region enriched in electrons (by replacing in their selection the photon reconstruction and identification criteria with the electron ones), estimating the yield of the prompt electron background there, and scaling it by $F_{e\to\gamma}$ factor.

[1]Given the equivalence in the Equation (7.3) in the plots the fake rate is labeled as $P(\gamma_{reco,id}|e_{reco,id})$.

The fake rate $F_{e\to\gamma}$ is determined from the number of di-electron candidates from $Z \to ee$ decays that are either reconstructed as ee or $e\gamma$. Such yields are estimated from the ee and $e\gamma$ invariant mass spectra observed in the data, looking in those spectra for a peak near the Z boson mass and subtracting the yields of background candidates obtained from the side-bands.

The study is performed using the data collected in pp collision at $\sqrt{s} = 13$ TeV during 2015 and 2016.

The events are required to contain at least two opposite-sign electrons or an electron and a photon with a $p_{\mathrm{T}} > 25$ GeV and a pseudorapidity $|\eta| < 2.37$, excluding the barrel-endcap transition region of the LAr calorimeter ($1.37 < |\eta| < 1.52$). Both photons and electrons are required to be isolated and to pass the *tight* identification criteria. If multiple ee and/or e/γ pairs in the same event pass the previous requirements, only the pair with the invariant mass closest to the Z boson mass (91.18 GeV (34)) is kept. Finally, only the events with invariant mass, m_{ee} or $m_{e\gamma}$, inside a small range ([86 GeV, 96 GeV]) around the Z boson mass peak are selected. The results in the next pages are shown for two different strategies used in ATLAS to deal with "overlaps" between electron and photon candidates, *i.e.* when both an electron and a photon are selected within a cone of radius $\Delta R = 0.4$: an overlap-removal procedure that discards the photon and keeps the electron ("OR retaining e" in the following figures), and an overlap-removal procedure that keeps the photon and discards the electron ("OR retaining γ" in the following figures).

7.3.1 Fake rate estimation

The fake rate is measured here as a function of the transverse momentum and absolute value of the pseudorapidity of the electron and photon candidates. It is obtained from the ratio

$$F_{e\to\gamma}(\eta, p_{\mathrm{T}}) = \frac{H_{e\gamma}(\eta^{\gamma}, p_{\mathrm{T}}^{\gamma})}{H_{ee}(\eta^{e}, p_{\mathrm{T}}^{e})} \tag{7.4}$$

of two bi-dimensional histograms that are filled in the following way. For events in which an ee ($e\gamma$) pair has been selected, the histogram H_{ee} ($H_{e\gamma}$) is filled twice (once), with the transverse momentum and pseudorapidity of both electron candidates (the photon candidate). A graphical illustration of the procedure used to fill the two histograms is given in Figure 7.4. The Equation 7.4 and the way that the histogram are filled can be more easily understood considering an inclusive case where no binning in η and p_{T} is applied. Given the probability ρ defined in the Equation 7.1, and the photon (electron) identification efficiencies ϵ_{γ} (ϵ_{e}), the probability to have a certain number of selected events for each final state (ee, $e\gamma$, $\gamma\gamma$) is described by the equations:

$$N_{ee} = \epsilon_e^2(1-\rho)^2 N_Z, \tag{7.5}$$

$$N_{e\gamma} = 2\epsilon_e\epsilon_\gamma\rho(1-\rho)N_Z, \tag{7.6}$$

$$N_{\gamma\gamma} = \epsilon_\gamma^2\rho^2 N_Z, \tag{7.7}$$

where N_Z is the number of true $Z \to ee$ events and N_{ee}, $N_{e\gamma}$, $N_{\gamma\gamma}$ are the number of reconstructed events for each possible final state. For the $e\gamma$ final state the factor 2 accounts for the cases when either the leading or the sub-leading electron is reconstructed as a photon.

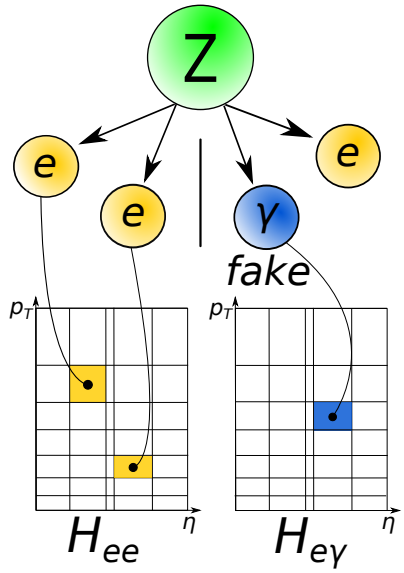

Figure 7.4: Graphical illustration of the procedure used to fill the histograms for the determination of the electron-to-photon fake rate (157).

Thus the Equation (7.3) can be expressed as:

$$F_{e\to\gamma} = \frac{N(e^{\text{truth}} \to \gamma^{\text{reco}})\epsilon_\gamma}{N(e^{\text{truth}} \to e^{\text{reco}})\epsilon_e} = \frac{N_{e\gamma} + 2N_{\gamma\gamma}}{2N_{ee} + N_{e\gamma}}, \tag{7.8}$$

which is equal to:

$$\frac{N_{e\gamma} + 2N_{\gamma\gamma}}{2N_{ee} + N_{e\gamma}} = \frac{2\epsilon_e\epsilon_\gamma\rho(1-\rho)N_Z + \epsilon_\gamma^2\rho^2 N_Z}{2\epsilon_e^2(1-\rho)^2 N_Z + 2\epsilon_e\epsilon_\gamma\rho(1-\rho)N_Z} \tag{7.9}$$

$$= \frac{\epsilon_e\epsilon_\gamma\rho(1-\rho) + \epsilon_\gamma^2\rho^2}{\epsilon_e^2(1-\rho)^2 + \epsilon_e\epsilon_\gamma\rho(1-\rho)} \tag{7.10}$$

$$= \frac{\epsilon_\gamma\rho\epsilon_e(1-\rho) + \epsilon_\gamma\rho]}{\epsilon_e(1-\rho)[\epsilon_e(1-\rho) + \epsilon_\gamma\rho]} \tag{7.11}$$

$$= \frac{\rho}{1-\rho}\frac{\epsilon_\gamma}{\epsilon_e}. \tag{7.12}$$

The same value can be obtained also from:

$$\frac{N_{e\gamma}}{2N_{ee}} = \frac{2\epsilon_e\epsilon_\gamma\rho(1-\rho)N_Z}{2\epsilon_e^2(1-\rho)^2 N_Z} = \frac{\rho}{1-\rho}\frac{\epsilon_\gamma}{\epsilon_e} \equiv F_{e\to\gamma}. \tag{7.13}$$

This is the same as Eq. (7.4) if $H_{e\gamma}$ is filled once for each $Z \to e\gamma^{\text{fake}}$ event and H_{ee} is filled twice for each ee pair selected. This is exactly what is done in the study: the $H_{e\gamma}(\eta^\gamma, p_{\text{T}}^\gamma)$ is filled once using only the transverse momentum and pseudorapidity of the photon, and $H_{ee}(\eta^e, p_{\text{T}}^e)$ is filled twice using the kinematic variables of both electrons.

Finally, it is possible to consider the complete model that is exploited in the measurement using the binned histograms. Given equation (7.1), let ρ_i be the true electron-to-photon misidentification rate, for an electron or photon whose true values of p_{T} and η lie in bin i of the p_{T}–η grid. Then, consider a sample of N Z bosons events with a true electron and positron both within the fiducial region in p_{T} and η. Let f_{ij} be the fraction of Z boson events for which the leading (sub-leading) electron falls into the i^{th} (j^{th}) bin of the grid. Then, assuming no background contribution, the number of entries N_i^e in the i^{th} bin of the electron-positron grid is (including contributions both from the leading and sub-leading electrons)

$$N_i^e = \sum_j \epsilon_i^e(1-\rho_i)\epsilon_j^e(1-\rho_j)f_{ij}N + \sum_j \epsilon_j^e(1-\rho_j)\epsilon_i^e(1-\rho_i)f_{ji}N \tag{7.14}$$

$$= \epsilon_i^e(1-\rho_i)N\sum_j((1-\rho_j)\epsilon_j^e f_{ij} + \epsilon_j^e(1-\rho_j)f_{ji})\,. \tag{7.15}$$

Similarly, the number of entries N_i^γ in the i^{th} bin of the electron-photon grid is

$$N_i^\gamma = \sum_j \rho_i\epsilon_i^\gamma(1-\rho_j)\epsilon_j^e f_{ij}N + \sum_j \epsilon_j^e(1-\rho_j)\epsilon_i^\gamma p_i f_{ji}N = \rho_i\epsilon_i^\gamma N\sum_j((1-\rho_j)\epsilon_j^e f_{ij} + \epsilon_j^e(1-\rho_j)f_{ji})\,. \tag{7.16}$$

From the measurement of N_i^e and N_i^γ the electron-to-photon fake factor, $F_{e\to\gamma}$, in bins of p_{T} and η can be determined as

$$F_{e\to\gamma}(\rho_{\mathrm{T}},\eta) \equiv \frac{N_i^\gamma}{N_i^e} = \frac{\rho_i\epsilon_i^\gamma}{(1-\rho_i)\epsilon_i^e}\ . \tag{7.17}$$

The measurement is performed using a p_{T}–η grid of $63 = 7\times 9$ $\eta - p_{\mathrm{T}}$ bins:

- 7 bins in $|\eta|$: 0.0-0.6, 0.6-0.8, 0.8-1.15, 1.15-1.37, 1.52-1.81, 1.81-2.01, 2.01-2.37 (the bin from 1.37 to 1.52 is excluded);
- 9 bins in p_{T}: 25-35, 35-45, 45-55, 55-65, 65-75, 75-90, 90-120, 120-180, 180-300 GeV.

A measurement of the fake rate as a function of η averaged over p_{T}, using 48 bins of 0.1 width for $\eta \in (-2.4, 2.4)$, is also reported.

Finally, the method has been validated using a $Z \to ee$ simulation sample. The fake rate measured on the MC has been compared to the ratio defined by the number of true electrons decaying from the Z boson and reconstructed and identified as photons and the number of true electrons correctly reconstructed as electrons. The two values are in a good agreement, with a relative difference $\lesssim 2\%$, smaller than the other uncertainties from the measurement. Figure 7.5 shows the validation test for the fake rate measured as a function of η considering the algorithm favoring photons over electrons.

7.3.2 Background contribution estimation

The previous equations are corrected to account for the background in the selected ee and $e\gamma$ samples. This correction is needed if the signal (S) over background (B) ratios in the ee and the $e\gamma$ samples are different. Indeed, considering an identical S/B value for the two samples, the background contamination does not affect the measurement:

$$F_{e\to\gamma} = \frac{N_{e\gamma}}{2N_{ee}} = \frac{S_{e\gamma}+B_{e\gamma}}{2(S_{ee}+B_{ee})} = \frac{S_{e\gamma}+S_{e\gamma}(\frac{1}{S/B})}{2(S_{ee}+S_{ee}(\frac{1}{S/B}))} = \frac{S_{e\gamma}}{2S_{ee}}\frac{(1+\frac{1}{S/B})}{(1+\frac{1}{S/B})} = \frac{S_{e\gamma}}{2S_{ee}}. \tag{7.18}$$

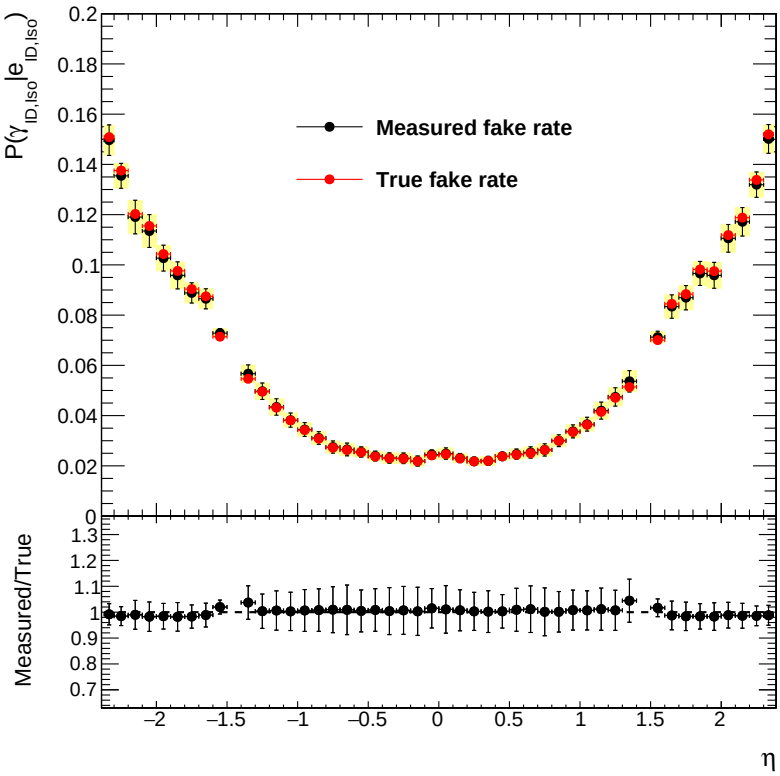

Figure 7.5: Closure test vs η. The fake rate is measured on a $Z \to ee$ MC sample using the overlap algorithm favoring photons over electron. The "MC truth" fake rate (i.e. the ratio between the number of true electrons decaying from the Z boson and reconstructed and identified as photons and the number of true electrons correctly reconstructed as electrons) is plotted with red circle, while the fake rate measured with the electron-to-photon algorithm is plotted with black circles. The solid line shows the total uncertainties, while the yellow and orange boxes shows respectively the systematic and the statistical errors.

A weight, determined as a function of the ee or $e\gamma$ invariant mass, and of the pseudorapidity and the relative transverse momentum of the two particles, is assigned for each event. It is computed as the "signal fraction" $\frac{S}{S+B}$ (S=signal, B=background) from an $S+B$ fit to the unweighted m_{ee} and $m_{e\gamma}$ distributions in data. The signal show up as a narrow peak over a broad non-resonant background. The signal invariant mass (m) distribution is modeled by a symmetric double-sided Crystal Ball function $N_S f_S(m)$ whose shape (μ, σ, α) and normalization (N_S) parameters are floating in the fit. The background invariant mass distribution is described by an analytic function (exponential or Bernstein polynomial) $N_B f_B(m)$ whose shape ($\{a_i\}$) and normalization (N_B) parameters are floating in the fit.

The ideal approach would be to have such a fit for each possible combination of the $|\eta|$ and p_{T} bins used in the measurement, but the available statistics in some bins is not sufficient to get reliable results. So a coarser set of bins is used. Moreover, it is not possible to use the transverse momentum as a binning variable because the kinematics of $Z \to ee$ decays would lead to very few events in bins where both particles have low-p_{T} or both particles have high-p_{T}. Instead of p_{T} ,the relative transverse momentum of each particle with respect to the invariant mass of the two-particle system is used to define the binning. The $p_{\mathrm{T}}/m_{ee,e\gamma}$ binning obviously does not define exclusive regions in p_{T}, but at least, since it shifts the mean of the p_{T} distribution of the considered sub-sample of events, it can account for an indirect dependency on p_{T}.

The fits are performed for all the combinations of intervals of the absolute value of the electron and photon pseudorapidities and relative transverse momentum ($p_{\mathrm{T}}/m_{ee,e\gamma}$) using the following bins:

- $|\eta| : \{0 - 1.37, 1.52 - 2.37\}$;
- $p_{\mathrm{T}}/m_{ee,e\gamma} : \{0 - 0.5, 0.5 - inf\}$.

We thus have 9 weighting functions for ee events (because we use unordered combinations) and 16 for the $e\gamma$ events, that are used to fill the $H_{e\gamma}$ and H_{ee} histograms based on the pseudorapidities and the transverse momenta of the two selected objects in data.

The weight is then calculated as follows:

$$w(m, \eta_1, \eta_2, \frac{p_{\mathrm{T}}^1}{m_{12}}, \frac{p_{\mathrm{T}}^2}{m_{12}}) = \frac{N_S f_S(m, \eta_1, \eta_2, \frac{p_{\mathrm{T}}^1}{m_{12}}, \frac{p_{\mathrm{T}}^2}{m_{12}})}{N_S f_S(m, \eta_1, \eta_2, \frac{p_{\mathrm{T}}^1}{m_{12}}, \frac{p_{\mathrm{T}}^2}{m_{12}}) + N_B f_B(m, \eta_1, \eta_2, \frac{p_{\mathrm{T}}^1}{m_{12}}, \frac{p_{\mathrm{T}}^2}{m_{12}})}. \tag{7.19}$$

Examples of such fits to the inclusive di-electron and electron-photon samples with their relative correction weight are shown in Figure 7.6.

7.3.3 Systematic uncertainties

Three main sources of systematic uncertainties have been evaluated. They are related to the width of the invariant mass region used in the selection, the background evaluation and the procedure used in the selection of the best ee or $e\gamma$ couple in the event. These systematic uncertainties on the measured fake rates have been estimated in the following way:

- varying the invariant mass range used to select the di-electron and electron-photon pairs. The nominal size ([86–96] GeV) has been changed to [88.5–93.5] GeV and to

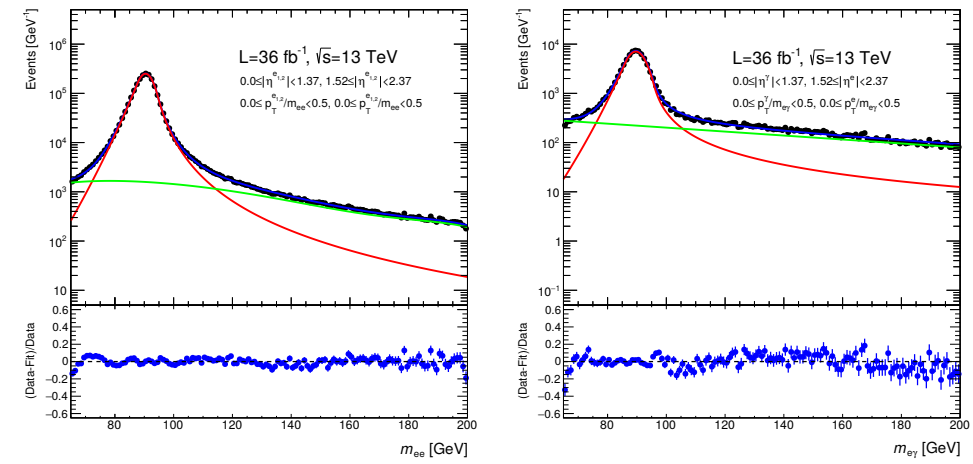

(a)

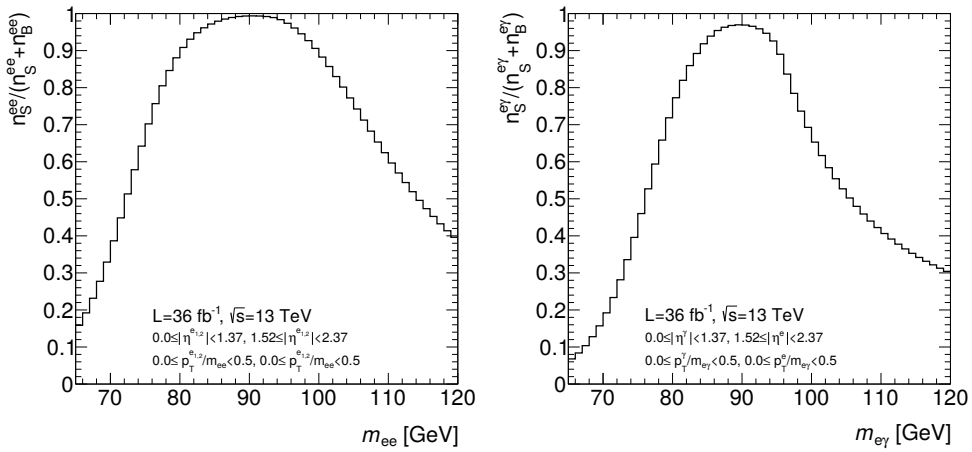

(b)

Figure 7.6: (a) Signal plus background model fits to the invariant mass distributions of the ee and $e\gamma$ pairs selected sample. The signal and background are shown by the red and green solid line respectively, while the blue line shows the global model fit. (b) Distributions of the correction weights that account for the signal fraction in the ee and $e\gamma$ selected sample.

[83.5–98.5] GeV, leading to selected samples that are more or less pure in events originating from Z boson decays. The whole measurement procedure is repeated using both the larger and the smaller mass window values and the variations of the fake rates with respect to the nominal have been considered as systematic uncertainties on those values. The impact of this systematic uncertainty is $\sim 7\%$.

- Varying the $S/(S+B)$ weight, which is usually close to 1. The weighting procedure has either been disabled, effectively doing no background subtraction and giving $S^{e\gamma}/B^{e\gamma} = S^{ee}/B^{ee}$, or it has been modified using weights with a larger difference

between the ee and the $e\gamma$ case: the measured difference between $w^{ee}(m, \eta, p_{\mathrm{T}}/m_{ee})$ and $w^{e\gamma}(m, \eta, p_{\mathrm{T}}/m_{e\gamma})$ is artificially increased by 100%, so that $S^{e\gamma}/B^{e\gamma} < S^{ee}/B^{ee}$. The impact of this systematic uncertainty is less than 3%. Again, the variations in the measured fake rate obtained with the alternative weights with respect to the nominal one have been considered as systematic uncertainties on those values.

- Selecting the ee or $e\gamma$ pair composed by the two leading electrons or photons of the event instead of the couple with the invariant mass closer to the Z boson mass pole, and repeating the whole measurement. This uncertainty has a negligible impact on the measurement.

7.3.4 Results

The global fake rate (*i.e.* averaged on η and p_{T}, with $p_{\mathrm{T}} > 25$ GeV) is:

- 0.049 ± 0.004 for the overlap algorithm favoring photons;
- 0.038 ± 0.003 for the overlap algorithm favoring electron;

The fake rate as a function of both η and p_{T} is shown in Figures 7.7 and 7.8. The fake rate is smaller (typically a few %) in the central η bins and increases in the forward ones, up to 10–20% in the most extreme cases. The fake rate is obviously larger for the overlap algorithm favoring photons over electrons. As a function of p_{T} the fake rate decreases for the overlap algorithm giving precedence to electrons; for the other one it first decreases and then start to increase for p_{T} above approximately 50 GeV. Such trends are a result of the combined p_{T} dependence of the efficiency of the electron identification and isolation requirements (increasing with p_{T}) and of the probability to misidentify an electron as a photon.

The fake rate averaged over p_{T} is shown as a function of η in Figure 7.9. For the overlap algorithm favoring electrons (photons) over photons (electrons), the fake rate is 2–5% (3–6%) in the barrel and 5–14% (6–18%) in the endcap. The absolute uncertainty, dominated by the systematic component, is typically around 0.5%. The numerical results measured from the events selected using the overlap algorithm favoring photons over electrons are given in Tables 7.2-7.8.

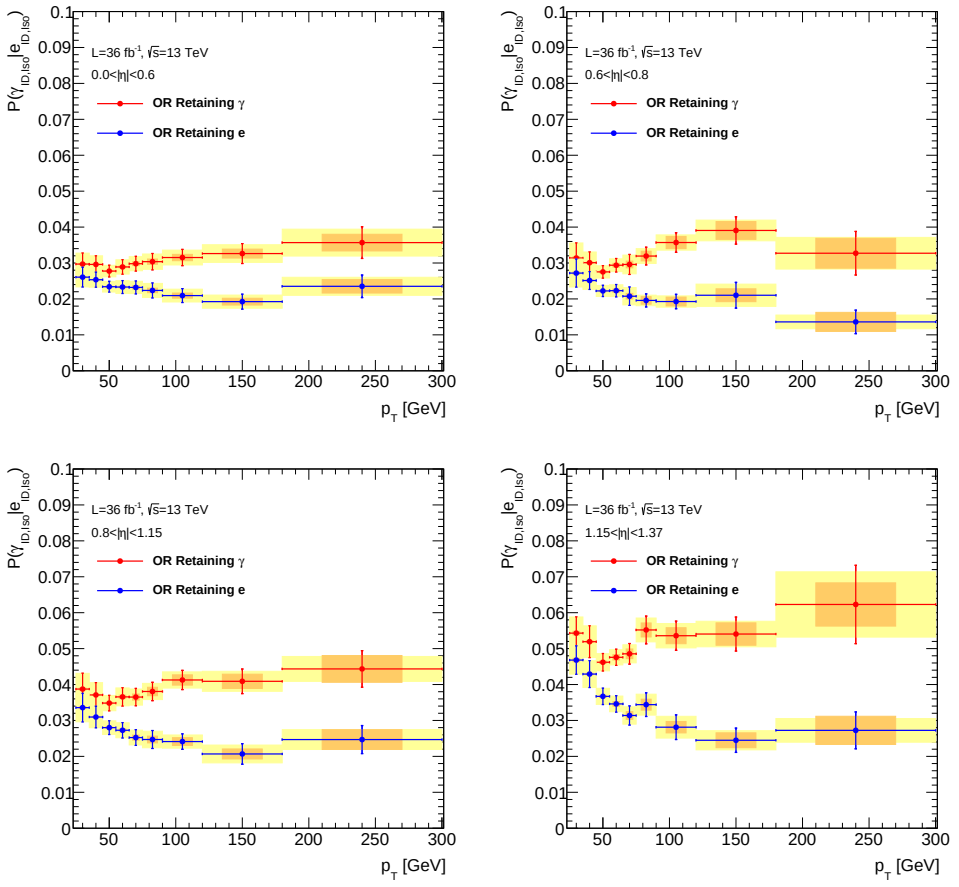

Figure 7.7: Fake rate as a function of p_{T} for electrons in the $|\eta|$ bins: 0.0-0.6, 0.6-0.8, 0.8-1.15, 1.15-1.37. Dots with error bars correspond to the results with their total uncertainties. Yellow bars correspond to the systematic uncertainties, while orange boxes corresponds to the statistical error.

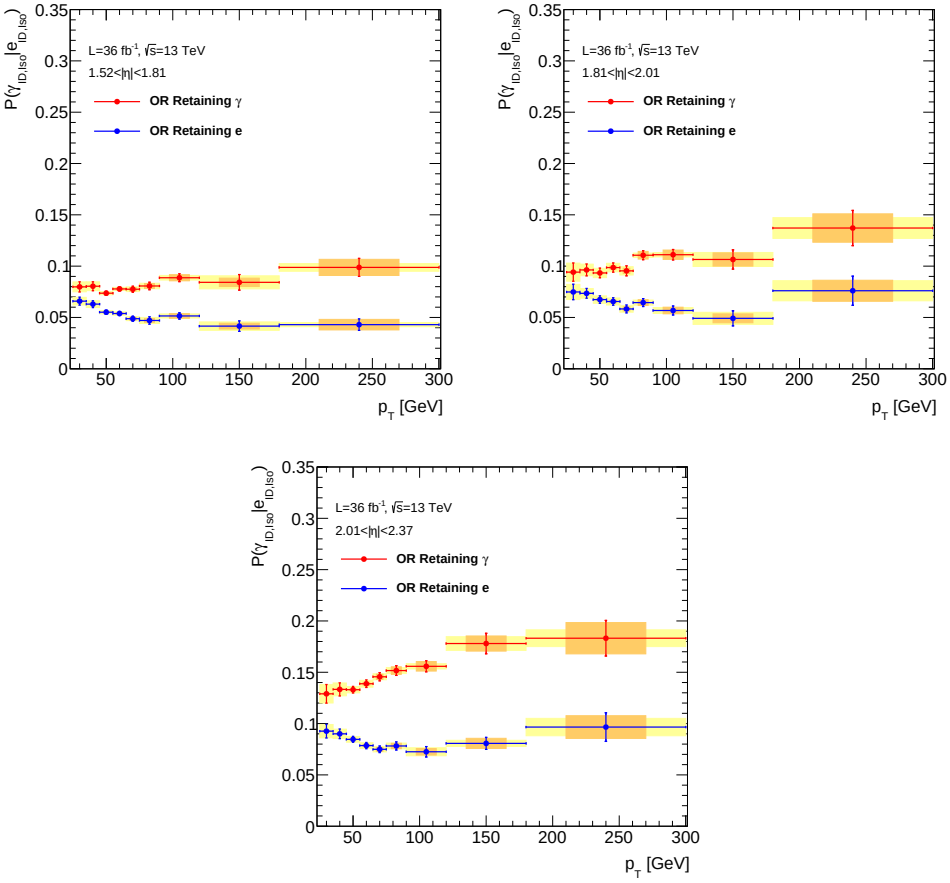

Figure 7.8: Fake rate as a function of p_{T} for electrons in the $|\eta|$ bins: 1.52-1.81, 1.81-2.01, 2.01-2.37. Dots with error bars correspond to the results with their total uncertainties. Yellow bars correspond to the systematic uncertainties, while orange boxes corresponds to the statistical error.

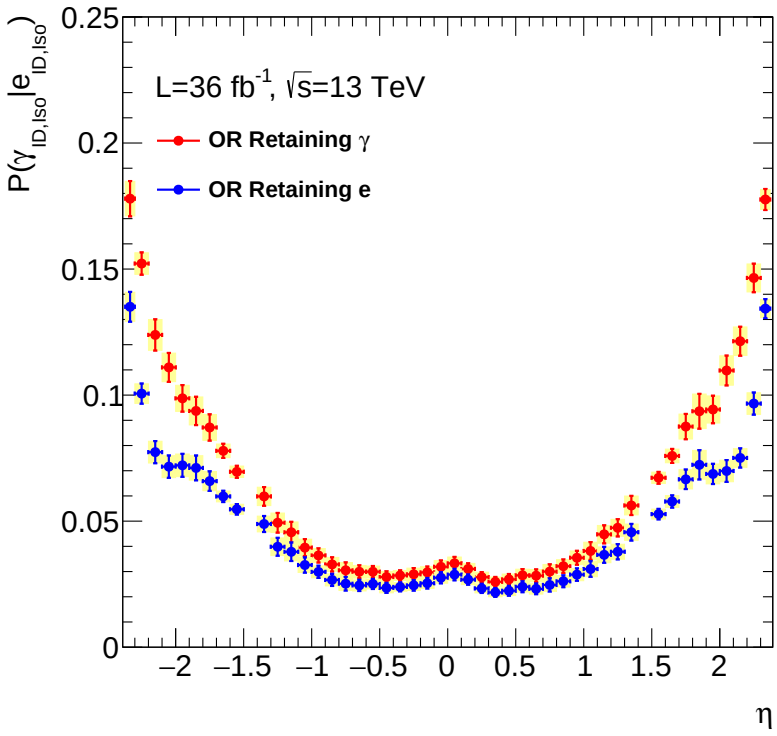

Figure 7.9: Fake rate vs η (averaged over p_{T}). Dots with error bars correspond to the results with their total uncertainties. Yellow bars correspond to the systematic uncertainties, while orange boxes corresponds to the statistical error.

Table 7.2: Fake rates for $p_{\mathrm{T}} \in [25\ \mathrm{GeV}, 300\ \mathrm{GeV}]$ and $0.0 \leq |\eta| < 0.6$, evaluated from the events selected using the overlap algorithm favoring photons. The table reports the central value, the statistical, the systematic and the total uncertainty. For the systematic error also the contribution from the different sources is listed: the uncertainty due to the variation of the invariant mass selection range (*Window*), the variation of the signal ratio weighting procedure (*Weighting*), and the different considered procedure of selection (*Selection*).

$0.0 \leq \lvert\eta\rvert < 0.6$							
p_{T} [GeV]	$F_{e\to\gamma}$	Stat.	Syst.				Total Unc.
			Window	Weighting	Selection	Total	
(25, 35)	0.0298	0.0002	0.0029	0.0012	0	0.0031	0.0031
(35, 45)	0.0297	0.0001	0.0023	0.001	0	0.0025	0.0025
(45, 55)	0.0277	0.0001	0.0013	0.0012	0	0.0018	0.0018
(55, 65)	0.0289	0.0003	0.0016	0.0014	0	0.0022	0.0022
(65, 75)	0.0298	0.0005	0.0014	0.0017	0	0.0022	0.0023
(75, 90)	0.0303	0.0007	0.0014	0.002	0	0.0024	0.0025
(90, 120)	0.0315	0.0009	0.001	0.0022	0	0.0024	0.0026
(120, 180)	0.0326	0.0012	0.0014	0.0025	0	0.0028	0.0031
(180, 300)	0.0356	0.0023	0.0029	0.0028	0	0.004	0.0046

Table 7.3: Fake rates for $p_{\mathrm{T}} \in [25\ \mathrm{GeV}, 300\ \mathrm{GeV}]$ and $0.6 \leq |\eta| < 0.8$, evaluated from the events selected using the overlap algorithm favoring photons. The table reports the central value, the statistical, the systematic and the total uncertainty. For the systematic error also the contribution from the different sources is listed: the uncertainty due to the variation of the invariant mass selection range (*Window*), the variation of the signal ratio weighting procedure (*Weighting*), and the different considered procedure of selection (*Selection*).

$0.6 \leq \lvert\eta\rvert < 0.8$							
p_{T} [GeV]	$F_{e\to\gamma}$	Stat.	Syst.				Total Unc.
			Window	Weighting	Selection	Total	
(25, 35)	0.0315	0.0003	0.0041	0.0012	0	0.0043	0.0043
(35, 45)	0.0302	0.0002	0.0029	0.0011	0	0.0031	0.0031
(45, 55)	0.0275	0.0002	0.0014	0.0013	0	0.0019	0.0019
(55, 65)	0.0293	0.0005	0.0014	0.0015	0	0.002	0.0021
(65, 75)	0.0296	0.0009	0.0022	0.0017	0	0.0028	0.0029
(75, 90)	0.0319	0.0014	0.0011	0.0021	0	0.0024	0.0027
(90, 120)	0.0357	0.0017	0.001	0.0023	0	0.0025	0.0031
(120, 180)	0.039	0.0025	0.0017	0.0028	0	0.0033	0.0041
(180, 300)	0.0327	0.0042	0.004	0.0023	0	0.0046	0.0062

Table 7.4: Fake rates for $p_{\mathrm{T}} \in [25\ \mathrm{GeV}, 300\ \mathrm{GeV}]$ and $0.8 \leq |\eta| < 1.15$, evaluated from the events selected using the overlap algorithm favoring photons. The table reports the central value, the statistical, the systematic and the total uncertainty. For the systematic error also the contribution from the different sources is listed: the uncertainty due to the variation of the invariant mass selection range (*Window*), the variation of the signal ratio weighting procedure (*Weighting*), and the different considered procedure of selection (*Selection*).

$0.8 \leq \lvert\eta\rvert < 1.15$							
p_{T} [GeV]	$F_{e\to\gamma}$	Stat.	Syst.				Total Unc.
			Window	Weighting	Selection	Total	
(25, 35)	0.0388	0.0003	0.0043	0.0014	0	0.0045	0.0045
(35, 45)	0.0372	0.0002	0.0032	0.0014	0	0.0035	0.0035
(45, 55)	0.0348	0.0002	0.0017	0.0017	0	0.0024	0.0024
(55, 65)	0.0365	0.0005	0.002	0.0019	0	0.0028	0.0028
(65, 75)	0.0365	0.0008	0.0015	0.0021	0	0.0026	0.0027
(75, 90)	0.038	0.0012	0.001	0.0025	0	0.0027	0.0029
(90, 120)	0.0412	0.0014	0.0003	0.0028	0	0.0028	0.0031
(120, 180)	0.0409	0.002	0.0012	0.003	0	0.0032	0.0038
(180, 300)	0.0443	0.0037	0.0022	0.0033	0	0.004	0.0054

Table 7.5: Fake rates for $p_{\mathrm{T}} \in [25\ \mathrm{GeV}, 300\ \mathrm{GeV}]$ and $1.15 \leq |\eta| < 1.37$, evaluated from the events selected using the overlap algorithm favoring photons. The table reports the central value, the statistical, the systematic and the total uncertainty. For the systematic error also the contribution from the different sources is listed: the uncertainty due to the variation of the invariant mass selection range (*Window*), the variation of the signal ratio weighting procedure (*Weighting*), and the different considered procedure of selection (*Selection*).

$1.15 \leq \lvert\eta\rvert < 1.37$							
p_{T} [GeV]	$F_{e\to\gamma}$	Stat.	Syst.				Total Unc.
			Window	Weighting	Selection	Total	
(25, 35)	0.0543	0.0005	0.0043	0.002	0	0.0047	0.0047
(35, 45)	0.052	0.0003	0.0041	0.002	0	0.0046	0.0046
(45, 55)	0.0461	0.0003	0.0017	0.0023	0	0.0028	0.0028
(55, 65)	0.0474	0.0007	0.001	0.0025	0	0.0027	0.0028
(65, 75)	0.0485	0.0013	0.0011	0.0028	0	0.003	0.0033
(75, 90)	0.0552	0.0019	0.0015	0.0036	0	0.0039	0.0044
(90, 120)	0.0536	0.0022	0.0013	0.0037	0	0.0039	0.0045
(120, 180)	0.0541	0.0031	0.0014	0.0039	0	0.0041	0.0052
(180, 300)	0.0626	0.006	0.008	0.0049	0	0.0094	0.0112

Table 7.6: Fake rates for $p_{\mathrm{T}} \in [25\ \mathrm{GeV}, 300\ \mathrm{GeV}]$ and $1.52 \leq |\eta| < 1.81$, evaluated from the events selected using the overlap algorithm favoring photons. The table reports the central value, the statistical, the systematic and the total uncertainty. For the systematic error also the contribution from the different sources is listed: the uncertainty due to the variation of the invariant mass selection range (*Window*), the variation of the signal ratio weighting procedure (*Weighting*), and the different considered procedure of selection (*Selection*).

$1.52 \leq \lvert\eta\rvert < 1.81$							
p_{T} [GeV]	$F_{e\to\gamma}$	Stat.	Syst.				Total Unc.
			Window	Weighting	Selection	Total	
(25, 35)	0.0798	0.0006	0.0048	0.0015	0	0.005	0.0051
(35, 45)	0.0804	0.0003	0.0042	0.0016	0	0.0045	0.0045
(45, 55)	0.0732	0.0004	0.0014	0.0017	0	0.0022	0.0023
(55, 65)	0.0773	0.0009	0.0012	0.002	0	0.0023	0.0025
(65, 75)	0.0771	0.0017	0.002	0.0023	0	0.003	0.0035
(75, 90)	0.0802	0.0024	0.0022	0.0027	0	0.0035	0.0042
(90, 120)	0.0882	0.003	0.0017	0.0031	0	0.0036	0.0047
(120, 180)	0.0838	0.0041	0.006	0.0032	0	0.0068	0.0079
(180, 300)	0.0983	0.0078	0.0032	0.0038	0	0.005	0.0093

Table 7.7: Fake rates for $p_{\mathrm{T}} \in [25\ \mathrm{GeV}, 300\ \mathrm{GeV}]$ and $1.81 \leq |\eta| < 2.01$, evaluated from the events selected using the overlap algorithm favoring photons. The table reports the central value, the statistical, the systematic and the total uncertainty. For the systematic error also the contribution from the different sources is listed: the uncertainty due to the variation of the invariant mass selection range (*Window*), the variation of the signal ratio weighting procedure (*Weighting*), and the different considered procedure of selection (*Selection*).

$1.81 \leq \lvert\eta\rvert < 2.01$							
p_{T} [GeV]	$F_{e\to\gamma}$	Stat.	Syst.				Total Unc.
			Window	Weighting	Selection	Total	
(25, 35)	0.0943	0.0008	0.0088	0.0017	0	0.009	0.009
(35, 45)	0.0964	0.0005	0.0056	0.0018	0	0.0059	0.0059
(45, 55)	0.093	0.0006	0.0044	0.0022	0	0.0049	0.005
(55, 65)	0.0982	0.0014	0.004	0.0025	0	0.0047	0.0049
(65, 75)	0.095	0.0025	0.0038	0.0027	0	0.0046	0.0053
(75, 90)	0.1101	0.0037	0.0011	0.0035	0	0.0037	0.0053
(90, 120)	0.1105	0.0045	0.001	0.0038	0	0.0039	0.006
(120, 180)	0.106	0.0064	0.0066	0.0037	0	0.0076	0.0099
(180, 300)	0.1365	0.0138	0.0097	0.0048	0	0.0108	0.0175

Table 7.8: Fake rates for $p_{\mathrm{T}} \in [25\ \mathrm{GeV}, 300\ \mathrm{GeV}]$ and $2.01 \leq |\eta| < 2.37$, evaluated from the events selected using the overlap algorithm favoring photons. The table reports the central value, the statistical, the systematic and the total uncertainty. For the systematic error also the contribution from the different sources is listed: the uncertainty due to the variation of the invariant mass selection range (*Window*), the variation of the signal ratio weighting procedure (*Weighting*), and the different considered procedure of selection (*Selection*).

$2.01 \leq \lvert\eta\rvert < 2.37$							
p_{T} [GeV]	$F_{e\to\gamma}$	Stat.	Syst.				Total Unc.
			Window	Weighting	Selection	Total	
(25, 35)	0.1292	0.0007	0.009	0.0022	0	0.0093	0.0093
(35, 45)	0.1335	0.0004	0.0062	0.0024	0	0.0066	0.0067
(45, 55)	0.1327	0.0006	0.0027	0.003	0	0.0041	0.0041
(55, 65)	0.1384	0.0014	0.0028	0.0034	0	0.0045	0.0047
(65, 75)	0.1451	0.0025	0.0021	0.004	0	0.0045	0.0052
(75, 90)	0.151	0.0037	0.0016	0.0047	0	0.0049	0.0062
(90, 120)	0.1551	0.0046	0.0006	0.005	0	0.0051	0.0069
(120, 180)	0.1772	0.0074	0.0058	0.0058	0	0.0082	0.011
(180, 300)	0.1825	0.0152	0.0074	0.006	0	0.0095	0.0179

Data to MC comparison

The value of the fake rate measured using the 2015 and 2016 data is compared with the evaluation of the fake rate obtained from a $Z \to ee$ Monte Carlo sample. The differences between the values obtained from data and from simulated events are described by scale factors that allow to reproduce in the simulation the behaviour observed in data. In particular, comparing the inclusive measurement the data and the MC differ by 6%, while comparing the measurement binned in η the scale factors vary between 0.9 and 1.5, as shown in Figure 7.10.

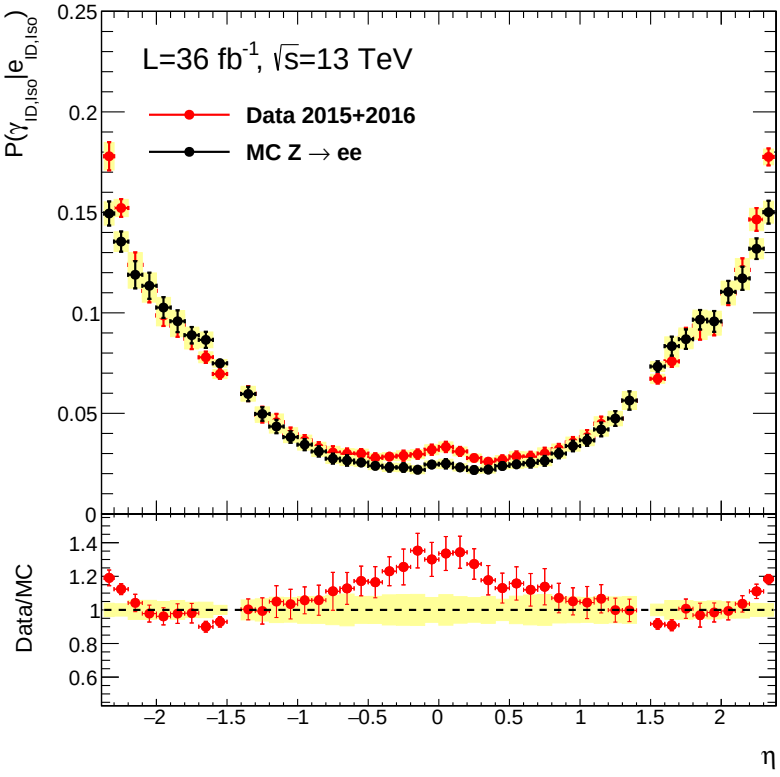

Figure 7.10: Comparison of the electron to photon fake rate measured using the 2015 and 2016 data (red dots) with the fake rate measured predicted by a $Z \to ee$ Monte Carlo sample (black dots). Dots with error bars correspond to the results with their total uncertainties. Yellow bars correspond to the systematic uncertainties, while orange boxes corresponds to the statistical error. The bottom plot show the ratio of the two measurements. The error bars correspond to the scaled data uncertainty and the yellow band corresponds to the relative MC uncertainty.

7.3.5 Fake rate application

In this section an example, which can also be considered as a data-driven cross check of the measurement presented in the previous sections, of the use of the electron-to-photon

fake rate is given in the framework of the search of di-photon resonances with masses close to that of the Z boson.

A sample of di-photon events is selected from the 2015 and 2016 data requiring two isolated and *tight* identified photons with $p_{\mathrm{T}} > 25$ GeV and pseudorapidity $|\eta| < 2.37$, excluding the barrel-endcap transition region of the LAr calorimeter ($1.37 < |\eta| < 1.52$).

The $m_{\gamma\gamma}$ invariant mass spectrum of this sample is expected to be almost flat, but a deviation from the expected trend is observed around $m_{\gamma\gamma} \simeq 90$ GeV due to the fake photon contribution coming from electron pairs produced by the Z boson decay.

Given the fake rate ρ defined in Eq. (7.1), the number of observed $\gamma\gamma$ event is:

$$N_{\gamma\gamma}^{obs} = \epsilon_\gamma^2 \hat{N}_{\gamma\gamma} + \rho\epsilon_\gamma^2 \hat{N}_{e\gamma} + \rho^2\epsilon_\gamma^2 \hat{N}_{ee}, \tag{7.20}$$

where $\hat{N}$ is the number of real events with the correspondent ee, $e\gamma$ or $\gamma\gamma$ final state and N^{obs} is the number selected in the three samples. For this calculation the contribution of photons mis-reconstructed as electrons is considered negligible. Then, for the other final states we have:

$$N_{e\gamma}^{obs} = (1-\rho)\epsilon_\gamma\epsilon_e \hat{N}_{e\gamma} + 2\rho(1-\rho)\epsilon_\gamma\epsilon_e \hat{N}_{ee}, \tag{7.21}$$

$$N_{ee}^{obs} = (1-\rho)^2\epsilon_e^2 \hat{N}_{ee}, \tag{7.22}$$

thus:

$$\hat{N}_{e\gamma} = \frac{N_{e\gamma}^{obs}}{(1-\rho)\epsilon_\gamma\epsilon_e} - 2\rho\hat{N}_{ee}, \tag{7.23}$$

$$\hat{N}_{ee} = \frac{N_{ee}^{obs}}{(1-\rho)^2\epsilon_e^2}. \tag{7.24}$$

Then the number of real $\gamma\gamma$ events passing the selection, $\hat{N}_{\gamma\gamma}^{obs}$ can be obtained as:

$$\hat{N}_{\gamma\gamma}^{obs} = \epsilon_\gamma^2 \hat{N}_{\gamma\gamma} = N_{\gamma\gamma}^{obs} - \rho\epsilon_\gamma^2 \hat{N}_{e\gamma} - \rho^2\epsilon_\gamma^2 \hat{N}_{ee} = \tag{7.25}$$

$$= N_{\gamma\gamma}^{obs} - \left[\rho\epsilon_\gamma^2 \frac{N_{e\gamma}^{obs}}{(1-\rho)\epsilon_\gamma\epsilon_e} - 2\rho^2\epsilon_\gamma^2 \hat{N}_{ee}\right] - \rho^2\epsilon_\gamma^2 \hat{N}_{ee} = \tag{7.26}$$

$$= N_{\gamma\gamma}^{obs} - \left[\rho\epsilon_\gamma \frac{N_{e\gamma}^{obs}}{(1-\rho)\epsilon_e} - 2\rho^2\epsilon_\gamma^2 \frac{N_{ee}^{obs}}{(1-\rho)^2\epsilon_e^2}\right] - \rho^2\epsilon_\gamma^2 \frac{N_{ee}^{obs}}{(1-\rho)^2\epsilon_e^2} = \tag{7.27}$$

$$= N_{\gamma\gamma}^{obs} - \frac{\rho}{(1-\rho)}\frac{\epsilon_\gamma}{\epsilon_e} N_{e\gamma}^{obs} + \left(\frac{\rho}{(1-\rho)}\frac{\epsilon_\gamma}{\epsilon_e}\right)^2 N_{ee}^{obs}.$$

(7.28)

Thus given Equation 7.2 we obtain:

$$\hat{N}_{\gamma\gamma}^{obs} = N_{\gamma\gamma}^{obs} - F_{e\to\gamma} N_{e\gamma}^{obs} + F_{e\to\gamma}^2 N_{ee}^{obs}. \tag{7.29}$$

For each bin of the di-photon invariant mass distribution we apply the correction defined in Equation 7.29 Finally we obtain an histograms describing the $\gamma\gamma$ invariant mass distribution filled following this equation:

$$\begin{aligned}\hat{H}_{\gamma\gamma}(m_{\gamma\gamma}) =& H_{\gamma\gamma}(m_{\gamma\gamma}) - \sum_{\eta}\sum_{p_T}\left[F_{e\to\gamma}(\eta,p_T)H_{e\gamma}(\eta,p_T,m_{e\gamma})\right. \\ & \left. -F_{e\to\gamma}(\eta,p_T)^2\frac{H_{ee}(\eta,p_T,m_{ee})}{2}\right]\end{aligned} , \tag{7.30}$$

where H_{ee} is divided by two because it is filled twice for each ee events (*i.e.* with both the leading and sub-leading electrons).

The $m_{\gamma\gamma}$ spectrum before and after the correction is shown in Figure 7.11.

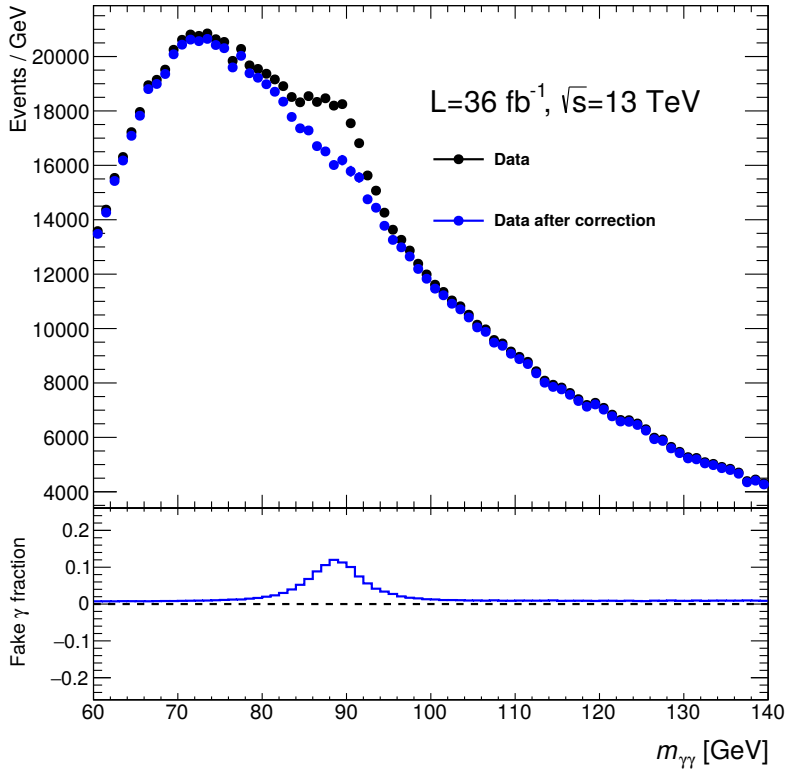

Figure 7.11: Di-photon invariant mass distribution obtained from 2015 and 2016 data before (black dots) and after (blue dots) the fake photon background subtraction.

Chapter 8

Measurement of the Higgs boson mass in the $H \to \gamma\gamma$ channel

The observation of a new particle in the search for the Standard Model Higgs boson by the ATLAS and CMS experiments (4; 5), with the LHC Run 1 data at center-of-mass energies of $\sqrt{s} = 7$ TeV and 8 TeV, has been a major step towards the understanding of the mechanism of electro-weak symmetry breaking (6; 7; 8). As already illustrated in Sec. 1.4, the mass of the Higgs boson obtained from the combination of the ATLAS and the CMS Run 1 measuerements is 125.09 ± 0.24 GeV (11). Measurements of the spin, parity and couplings of the new particle have shown no significant deviations from the predictions for the SM Higgs boson (40; 59; 62; 158). With the increased center-of-mass energy and higher integrated luminosity of the Run 2 LHC data, the Higgs boson properties can be measured with higher accuracy.

This chapter presents the measurement of the Higgs boson mass m_H in the $H \to \gamma\gamma$ channel, using 36.1 fb^{-1} of pp collision data recorded with the ATLAS detector at a center-of-mass energy of $\sqrt{s}$=13 TeV.

The dataset used in this analysis, as well as the simulated samples employed for the signal and background predictions, are outlined in Sec. 8.1. The event selection requirements are summarized in Sec. 8.2. To optimize the analysis sensitivity and the measurement precision the events are further classified in 31 categories, that are illustrated in Sec. 8.3.

Higgs boson decays in two photons lead to a narrow resonant peak in the $m_{\gamma\gamma}$ invariant mass distribution above a large falling continuum background from SM $\gamma\gamma$, γ+jet and di-jet events. The position of such peak is measured through a binned maximum likelihood fit and leads to the determination of m_H, as shown in Sec. 8.7. The signal and background model on which the likelihood function is built, as well the expected number of events for each considered category, are described in Sec. 8.4 and Sec. 8.5. The likelihood function includes also systematic uncertainties as nuisance parameters (NP) that model the deviations from the nominal expectation in the fit. The evaluation of these systematic uncertainties, that mainly arise from the photon energy scale systematic uncertainties, is described in Sec. 8.6.

The expected and observed results of the Higgs boson mass measurement in the di-photon channel are summarized in Sec. 8.8 and Sec. 8.9. Sec. 8.10 presents the cross-check measurement performed to guarantee the robustness against possible calibration bias depending on the different region of the detector or different combination of photon types (unconverted or converted) considered. Finally, Sec. 8.11 reports the combination with the mass measurement performed by the ATLAS combination in the $H \to ZZ^* \to 4\ell$ channel.

8.1 Data and simulated samples

The analysis discussed here is based on the pp collision data collected at a center-of-mass energy of 13 TeV during 2015 and 2016. Di-photon events are selected using a di-photon trigger which requires transverse energy thresholds of 35 GeV and 25 GeV for the highest-E_{T} and second highest-E_{T} photon candidates. This dataset corresponds to an integrated luminosity of 3.2 fb^{-1} of data taken in 2015 and 32.9 fb^{-1} taken in 2016, thus giving a total luminosity of 36.1 fb^{-1}, with an uncertainty of 3.2 % (see Sec. 3.2.1).

The simulated samples are used in the analysis to model the detector response both for signal and background processes. Except when noted, the generated events are passed through a Geant4 (149) simulation of the response of the ATLAS detector (159) and reconstructed with the same algorithms as the data.

Higgs boson production and decay in two photons are simulated for several values of m_H and different production modes: in particular for m_H equal to 110, 120, 122, 124, 125, 126, 127, 130, 140 GeV for gluon-gluon fusion (ggH), vector boson fusion (VBF), associated production with a vector boson WH, ZH, for both $q\bar{q} \to ZH$ and $gg \to ZH$. Moreover, $t\bar{t}H$, $b\bar{b}H$, $tHjb$, tWH are generated but only for $m_H = 125$ GeV since these samples give a negligible contribution to the global cross-section of the process $pp \to H \to \gamma\gamma$. The samples are normalized to the latest theoretical calculations of the corresponding SM production cross sections (41) as detailed below. The normalization also account for the $H \to \gamma\gamma$ branching ratio calculated with HDECAY (160) and PROPHECY4F (161; 162; 163) and predicted to be $(2.27 \pm 0.07) \times 10^{-3}$ at $m_H = 125.09$ GeV (41).

The ggH events are generated at NNLO in QCD using Powheg NNLOPS (164; 165) with the PDF4LHC15 (166) parton distribution functions (PDF), interfaced with Pythia8 (167) with AZNLO parameter set for showering, hadronization and underlying events. The sample is normalized to reproduce the total cross section predicted by a next-to-next-to-next-to-leading-order QCD calculation with NLO electroweak corrections applied (168; 44; 169; 170).

Vector-boson fusion (VBF) events are generated at NLO precision in QCD with Powheg Box (171; 172; 173; 164; 174) with the PDF4LHC15 set and interfaced with Pythia8 for parton showering, hadronization and multiple parton interactions (MPI), using the AZNLO parameter set. The sample is normalized to a cross section calculated with full NLO QCD and EW corrections (175; 176; 177), with an approximate NNLO QCD correction applied (178).

The events from WH and ZH associated production are generated at NLO accuracy in QCD using Powheg Box with the PDF4LHC15 PDF set. Pythia8 with the AZNLO tune is used for parton showering, hadronization and MPI. The samples are normalized to VH cross sections calculated at NNLO in QCD with NLO EW radiative corrections (179; 180; 181) applied.

The events from the $t\bar{t}H$ associated production are generated with the MadGraph5_aMC@NLO (182) generator with the NNPDF3.0 (183) PDF set and interfaced with Pythia8 to provide parton showering, hadronization and MPI, using the A14 parameter set (184). For the $t\bar{t}H$ normalization, full NLO QCD corrections have been calculated with NLO electroweak corrections (185; 186; 187; 188).

The irreducible $\gamma\gamma$ background events are generated using Sherpa 2.1 (189). The CT10 PDF set and the Sherpa default parameter set for underlying event activity are used. The leading order matrix elements for $\gamma\gamma$ production with real emission of up to three partons are included in the generation. The 100 M events sample size required for the

modelling of the $\gamma\gamma$ background processes is obtained through a fast parametric simulation of the ATLAS detector response (159). The study of the reducible backgrounds is not based on Monte Carlo samples but on data-driven techniques as explained in Sec. 8.5. Table 8.1 summarizes the event generators and PDF sets used to model the signal and the main background processes, as well as their cross section for the Higgs boson with $m_H = 125.09$ GeV for $\sqrt{s} = 13$ TeV.

Table 8.1: Summary of the event generators and PDF sets used to model the signal and the main background processes. The SM cross sections σ for the Higgs boson production processes with $m_H = 125.09$ GeV are also given separately for $\sqrt{s} = 13$ TeV, together with the orders of the calculations corresponding to the quoted cross sections, which are used to normalize the samples, after multiplication by the Higgs branching ratio to di-photon (9).

Process	Generator	Showering	PDF set	Order of calculation	σ[pb] $\sqrt{s} = 13$ TeV
ggH	Powheg NNLOPS	Pythia8	PDF4LHC15	N^{3}LO(QCD)+NLO(EW)	48.52
VBF	Powheg Box	Pythia8	PDF4LHC15	NNLO(QCD)+NLO(EW)	3.78
WH	Powheg Box	Pythia8	PDF4LHC15	NNLO(QCD)+NLO(EW)	1.37
$q\bar{q}' \to ZH$	Powheg Box	Pythia8	PDF4LHC15	NNLO(QCD)+NLO(EW)	0.76
$gg \to ZH$	Powheg Box	Pythia8	PDF4LHC15	NNLO(QCD)+NLO(EW)	0.12
$t\bar{t}H$	MadGraph5_aMC@NLO	Pythia8	NNPDF3.0	NLO(QCD)+NLO(EW)	0.51
$b\bar{b}H$	MadGraph5_aMC@NLO	Pythia8	CT10	5FS(NNLO)+4FS(NLO)	0.49
$tHq\bar{b}$	MadGraph5_aMC@NLO	Pythia8	CT10	4FS(LO)	0.07
tHW	MadGraph5_aMC@NLO	Herwig++	CT10	5FS(NLO)	0.02
$\gamma\gamma$	Sherpa	Sherpa	CT10		

In order to compare coherently data and MC events and to improve their agreement, in addition to the internal weights provided by the event generator, some extra corrections are applied to the simulation. In particular, the following corrections are applied:

- the MC samples are weighted to match the pileup conditions of data, according to the observed distribution of the average numbers of interactions per bunch crossing, $\langle\mu\rangle$;
- the width of the beam spot along the beam axis, σ_z, is slightly wider in MC samples than in data. A weighting is therefore applied to match the spread (and mean) of the beam spot observed in data;
- shifts are applied to the photon shower shape variables and to the photon calorimeter isolation. Such shifts are determined as the average data-MC difference in photon-enriched control samples (see Chap. 7);
- scale factors determined from data control samples are applied to correct the object selection efficiency. Similarly, energy scale and resolution corrections for all simulated objects are also taken into account.

8.2 Event selection

In order to reduce the number of background events and to increase the significance of the Higgs boson signal, several requirements are applied to the data. A first pre-selection is applied, requiring that the events were recorded in the optimal detector condition in which all the ATLAS sub-detectors are fully operational and with no data integrity errors

or corruption due to some hardware failure (e.g. trips of the calorimeter). At least two photons have to be reconstructed in the event with $E_{\mathrm{T}} > 25\,\mathrm{GeV}$ and $|\eta| < 2.37$, excluding the region $1.37 \leq |\eta| \leq 1.52$. Photons are required to pass *loose* (see Sec. 7.1) identification criteria.

The two reconstructed photon candidates with the largest E_{T} are considered and used to identify the di-photon primary vertex (PV) among all reconstructed vertices. Identifying correctly the position of the primary vertex corresponding to the *pp* collision that produced the di-photon candidate is important to keep the contribution of the opening angle resolution to the di-photon mass resolution smaller than the energy resolution contribution. In most analysis the primary vertex is defined as the vertex with the highest sum of the square of the associated track transverse momenta ($\sum p_{\mathrm{T}}^2$). However this choice is often incorrect for di-photon events with small extra energy in the event.

A neural network algorithm, which combines the information from the tracks and primary vertex candidates, as well as the direction of the photons measured profiting from the longitudinal segmentation of the calorimeter and from the inner detector information in the case of converted photons, has been developed for the Run 1 $H \to \gamma\gamma$ analysis (190) and adapted to be applied in Run 2 (191). The algorithm selects the correct di-photon vertex within 0.3 mm along the *pp* collision axis in 79% of simulated gluon-fusion events, while the standard vertex selection on the same sample has an efficiency of 56%. For the other Higgs boson production modes this fraction ranges from 84% to 97%, increasing with jet activity or the presence of charged leptons. Once the di-photon primary vertex is identified by the neural network algorithm, the position of the two photons is updated redefining η using the straight line that connects the impact point of the particles in the first layer of the EM calorimeter with the new PV.

The leading and the sub-leading photons are required to have $E_{\mathrm{T}}/m_{\gamma\gamma} > 0.35$ and 0.25 respectively, and to pass the *tight* identification criteria and isolation criteria based on calorimeter and tracking information (see Chap. 7). In particular, the calorimeter isolation in a cone size $\Delta R = \sqrt{\Delta\eta^2 + \Delta\phi^2} < 0.2$ must satisfy the criterion $E_{\mathrm{T}}^{\mathrm{iso}} < 0.065 \times p_{\mathrm{T}}$, while the track isolation in the same cone size must satisfy the criterion $p_{\mathrm{T}}^{\mathrm{iso}} < 0.05 \times p_{\mathrm{T}}$, where only tracks associated to the di-photon primary vertex are considered in the track isolation calculation.

Only events with $105\,\mathrm{GeV} \leq m_{\gamma\gamma} \leq 160\,\mathrm{GeV}$ are kept, where $m_{\gamma\gamma}$ is defined as:

$$m_{\gamma\gamma} = \sqrt{2E_1E_2(1 - \cos(\theta))}. \tag{8.1}$$

Here E_1 and E_2 are the energies of the two photons and θ is the angle between them. Table 8.2 presents the cut flow on the data for the di-photon selection.

For the events passing the selection discussed above, other objects are reconstructed and selected as jets, b-jets, electrons, muons and missing transverse momentum.

Electrons are required to have $p_{\mathrm{T}} > 10$ GeV and $|\eta| < 2.47$ (excluding the region $1.37 < |\eta| < 1.52$). They must satisfy *medium* identification criteria and have a minimum number of hits associated with the track in the ID. They are also required to satisfy the following isolation criteria: the calorimeter isolation, in a cone size $\Delta R < 0.2$, must satisfy the criterion $E_{\mathrm{T}}^{\mathrm{iso}} < 0.020 \times p_{\mathrm{T}}$, while the track isolation, in a cone size $\Delta R < 0.2$, must satisfy the criterion $p_{\mathrm{T}}^{\mathrm{iso}} < 0.15 \times p_{\mathrm{T}}$.

Muons are required to have $p_{\mathrm{T}} > 10$ GeV and $|\eta| < 2.7$ and pass *medium* identification criteria.

Lepton candidates are discarded if they are within $\Delta R = 0.4$ of a selected photon . Tracks associated to either electrons and muons are required to be consistent with

Table 8.2: Cut flow of the di-photon selection on the 2015 and 2016 data.

Step of selection	events 2015	events 2016	events total
All events	11202266	104334488	115536752
Optimal detector condition	10946209	99482000	110428208
Pass trigger	8649862	91242336	99892200
Optimal object quality	8649084	91239680	99888768
Has PV	8649050	91239680	99888728
2 loose photons	2662080	27934244	30596324
tight photon identification	414418	4113790	4528208
isolation	156646	1517170	1673816
rel. p_T cuts	136678	1323154	1459832
$m_{\gamma\gamma} \in [105, 160]$ GeV	30712	302183	332895

originating from the di-photon primary vertex by requiring their longitudinal impact parameter z_0 with respect to the PV to satisfy $|z_0 \sin\theta| < 0.5$ mm and their unsigned transverse impact parameter $|d_0|$ with respect to the beam axis to be respectively smaller than five or three times its uncertainty, $|d_0/\sigma(d_0)|$ <5 or 3.

Jets are reconstructed using the *anti-k_t* algorithm with the distance parameter $R = 0.4$ and are required to have a pseudorapidity $|\eta| < 4.4$ and $p_{\mathrm{T}} > 25$ GeV. To further suppress jets produced in additional pile-up interactions, jets that do not originate from the di-photon primary vertex are identified, for $|\eta| < 2.4$, using the Jet Vertex Tagging algorithm. Jets consistent with the decay of a b-hadron are identified using a multivariate discriminant, having as input information from track impact parameters and secondary vertices.

8.3 Event Categorization

8.3.1 Coupling analysis categorization

The mass measurements uses the same event selection and classification optimized for the measurement, with $H \to \gamma\gamma$, of the cross sections in simplified fiducial phase-space regions defined by the stage-1 of the simplified template cross section (STXS) framework (41; 192).

The simplified template cross sections framework was developed as an evolution of the signal strength measurements of Run 1 (40), see Sec. 1.4.2. It was designed to allow the measurement of the different Higgs boson production processes in defined regions of the phase space. Compared to the signal strength measurements, this framework provides a higher granularity and reduces the theoretical uncertainties that are directly folded into the measurements. Additionally, the STXS can simplify the combination of the measurements from many decay channels, resulting in a more sensitive combined measurement.

The events are divided in 31 categories: 10 categories optimized to measure gluon fusion properties, 4 categories that target the vector boson fusion production, 8 categories aimed at measuring the associate production with a vector boson and finally 9 categories optimized to measure the associate production with a top-antitop pair or a single top quark. The categorization proceeds from the production modes with the smallest expected cross sections to the production modes with largest expected cross sections in the order presented in the Table 8.3. Figure 8.1 shows the relative contribution of each Higgs boson

production mode in each category. A more extensive description of these categories can be found in Ref. (9).

Table 8.3: Event selection defining each category. The category names denote the predominant production process or kinematic properties the category targets. Jets are required to have $p_{\mathrm{T}} > 30$ GeV unless otherwise noted. Jets are considered as forward (fwd) if they have $|\eta| > 2.5$. The categories are mutually exclusive and criteria are applied in descending order of the shown categories (9).

Category	Selection
tH lep 0fwd	$N_{\mathrm{lep}} = 1$, $N_{\mathrm{jets}}^{\mathrm{cen}} \leq 3$, $N_{\mathrm{b-tag}} \geq 1$, $N_{\mathrm{jets}}^{\mathrm{fwd}} = 0$ ($p_{\mathrm{T}}^{\mathrm{jet}} > 25\,\mathrm{GeV}$)
tH lep 1fwd	$N_{\mathrm{lep}} = 1$, $N_{\mathrm{jets}}^{\mathrm{cen}} \leq 4$, $N_{\mathrm{b-tag}} \geq 1$, $N_{\mathrm{jets}}^{\mathrm{fwd}} \geq 1$ ($p_{\mathrm{T}}^{\mathrm{jet}} > 25\,\mathrm{GeV}$)
ttH lep	$N_{\mathrm{lep}} \geq 1$, $N_{\mathrm{jets}}^{\mathrm{cen}} \geq 2$, $N_{\mathrm{b-tag}} \geq 1$, $Z_{\ell\ell}$ veto ($p_{\mathrm{T}}^{\mathrm{jet}} > 25\,\mathrm{GeV}$)
ttH had BDT1	$N_{\mathrm{lep}} = 0$, $N_{\mathrm{jets}} \geq 3$, $N_{\mathrm{b-tag}} \geq 1$, $\mathrm{BDT}_{\mathrm{ttH}} > 0.92$
ttH had BDT2	$N_{\mathrm{lep}} = 0$, $N_{\mathrm{jets}} \geq 3$, $N_{\mathrm{b-tag}} \geq 1$, $0.83 < \mathrm{BDT}_{\mathrm{ttH}} < 0.92$
ttH had BDT3	$N_{\mathrm{lep}} = 0$, $N_{\mathrm{jets}} \geq 3$, $N_{\mathrm{b-tag}} \geq 1$, $0.79 < \mathrm{BDT}_{\mathrm{ttH}} < 0.83$
ttH had BDT4	$N_{\mathrm{lep}} = 0$, $N_{\mathrm{jets}} \geq 3$, $N_{\mathrm{b-tag}} \geq 1$, $0.52 < \mathrm{BDT}_{\mathrm{ttH}} < 0.79$
tH had 4j1b	$N_{\mathrm{lep}} = 0$, $N_{\mathrm{jets}}^{\mathrm{cen}} = 4$, $N_{\mathrm{b-tag}} = 1$ ($p_{\mathrm{T}}^{\mathrm{jet}} > 25\,\mathrm{GeV}$)
tH had 4j2b	$N_{\mathrm{lep}} = 0$, $N_{\mathrm{jets}}^{\mathrm{cen}} = 4$, $N_{\mathrm{b-tag}} \geq 2$ ($p_{\mathrm{T}}^{\mathrm{jet}} > 25\,\mathrm{GeV}$)
VH dilep	$N_{\mathrm{lep}} \geq 2$, $70\,\mathrm{GeV} \leq m_{\ell\ell} \leq 110\,\mathrm{GeV}$
VH lep HIGH	$N_{\mathrm{lep}} = 1$, $\lvert m_{e\gamma} - 89\,\mathrm{GeV}\rvert > 5\,\mathrm{GeV}$, $p_{\mathrm{T}}^{l+E_{\mathrm{T}}^{\mathrm{miss}}} > 150\,\mathrm{GeV}$
VH lep LOW	$N_{\mathrm{lep}} = 1$, $\lvert m_{e\gamma} - 89\,\mathrm{GeV}\rvert > 5\,\mathrm{GeV}$, $p_{\mathrm{T}}^{l+E_{\mathrm{T}}^{\mathrm{miss}}} < 150\,\mathrm{GeV}$, $E_{\mathrm{T}}^{\mathrm{miss}}$ significance > 1
VH MET HIGH	$150\,\mathrm{GeV} < E_{\mathrm{T}}^{\mathrm{miss}} < 250\,\mathrm{GeV}$, $E_{\mathrm{T}}^{\mathrm{miss}}$ significance > 9 or $E_{\mathrm{T}}^{\mathrm{miss}} > 250\,\mathrm{GeV}$
VH MET LOW	$80\,\mathrm{GeV} < E_{\mathrm{T}}^{\mathrm{miss}} < 150\,\mathrm{GeV}$, $E_{\mathrm{T}}^{\mathrm{miss}}$ significance > 8
jet BSM	$p_{\mathrm{T,j1}} > 200\,\mathrm{GeV}$
VH had tight	$60\,\mathrm{GeV} < m_{\mathrm{jj}} < 120\,\mathrm{GeV}$, $\mathrm{BDT}_{\mathrm{VH}} > 0.78$
VH had loose	$60\ GeV < m_{\mathrm{jj}} < 120\,\mathrm{GeV}$, $0.35 < \mathrm{BDT}_{\mathrm{VH}} < 0.78$
VBF tight, high p_T^{Hjj}	$\Delta\eta_{\mathrm{jj}} > 2$, $\lvert\eta_{\gamma\gamma} - 0.5(\eta_{\mathrm{j1}} + \eta_{\mathrm{j2}})\rvert < 5$, $p_T^{Hjj} > 25\,\mathrm{GeV}$, $\mathrm{BDT}_{\mathrm{VBF}} > 0.47$
VBF loose, high p_T^{Hjj}	$\Delta\eta_{\mathrm{jj}} > 2$, $\lvert\eta_{\gamma\gamma} - 0.5(\eta_{\mathrm{j1}} + \eta_{\mathrm{j2}})\rvert < 5$, $p_T^{Hjj} > 25\,\mathrm{GeV}$, $-0.32 < \mathrm{BDT}_{\mathrm{VBF}} < 0.47$
VBF tight, low p_T^{Hjj}	$\Delta\eta_{\mathrm{jj}} > 2$, $\lvert\eta_{\gamma\gamma} - 0.5(\eta_{\mathrm{j1}} + \eta_{\mathrm{j2}})\rvert < 5$, $p_T^{Hjj} < 25\,\mathrm{GeV}$, $\mathrm{BDT}_{\mathrm{VBF}} > 0.87$
VBF loose, low p_T^{Hjj}	$\Delta\eta_{\mathrm{jj}} > 2$, $\lvert\eta_{\gamma\gamma} - 0.5(\eta_{\mathrm{j1}} + \eta_{\mathrm{j2}})\rvert < 5$, $p_T^{Hjj} < 25\,\mathrm{GeV}$, $0.26 < \mathrm{BDT}_{\mathrm{VBF}} < 0.87$
ggH 2J BSM	≥ 2 jets, $p_{\mathrm{T}}^{\gamma\gamma} \geq 200\,\mathrm{GeV}$
ggH 2J HIGH	≥ 2 jets, $p_{\mathrm{T}}^{\gamma\gamma} \in [120, 200]$ GeV
ggH 2J MED	≥ 2 jets, $p_{\mathrm{T}}^{\gamma\gamma} \in [60, 120]$ GeV
ggH 2J LOW	≥ 2 jets, $p_{\mathrm{T}}^{\gamma\gamma} \in [0, 60]$ GeV
ggH 1J BSM	$= 1$ jet, $p_{\mathrm{T}}^{\gamma\gamma} \geq 200\,\mathrm{GeV}$
ggH 1J HIGH	$= 1$ jet, $p_{\mathrm{T}}^{\gamma\gamma} \in [120, 200]$ GeV
ggH 1J MED	$= 1$ jet, $p_{\mathrm{T}}^{\gamma\gamma} \in [60, 120]$ GeV
ggH 1J LOW	$= 1$ jet, $p_{\mathrm{T}}^{\gamma\gamma} \in [0, 60]$ GeV
ggH 0J FWD	$= 0$ jets, one photon with $\lvert\eta\rvert > 0.95$
ggH 0J CEN	$= 0$ jets, two photons with $\lvert\eta\rvert \leq 0.95$

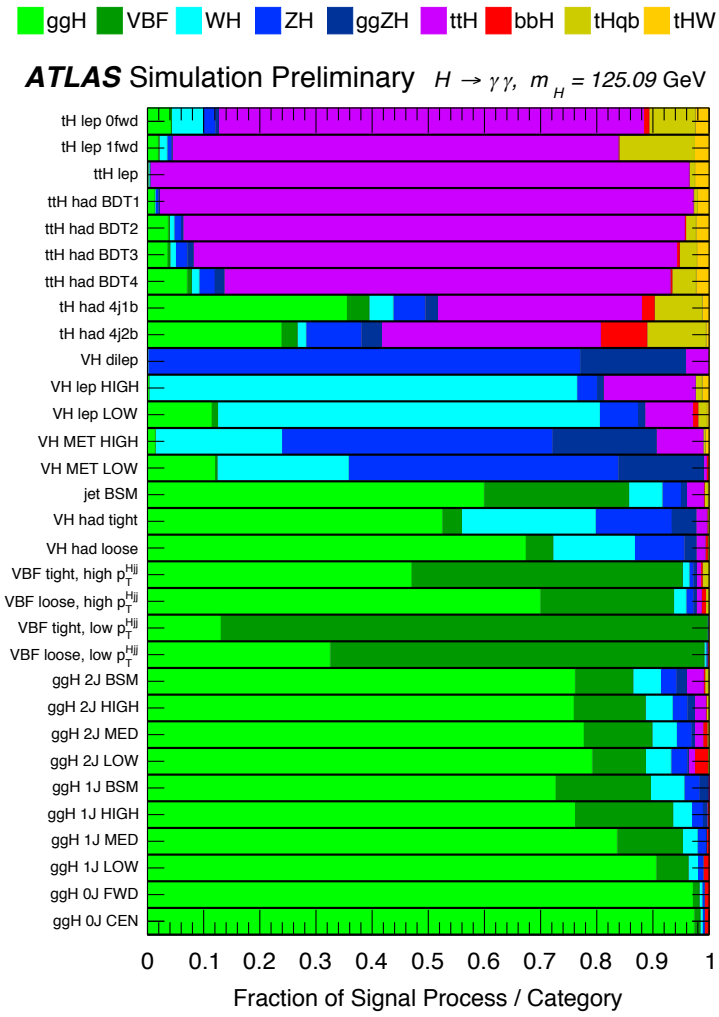

Figure 8.1: The expected composition of the selected Higgs boson events, in terms of the different production modes, for each reconstructed category (9).

8.3.2 Choice of the event categorization for the mass measurement

Since the categorization was optimized primarily for the measurement of the simplified template cross sections, alternative categorizations have been investigated to see if it is possible to find a more suited optimization for the mass measurement and improve the expected statistical and systematic uncertainties on m_H. In particular, the categorization used for the Higgs boson mass measurement in Run 1 (45; 193) has been tested, as well as some other variants.

For each tested categorization all the major steps of the analysis have been repeated: determination of the signal $m_{\gamma\gamma}$ model and acceptance (see Sec. 8.4), determination of the background $m_{\gamma\gamma}$ model (see Sec. 8.5), evaluation of the systematic uncertainties (see Sec. 8.6), and likelihood fit to an Asimov dataset to extract the result (see Sec. 8.7). The "Asimov data-set" is a toy dataset built to perfectly follow a probability distribution function (for instance the likelihood of the global model that is used in this analysis), without statistical fluctuations (194). The systematic uncertainties on the photon energy scale and resolution have been computed using the e/γ calibration uncertainties as of February 2017, which are slightly different to the ones used to obtain the final result described in Sec. 8.9.

The investigated categorizations are:

- the same categories used in the coupling analysis as summarized in Sec. 8.3.1;
- the ten categories used for the mass measurement in Run 1 (Run 1 categories), that are described in the following paragraph.
- the events classified as ggH by the coupling analysis are divided in the ten Run 1 mass categories, while all the other events are put in a common category, for a total of 11 categories considered;
- similarly to the previous categorization, with ten categories using ggH tagged events plus one category merging *VBF tight, low* p_T^{Hjj} and *VBF tight, high* p_T^{Hjj} events (that have high purity, see Table 8.7), one category merging *ggH 1J BSM* and *ggH 2J BSM* events (that have good resolution, see Table 8.7) and merging all the other events in one category, for a total of 13 categories;
- the four VBF couplings categories plus the rest of the events split in the 10 Run 1 mass categories, for a total of 14 categories;
- mixing Run 1/Run 2 coupling categories: four VBF categories, plus the Run 1 ggH coupling categories (4 categories $\eta \leqslant 0.95$ and $p_{\mathrm{T}} \leqslant 70$ GeV) plus the rest of the events in a single category, for a total of 9 categories;
- coupling merged: ggH and VBF categories as in the coupling analysis plus all the rest merged in a single category, for a total of 15 categories.

The categorization used in Run 1 is connected to the detector performance, trying to separate events based on the expected mass resolution and systematic uncertainties. In particular, it defines 10 categories using only properties related to the two selected photon candidates: $|\eta_{S2}|$, which is the pseudorapity measured in the second layer of the EM calorimeter, the conversion status of the photons (converted/unconverted), and $p_{\mathrm{T}t}$. The $p_{\mathrm{T}t}$ is defined as the orthogonal projection of the di-photon momentum on the trust

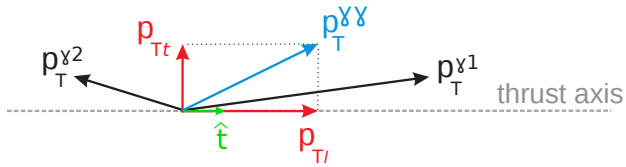

Figure 8.2: Illustration of the $p_{\mathrm{T}t}$ quantity (142).

axis $\hat{t}$, which is defined as the direction of the vectorial difference between the transverse momenta of the photons (see Figure 8.2).

The categories used for the Run 1 mass measurement are the following:

- c1: both photons are unconverted, and they have $|\eta_{S2}| < 0.75$, and $p_{\mathrm{T}t} < 70$ GeV.
- c2: both photons are unconverted, and they have $|\eta_{S2}| < 0.75$, and $p_{\mathrm{T}t} > 70$ GeV.
- c3: both photons are unconverted and at least one photon has $|\eta_{S2}| > 0.75$ but not $1.3 < |\eta_{S2}| < 1.37$ or $1.52 < |\eta_{S2}| < 1.75$, and $p_{\mathrm{T}t} < 70$ GeV.
- c4: both photons are unconverted and at least one photon has $|\eta_{S2}| > 0.75$ but not $1.3 < |\eta_{S2}| < 1.37$ or $1.52 < |\eta_{S2}| < 1.75$, and $p_{\mathrm{T}t} > 70$ GeV.
- c5: both photons are unconverted and at least one photon has $1.3 < |\eta_{S2}| < 1.37$ or $1.52 < |\eta_{S2}| < 1.75$
- c6: at least one photon is converted, and both photons have $|\eta_{S2}| < 0.75$, and $p_{\mathrm{T}t} < 70$ GeV.
- c7: at least one photon is converted, and both photons have $|\eta_{S2}| < 0.75$, and $p_{\mathrm{T}t} > 70$ GeV.
- c8: at least one photon is converted and at least one photon has $|\eta_{S2}| > 0.75$ but not $1.3 < |\eta_{S2}| < 1.37$ or $1.52 < |\eta_{S2}| < 1.75$, and $p_{\mathrm{T}t} < 70$ GeV.
- c9: at least one photon is converted and at least one photon has $|\eta_{S2}| > 0.75$ but not $1.3 < |\eta_{S2}| < 1.37$ or $1.52 < |\eta_{S2}| < 1.75$, and $p_{\mathrm{T}t} > 70$ GeV.
- c10: at least one photon is converted and at least one photon has $1.3 < |\eta_{S2}| < 1.37$ or $1.52 < |\eta_{S2}| < 1.75$.

Table 8.4 summarizes the expected invariant mass resolution together with the expected number of signal and background events for each category.

The values of the expected uncertainties on m_H for each categorization are reported in table 8.5.

Using categorizations different from the nominal one leads to an improvement on the expected uncertainties of 4.2% or less. This improvement was considered too small to motivate choosing different categorization for two $H \to \gamma\gamma$ measurements (mass and STXS), and it was chosen to keep the coupling categories which had already been studied in detail.

Table 8.4: For the Run 1 mass measurement categories (c1-c10) and for the inclusive cases, the various columns give: number of expected signal events (n_{sig}), mean and resolution of the signal invariant mass distribution, number of background events (n_{bkg}) in the full fit range and in a region containing 90% of the expected signal, signal-to-background ratio and signal significance in that $m_{\gamma\gamma}$ window.

Category	n_{sig}	mean [GeV]	resolution [GeV]	n_{bkg} in [105-160 GeV]	n_{bkg} in $\pm\sigma_{\text{eff90}}$	S/B [%]	$S/\sqrt{B}$
c1	214	124.95	1.46	30611	6283	3.06	2.43
c2	36	125.00	1.25	1535	332	9.75	1.78
c3	366	124.92	1.7	87411	17657	1.87	2.48
c4	56	125.00	1.46	4768	999	5	1.58
c5	128	124.98	2.14	29447	5998	1.92	1.48
c6	156	125.05	1.67	22648	4605	3.06	2.07
c7	27	125.04	1.39	1223	283	8.47	1.43
c8	457	125.05	2.1	104792	21243	1.94	2.82
c9	69	125.07	1.77	5887	1270	4.85	1.73
c10	225	125.05	2.73	44562	9123	2.22	2.12
Inclusive	1734	125.01	1.87	332893	67792	2.30	5.99

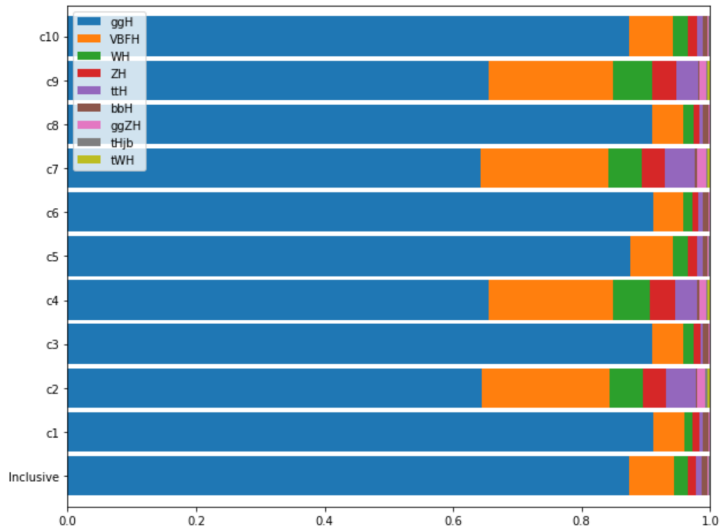

Figure 8.3: Fraction of each production mode contributing to the total signal yield expected in each of the categories used for the Run 1 mass measurement.

Table 8.5: Expected uncertainty on m_H for different categorizations. The difference of the total uncertainty with respect to the one using the coupling categories is also reported in the last column. The expected uncertainties in the Run 1 analysis based on 7+8 TeV data is also included for reference in the last line.

Categorization	stat error [GeV]	sys error [GeV]	total error [GeV]	variation [%] (vs coupling)
Coupling categories	$^{+0.256}_{-0.266}$	$^{+0.313}_{-0.313}$	0.41	0
Run 1 categories	$^{+0.255}_{-0.248}$	$^{+0.302}_{-0.300}$	0.39	-3.8
Run 1 categories ggH $\oplus$ non-ggH	$^{+0.26}_{-0.26}$	$^{+0.30}_{-0.30}$	0.40	-2.6
Run 1 cat. ggH $\oplus$ good res $\oplus$ good pur $\oplus$ rest	$^{+0.26}_{-0.25}$	$^{+0.30}_{-0.30}$	0.39	-3.4
4 VBF $\oplus$ Run 1 categories	$^{+0.25}_{-0.25}$	$^{+0.30}_{-0.30}$	0.39	-4.2
Mixing Run 1/Run 2 coupling	$^{+0.24}_{-0.26}$	$^{+0.31}_{-0.30}$	0.39	-3.2
Coupling merged	$^{+0.26}_{-0.27}$	$^{+0.32}_{-0.31}$	0.41	+1.0
Inclusive	$^{+0.34}_{-0.30}$	$^{+0.32}_{-0.29}$	0.44	+8.5
Run 1 (7+8 TeV)	0.45	0.27	0.52	+ 27

8.4 Signal Model

8.4.1 Yields and efficiencies

The expected yield (s_c) in a given category c is defined as the product of the cross-section (σ_i) times the $H \to \gamma\gamma$ branching ratio (BR), the detector acceptance (A_{ic}) times the selection efficiency (ϵ_{ic}) and luminosity summed over the different Higgs boson production modes i:

$$s_c = \sum_{i=ggH,VBF,WH,ZH,ttH,\ldots} \mathcal{L} \times BR(m_H) \times \sigma_i(m_H) \times (A \times \epsilon)_{ic}, \tag{8.2}$$

Table 8.6 shows the values of $A \times \epsilon$ in each categories for the different Higgs boson production modes evaluated using the MC samples generated at $m_H = 125$ GeV.

Table 8.6: Signal efficiencies times acceptance, $A \times \epsilon$, in each category for $\sqrt{s} = 13$ TeV and $m_H = 125.09$ GeV. The second-to-last row shows the total efficiency per production process summed over the categories. Values labeled as 'nil' correspond to efficiencies or fractions that are smaller than 0.05%. The total number of expected signal events, N_S, in the last row corresponds to an integrated luminosity of 36.1 fb^{-1}.

	ggH	VBF	WH	ZH	$t\bar{t}H$	$b\bar{b}H$	$tHq\bar{b}$	tHW	All
Category				$A \times \epsilon$ [%]					N_S
ggH 0J Cen	8.9	1.2	1.4	1.9	nil	8.2	nil	nil	333.5
ggH 0J Fwd	15.5	2.4	3.0	3.7	nil	14.7	0.2	0.1	579.5
ggH 1J Low	7.2	5.7	5.0	4.4	0.1	9.1	0.5	0.2	289.9
ggH 1J Med	3.6	6.4	4.2	4.1	0.1	1.9	0.6	0.3	156.2
ggH 1J High	0.7	1.9	1.1	1.4	0.1	0.3	0.2	0.1	31.5
ggH 1J BSM	nil	0.1	0.1	0.2	nil	nil	nil	nil	2.2
ggH 2J Low	1.8	2.7	3.7	4.1	2.2	5.4	3.9	1.9	81.1
ggH 2J Med	1.5	3.1	3.2	3.8	2.6	1.6	4.5	2.4	72.4
ggH 2J High	0.6	1.3	1.4	1.9	1.4	0.1	2.2	1.6	29.2
ggH 2J BSM	0.2	0.3	0.4	0.6	0.6	0.1	0.8	1.3	7.6
VBF loose, low p_{T}^{Hjj}	0.2	4.5	0.1	0.1	nil	0.1	0.3	nil	19.4
VBF tight, low p_{T}^{Hjj}	nil	4.2	nil	nil	nil	nil	0.3	nil	13.8
VBF loose, high p_{T}^{Hjj}	0.3	1.4	0.4	0.5	0.4	0.4	1.8	0.5	16.5
VBF tight, high p_{T}^{Hjj}	0.3	3.4	0.2	0.4	0.4	0.2	4.4	0.6	20.2
VH had loose	0.3	0.3	2.4	2.9	0.6	0.2	0.8	0.8	16.5
VH had tight	0.2	0.1	3.0	3.5	0.6	nil	0.5	1.0	12.3
jet BSM	0.4	2.4	1.6	1.9	2.0	0.1	3.1	5.1	26.7
VH MET LOW	nil	nil	0.1	0.6	nil	nil	nil	nil	0.6
VH MET HIGH	nil	nil	0.3	1.4	0.3	nil	0.1	0.8	1.3
VH lep Low	nil	nil	4.4	0.8	1.3	0.2	1.8	2.2	6.4
VH lep High	nil	nil	1.2	0.1	0.6	nil	0.3	1.6	1.5
VH dilep	nil	nil	nil	1.4	0.1	nil	nil	0.1	0.9
tH had 4j2b	nil	nil	nil	0.1	0.6	0.1	1.2	0.3	0.6
tH had 4j1b	nil	nil	0.1	0.3	2.2	0.2	3.8	2.6	2.5
ttH had BDT4	nil	nil	nil	0.2	4.8	nil	1.9	4.7	2.5
ttH had BDT3	nil	nil	nil	nil	1.3	nil	0.3	1.1	0.6
ttH had BDT2	nil	nil	nil	nil	3.8	nil	0.6	3.4	1.8
ttH had BDT1	nil	nil	nil	nil	3.4	nil	0.2	2.5	1.4
ttH lep	nil	nil	nil	nil	5.6	nil	0.4	5.0	2.4
tH lep 1fwd	nil	nil	nil	nil	2.1	nil	2.6	2.3	1.1
tH lep 0fwd	nil	nil	0.1	nil	1.9	nil	1.5	2.1	1.0
Total efficiency	41.8	41.3	37.6	40.5	39.1	42.8	38.9	44.5	41.8
Events	1518.4	119.1	37.1	25.2	16.0	14.8	2.2	0.5	1733.2

8.4.2 Signal $m_{\gamma\gamma}$ distribution

For each category the shape of the diphoton invariant mass distribution of the selected signa events is modeled with a double-sided Crystal Ball function, *i.e.* a Gaussian function in the peak region with power-law functions in both tails. Ignoring a normalization factor, the distribution is described by the function:

$$f(m_{\gamma\gamma}) = \begin{cases} e^{-t^2/2} & \text{if } -\alpha_{\text{low}} \leq t \leq \alpha_{\text{high}} \\ \dfrac{e^{-\frac{1}{2}\alpha_{\text{low}}^2}}{\left[\frac{1}{R_{\text{low}}}(R_{\text{low}} - \alpha_{\text{low}} - t)\right]^{n_{\text{low}}}} & \text{if } t < -\alpha_{\text{low}} \\ \dfrac{e^{-\frac{1}{2}\alpha_{\text{high}}^2}}{\left[\frac{1}{R_{\text{high}}}(R_{\text{high}} - \alpha_{\text{high}} + t)\right]^{n_{\text{high}}}} & \text{if } t > \alpha_{\text{high}} \end{cases},$$

where $t = (m_{\gamma\gamma} - \mu_{\text{CB}})/\sigma_{\text{CB}}$, $R_{\text{low}} = \frac{n_{\text{low}}}{\alpha_{\text{low}}}$, and $R_{\text{high}} = \frac{n_{\text{high}}}{\alpha_{\text{high}}}$. μ_{CB} and σ_{CB} represent the position of the peak and the width of the Gaussian distribution, while α_{low}, α_{high}, n_{low} and n_{high} are parameters related to the tails of the function. In particular, the exponential tails begin for $m_{\gamma\gamma}$ values that differ from the peak by $\alpha \times \sigma$.

The dependence of the parameters on the Higgs boson mass m_H is parametrized in the following way:

$$\begin{aligned} \mu_{\text{CB}}(m_H) &= m_H + B_{\mu_{\text{CB}}}(m_H = 125 \text{ GeV}) + A_{\mu_{\text{CB}}}(m_H - 125 \text{ GeV}), \\ \sigma_{\text{CB}}(m_H) &= \sigma_{\text{CB}}(m_H = 125 \text{ GeV}) + A_{\sigma_{\text{CB}}}(m_H - 125 \text{ GeV}), \\ \alpha_{\text{low}}(m_H) &= \alpha_{\text{low}}, \\ \alpha_{\text{high}}(m_H) &= \alpha_{\text{high}}, \\ n_{\text{low}}(m_H) &= 10, \\ n_{\text{high}}(m_H) &= 10. \end{aligned}$$

The mass dependence is fixed by fitting simultaneously all the simulated signal samples generated for different values of m_H, weighting properly the production modes for the different cross-sections, with the functional dependence mentioned above.

The n parameters only model the slope in the tails and do not affect the mass measurement both because they do not affect the peak of the distribution and because the fraction of signal events in the power-law tails, *i.e.* behind $\mu \pm \alpha \times \sigma$, is very small.

As an example, Figure 8.4 shows, for each parameter of the signal model, the result of the global fit in the inclusive categorization superimposed with the result of separate fits, each one done considering only one value of m_H. The comparison can be strongly affected by the correlation of several parameters, in particular the ones describing the tails.

To check the goodness of the fit, the full procedure is repeated ignoring samples at one particular value of $m_H = m_H^{\text{test}}$. Then the resulting signal model is extrapolated and evaluated for $m_H = m_H^{\text{test}}$ and compared with the signal model obtained fitting only the Monte Carlo samples generated with $m_H = m_H^{\text{test}}$. The relative difference of the means of the two distributions is on average smaller than 0.05%.

The $m_{\gamma\gamma}$ resolution σ_{68} at $m_H = 125.09$ GeV is estimated as half of the smallest range containing 68% of the expected signal events and its value ranges between 1.42 GeV and

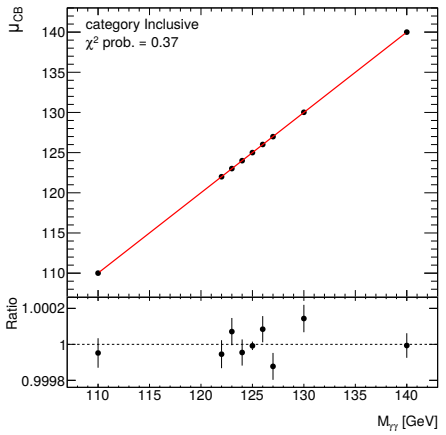

(a) μ_{CB}

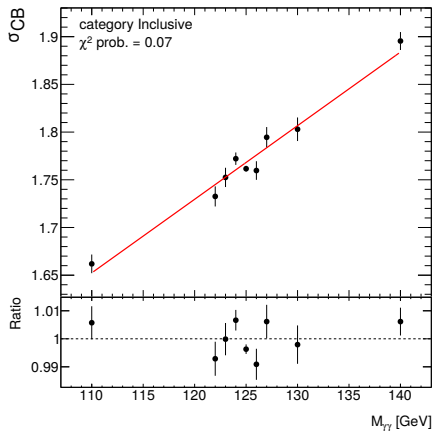

(b) σ_{CB}

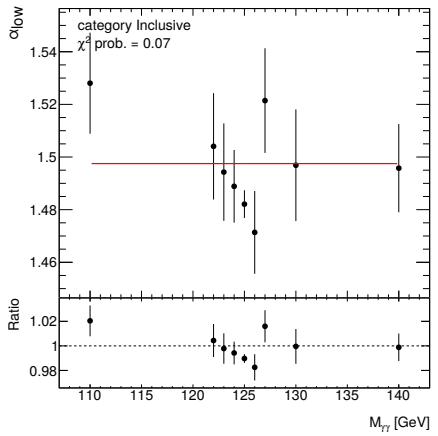

(c) α_{low}

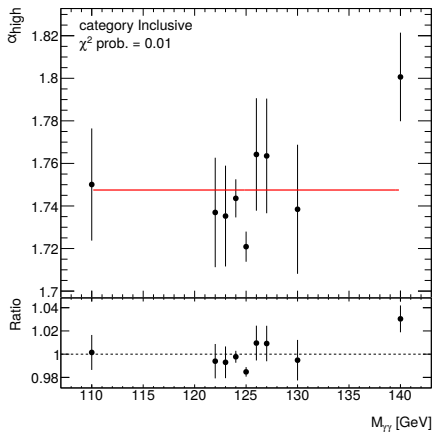

(d) α_{high}

Figure 8.4: Result of the global fit in the inclusive categorization. For each parameter ((a): μ_{CB}, (b): σ_{CB}, (c): α_{low}, (d): α_{high}) the value as a function of m_H obtained by the fit (red line) is shown, superimposed with the value obtained in individual fits for each value of m_H (black dot).

2.14 GeV depending on the category, while for the inclusive case its value is 1.87 GeV. Figure 8.5 shows the signal model for the two most relevant categories for the mass measurement (*i.e ggH 0j CEN* and *ggH 0j FWD*). Table 8.7 summarizes the properties of the signal in each category.

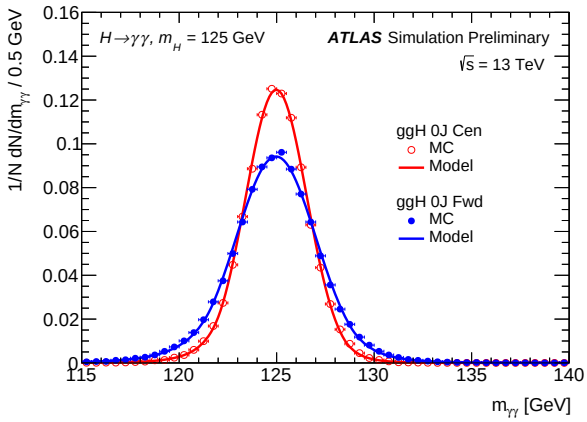

Figure 8.5: Invariant mass distributions (circles) of simulated $H \to \gamma\gamma$ events reconstructed in the two most relevant categories for the mass measurement: *ggH 0J CEN* (open circles) and *ggH 0J FWD* (solid circles). The signal model derived from a fit of the simulated events is superimposed (solid lines) (10).

8.5 Background Model

The main backgrounds to the $H \to \gamma\gamma$ events are the irreducible di-photon QCD production ($\gamma\gamma$), the reducible photon plus jet (γj) and multi-jet (jj) production when the jets are mis-identified as photons. Finally, Drell-Yan events where both electrons are misidentified as photons contribute a small fraction of the selected samples ($< 1\%$).

8.5.1 Background composition

The number of $\gamma\gamma$, γj and jj events entering each category after the final selection is estimated using a double two-dimensional sideband method (195; 196). This data-driven method uses the number of di-photon candidates observed in background enriched control regions to estimate the amount γj and jj events entering the signal region. This method defines 16 orthogonal regions inverting the photon isolation requirement and requesting the photon to pass a looser identification selection (and to fail the tight one). The region where both the photons pass the nominal criteria corresponds to the signal region used in this analysis, while the other 15 regions provide control regions enriched by background events. The composition of the events in the signal region is estimated using the event counts in the 16 regions and solving a system of linear equations that correlate the fraction of background events in the signal regions and in the control region.

The number of events and the relative fraction of the $\gamma\gamma$, γj and jj contributions evaluated using the 2015 and 2016 data are shown in Figure 8.6 as function of $m_{\gamma\gamma}$.

Table 8.7: Summary of the properties of the signal models, background models and observed number of events in data for each category. The numbers in the inclusive case are also reported in the last row of the table. Columns show the half-width σ_{68} of the smallest $m_{\gamma\gamma}$ interval containing 68% of the expected signal events, the number of fitted signal events in the smallest interval expected to contain 90% of the signal events (s_{90}), the number of background events in the smallest interval containing 90% of the signal model b_{90}, the purity $s_{90}/(b_{90}+s_{90})$ in the same interval, and the total number of selected events in data in the range 105 GeV $< m_{\gamma\gamma} <$ 160 GeV used for the fit (10).

category	σ_{68} [GeV]	s_{90}	b_{90}	$s_{90}/(b_{90}+s_{90})$	obs events
ggH 0J CEN	1.61	254	5338	0.05	51722
ggH 0J FWD	2.14	445	20224	0.02	140729
ggH 1J LOW	1.91	329	7934	0.04	62330
ggH 1J MED	1.82	135	2839	0.05	23355
ggH 1J HIGH	1.63	27	235	0.10	2313
ggH 1J BSM	1.44	1.9	7	0.21	88
ggH 2J LOW	1.92	121	3102	0.04	23888
ggH 2J MED	1.82	72	1725	0.04	13955
ggH 2J HIGH	1.64	27	284	0.09	2678
ggH 2J BSM	1.42	7	25	0.21	303
VBF loose, low p_{T}^{Hjj}	1.84	19	109	0.15	895
VBF tight, low p_{T}^{Hjj}	1.64	12	16	0.49	136
VBF loose, high p_{T}^{Hjj}	1.80	23	256	0.08	2009
VBF tight, high p_{T}^{Hjj}	1.66	23	111	0.16	1085
VH had loose	1.71	15	222	0.06	1893
VH had tight	1.54	11	46	0.19	473
jet BSM	1.42	25	280	0.08	2912
VH MET LOW	1.83	0.5	3.4	0.13	26
VH MET HIGH	1.56	1.2	2.3	0.34	25
VH lep LOW	1.78	6	51	0.10	414
VH lep HIGH	1.52	1.4	2.4	0.37	24
VH dilep	1.74	0.8	1.1	0.44	10
tH had 4j2b	1.70	0.6	7	0.08	59
tH had 4j1b	1.66	2.3	48	0.05	422
ttH had BDT4	1.63	2.3	14	0.14	125
ttH had BDT3	1.62	0.6	2.3	0.19	22
ttH had BDT2	1.59	1.6	3.9	0.29	37
ttH had BDT1	1.60	1.3	2.0	0.40	21
ttH lep	1.62	2.2	2.7	0.44	28
tH lep 1fwd	1.72	1.0	1.9	0.35	19
tH lep 0fwd	1.67	0.9	3.6	0.20	34

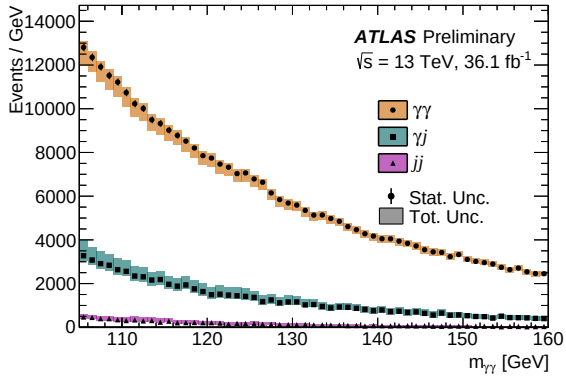

(a)

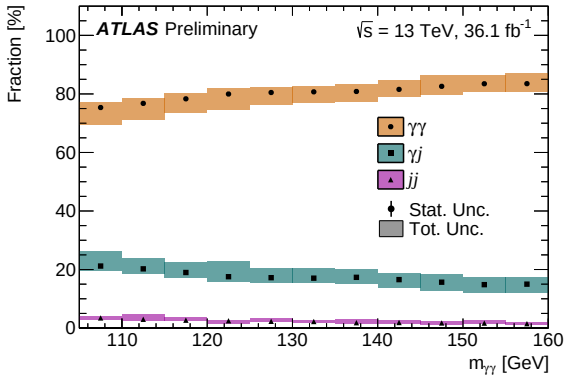

(b)

Figure 8.6: The data-driven determination of (a) event yields and (b) event fractions for $\gamma\gamma$, γj and jj events as a function of of $m_{\gamma\gamma}$ after the final selection outlined in Sec. 8.2 (9).

The fractions of the $\gamma\gamma$, γj and jj background sources in the inclusive di-photon sample are $78.7 \pm 0.2^{+1.8}_{-5.2}\%$, $18.6 \pm 0.2^{+4.2}_{-1.6}\%$ and $2.6 \pm 0.1^{+0.5}_{-0.4}\%$ respectively.

8.5.2 Background $m_{\gamma\gamma}$ distribution

The background $m_{\gamma\gamma}$ distribution is modeled using analytic functional forms for each category. Their parameters are not fixed and are evaluated in the final maximum likelihood fit to the data, but these functional forms are tested on a high statistic background-only Monte Carlo sample.

For each category a template that describes the background $m_{\gamma\gamma}$ distribution is built using the information from data and simulation samples. In particular the shape of the $\gamma\gamma$ background process is directly taken from the simulated $\gamma\gamma$ sample (see Sec. 8.1), while the $m_{\gamma\gamma}$ shapes of γj and jj backgrounds are taken from control regions in data enriched of γj and jj background events by requiring a looser identification criteria (*i.e. loose* identification but failing *tight* requirements) on one or both photons respectively.

The final $m_{\gamma\gamma}$ template in each category is the sum of the $\gamma\gamma$, γj and jj shapes. The relative normalization between them is determined by the composition study explained in the previous section, while the absolute normalization is obtained from a fit to the $m_{\gamma\gamma}$ data distribution in the side-bands region (i.e $105 < m_{\gamma\gamma} < 120$ GeV and $130 < m_{\gamma\gamma} < 160$ GeV).

The composition of background of VH non hadronic categories also contains electroweak contributions from $Z{\to}\nu\nu\gamma\gamma$ (predominantly contributing to the *VH MET* categories), $W{\to}l\nu\gamma\gamma$ (contributing to *VH MET* and leptonic categories) and $Z{\to}\ell\ell\gamma\gamma$ (contributing to *VH dilep*). The background templates for these categories is built from the sum of the electroweak contribution simulated sample and the di-photon MC events normalize to the number of the evens in the side-bands region.

Finally, for the $t\bar{t}H/tH$ categories the background-only template is estimated using two data control regions. This approach is used because the background for these categories consists of a several components ($Z(ll)\gamma\gamma$, $tt\gamma\gamma$, $bb\gamma\gamma$, $cc\gamma\gamma$, $jj\gamma\gamma$, $bc\gamma\gamma$, $WW\gamma\gamma$, etc.), whose modelling and normalization is not well known.

The functional form, that is used to describe the background $m_{\gamma\gamma}$ distribution in the final maximum likelihood fit, is chosen in each category as the one that minimizes the fitted signal yield on the background-only template. In particular, this potential bias induced by the choice of the background model, called *spurious signal*, is estimated as the maximum of the absolute value of the fitted signal yield using a signal model with mass between 121 and 129 GeV. Moreover, the spurious signal is required to be, within 95% confidence level (CL), less than 10% of the expected SM signal yield or less than 20% of the expected statistical uncertainty on the fitted number of signal events. Finally, a minimum χ^2 probability requirement for the fit of the background template with the chosen function is also required (p-value(χ^2) >1%). This requirements is added in order to exclude functions that happen to describe the background in the region $121 < m_{\gamma\gamma} < 129$ GeV, but whose overall fit quality is poor. In case two ore more functions satisfy the requirements, the one with the least number of parameters is chosen.

The functional forms tested are polynomial functions (Poly.), exponential function (Exp.), exponential of second order polynomial (ExpPoly2), Bernstein polynomials (Bern.) of order 3, 4 and 5, and power-law functions (Pow).

An F-test is performed on data-side-bands to check whether functions with extra degrees of freedom describe the data significantly better. A test statistic is computed from the number of degrees of freedoms and χ^2 values of two binned fits to the data, with

the nominal background model or with a model with an extra degree of freedom. It is computed as:

$$F_{1,2} = \frac{(\chi_1^2 - \chi_2^2)/(p_2 - p_1)}{\chi_2^2/(n_{\text{bins}} - p_2)}, \tag{8.3}$$

where χ_1^2 and χ_2^2 are the χ^2 values computed in n bins of the two fits with p_1 and p_2 degrees of freedom, respectively.

The value of the test statistic obtained in the data is compared to the expected distribution obtained from pseudo data produced by assuming that the function with fewer degrees of freedom is the true underlying model. The simpler model is rejected in favor of the more complex one if the probability of finding larger values of the test statistic than in data is lower than 5%.

Finally the spurious signal value of the selected functional form is used as a systematic uncertainty on the signal yield due to the chosen background model. Table 8.8 presents the selected functions for each category and the corresponding background modelling systematic uncertainties.

Table 8.8: Summary of the spurious signal results. In each category, the function chosen to model the background $m_{\gamma\gamma}$ distribution is listed, along with the associated systematic uncertainties on the signal yields expressed in the number of the spurious signal events (N_{spur}), its size relative to the expected statistical error on the signal measurement (Z_{spur}), and its ratio to the predicted number of signal events (μ_{spur}). The "Exponential" and "ExpPoly2" models are exponentials of first- and second-order polynomials; "Pow" refers to first-order Power Law. Bernstein functions of degree 3, 4, and 5 are also considered. All results assume an integrated luminosity of 36.1 fb^{-1} of data.

Category	Model	N_{spur}	Z_{spur} [%]	μ_{spur} (syst) [%]
ggH 0J Cen	ExpPoly2	-26.5	-29.4	-7.95
ggH 0J Fwd	ExpPoly2	-46.0	-24.4	-7.96
ggH 1J LOW	ExpPoly2	32.2	29.3	11.1
ggH 1J MED	ExpPoly2	8.69	13.1	5.54
ggH 1J HIGH	Pow	-3.61	-21.6	-11.5
ggH 1J BSM	Exp.	1.32	43.9	59.7
ggH 2J LOW	ExpPoly2	-13.9	-21.2	-17.1
ggH 2J MED	ExpPoly2	7.78	16.0	10.7
ggH 2J HIGH	Pow	3.64	18.9	12.7
ggH 2J BSM	Pow	2.02	-36.8	-27.2
VBF loose, low p_{T}^{Hjj}	Exp.	3.94	31.2	20.2
VBF tight, low p_{T}^{Hjj}	Exp.	0.417	10.7	2.99
VBF loose, high p_{T}^{Hjj}	Exp.	-2.33	-12.8	-14.0
VBF tight, high p_{T}^{Hjj}	Exp.	2.28	18.8	11.3
VH had loose	Exp.	3.32	18.8	20.1
VH had tight	Exp.	2.27	27.7	18.5
jet BSM	Exp.	7.14	37.3	26.7
VH MET LOW	Exp.	-0.50	-24.1	-81.1
VH MET HIGH	Exp.	0.56	26.6	43.5
VH lep LOW	Exp.	-1.90	-26.3	-29.7
VH lep HIGH	Exp.	0.43	25.6	28.6
VH dilep	Pow	-0.18	-18.0	-19.1
tH had 4j2b	Pow	-0.037	-1.38	-6.52
tH had 4j1b	Pow	-0.25	-3.47	-9.73
ttH had BDT4	Exp.	0.38	10.1	15.4
ttH had BDT3	Exp.	0.06	3.72	9.72
ttH had BDT2	Exp.	0.08	4.55	4.77
ttH had BDT1	Exp.	0.05	3.57	3.75
ttH lep	Pow	-0.25	-16.2	-10.7
tH lep 1fwd	Pow	-0.29	-19.6	-26.2
tH lep 0fwd	Pow	0.29	12.9	28.5

8.6 Systematic uncertainties

The main systematic uncertainties that affect the mass measurement in the di-photon channel are the uncertainties coming from the energy calibration of the photons (energy scale and resolution uncertainties), since they affect the shape of the expected signal model. In particular, the photon energy scale systematic uncertainty induces an uncertainty on the position of the $m_{\gamma\gamma}$ peak of the expected signal, while the photon energy resolution uncertainties result in an uncertainty on the width of the $m_{\gamma\gamma}$ signal distribution.

Since the mass measurement is strictly related to the peak position, the dominant effect on the total m_H systematic uncertainty is due to the photon energy scale uncertainties.

For each source of uncertainty, listed in Sec. 6.5, an alternative invariant mass distribution is obtained by changing the calibration corrections of the photons by $\pm 1\sigma$ in the signal Monte Carlo samples. These distributions undergo a binned fit of the signal model (i.e double sided Crystal Ball) and the propagated uncertainty is defined as the relative difference of the fitted signal parameters with respect to the nominal calibration. The fits are evaluated in the window $m_{\gamma\gamma} \in [115\ \text{GeV}, 135\ \text{GeV}]$. The nominal distribution is first fitted, keeping all of the pdf parameters free. The alternative distributions undergo a fit where the tails parameter of the double-sided Crystal Ball function (α_{low}, n_{low}, α_{high}, n_{high}) are fixed to their nominal values and the mean and width of the distribution are simultaneously floated in order to include the correlation between the two variables.

As explained in Sec. 6.5 the global calibration uncertainty model ("FULL") accounts for 77 independent sources of systematic for the energy scale and 9 independent sources for the energy resolution. An alternative simplified model with only one global variation (*i.e.* 1 nuisance parameter, 1NP) is provided by the ATLAS e/γ calibration group. The 1NP model considers all the systematic effects to be uncorrelated, but fully correlated across η, and sums them in quadrature for a single nuisance parameter for the energy scale and one for the energy resolution. This model leads to a sizeable overestimation of the systematic uncertainty which is not suitable for the precision Higgs boson mass measurement.

To improve the convergence of the final likelihood fit, an intermediate model has been developed according to the Run 1 methodology. The model is hereafter referred to as "FULL Merged". This model merges a given set of nuisance parameters that share the same correlation among categories into a single systematic variation with the same correlation. Scale uncertainties related to material effects are often decorrelated in $|\eta|$. For a given systematic uncertainty source, the number of $|\eta|$ bins will be reduced to two: barrel and endcap. Four sources of systematic uncertainties undergo this procedure: the cryostat material (MATCRYO), the calorimeter material (MATCALO), the pre-sampler material (PS) and the inter-layer calibration (S12). The up and down fluctuation uncertainties of each uncertainty source must first be evaluated. In each category, the final up ($+\sigma$) or down ($-\sigma$) uncertainty is defined as the quadratic sum of the up (down) uncertainty of the merged systematic uncertainty. The sign of the systematic uncertainty is defined as the sign of the linear sum of all the merged up (down) uncertainties.

The FULL Merged model finally reduces the number of NP down to 40 for the energy scale uncertainty, and it does not lead to any deterioration of the total m_H systematic uncertainty. No merging is performed for the energy resolution systematic uncertainties. The complete model, which accounts for 9 sources of systematic uncertainties, is implemented in the analysis.

Figure 8.7 and Figure 8.8 show the uncertainty values for each photon energy scale and resolution variation respectively, propagated to the μ_{CB} peak position and the σ_{CB} resolution parameter in the inclusive event selection. In particular Figure 8.7 shows both the FULL calibration uncertainty model and the FULL Merged one.

Figure 8.9 and Figure 8.10 show respectively the squared sum of all the energy scale and resolution systematic contribution for each categories. The total effect on the mass ranges from $\pm 0.22\%$ in the *ggH 0J CEN* category to $\pm \sim 0.36\%$ in the *ggH 1J BSM* and *ggH 2J BSM* categories. All the energy scale effects are considered fully correlated across categories. Systematic uncertainties in the di-photon mass resolution due to uncertainties in the photon energy resolution vary between $\pm 6\%$ (for the *ggH 0J CEN* category) and 13% (for the *ggH 1J BSM* category), and are expected to have a negligible impact on the mass measurement.

8.6.1 Cross-checks of the mass systematic uncertainty

Three additional methods are implemented in order to validate the systematic uncertainty baseline values obtained as explained in the previous paragraphs. These method are more sensible than the baseline method to the tails of the $m_{\gamma\gamma}$ distributions, since no explicit request on the di-photon invariant mass range are applied.

- $\frac{\langle m_{\gamma\gamma}^{\mathrm{syst}} \rangle}{\langle m_{\gamma\gamma}^{\mathrm{nominal}} \rangle} - 1$ (*ratio-of-mean*). Given, for each scale systematic uncertainty, the nominal di-photon invariant mass distributions, $m_{\gamma\gamma}^{\mathrm{nominal}}$, and the distorted distribution, $m_{\gamma\gamma}^{\mathrm{syst}}$, the uncertainty value is obtained as the relative difference between the mean of the distorted and the nominal distribution.
- $\langle \frac{m_{\gamma\gamma}^{\mathrm{syst}}}{m_{\gamma\gamma}^{\mathrm{nominal}}} - 1 \rangle$ (*mean-of-ratio*). Given a systematic variation, for each event the ratio between the distorted invariant mass value and the nominal one is calculated. Then, the systematic uncertainty values are evaluated as the average of the distribution of the ratios minus 1.
- $\frac{\mu_{\mathrm{CB}}^{\mathrm{syst}}}{\mu_{\mathrm{CB}}^{nom}} - 1$ (*mu-fit*). Similar to the baseline method, the systematic uncertainty is evaluated by fitting a double-sided Crystal Ball to the signal $m_{\gamma\gamma}$ distribution of the distorted samples and the nominal sample. However in this cross-check we use a larger range, $m_{\gamma\gamma} \in [105, 160]$ GeV, and we fix the width parameter σ_{CB} to the value obtained in the fit to the nominal $m_{\gamma\gamma}$ distribution, so that the mean parameter μ_{CB} is the only free parameter in the fit to the distorted cases. Differently from the baseline method, the *mu-fit* method considers as decorrelated the photon energy scale and photon energy resolution effects.

The three methods give an estimation of the systematic uncertainties in good agreement between themselves and also with respect to the reference uncertainty values, as shown in Figure 8.11.

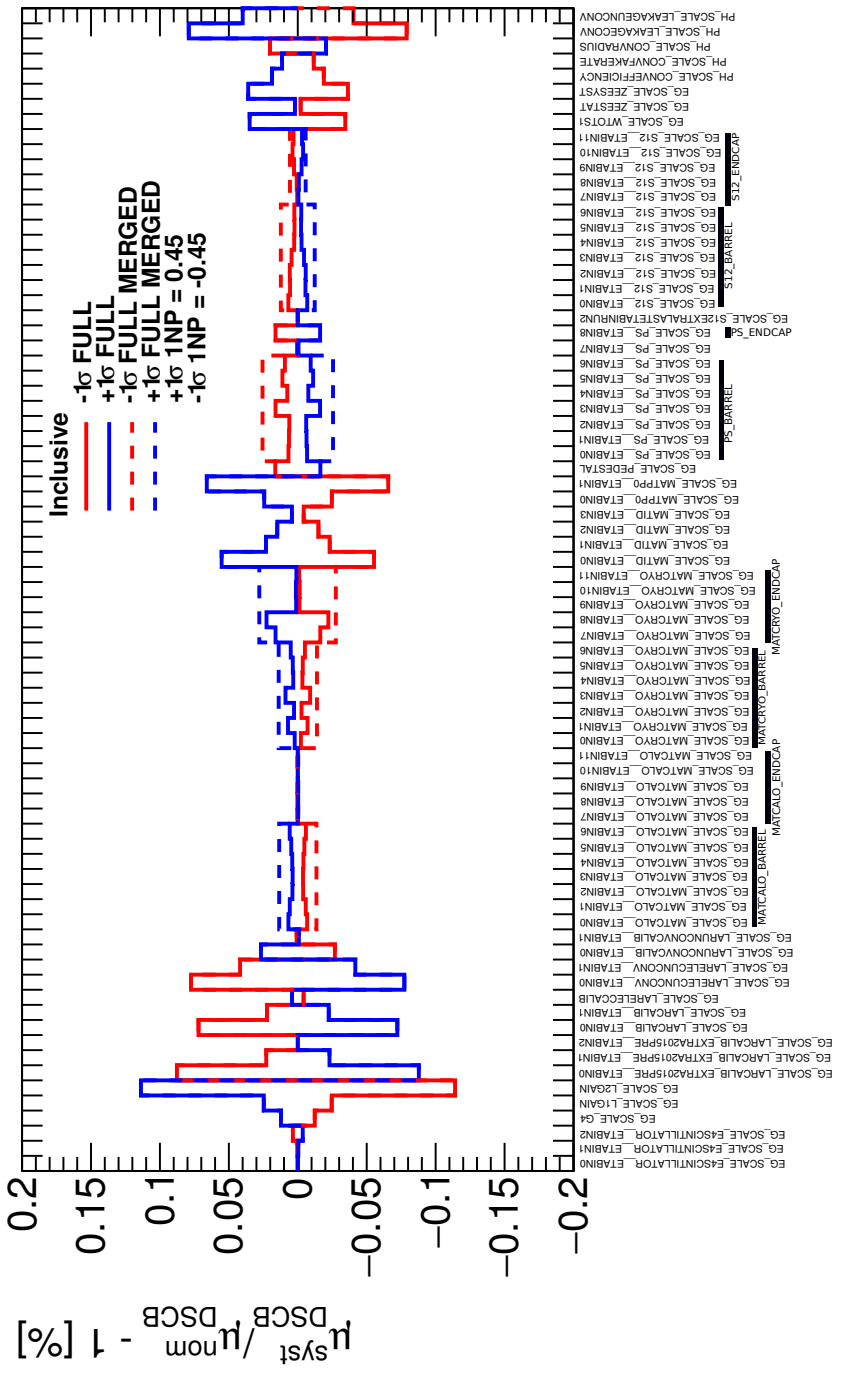

Figure 8.7: Impact of the photon energy scale systematic uncertainties on the $m_{\gamma\gamma}$ peak position in the inclusive event analysis for the FULL (solid line), FULL Merged (dashed line) models propagated from the energy scale systematic variations. In the legend the contribution evaluated using the 1NP model is also reported.

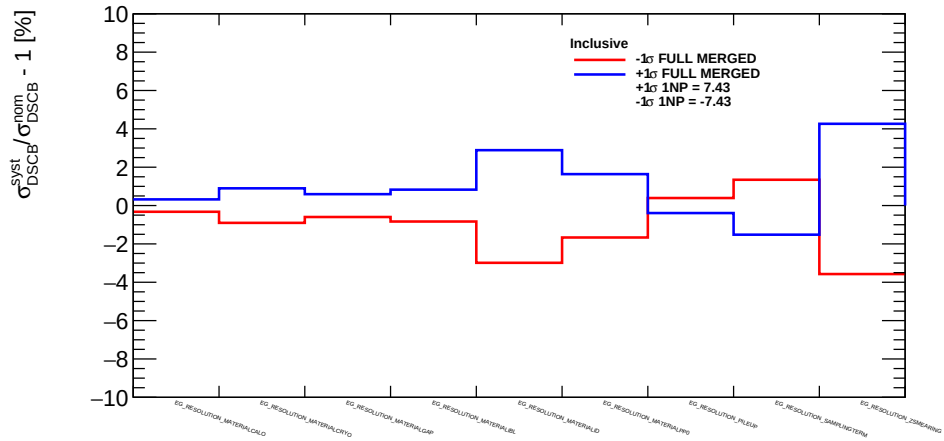

Figure 8.8: Impact of the photon energy resolution systematic uncertainties on the signal $m_{\gamma\gamma}$ width in the inclusive category. In the legend the contribution evaluated using the 1NP model is reported.

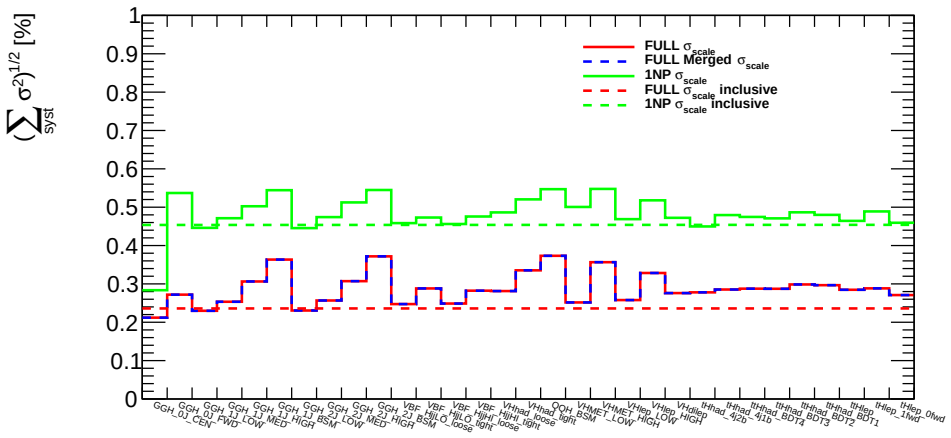

Figure 8.9: $m_{\gamma\gamma}$ scale uncertainties evaluated using the 1NP (green), FULL (red) and FULL Merged (blue) correlation models. The value per category is defined as the quadratic sum of the impact of all systematic contributions on μ_{CB}. In the plot the uncertainty values in the inclusive category for 1NP (dashed green line) and FULL or FULL Merged (dashed red line) are also shown.

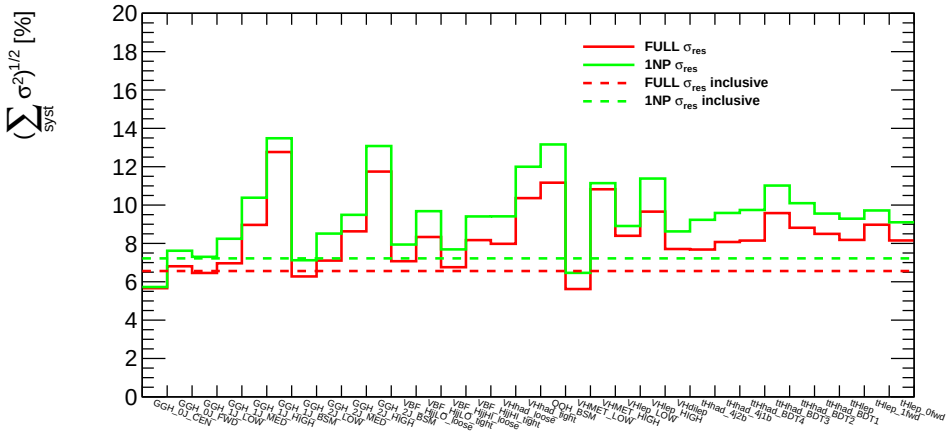

Figure 8.10: Resolution uncertainties evaluated using the 1NP (green), FULL (red) correlation models. The value per category is defined as the quadratic sum of the impact of all systematic contributions on σ_{CB}. In the plot the uncertainty values in the inclusive category for 1NP (dashed green line) and FULL (dashed red line) are also shown.

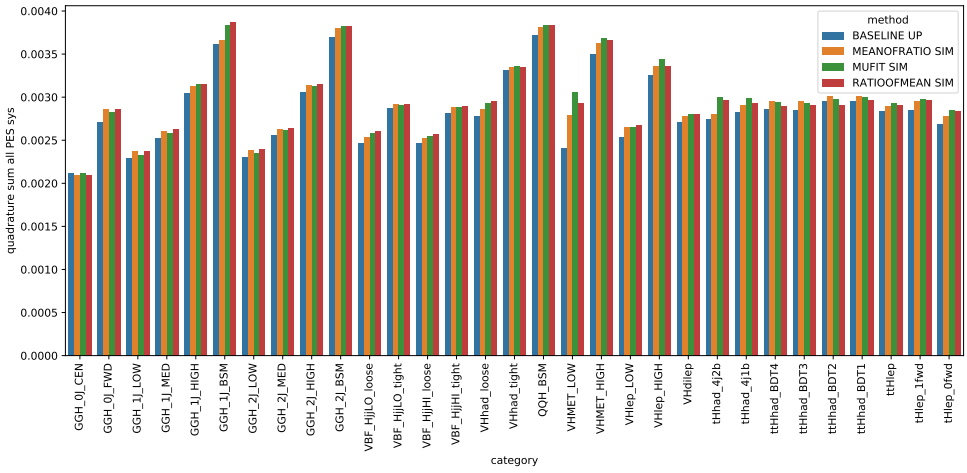

Figure 8.11: Comparison for each category of the total squared sum of the scale systematic uncertainties obtained with the baseline method (blue) and the three methods used as cross-checks (*ratio-of-mean* in red, *mean-of-ratio* in orange, *mu-fit* in green).

8.6.2 Photon energy scale systematic uncertainties as a function of m_H

The propagation of all the components of the photon energy scale to the di-photon mass scale is done using only the signal samples at $m_H = 125$ GeV. The same procedure has been repeated for the other m_H values to check if the uncertainties show a significant dependence on m_H. Since the systematic error on the measured m_H will be quoted with a precision of 10 MeV, it has been decided to ignore the m_H dependency of the mass uncertainty if the sum in quadrature of all the components of the scale systematic does not vary significantly more than 10 MeV in a window which is approximately ± 3 times the total error of Run 1 (11) of the combined measurement: $[124.4, 125.8]$ GeV.

For this study the method *mean-of-ratio* described in Sec. 8.6.1 has been used. No significative changes have been observed when using the method *ratio-of-mean*. Figure 8.12 shows the relative uncertainty on $m_{\gamma\gamma}$ for all the variations of the FULL model for the inclusive categorization using different samples, generated with three different values of m_H: 110 GeV, 125 GeV and 140 GeV. As expected, the systematic uncertainty which shows the largest dependence on m_H is the gain of the electronics in the second layer of the calorimeter. This is due to the fact that the dependency of the value of this uncertainty as a function of p_{T} is quite steep around the average p_{T} value of photons considered in this analysis (~ 60 GeV) as shown by Figure 6.19. Assuming a linear dependence of the uncertainties on m_H the maximum expected variation in the systematic uncertainty is 3 MeV over the range $124.4 < m_H < 125.8$ GeV (for the L2 gain), therefore the $m_{\gamma\gamma}$ scale uncertainties are considered to be constant as a function of m_H.

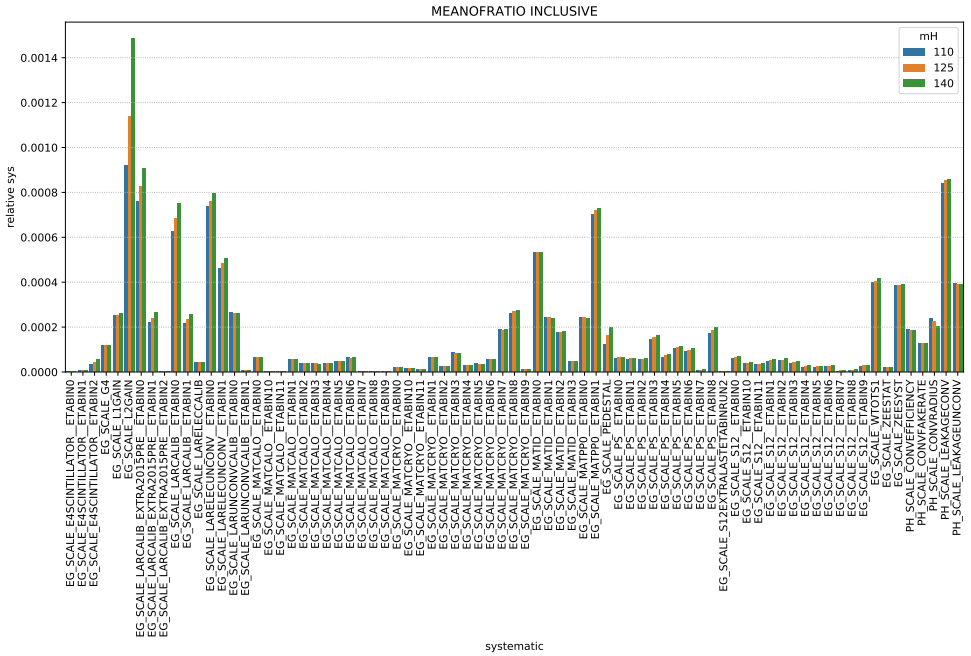

Figure 8.12: Relative uncertainty on $m_{\gamma\gamma}$ due to the photon energy scale uncertainties for each source and for the signal samples generated at m_H equal to 110 GeV (blue), 125 GeV (orange) and 140 GeV (green) for the inclusive case.

8.6.3 Additional systematic uncertainties

Additional potential sources of uncertainty affecting the mass measurement have been considered: the effect of an inaccurate modelling of the signal and the background, and the uncertainty related to the choice of the primary vertex which can affect the angle between the two photons.

A potential bias on the measured m_H can be introduced by the mismodeling of the signal and of the background $m_{\gamma\gamma}$ distribution. An injection test is performed on a sample of simulated background and signal events, properly weighted according to their respective cross sections. To study the bias on the measured Higgs boson mass due to the choice of the background modelling, simulated background events are mixed with Asimov signal samples (see Sec. 8.8), that follow the signal model distribution. The signal is injected using the same functional form used in the fit, so the fitted Higgs boson mass is sensitive only to the accuracy of the background modelling. The samples are then fitted using the nominal signal plus background model. The shift of the extracted mass with respect to the injected one gives an estimate on the bias due to the background modelling. This study is repeated for different injected Higgs boson masses. The spread of the results is shown in Figure 8.13a. The maximum shift between the one at 124, 125 and 126 GeV has been assigned as a systematic uncertainty and it is assumed to be completely decorrelated between each category.

Similarly, the bias induced by the chosen signal model is evaluated using a sample composed by a background Asimov sample and a signal simulation sample, and fitted using the nominal signal plus background model. The measurement has been repeated using MC signal samples generated at different Higgs mass values, as shown in Figure 8.13b. Since the larger shifts observed at $m_H = 124\,\text{GeV}$ and $m_H = 126\,\text{GeV}$ are mainly due the to the smaller size of the signal samples generated at that mass values with respect to the samples generated at $m_H = 125\,\text{GeV}$, only the shifts for the $m_H = 125\,\text{GeV}$ case are used as systematic uncertainties. This systematic uncertainty is assumed to be fully correlated across each category.

Another uncertainty source is the determination of the primary vertex, since this affects the measurement of the angle between the two photons which is used to compute the di-photon invariant mass. The systematic uncertainty related to the reconstruction of the position of the primary vertex is evaluated using $Z \to ee$ events and described in Ref (45). The primary vertex of $Z \to ee$ simulated events is reconstructed with the same technique used for the di-photon events, ignoring the tracks associated to the electrons. The di-electron invariant mass is then recomputed as the di-photon one and compared to the one obtained with the same procedure in the data, leading to a relative uncertainty of $\pm 0.03\%$ on m_H, which is used for all the categories and assumed to be fully correlated across different categories.

Finally, the systematic uncertainty model includes also the uncertainties on the signal yield and on the migration of events between categories described in detail in Ref. (9). These uncertainties have a negligible impact on the Higgs boson mass measurement and therefore they are not further discussed in this document.

Table 8.9 summarizes the main source of systematic uncertainties for the m_H measurement in the di-photon channel and their expected values.[1]

[1] Few values do not completely agree with the one shown in Figure 8.9 since the tables and the plot refer to different e/γ calibration recommendations

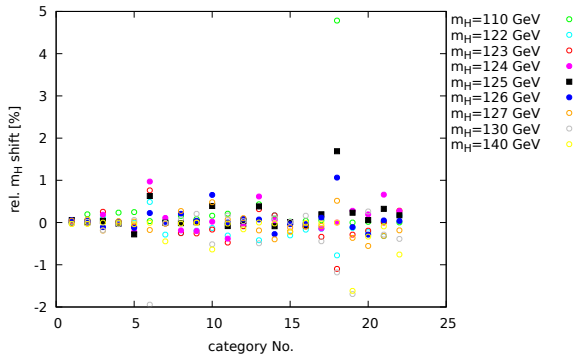

(a)

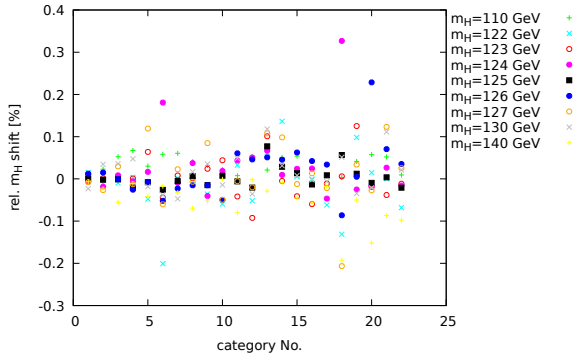

(b)

Figure 8.13: (a) Relative shift of the fitted mass for different injected values of m_H using MC background and Asimov signal. The maximum between the point from 124, 125 and 126 GeV is taken as the systematic uncertainty in each category. (b) Relative shift of the fitted mass for different injected values of m_H using Asimov background and MC signal. The values from $m_H = 125\,\text{GeV}$ are used as the systematic uncertainty in each category.

Table 8.9: Summary of the relative systematic uncertainties in the Higgs boson mass measurement in the $H \to \gamma\gamma$ channel for each category. Values are in %. The impact of the photon energy scale uncertainties is summarized in the first seven columns (10).

	$Z \to ee$ calibration	LAr cell non-linearity	Layer calibration	ID material	Other material	Conversion reconstruction	Lateral shower shape	Vertex measurement	Background modelling	Total
ggH 0J CEN	0.02	0.07	0.16	0.07	0.06	0.04	0.09	0.03	0.06	0.23
ggH 0J FWD	0.05	0.13	0.16	0.13	0.13	0.05	0.10	0.03	0.04	0.31
ggH 1J LOW	0.04	0.11	0.14	0.09	0.10	0.04	0.09	0.03	0.18	0.31
ggH 1J MED	0.04	0.15	0.15	0.09	0.10	0.04	0.09	0.03	0.02	0.27
ggH 1J HIGH	0.04	0.21	0.17	0.09	0.11	0.04	0.09	0.03	0.13	0.35
ggH 1J BSM	0.04	0.26	0.20	0.08	0.10	0.04	0.09	0.03	0.97	1.04
ggH 2J LOW	0.04	0.11	0.14	0.09	0.10	0.04	0.09	0.03	0.11	0.27
ggH 2J MED	0.04	0.15	0.15	0.09	0.10	0.04	0.09	0.03	0.21	0.34
ggH 2J HIGH	0.04	0.21	0.18	0.09	0.11	0.04	0.09	0.03	0.04	0.33
ggH 2J BSM	0.04	0.27	0.21	0.08	0.11	0.04	0.09	0.03	0.65	0.76
VBF loose, low p_T^{Hjj}	0.04	0.14	0.15	0.09	0.10	0.04	0.09	0.03	0.00	0.27
VBF tight, high p_T^{Hjj}	0.04	0.19	0.17	0.08	0.10	0.04	0.09	0.03	0.09	0.31
VBF loose, low p_T^{Hjj}	0.04	0.15	0.15	0.09	0.10	0.04	0.09	0.03	0.62	0.68
VBF tight, high p_T^{Hjj}	0.04	0.19	0.17	0.08	0.10	0.04	0.09	0.03	0.05	0.31
VH had loose	0.04	0.18	0.16	0.09	0.10	0.04	0.09	0.03	0.01	0.30
VH had tight	0.04	0.23	0.19	0.09	0.11	0.04	0.09	0.03	0.04	0.35
jet BSM	0.04	0.28	0.21	0.08	0.11	0.04	0.09	0.03	0.20	0.44
VH MET LOW	0.05	0.19	0.17	0.11	0.11	0.04	0.09	0.03	1.69	1.72
VH MET HIGH	0.04	0.26	0.20	0.09	0.11	0.04	0.09	0.03	0.28	0.47
VH lep LOW	0.04	0.15	0.15	0.09	0.10	0.04	0.09	0.03	0.19	0.34
VH lep HIGH	0.04	0.26	0.19	0.09	0.11	0.04	0.09	0.03	0.66	0.76
VH dilep	0.04	0.17	0.16	0.08	0.10	0.04	0.09	0.03	0.27	0.40
tH had 4j2b	0.04	0.17	0.16	0.09	0.10	0.04	0.09	0.03	0.00	0.29
tH had 4j1b	0.04	0.18	0.17	0.08	0.10	0.04	0.09	0.03	0.00	0.30
ttH had BDT4	0.04	0.19	0.17	0.08	0.10	0.04	0.09	0.03	0.00	0.31
ttH had BDT3	0.04	0.19	0.18	0.08	0.10	0.04	0.09	0.03	0.00	0.31
ttH had BDT2	0.04	0.20	0.18	0.08	0.10	0.04	0.09	0.03	0.00	0.32
ttH had BDT1	0.04	0.20	0.18	0.08	0.10	0.04	0.09	0.03	0.00	0.32
ttH lep	0.03	0.19	0.17	0.08	0.10	0.04	0.09	0.03	0.00	0.30
tH lep 1fwd	0.04	0.19	0.17	0.09	0.11	0.04	0.09	0.03	0.00	0.31
tH lep 0fwd	0.04	0.17	0.16	0.08	0.10	0.04	0.09	0.03	0.00	0.29

8.7 Statistical Model

The parameter of interest (POI) m_H is estimated with a maximum likelihood fit to a binned dataset using $m_{\gamma\gamma}$ and the index of the category as observables (194; 197). The $m_{\gamma\gamma}$ bin width is 0.10 GeV. An extended likelihood function is built from the number of observed di-photon events n_c in each category, their invariant mass $\vec{m}_{\gamma\gamma}$, the signal model and the background model described in Sec. 8.4.2 and 8.5.

The likelihood function $L(m_H, \vec{\theta})$ depends on the parameter of interest m_H and on a set of nuisance parameters $\vec{\theta}$ corresponding to the systematic uncertainty sources and the parameters describing the background functional form. It is constructed as the product of the individual likelihood functions for each of the $N_{\rm cat} = 31$ analysis categories:

$$L(m_H, \vec{\theta}; \vec{n}, \vec{m}_{\gamma\gamma}) = \prod_{c=1}^{N_{\rm cat}} \mathrm{Pois}(n_c|\nu_c(m_H, \vec{\theta})) \prod_{i=1}^{n_c} f_c\left(m^i_{\gamma\gamma}, m_H, \vec{\theta}\right) \prod_k G(\theta_k), \tag{8.4}$$

where θ is a nuisance parameter and $G(\theta)$ is the corresponding unit Gaussian constraint, as described in the following, while $\nu_c(m_H, \theta)$ is:

$$\nu_c(m_H, \vec{\theta}) = s_c(m_H, \vec{\theta}) + b_c + n^c_{\rm spur}\, \theta^c_{\rm spur}, \tag{8.5}$$

where s_c is the number of the Higgs signal expected events , b_c is the number of background events and $n^c_{\rm spur}$ is the spurious signal in the analysis category c. The di-photon mass probability density function is given by

$$f_c\left(m^i_{\gamma\gamma}, m_H, \vec{\theta}\right) = \frac{1}{\nu_c}\left[\left(s_c(m_H, \vec{\theta}) + n^c_{\rm spur}\, \theta^c_{\rm spur}\right) f^c_{\rm sig}(m^i_{\gamma\gamma}, \vec{\theta}_{\text{s-shape}}) + b_c\, f^c_{\rm bkg}(m^i_{\gamma\gamma}, \vec{\theta}^c_{\text{b-shape}})\right], \tag{8.6}$$

where $f^c_{\rm sig}(m_{\gamma\gamma})$ is the mass PDF (see Sec. 8.4.2) with associated uncertainties $\vec{\theta}_{\text{s-shape}}$ related to the di-photon resolution and peak position as described in Sec. 8.6. The background PDF $f^c_{\rm bkg}(m_{\gamma\gamma})$ is described in Sec. 8.5, and has a set of associated shape parameters $\vec{\theta}_{\text{b-shape}}$ and a normalization b_c. These parameters are free to float and are not constrained.

The number of expected signal events is parametrized as a function of the expected SM yield for each of the four main production mode of the Higgs boson at the LHC and as a function of the four signal strength μ_{ggH} , μ_{VBF} , μ_{VH} , μ_{top}.

$$s_c = \sum_{i=ggH,VBF,VH,top} \mu_i\, s_{ic}(\vec{\theta}_{\rm sig}, \theta_{\rm lumi}, \theta_{\rm BR}), \tag{8.7}$$

where the central value of the number of SM expected Higgs events s_{ic} in the category is obtained as:

$$\nu_{ic} = BR(m_H, \theta_{\rm BR}) \times \sigma_i(m_H, \vec{\theta}_{\rm sig}) \times (A \times \epsilon)_{ic}(\vec{\theta}_{\rm sig}) \times \mathcal{L}(\theta_{\rm lumi}), \tag{8.8}$$

where the parameterizations of the production cross section (σ) and di-photon branching ratio (BR) is taken from the Ref. (41) and the acceptance times efficiency per production mode is evaluated as explained in Sec. 8.4.1.

For a systematic uncertainty for which a Log-normal function is used, the quantity in the likelihood affected by this uncertainty is multiplied by a term of the form:

$$K(\theta) = e^{\sqrt{\log(1+\sigma^2)}\theta}, \tag{8.9}$$

where σ is the "best estimate" of the relative uncertainty of the considered systematic variation, and θ, is the nuisance parameter and nominally is equal to 0. The likelihood is then multiplied by $G(a = 0|\theta, 1)$, where G is a normal distribution with width equal to unity and centered at θ and a is called the *global observable*. This means that the logarithm of the quantity $e^{\sqrt{\log(1+\sigma^2)}\theta}$ has a Gaussian p.d.f with mean 0 and width equal to one.

For a systematic uncertainty for which a Gaussian form is used, the quantity in the likelihood affected by this uncertainty is multiplied by a term of the form:

$$K(\theta) = (1 + \sigma\theta), \tag{8.10}$$

and the likelihood is multiplied by $G(\theta)$, which is still a Gaussian with mean equal to zero and width equal to 1.

When two uncertainties are considered fully correlated, they share the same nuisance parameter θ with different values of σ.

The parameter of interest m_H and its uncertainty are determined with the profile likelihood ratio test statistic:

$$\lambda(m_H) = -2 \ln \frac{L(m_H,\ \hat{\hat{\vec{\theta}}}_{m_H})}{L(\hat{m}_H,\ \hat{\vec{\theta}})}, \tag{8.11}$$

where $\hat{m}_H$ and $\hat{\vec{\theta}}$ are the values of the combined parameter of interest and nuisance parameters that unconditionally maximize the likelihood while $\hat{\hat{\vec{\theta}}}_{m_H}$ are the values of the nuisance parameters that maximize the likelihood on the condition that m_H is held fixed to a given value (194).

The total uncertainty is obtained from the width of the negative log-likelihood ratio scan with all parameters profiled (*i.e* given a value of m_H, $\lambda(m_H)$ is maximized with respect to the nuisance parameters). The statistical uncertainty is determined by fixing all nuisance parameters to their best-fit values, except for the signal-strength scale factors and the background function parameters, which are profiled. The systematic uncertainty is determined by subtracting in quadrature the statistical uncertainty from the total uncertainty.

8.8 Expected results

In order to estimate the expected values of the uncertainties on the m_H value, a fit on an Asimov dataset corresponding to the SM expectations (*i.e.* all μ set to 1.0, m_H = 125.09 GeV, all nuisance parameters set to 0) is performed.

The best value obtained for m_H from the fit is:

$$m_H^{\gamma\gamma} = 125.09 \pm 0.42\,\text{GeV} = 125.09 \pm 0.25(\text{stat}) \pm 0.33(\text{syst})\,\text{GeV},$$

where the first error is the statistical uncertainty while the second is the total systematic uncertainty. They correspond to a total relative error of 0.33% and a relative systematic uncertainty of 0.26%.

Figure 8.18 shows the ranking plot of the contributions to the Higgs boson mass systematic uncertainty. As expected, the photon energy scale uncertainties give the dominant

contribution, in particular the L2 gain uncertainty, while other effects, including energy resolution uncertainties, play a negligible role. The same figure also shows the difference between the best-fit value of the nuisance parameters and the initial one ($\theta_0 = 0$) normalized with respect do their uncertainty ("the pull"). Their compatibility with zero is a check of the robustness of the fit procedure.

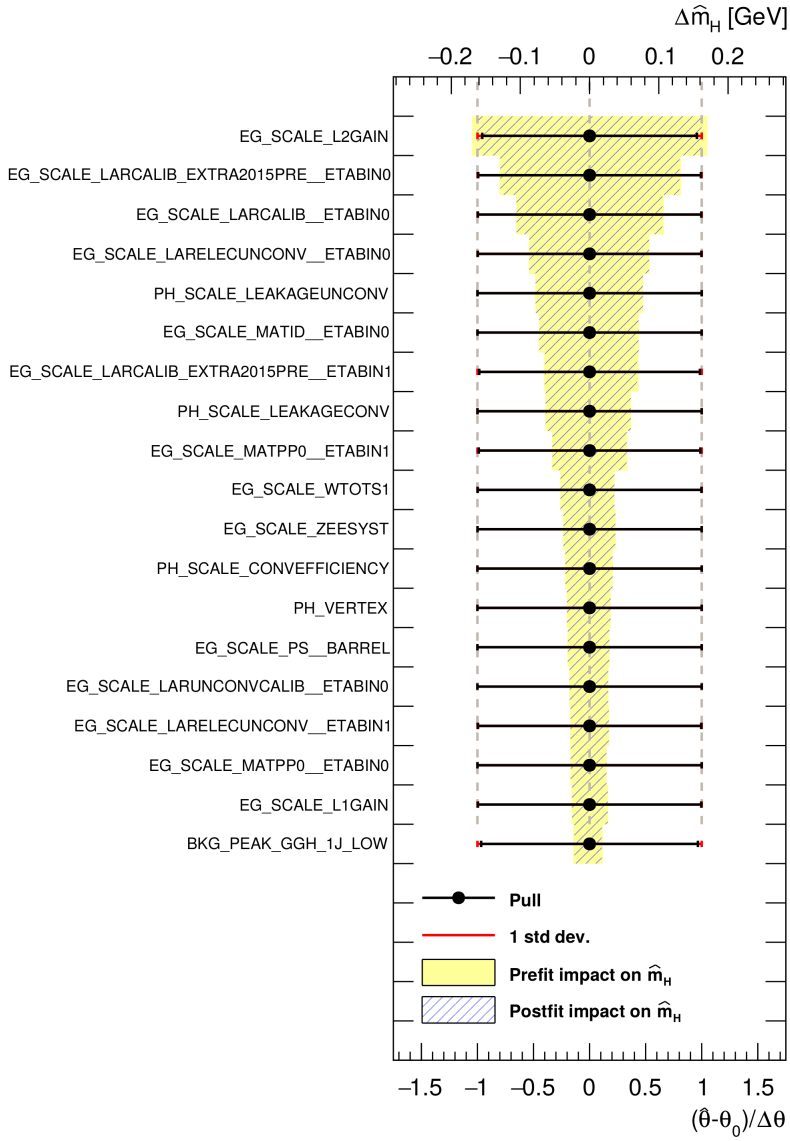

Figure 8.14: Ranking plot of the contribution to the Higgs boson mass systematic uncertainty obtained by a fit on an Asimov dataset corresponding to the SM expectations.

8.9 Results

The measured mass of the Higgs boson in the di-photon channel is:

$$m_H^{\gamma\gamma} = 125.11 \pm 0.42\,\text{GeV} = 125.11 \pm 0.21(\text{stat}) \pm 0.36(\text{syst})\,\text{GeV},$$

where ± 0.42 GeV is the total uncertainty, ± 0.21 GeV is the statistical uncertainty while ± 0.36 GeV is the total systematic uncertainty, dominated by the photon energy scale uncertainty. They correspond to a total relative error of 0.34% and a relative systematic uncertainty of 0.29%. The measurement is dominated by the photon energy scale uncertainty (10).

Figure 8.15 shows the inclusive distribution of the data superimposed with the result of the simultaneous fit and Figure 8.16 shows the invariant mass distributions for the sums of the categories most sensitive to the different production modes; for illustration purposes events in each category are weighted by the corresponding factor $\log(1+s_{90}/b_{90})$, where s_{90} and b_{90} are the signal and background yields evaluated in the smallest interval expected to contain 90% of the signal events.

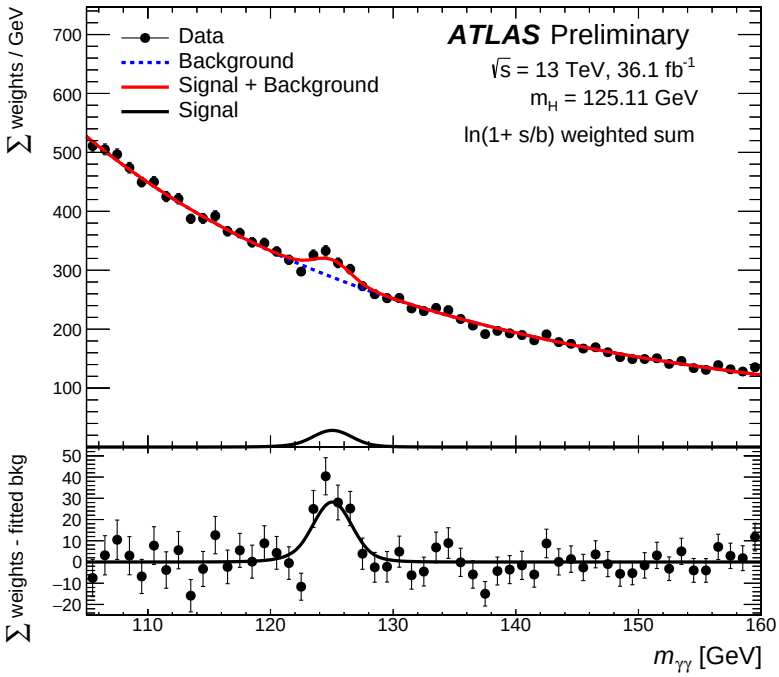

Figure 8.15: Diphoton invariant mass distribution of the data superimposed with the result of the fit. Both for data and the fit each category is weighted by a factor $\log(1 + s_{90}/b_{90})$, where s_{90} and b_{90} are the signal and background yields evaluated in the smallest interval expected to contain 90% of the signal events. The dashed line represents the background component of the model, while the black line the signal component. The bottom inset is the difference between the sum of weights and the background component of the fitted model (10).

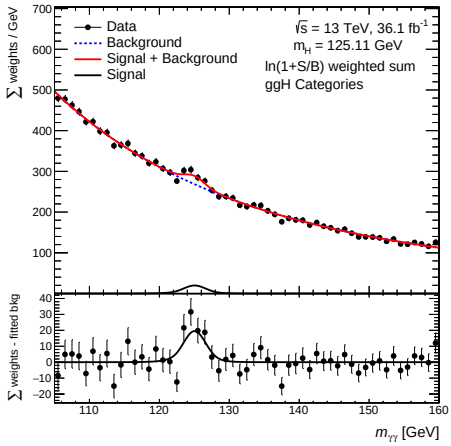

(a) ggH

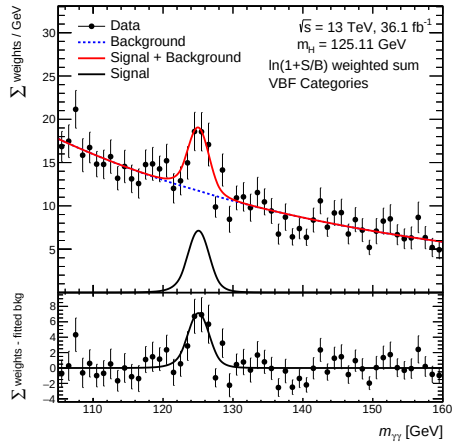

(b) VBF

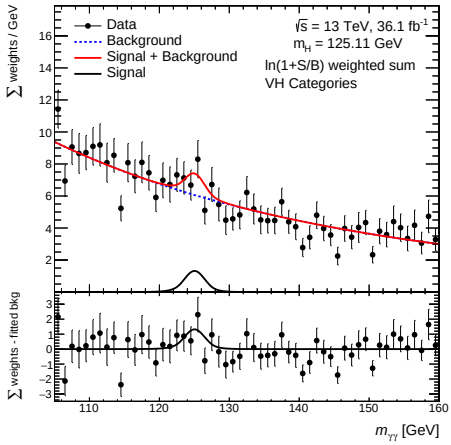

(c) VH

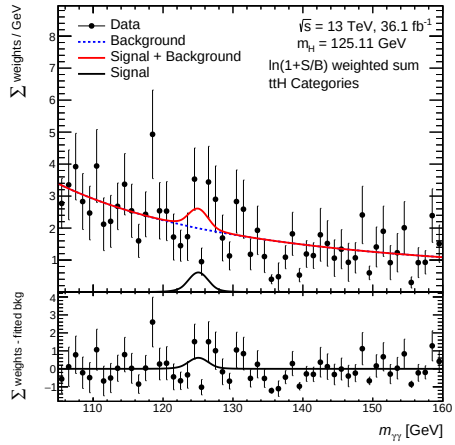

(d) $t\bar{t}H$

Figure 8.16: Di-photon invariant mass distribution of the data superimposed with the result of the fit for events belonging to: (a) ggH categories, (b) VBF categories, (c) VH categories and (d) $t\bar{t}H$ categories. Both for data and the fit each category is weighted by a factor $\log(1 + s_{90}/b_{90})$, where s_{90} and b_{90} are the signal and background yields evaluated in the smallest interval expected to contain 90% of the signal events. The dashed line represents the background component of the model, while the black line the signal component. The bottom inset is the difference between the sum of weights and the background component of the fitted model.

Figure 8.17 shows the scan of the profiled likelihood ratio comparing the expected results obtained by the fit to the Asimov dataset to the result obtained with the data.

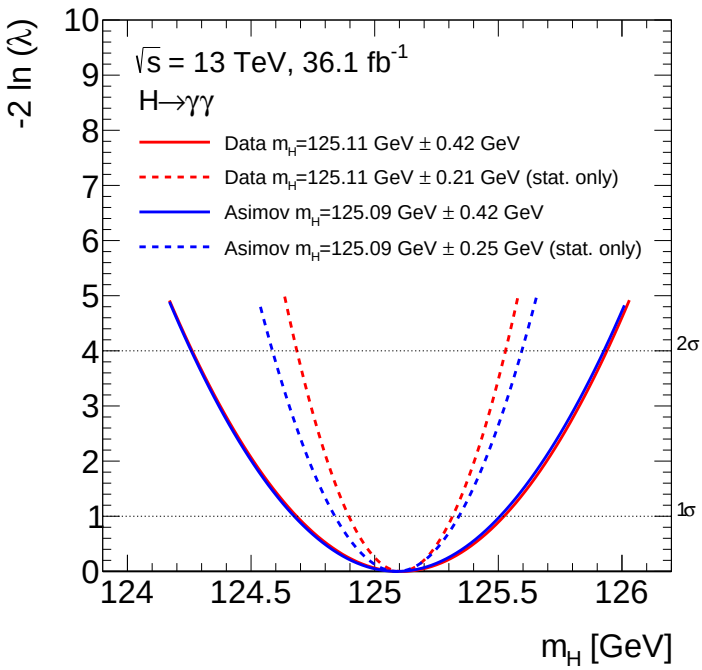

Figure 8.17: Profile likelihood ratio obtained by a fit on an Asimov dataset corresponding to the SM expectations and data corresponding to 36.1 fb^{-1} of pp collision collected at $\sqrt{s} = 13$ TeV.

The main systematic contributions are shown in the post-fit pulls plot in Figure 8.18. Overall the values of the nuisance parameters associated with the systematic uncertainties show no large ($> 1\sigma$) shifts in the fit to the data with respect to their expectations.

For illustration purposes the effects of systematic uncertainties coming from similar underlying sources are summed together and shown in Table 8.10. The main contributions arise from the *LAr cell non-linearity* term, which includes the gain uncertainty, and the systematic uncertainties coming from the layer inter-calibration, in particular from the additional nuisance parameters which describe the Run 1-Run 2 difference in the measurement of $\alpha_{1/2}$ (see Sec. 6.5).

The uncertainty induced on the mass value from each systematic uncertainty source is determined both from the difference of the global uncertainty for m_H when the corresponding nuisance parameter is removed by fixing it to its best-fit value, and from the difference between the m_H statistical only uncertainty value and the one obtained fixing all the nuisance parameters to their best-fit values except for the one under investigation. The two methods give results in good agreement with each other.

The larger systematic uncertainty observed in data with respect to the expectation is due to a negative fluctuation of the signal yield with respect to the SM expectation in some categories with large expected yield and small photon energy scale uncertainty (*e.g. ggH 0J CEN*). The smaller statistical uncertainty observed in data is due to the fitted

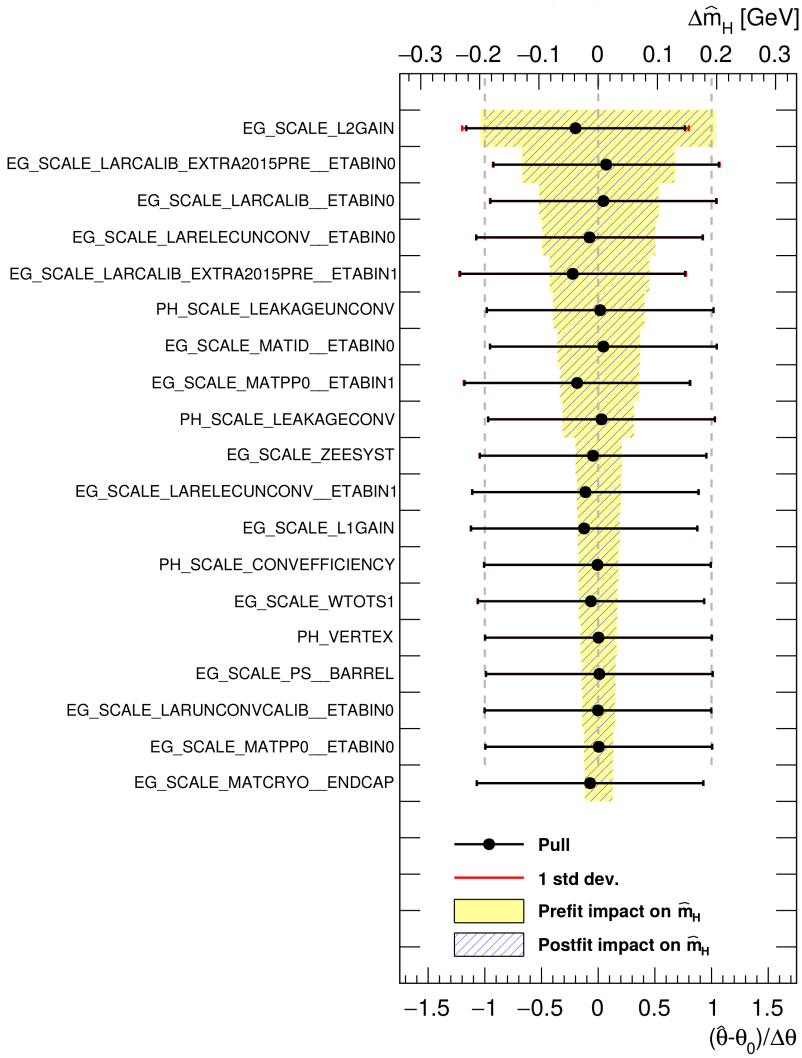

Figure 8.18: Ranking plot of the contribution to the Higgs boson mass systematic uncertainty obtained by a fit on data corresponding to 36.1 fb^{-1} of pp collision collected at $\sqrt{s} = 13$ TeV.

Table 8.10: Main sources of systematic uncertainty on $m_H^{\gamma\gamma}$ (10)

Source	Systematic uncertainty on $m_H^{\gamma\gamma}$ [MeV]
LAr cell non-linearity	± 200
LAr layer calibration	± 190
Non-ID material	± 120
Lateral shower shape	± 110
ID material	± 110
Conversion reconstruction	± 50
$Z \to ee$ calibration	± 50
Background model	± 50
Primary vertex effect on mass scale	± 40
Resolution	$^{+20}_{-30}$
Signal model	± 20

resolution in data being a few percent better than in the simulation (but still agreeing with it within less than one standard deviation).

In order to obtain this information an Asimov dataset is generated using as input the post-fit values for the signal strength per reconstructed category (*i.e.* the ratio between the observed and the expected total events in each category) and the resolution parameters. When the nominal model described in Sec. 8.7 is fitted on this modified Asimov dataset, results compatible with the ones observed in data are obtained.

8.10 Cross-Checks

In order to verify the robustness of the mass measurement and to check the possible presence of biases in the photon calibration, the entire analysis is repeated for two additional detector-oriented categorizations, that are based on:

- the conversion status of the two photons (UU: both unconverted; CC: both converted; UC: one photon converted and one unconverted), in order to verify biases between the unconverted and converted photon calibration;

- pseudorapidity (BB: both photons in the barrel; EE: both photons in the endcap; BE: one photon in the barrel and one in the endcap), in order to verify biases between the barrel and the endcap region.

Instead of a single value of m_H, the fit is repeated allowing for a different value of m_H in each category. Then the compatibility of all these values with a common one (*i.e.* $\hat{\hat{m}}_H$, averaged over the other categories) is estimated. In particular, in each category i we parametrize m_H^i as $\hat{\hat{m}}_H + \Delta_i$ and then evaluate the compatibility of $\vec{\Delta}$ with $\vec{0}$ using asymptotic formula for a χ^2 distribution with $N_{\text{cat}} - 1$ degrees of freedom.

The compatibility test is performed trying to exclude the null hypothesis: "m_H is the same in all the categories." This can be checked assuming as alternative hypothesis two kind of hypotheses, for example: "only m_H in category i is different" or "the values of m_H in all the categories are different." The test based on the second hypothesis is less powerful, but more general. The test is done implementing a likelihood function where the value of the mass of the Higgs boson is replaced by $m_H + \Delta_i$, where i is the index of

the category. For the first alternative hypothesis the following test statistic is used:

$$q_0^{(1)} = -2\ln\frac{L(\Delta_1 = 0, \Delta_2 = 0, \ldots \Delta_n = 0, \hat{\hat{m_H}})}{L(\hat{\Delta}_1, \Delta_2 = 0, \ldots, \Delta_n = 0, \hat{m_H})}.$$

All the other parameters, including m_H, the four μ and all the pulls are profiled. The asymptotic approximation is assumed, so $q_0^{(1)}$ is assumed to be distributed as a χ^2 with 1 degree of freedom. For the second kind of alternative hypothesis, which is the one implemented for the cross check, the test statistic

$$q_0 = -2\ln\frac{L(\Delta_1 = 0, \Delta_2 = 0, \ldots \Delta_n = 0, \hat{\hat{m_H}})}{L(\hat{\Delta}_1, \hat{\Delta}_2, \ldots, \hat{\Delta}_n, \hat{m_H})},$$

is used and it is assumed to be distributed as a χ^2 with $n-1$ degree of freedom.

All the cross checks with specific categories are shown in Figure 8.19: no significant discrepancy is observed, the p-value for the conversion based categorization is 83%, and the p-value for the barrel/endcap categorization is 52%. The same procedure is applied to the categories used in the analysis: the smallest p-value computed on single categories is 7% while the global one is 94%.

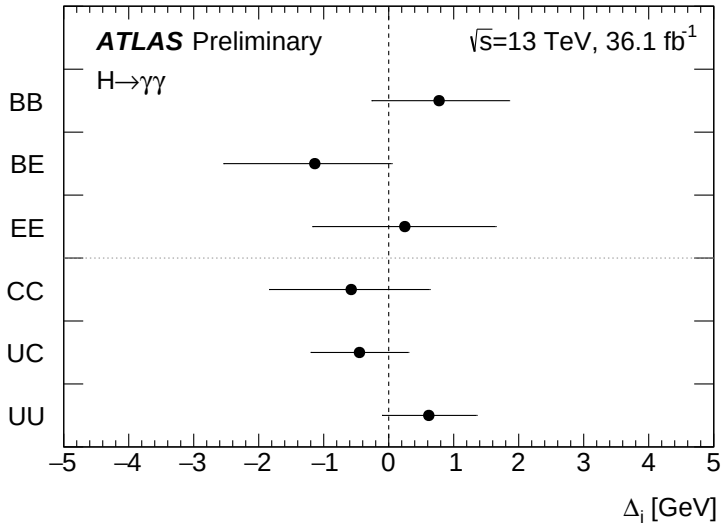

Figure 8.19: Difference between the Higgs boson mass m_H measured with di-photon decays using a single category and the one obtained with a combined fit to all the categories, using two different categorizations. The top three points with error bars correspond to categories based on the pseudorapidity of the two photon candidates: both photons are in the barrel calorimeter (BB), one in the barrel and one in the endcap calorimeter (EB), or both photons are in the endcap calorimeter (EE). The bottom three points with error bars correspond to categories based on the conversion status of the two photon candidates: both photons are reconstructed as converted ones (CC), one photon is unconverted and the other one is converted (UC), both photons are unconverted ones (UU). The error bars represent the total uncertainty (10).

8.11 Combination with the $H \to ZZ^* \to 4\ell$ channel

The Higgs boson mass measured in the di-photon channel is combined with the information from the $H \to ZZ^* \to 4\ell$ channel.

8.11.1 Mass measurement in $H \to ZZ^* \to 4\ell$ channel

A measurement of the Higgs boson mass using 36.1 pb^{-1} of pp collision is also performed by the ATLAS collaboration using the $H \to ZZ^* \to 4\ell$ channel (10). The measured value of m_H is:

$$m_H^{ZZ^*} = 124.88 \pm 0.37 \text{ (stat)} \pm 0.05 \text{ (syst) GeV} = 124.88 \pm 0.37 \text{ GeV}.$$

The total uncertainty is in agreement with the expectation of ± 0.35 GeV and is dominated by the statistical component. The total systematic uncertainty is 47 MeV, with the leading sources being the muon momentum scale (40 MeV), the electron energy scale (20 MeV), the background modelling (10 MeV) and the simulation statistics (8 MeV), as summarized in Table 8.11. With respect to the di-photon channel, the measurement of m_H in the four lepton channel is characterized by a smaller systematic uncertainty. This is due to the fact that this measurement is dominated by the information extracted from the four muon final state, that is affected by smaller calibration uncertainties, as shown from Figure 8.20.

Table 8.11: Leading sources of systematic uncertainty on m_H in the $H \to ZZ^* \to 4\ell$ channel (10).

Systematic effect	Uncertainty on $m_H^{ZZ^*}$ [MeV]
Muon momentum scale	40
Electron energy scale	20
Background modelling	10
Simulation statistics	8

8.11.2 Combination

Different m_H values are tested using a profile likelihood ratio defined in terms of a common mass m_H, while treating the signal strengths (μ^{ZZ}, $\mu^{\gamma\gamma}_{\text{ggH}}$, $\mu^{\gamma\gamma}_{\text{VBF}}$, $\mu^{\gamma\gamma}_{\text{VH}}$, $\mu^{\gamma\gamma}_{\text{ttH}}$) as independent nuisance parameters:

$$\Lambda(m_H) = \frac{L\big(m_H, \hat{\hat{\mu}}^{ZZ}(m_H), \hat{\hat{\mu}}^{\gamma\gamma}_{\text{ggH}}(m_H), \hat{\hat{\mu}}^{\gamma\gamma}_{\text{VBF}}(m_H), \hat{\hat{\mu}}^{\gamma\gamma}_{\text{VH}}(m_H), \hat{\hat{\mu}}^{\gamma\gamma}_{\text{ttH}}(m_H), \hat{\hat{\theta}}\big)}{L\big(\hat{m}_H, \hat{\mu}^{ZZ}, \hat{\mu}^{\gamma\gamma}_{\text{ggH}}, \hat{\mu}^{\gamma\gamma}_{\text{VBF}}, \hat{\mu}^{\gamma\gamma}_{\text{VH}}, \hat{\mu}^{\gamma\gamma}_{\text{ttH}}, \hat{\theta}\big)}.$$

The correlations between the systematic uncertainties in the four leptons and di-photon channels are included in the model. The energy scale and resolution systematic uncertainties are correlated between the two analyses since they affect both photon and electron energy measurement. The yield uncertainties coming from the luminosity measurement and the pileup modelling are considered correlated as well. The other shape

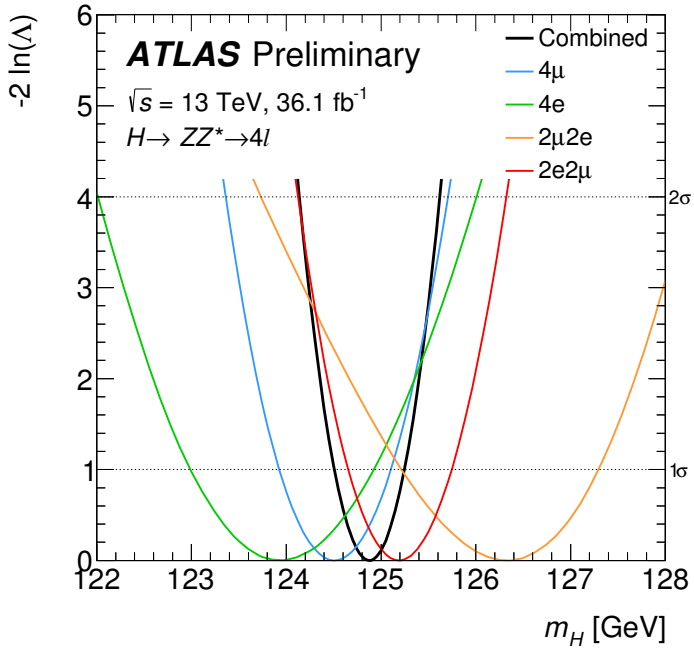

Figure 8.20: Value of $-2\ln\Lambda$ as a function of m_H for the combined fit to all $H \to ZZ^* \to 4\ell$ categories (10).

systematic uncertainties (*e.g.* signal modelling, background modelling and vertex definition), that have been illustrated in Sec. 8.6.3, affect only the mass measurement in the $H \to \gamma\gamma$ channel and therefore are considered uncorrelated between the two analysis.

Figure 8.21 shows the value obtained from the likelihood scan as a function of m_H for $H \to ZZ^* \to 4\ell$, $H \to \gamma\gamma$, and their combination. The combined mass measured is

$$m_H = 124.98 \pm 0.19\ (\text{stat}) \pm 0.21\ (\text{syst})\ \text{GeV} = 124.98 \pm 0.28\ \text{GeV},$$

where the first (second) uncertainty corresponds to the statistical (systematic) component. They correspond to a total relative uncertainty of 0.22% and a relative systematic uncertainty of 0.17%.

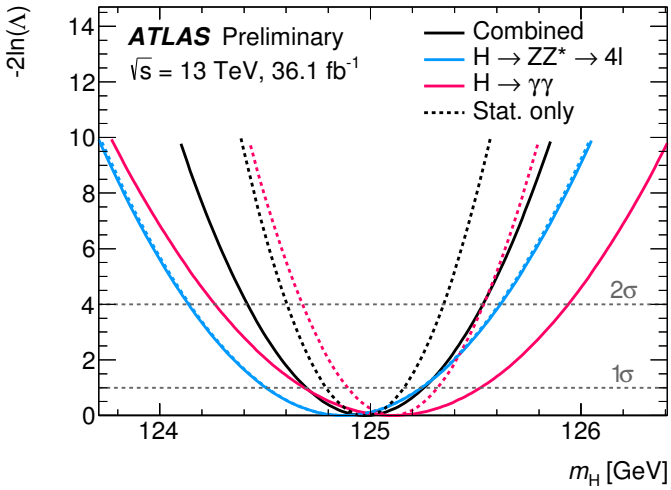

Figure 8.21: The value of $-2\ln\Lambda$ as a function of m_H for the individual channels $H \to ZZ^* \to 4\ell$ and $H \to \gamma\gamma$, and their combination (blue, red, and black respectively). The dashed lines show the statistical component of the mass measurements (10).

The contributions of the main sources of systematic uncertainty to the combined mass measurement are summarized in Table 8.12. No significant deviations from the pre-fit input values of the most significant nuisance parameters are observed after the fit.

Table 8.12: Main sources of systematic uncertainty on the combined mass m_H (10).

Source	Systematic uncertainty on m_H [MeV]
LAr cell non-linearity	90
LAr layer calibration	90
Non-ID material	60
ID material	50
Lateral shower shape	50
$Z \to ee$ calibration	30
Muon momentum scale	20
Conversion reconstruction	20

The difference between the masses measured in the $H \to ZZ^* \to 4\ell$ and $H \to \gamma\gamma$ channels, obtained using a dedicated test statistic (see Sec. 8.10), is measured to be

$$\Delta m_H = 0.23 \pm 0.42 \text{ (stat)} \pm 0.36 \text{ (syst)} \text{ GeV} = 0.23 \pm 0.55 \text{ GeV}.$$

The combined mass measured is in excellent agreement with, and has similar precision to, the value that was measured with a combined fit to the ATLAS and CMS Run 1 data (11):

$$m_H = 125.09 \pm 0.21 \text{ (stat)} \pm 0.11 \text{ (syst)} \text{ GeV} = 125.09 \pm 0.24 \text{ GeV}.$$

The results from each of the individual channels and their combination, along with the LHC Run 1 result, are summarized in Figure 8.22.

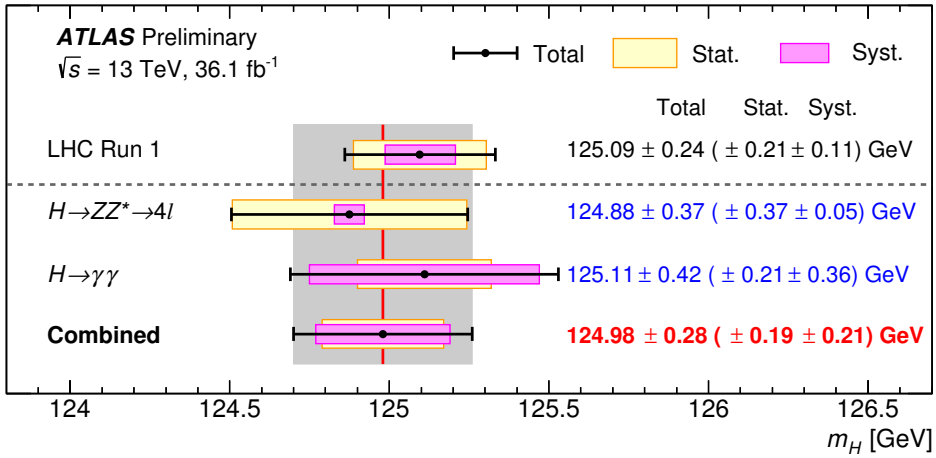

Figure 8.22: Summary of the Higgs boson mass measurements from the individual and combined analyses performed here, compared to the combined Run 1 measurement by ATLAS and CMS (11). The systematic (magenta-shaded bands), statistical (yellow-shaded bands), and total (black error bars) uncertainties are indicated. The (red) vertical line and corresponding (gray) shaded column indicate the central value and the total uncertainty of the combined measurement, respectively (10).

Chapter 9

Search for Superymmetry in $\gamma\gamma + E_{\mathrm{T}}^{\mathrm{miss}}$ final state

This chapter presents a search for signatures of supersymmetry in events containing two energetic isolated photons and large missing transverse momentum generated in proton-proton collision data at $\sqrt{s} = 13$ TeV recorded with the ATLAS detector (26). The results are interpreted in the context of the supersymmetric general gauge mediation (GGM) models (19; 20; 21; 22; 23; 24; 25) (see Chap. 2). These results extend those of prior studies with 8 TeV collision data from Run 1 by the ATLAS (27) and CMS (77) experiments.

In all GGM models, the lightest supersymmetric particle is the gravitino $\tilde{G}$, with a mass significantly less than 1 GeV. In the GGM model considered here, the decay of the supersymmetric states produced in pp collisions proceeds through a degenerate octet of gluinos through the next-to-lightest supersymmetric particle, the neutralino $\tilde{\chi}_1^0$. This would then decay to the $\tilde{G}$ LSP and one or more SM particles, with a high probability of decay into $\gamma + \tilde{G}$. In particular, the SUSY sparticle production proceeds through the creation of pairs of gluino states, each of which subsequently decays via a virtual squark to a quark–antiquark pair plus the NLSP neutralino, which is assumed to be electrically neutral and purely bino-like (the SUSY partner of the SM $U(1)$ gauge boson). Other SM particles (jets, leptons, photons) may be produced in these cascades. The $\tilde{\chi}_1^0$ branching fraction to $\gamma+\tilde{G}$ goes to 100% for $m_{\tilde{\chi}_1^0} \to 0$ and approaches $\cos^2\theta_W$ for $m_{\tilde{\chi}_1^0} \gg m_Z$, in the latter case the remaining branching fraction is due to the decay of the $\tilde{\chi}_1^0$ to a Z boson and a $\tilde{G}$. For all $\tilde{\chi}_1^0$ masses, then, the branching fraction is dominated by the photonic decay, leading to the di-photon plus $E_{\mathrm{T}}^{\mathrm{miss}}$ signature in the detector. Figure 9.1 shows the Feynman diagram which describes this process. The masses of both the neutralino and the gluino are taken to be free parameters of the model, while all other masses except for those of the gravitino and SM-like Higgs state are decoupled (*i.e.* set to inaccessibly large values). The mass of the gravitino is chosen so that the $\tilde{\chi}_1^0$ decay length $c\tau$ is never greater than 0.1 mm (see Sec. 2.7). This ensures that all particles arising from the decay of the neutralino are prompt.

The presence of a supersymmetric signal is investigated by looking for an excess in the number of the selected events in a dedicated signal region with respect to the number expected by accounting only for the SM process contributions (*i.e* backgrounds), that leads to the same di-photon plus missing transverse momentum final state. The background arises from $W\gamma\gamma$ and $Z\gamma\gamma$ events ("irreducible background") where the W and Z boson decays include neutrinos ($W \to \ell\nu$, $\ell = e$, μ, τ, and $Z \to \nu\nu$), that lead to a significant missing transverse energy contribution. Another source of background is due to the production of $W(W \to e\nu)\gamma$ or $t\bar{t}(t \to be\nu)\gamma$ events, where the electron is mis-reconstructed as a photon ("electro-weak background"). Finally, SM $\gamma\gamma$, $\gamma + j$ and

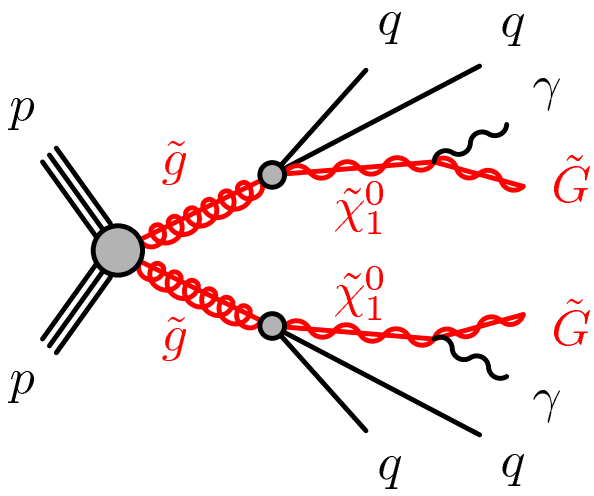

Figure 9.1: Typical production and decay-chain processes for the gluino-pair production in the GGM model for which the NLSP is a bino-like neutralino (26).

di-jet events ("QCD background") can contribute to the signal region. In these events the missing transverse energy is originated by mis-calibrated or mis-reconstructed objects, and the two photon candidates can be both coming from real prompt photons or from mis-reconstructed hadronic jets.

This chapter is divided in two main parts. The first one, from Sec. 9.1 to Sec. 9.5, describes in detail the search performed using the data collected by ATLAS during 2015, equivalent to an integrated luminosity of 3.2 fb^{-1}. In particular, Sec. 9.1 describes the data and the simulated samples used in the analysis. Monte Carlo background samples are mainly used to optimize the signal region (SR) selection, as described in Sec. 9.2, but also to evaluate the expected irreducible background contribution to the selected events. The complete procedure used to evaluate the contribution of the SM yields to the SR events number, based both on simulation and data-driven technique, is explained in Sec. 9.3. Sec. 9.4 shows the expected selection efficiency for the GGM signal model as a function of $m_{\tilde{g}}$ and $m_{\tilde{\chi}_1^0}$, and the main experimental and theoretical uncertainties affecting this value. Finally, Sec. 9.5 summarizes the results of the search, together with a description of the statistical framework used for their interpretation.

The second part of the chapter consists of a single section, Sec. 9.6, which describes the extension of the analysis exploiting the data collected both in 2015 and 2016. This section summarizes the main updates of the analysis, such as additional theoretical interpretations or different signal region definitions, and illustrates the observed results based on an integrated luminosity of 36.1 fb^{-1}.

As one of the two main analyzers in this search I was involved in almost all the steps of the analysis. I followed the generation and validation of the background MC samples. I also implemented both the analysis framework on which the event selection relies, and the statistical framework used to define the optimal signal region requirements. I evaluated the expected contribution of the electro-weak and irreducible background events in the SR. Finally, I performed the statistical interpretation of the final results in term of signal

significance or upper limit on the parameter of the model under test.

9.1 Data and simulated samples

The analysis discussed in the next sections is based on the *pp* collision data collected at a center-of-mass energy of 13 TeV during 2015. Diphoton events are selected using a trigger which requires two *loose* photons with transverse energy thresholds of 50 GeV. This dataset corresponds to an integrated luminosity of 3.2 fb^{-1}.

The simulated samples are used in the analysis to model the detector response both for signal and background processes. Except when noted, the generated events are passed through a Geant4 (149) simulation of the response of the ATLAS detector (159) and reconstructed with the same algorithms as the data.

While most of the backgrounds to the GGM model under examination are estimated through the use of control samples selected from data (see Sec. 9.3), the extrapolation from control regions (CRs) to the signal region (SR) depends on simulated samples, as do the optimization studies. Diphoton, photon+jet, $W\gamma$, $Z\gamma$, $W\gamma\gamma$ and $Z\gamma\gamma$ SM processes are generated using the SHERPA 2.1.1 simulation package (189), making use of the CT10 PDFs (198). The matrix elements are calculated with up to three parton emissions at leading order (four in the case of photon+jet samples) and merged with the SHERPA parton shower (199) using the ME+PS@LO prescription (200). The phase space of the sherpa generation can eventually be defined by additional requirements applied to the objects at the matrix element level. The photon transverse momentum is used to define exclusive regions of the phase space in order to divide the event generation in several sub samples, characterized by different cross-sections, and thus populate the full phase space with a sufficient, though not too large, number of events. Moreover, the generated photons are required to be isolated from quarks and gluons through a requirement on their "continuous" isolation energy (201), in order to reduce the number of events that do not pass the photon isolation selection implemented by the analysis.

Tables 9.1 and 9.2 summarize the cross-sections and the number of events generated for the $\gamma\gamma$, $W\gamma$, $Z\gamma$, $W\gamma\gamma$ and $Z\gamma\gamma$ SM processes.

For the GGM model, the SUSY mass spectra and branching fractions are calculated using SUSPECT2.41 (202) and SDECAY 1.3b (203), respectively, inside the package SUSY-HIT1.3 (204). The Monte Carlo SUSY signal samples are produced using HERWIG++ 2.7.1 (205) with the CTEQ6L1 parton distribution functions (206). All signal samples were simulated through a fast parametric simulation of the ATLAS detector response (207).

Signal cross-sections are calculated at next-to-leading order in the strong coupling constant, including the resummation of soft gluon emission at next-to-leading-logarithmic accuracy (NLO+NLL) (208; 209; 210; 211; 212). The nominal cross-section and its uncertainty are taken from an envelope of cross-section predictions using different PDF sets and factorization and renormalization scales (213) (see Sec. 9.4). At fixed centre-of-mass energy, SUSY production cross-sections decrease rapidly with increasing SUSY particle masses. At $\sqrt{s} = 13$ TeV, the gluino-pair production cross-section is approximately 25 fb for a gluino mass of 1.4 TeV and falls to below 1 fb for a gluino mass of 2.0 TeV. The gluino-pair cross-section bears only a slight dependence on the neutralino mass. Table 9.3 summarizes the signal production cross-sections and their uncertainties, as a function of the gluino mass.

A total of 130 signal samples are generated in the gluino-neutralino mass grid, with

Table 9.1: Monte Carlo samples of $W\gamma$ and $Z\gamma$ diboson production used in this analysis. The table includes cross-section,the number of events in each sample, and the equivalent integrated luminosity.

Process	Final state	Cross-section [fb]	N_{gen}	L [fb^{-1}]
$W\gamma$	$e\nu\gamma$, with $35 < p_{\text{T}}^{\gamma} < 70$ GeV	1.54×10^4	500000	30
	$e\nu\gamma$, with $70 < p_{\text{T}}^{\gamma} < 140$ GeV	1.53×10^3	250000	160
	$e\nu\gamma$, with $p_{\text{T}}^{\gamma} > 140$ GeV	2.42×10^2	250000	1030
	$\mu\nu\gamma$, with $35 < p_{\text{T}}^{\gamma} < 70$ GeV	1.53×10^4	500000	30
	$\mu\nu\gamma$, with $70 < p_{\text{T}}^{\gamma} < 140$ GeV	1.52×10^3	250000	160
	$\mu\nu\gamma$, with $p_{\text{T}}^{\gamma} > 140$ GeV	2.42×10^2	250000	1030
	$\tau\nu\gamma$, with $35 < p_{\text{T}}^{\gamma} < 70$ GeV	1.53×10^4	500000	30
	$\tau\nu\gamma$, with $70 < p_{\text{T}}^{\gamma} < 140$ GeV	1.53×10^3	250000	160
	$\tau\nu\gamma$, with $p_{\text{T}}^{\gamma} > 140$ GeV	2.43×10^2	250000	1030
$Z\gamma$	$ee\gamma$, with $35 < p_{\text{T}}^{\gamma} < 70$ GeV	5.24×10^3	500000	95
	$ee\gamma$, with $70 < p_{\text{T}}^{\gamma} < 140$ GeV	3.85×10^2	250000	650
	$ee\gamma$, with $p_{\text{T}}^{\gamma} > 140$ GeV	4.72×10^1	250000	5300
	$\mu\mu\gamma$, with $35 < p_{\text{T}}^{\gamma} < 70$ GeV	5.25×10^3	500000	95
	$\mu\mu\gamma$, with $70 < p_{\text{T}}^{\gamma} < 140$ GeV	3.86×10^2	250000	650
	$\mu\mu\gamma$, with $p_{\text{T}}^{\gamma} > 140$ GeV	4.72×10^1	250000	5300
	$\tau\tau\gamma$, with $35 < p_{\text{T}}^{\gamma} < 70$ GeV	5.25×10^3	500000	95
	$\tau\tau\gamma$, with $70 < p_{\text{T}}^{\gamma} < 140$ GeV	3.85×10^2	250000	650
	$\tau\tau\gamma$, with $p_{\text{T}}^{\gamma} > 140$ GeV	4.70×10^1	250000	5300
	$\nu\nu\gamma$, with $35 < p_{\text{T}}^{\gamma} < 70$ GeV	4.04×10^3	500000	120
	$\nu\nu\gamma$, with $70 < p_{\text{T}}^{\gamma} < 140$ GeV	9.72×10^2	250000	260
	$\nu\nu\gamma$, with $p_{\text{T}}^{\gamma} > 140$ GeV	1.71×10^2	250000	1460

Table 9.2: Monte Carlo samples of di-photon and of $W\gamma\gamma$ and $Z\gamma\gamma$ triboson production used in this analysis. The table includes cross-section and the number of events in each sample, and the equivalent integrated luminosity.

Process	Final state	Cross-section [fb]	N_{gen}	L [fb^{-1}]
Diphoton	$\gamma\gamma$, with $p_{\text{T}}^{\gamma} > 50$ GeV	2.86×10^4	3000000	105
$W\gamma\gamma$	$e\nu\gamma\gamma$, with $p_{\text{T}}^{\gamma} > 50$ GeV	5.55	10000	1800
	$\mu\nu\gamma\gamma$, with $p_{\text{T}}^{\gamma} > 50$ GeV	5.61	10000	1800
	$\tau\nu\gamma\gamma$, with $p_{\text{T}}^{\gamma} > 50$ GeV	5.65	10000	1800
$Z\gamma\gamma$	$ee\gamma\gamma$, with $p_{\text{T}}^{\gamma} > 50$ GeV	1.89	10000	5260
	$\mu\mu\gamma\gamma$, with $p_{\text{T}}^{\gamma} > 50$ GeV	1.90	10000	5260
	$\tau\tau\gamma\gamma$, with $p_{\text{T}}^{\gamma} > 50$ GeV	1.90	10000	5260
	$\nu\nu\gamma\gamma$, with $p_{\text{T}}^{\gamma} > 50$ GeV	2.77	10000	3610

Table 9.3: The total LO and NLO+NLL cross-sections with uncertainties for GGM gluino-neutralino production.

$m_{\tilde{g}}$[GeV]	σ(LO) [fb]	σ(NLO + NLL) [fb]	Uncertainty [%]
1200	3.88×10^{1}	8.56×10^{1}	18
1300	2.05×10^{1}	4.60×10^{1}	20
1400	1.11×10^{1}	2.52×10^{1}	21
1500	6.14×10^{0}	1.42×10^{1}	23
1600	3.46×10^{0}	8.09×10^{0}	24
1700	1.97×10^{0}	4.70×10^{0}	26
1800	1.14×10^{0}	2.76×10^{0}	28
1900	6.64×10^{-1}	1.63×10^{0}	30
2000	3.90×10^{-1}	9.80×10^{-1}	32
2100	2.30×10^{-1}	5.92×10^{-1}	34
2200	1.36×10^{-1}	3.59×10^{-1}	36
2300	8.11×10^{-2}	2.19×10^{-1}	39

gluino masses ranging in 100 GeV steps from 1200 GeV to 2300 GeV, and, for fixed gluino mass, with neutralino mass varying generally in steps of 150 GeV up to the gluino mass. In addition, for each value of the gluino mass, signal points are generated with neutralino masses of 10 GeV and 50 GeV, and within 10, 50, and 100 GeV of the gluino mass. For each signal sample 10000 events are generated. Figure 9.2 shows the distribution of the mass points chosen for the simulation in the $(m_{\tilde{g}}, m_{\tilde{\chi}_1^0})$ plane .

Additionally, two mass points in the gluino-neutralino grid, defined as $(m_{\tilde{g}}, m_{\tilde{\chi}_1^0}) = (1500\,\text{GeV}, 1300\,\text{GeV})$ and $(m_{\tilde{g}}, m_{\tilde{\chi}_1^0}) = (1500\,\text{GeV}, 100\,\text{GeV})$, are generated using the full (*i.e.* not parametrized) ATLAS simulation (159). These samples provide a benchmark for the optimization of the requirements that define the signal region. These points are chosen to be just above the gluino mass value excluded by the Run 1 analysis ($\sim$ 1350 GeV, see Sec. 2.8), and at low (100 GeV) and high (1300 GeV) mass value of the neutralino in order to test the signal region optimization against the difference in the final state kinematic distributions induced by a small or a large mass difference between $m_{\tilde{g}}$ and $m_{\tilde{\chi}_1^0}$.

All the MC samples, in order to be coherently compared with the data, are corrected for data-MC discrepancies as already explained in Sec. 8.1.

9.2 Event Selection

First a pre-selection is applied, requiring that the events were recorded in the optimal detector conditions in which all the ATLAS sub-detectors are fully operational. Moreover, each event has to contain at least one primary vertex, which is formed from a set of two or more tracks, with transverse momentum $p_{\text{T}}^{\text{track}} > 400$ MeV, that are mutually consistent with having originated from the interaction point. At least two photons have to be reconstructed in the event with $E_{\text{T}} > 50\,\text{GeV}$ and $|\eta| < 2.37$, excluding the region $1.37 \leq |\eta| \leq 1.52$. Photons are required to pass *tight* identification criteria and isolation criteria based on calorimeter information (see Chap. 7). In particular, the calorimeter isolation, $E_{\text{T}}^{\text{iso}}$, evaluated in a cone size $\Delta R = 0.4$, must satisfy the criterion $E_{\text{T}}^{\text{iso}} < 2.45\,\text{GeV} + 0.022 \times E_{\text{T}}^{\gamma}$.

For the events passing the previous selection, further requirements are applied to electrons, jets and muons reconstructed in the events.

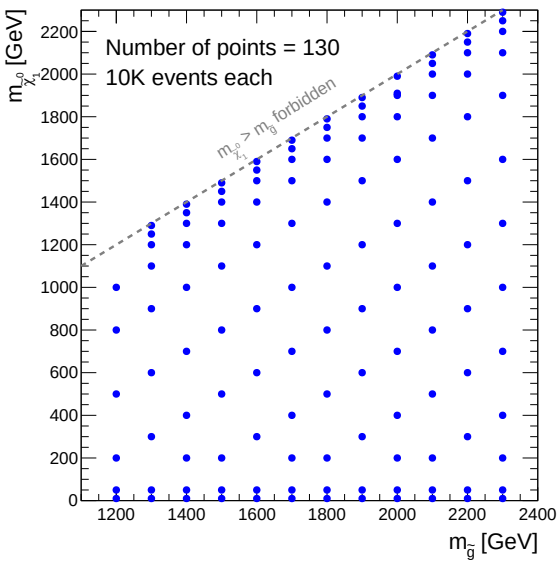

Figure 9.2: Values of the gluino and neutralino masses chosen for the signal event generation and simulation.

- Electron candidates are required to have $p_{\mathrm{T}} > 25$ GeV and $|\eta| < 2.37$, and to be reconstructed outside the transition region $1.37 < |\eta| < 1.52$. They also have to pass *medium* identification and isolation criteria. In particular, the isolation requirement is defined on calorimeter and tracking information in a cone size $\Delta R = 0.2$. This selection is tuned to provide an efficiency increasing with electron momentum from 95% for $p_{\mathrm{T}} = 25$ GeV to 99% for $p_{\mathrm{T}} = 60$ GeV. Finally, electrons are required to be compatible with originating from the primary vertex.

- Muons are required to have $p_{\mathrm{T}} > 25$ GeV and $|\eta| < 2.7$ and to fulfil the *medium* identification criteria. Tracks associated to either electrons and muons are required to be consistent with originating from the primary vertex.

- Jets are reconstructed from three-dimensional energy clusters in the calorimeter using the anti-k_t algorithm with a radius parameter R = 0.4. Jets are required to have $p_{\mathrm{T}} > 40$ GeV and $|\eta| < 2.8$. In order to remove jets originating from pileup, a requirement on the jet vertex tagger variable (JVT > 0.64) is applied to jets with $|\eta| < 2.47$ and $p_{\mathrm{T}} < 60$ GeV.

The following overlap rules are applied to correct for double counting between the different object selections:

- if a jet and an electron are found within $\Delta R < 0.2$, the object is interpreted as an electron and the overlapping jet is removed from the jet list;

- if a jet and an electron are found within $0.2 < \Delta R < 0.4$, the object is interpreted as a jet and the electron is removed;

- if a jet and a muon are found within $\Delta R < 0.4$, the object is interpreted as a jet and the muon is removed;
- if an electron and a photon are found within $\Delta R < 0.4$, the object is interpreted as an electron and the overlapping photon is removed from the photon candidates;
- if a muon and a photon are found within $\Delta R < 0.4$, the object is interpreted as a muon and the overlapping photon is removed from the photon list;
- if a jet and a photon are found within $\Delta R < 0.4$, the object is interpreted as a photon and the overlapping jet is removed from the jet list.

Finally the event selection exploits two event variables: the missing transverse energy, $E_{\mathrm{T}}^{\mathrm{miss}}$, to quantify the significant undetectable transverse momentum carried away by the gravitinos, and m_{eff}, which is the scalar sum of the transverse momenta of all individual selected objects (H_T) and the missing transverse energy:

$$m_{\mathrm{eff}} \equiv H_T + E_{\mathrm{T}}^{\mathrm{miss}} = \sum_{i=1}^{N_{\mathrm{obj}}} p_{\mathrm{T}}^{i} + E_{\mathrm{T}}^{\mathrm{miss}}. \tag{9.1}$$

Additionally, to suppress backgrounds associated with the mismeasurement of hadronic jets that can contribute to a fake missing transverse energy measurement, a requirement of $\Delta\phi_{\mathrm{min}}(\mathrm{jet}, E_{\mathrm{T}}^{\mathrm{miss}}) > 0.5$ is imposed. $\Delta\phi_{\mathrm{min}}(\mathrm{jet}, E_{\mathrm{T}}^{\mathrm{miss}})$ is the minimum distance along ϕ between the missing transverse energy vector and the two leading selected jets, if jets are selected. Usually if the $E_{\mathrm{T}}^{\mathrm{miss}}$ arises from a miscalibration of a jet, the E_T^{miss} will be aligned (or opposite to) the jet direction.

The final selection requirements, which define the signal region of the analysis, are optimized as a function of $E_{\mathrm{T}}^{\mathrm{miss}}$, m_{eff} and p_{T}^{γ} by maximizing the expected discovery significance of the analysis, considering the signal scenarios described by the benchmark mass points $(m_{\tilde{g}}, m_{\tilde{\chi}_1^0}) = (1500\,\mathrm{GeV}, 1300\,\mathrm{GeV})$ and $(m_{\tilde{g}}, m_{\tilde{\chi}_1^0}) = (1500\,\mathrm{GeV}, 100\,\mathrm{GeV})$ scaled to integrated luminosity of 3.5 fb^{-1} ($L = 3.5$ fb^{-1} was the expected integrated luminosity value that would be collected during 2015 at the date when the optimization was performed).

The expected discovery significance is calculated according to (214):

$$Z_A = \left[2 \left((s+b) \ln \left[\frac{(s+b)(b+\sigma_b^2)}{b^2 + (s+b)\sigma_b^2} \right] - \frac{b^2}{\sigma_b^2} \ln \left[1 + \frac{\sigma_b^2 s}{b(b+\sigma_b^2)} \right] \right) \right]^{1/2}, \tag{9.2}$$

where s and b are the expected signal and background yields respectively. The background yield is defined based on estimates derived from the MC samples, described in Sec. 9.1, scaled to $L = 3.5$ fb^{-1}, and σ_b is the uncertainty on the total SM background. Based on the result of the analysis performed at 8 TeV, a relative uncertainty of $\pm 100\%$ was assigned in this optimization study to the electro-weak and irreducible backgrounds, while a relative uncertainty of $\pm 400\%$ is assigned to the QCD background. A minimum absolute background systematic uncertainty was imposed and set to 0.2 event. This value is used in order to disfavour the region of the phase space where the number of the background events becomes too small and it is evaluation in the analysis is not reliable.

The selection criteria for this SR are shown in Table 9.4. No additional veto on isolated leptons are applied to maintain the signal region selection at least partially model independent.

Table 9.4: Requirements defining the signal region.

SR selection criteria
2 tight photons with $E_{\mathrm{T}} > 75$ GeV
$\Delta\phi_{\mathrm{min}}(\mathrm{jet}, E_{\mathrm{T}}^{\mathrm{miss}}) > 0.5$
$E_{\mathrm{T}}^{\mathrm{miss}} > 175$ GeV
$m_{\mathrm{eff}} > 1500$ GeV

9.3 Background

The Standard Model processes that contribute to the number of events in the SR can be classified in three categories: "QCD background", "electro-weak background", and "irreducible background."

- "QCD background." The largest contribution to the inclusive signal di-photon spectrum arises from two real photons produced in association with jets, and from $\gamma+jet$ and multi-jet events, where one or both jets are mis-identified as photons. In these events the measured $E_{\mathrm{T}}^{\mathrm{miss}}$ is due to mis-reconstructed or mis-calibrated objects that bias the balance of the total transverse momentum in the events.

- "Electro-weak background." W, Z boson and $t\bar{t}$ events can contribute to the expected background in the signal region if they are produced together with a photon. In particular, considering $W(\rightarrow e\nu) + \gamma$, $Z(\rightarrow \tau\tau) + \gamma$ and $t\bar{t}(\rightarrow be\nu) + \gamma$, they are characterized by a real contribution to $E_{\mathrm{T}}^{\mathrm{miss}}$ coming from neutrino and can pass the SR selection requirements in the case an electron is misidentified as a photon.

- "Irreducible background." $W\gamma\gamma$ and $Z\gamma\gamma$ processes, where $W \rightarrow \ell\nu$ and $Z \rightarrow \nu\nu$, lead to a final state identical to the one produced by the searched GGM signal.

The evaluation of the contribution to the signal region of the irreducible background events and also of the di-photon component of the QCD backgrounds rely on Monte Carlo samples, the $Z\gamma\gamma$ component is purely evaluated from the MC, while $W\gamma\gamma$ and di-photon MC are normalized in data control region. The contributions of the QCD background arising from jets faking photons and the electrons-faking-photons background are both estimated with a data-driven "fake-factor" method, for which events in data samples enriched in the background of interest are weighted by factors parametrizing the misidentification rate, as explained in the next paragraphs.

9.3.1 QCD background

The QCD background contribution arises from real di-photon events and from γ+jet and multi-jet events production.

The component arising from di-photon events is estimated directly from the simulation, although a weighting procedure is applied to reproduce the observed di-photon $E_{\mathrm{T}}^{\mathrm{miss}}$ distribution, to account for the fact that $E_{\mathrm{T}}^{\mathrm{miss}}$ distribution in the di-photon simulated sample shows a larger tail for high missing transverse energy values than in the data.

To improve the modeling of the $E_{\mathrm{T}}^{\mathrm{miss}}$ distribution in the di-photon sample and its agreement with the data distribution, a set of scale factors in bins of $E_{\mathrm{T}}^{\mathrm{miss}}$and N(jets) (0 jets, 1 jets, 2 jets, 3 or more jets) is evaluated in a control region containing events with two photons with $E_{\mathrm{T}} > 75$ GeV and $E_{\mathrm{T}}^{\mathrm{miss}} < 100$ GeV, after the subtraction from the

data of all the background contributions other than SM $\gamma\gamma$ events, that are illustrated in the following paragraphs.

The weights vary between ≈ 0.2 and 1.6, and decrease with $E_{\mathrm{T}}^{\mathrm{miss}}$. Due to limited statistics, the scale factor evaluated in the highest bin in $E_{\mathrm{T}}^{\mathrm{miss}} = (60\text{–}100)$ GeV is used to weight all the events with $E_{\mathrm{T}}^{\mathrm{miss}} > 100$ GeV. While this background dominates the inclusive di-photon sample, it decreases steeply at high value of $E_{\mathrm{T}}^{\mathrm{miss}}$, making its contribution small, relative to backgrounds with real $E_{\mathrm{T}}^{\mathrm{miss}}$ for $E_{\mathrm{T}}^{\mathrm{miss}} \gtrsim 100$ GeV, independent of the weighting, as shown in Figure 9.4.

The photon+jet and multi-jet background contributions arise from events where the jets are mis-identified as photons. This background is estimated using a data-driven technique. The idea is to loosen the photon selection criteria and estimate the rate at which those "looser" photons pass the nominal criteria. Each event, with both candidates satisfying the *tight* identification criteria, is classified in four different categories depending on whether the leading and/or the subleading photon passes (I) or fails ($\widetilde{I}$) the isolation selection. The four categories are called: II, $I\widetilde{I}$, $\widetilde{I}I$, $\widetilde{I}\widetilde{I}$. In particular a photon candidate is considered isolated if it passes the signal isolation requirement $E_{\mathrm{T}}^{\mathrm{iso}} < 2.45\,\mathrm{GeV} + 0.022 \times p_{\mathrm{T}}^{\gamma}$, while the anti-isolated photons are required to have: $E_{\mathrm{T}}^{\mathrm{iso}} > 10\,\mathrm{GeV} + 0.022 \times p_{\mathrm{T}}^{\gamma}$ and $E_{\mathrm{T}}^{\mathrm{iso}} < 30\,\mathrm{GeV} + 0.022 \times p_{\mathrm{T}}^{\gamma}$. The yields in these categories are related to the number of real (R) or fake (F) photon candidates passing the looser selection by the following equation:

$$\begin{pmatrix} N_{II} \\ N_{I\widetilde{I}} \\ N_{\widetilde{I}I} \\ N_{\widetilde{I}\widetilde{I}} \end{pmatrix} = \begin{pmatrix} 1 & f_2 & f_1 & f_1 f_2 \\ 0 & (1-f_2) & 0 & f_1(1-f_2) \\ 0 & 0 & (1-f_1) & (1-f_1)f_2 \\ 0 & 0 & 0 & (1-f_1)(1-f_2) \end{pmatrix} \begin{pmatrix} N_{RR} \\ N_{RF} \\ N_{FR} \\ N_{FF} \end{pmatrix}. \tag{9.3}$$

Here f_i denotes the probability that a reconstructed fake photon passes the isolation selection and is defined as:

$$f = \frac{N_I^{\mathrm{fake}}}{N^{\mathrm{fake}}}. \tag{9.4}$$

Thus the background composition of the signal region is defined by the first row of Eq. (9.3):

$$N_{II}^{\gamma+j} = f_2 N_{RF} + f_1 N_{FR}, \tag{9.5}$$

$$N_{II}^{jj} = f_1 f_2 N_{FF}, \tag{9.6}$$

$$N_{II}^{bkg} = f_2 N_{RF} + f_1 N_{FR} + f_1 f_2 N_{FF}. \tag{9.7}$$

By inverting the matrix in Eq. (9.3), it is possible to express the true yields (N_{RF}, N_{FR}, N_{FF}) as a function of the observable yields $N_{I\widetilde{I}}$, $N_{\widetilde{I}I}$ $N_{\widetilde{I}\widetilde{I}}$.

$$\begin{pmatrix} N_{RR} \\ N_{RF} \\ N_{FR} \\ N_{FF} \end{pmatrix} = \frac{1}{(1-f_1)(1-f_2)} \begin{pmatrix} (f_1-1)(f_2-1) & (f_1-1)f_2 & f_1(f_2-1) & f1f2 \\ 0 & 1-f_1 & 0 & -f1 \\ 0 & 0 & 1-f_2 & -f_2 \\ 0 & 0 & 0 & 1 \end{pmatrix} \begin{pmatrix} N_{II} \\ N_{I\widetilde{I}} \\ N_{\widetilde{I}I} \\ N_{\widetilde{I}\widetilde{I}} \end{pmatrix}. \tag{9.8}$$

Thus, N_{II}^{bkg} becomes:

$$N_{II}^{bkg} = F_2 N_{I\widetilde{I}} + F_1 N_{\widetilde{I}I} - F_1 F_2 N_{\widetilde{I}\widetilde{I}}, \tag{9.9}$$

where the "fake factor" F_i is defined as:

$$F_i = \frac{f_i}{1-f_i} = \frac{N_I^{\text{fake}}/N^{\text{fake}}}{1-N_I^{\text{fake}}/N^{\text{fake}}} = \frac{N_I^{\text{fake}}}{N^{\text{fake}}-N_I^{\text{fake}}} = \frac{N_I^{\text{fake}}}{N_{\widetilde{I}}^{\text{fake}}}. \tag{9.10}$$

In particular, for this analysis the fake factor has been measured in a data control sample selecting two anti-isolated photons with $E_{\text{T}} > 75$ GeV, additionally requiring the sub-leading photon to pass the *loose* but not the *tight* identification criteria. Then the fake rate is evaluated from the ratio between the number of sub-leading loose photons that are either isolated or anti-isolated:

$$F_{\gamma-\text{iso}}(p_{\text{T}},\eta) \equiv \left.\frac{N_{\text{data}}^{I\gamma_2}(p_{\text{T}},\eta) - N_{\text{contam.}}^{I\gamma_2}(p_{\text{T}},\eta)}{N_{\text{data}}^{\widetilde{I}\gamma_2}(p_{\text{T}},\eta) - N_{\text{contam.}}^{\widetilde{I}\gamma_2}(p_{\text{T}},\eta)}\right|_{\text{loose}-\gamma}. \tag{9.11}$$

Here the $N_{\text{contam.}}$ terms account for the signal photon contamination that leaks from the signal region. This contribution is evaluated using the Monte Carlo di-photon sample and is negligible in the anti-isolated selection, while it accounts for ~ 10 % of the events in the isolated sample. The fake factor varies between 10% to 30%.

The jet-faking-photon background contribution to the SR is then evaluated as:

$$N_{\text{j}\to\gamma} = F_{\gamma-\text{iso}}(p_{\text{T}},\eta)\cdot\left(N_{\text{data}}^{\widetilde{I}} - N_{\text{contam.}}^{\widetilde{I}}\right) - F_{\gamma-\text{iso}}(p_{\text{T},1},\eta_1)\cdot F_{\gamma-\text{iso}}(p_{\text{T},2},\eta_2)\cdot\left(N_{\text{data}}^{\widetilde{I}\widetilde{I}} - N_{\text{contam.}}^{\widetilde{I}\widetilde{I}}\right), \tag{9.12}$$

where the fake factor for the leading and the subleading photon is assumed to be the same. Events with tight and anti-isolated photons are weighted by their isolation fake factors to predict the background from jets faking photons in the signal region. The small contamination from real photons is subtracted using the SM di-photon simulation.

Finally, the global contribution of the QCD background is given by the integral of the E_{T}^{miss}-weighted di-photon Monte Carlo sample and the data-driven jet-faking-photon estimate above the signal region requirements of $E_{\text{T}}^{\text{miss}} > 175$ GeV and $m_{\text{eff}} > 1500$ GeV. However, since no events from either the di-photon simulation or in the jet-faking-photon control region pass such selection, only an upper limit can be placed on the number of expected QCD background events. If 0 events are observed, the Poisson statistic predicts an upper limit on the number of expected events at 68% CL equal to 1.14. Making this assumption and scaling 1.14 true di-photon Monte Carlo events by the luminosity and $E_{\text{T}}^{\text{miss}}$-weighting scale factors leads to an estimate of less than 0.007 events at 68% CL for the true di-photon contribution. For the jet-fake contribution, scaling 1.14 jet-faking-photon events by an averaged jet-faking-photon scale factor leads to an estimate of less than 0.25 events at 68% CL.

Additional information on the $\gamma+j$ and di-jet background component can be obtained evaluating their expected yields without applying any $E_{\text{T}}^{\text{miss}}$ requirement to the signal events. In this case the contribution of the jet-faking-photon events is 0.2 ± 0.2. Then, if we assume that $E_{\text{T}}^{\text{miss}}$ and m_{eff} are largely uncorrelated because of the small contribution to m_{eff} arising from the $E_{\text{T}}^{\text{miss}}$, the contribution of the jet-faking-photon background to the modified SR can be scaled to the nominal SR by considering a looser m_{eff} selection ($m_{\text{eff}} > 700$ GeV) and measuring the fraction of the $\gamma + jet$ and di-jet background events that pass the $E_{\text{T}}^{\text{miss}} > 175$ GeV requirement.

Given the robust, conservative upper limit of 0.25 events, and the estimate under the assumption of no $E_{\text{T}}^{\text{miss}}$–$m_{\text{eff}}$ correlation of 0.02 events for the $\gamma+j$ and di-jet background, the final conservative estimation of the overall QCD background is of $0.05^{+0.20}_{-0.05}$ events.

9.3.2 Electro-weak background

The electro-weak background arises mainly from SM $W\gamma$ and $t\bar{t}\gamma$ events, where the W boson and the top quark decay in a final state with an electron and a neutrino, and the electron is mis-identified as a photon.

The contribution of this background is evaluated by using an electron enriched control region in data, orthogonal (*i.e.* not overlapping) to the signal region, containing events passing SR $E_{\mathrm{T}}^{\mathrm{miss}} > 175$ GeV, $m_{\mathrm{eff}} > 1500$ GeV and $\Delta\phi_{\mathrm{min}}(\mathrm{jet}, E_{\mathrm{T}}^{\mathrm{miss}}) > 0.5$ requirements, but with exactly one signal photon with $p_{\mathrm{T}}^{\gamma} > 75$ GeV and at least one electron with $p_{\mathrm{T}}^{e} > 75$ GeV. The number of events selected in this control region is then scaled to obtain the expected contribution in the SR according to:

$$N_{e\to\gamma}^{\mathrm{SR}} = F_{e\to\gamma}(p_{\mathrm{T}}, \eta) \times N_{e\gamma}(p_{\mathrm{T}}^{e}, \eta^{e}), \tag{9.13}$$

where $N_{e\to\gamma}^{\mathrm{SR}}$ is the expected number of events contributing to the SR, $N_{e\gamma}$ is the event yield in the electron enriched control region, and $F_{e\to\gamma}$ is the electron-to-photon fake rate evaluated as explained in Sec. 7.3.

Two $e\gamma$ events are observed in data after applying the CR selection. The properties of these events are listed in Table 9.5.

Table 9.5: Properties of the observed $e\gamma$ events used to form the data-driven electron-faking-photon background estimate in the signal region.

p_{T}^{e} [GeV]	η^{e}	p_{T}^{γ} [GeV]	η^{γ}	m_{eff} [GeV]	$E_{\mathrm{T}}^{\mathrm{miss}}$ [GeV]	$F_{e\to\gamma}$
113	-0.606	88	-1.849	1792	186	0.019
166	0.581	105	-1.273	1619	586	0.012

The expected contribution of the electro-weak background to the signal region is thus 0.03 ± 0.02 events.

9.3.3 Irreducible background

The irreducible background from $W\gamma\gamma$ and $Z\gamma\gamma$ is evaluated from the Monte Carlo simulation described in Sec. 9.1.

The background contribution from $Z(\to \nu\nu)\gamma\gamma$ events is evaluated directly from the number of predicted events from the Monte Carlo simulation, that is found to be 0.02 events. A conservative uncertainty of $\pm 100\%$ is applied to account for modelling uncertainties (215).

$W\gamma\gamma$ events are expected to be affected by a large and uncertain production K-factor (*i.e.* the ratio between the expected cross-section evaluated at LO and NLO accuracy in QCD) that depends strongly upon the momentum of the $W\gamma\gamma$ system (216). The Sherpa $W\gamma\gamma$ samples are not pure LO simulations, since they include the matrix element of real emission up to 3 partons and can partially account for this K-factor dependence on the $p_{\mathrm{T}}^{\ell\ell\gamma}$, therefore a constant normalization factor is evaluated for the $W\gamma\gamma$ MC sample.

The overall normalization of the $W\gamma\gamma$ simulation is constrained in a $\ell\gamma\gamma$ ($\ell = e, \mu$) data control region defined as follows. Events in the $W\gamma\gamma$ CR are required to have at least two *tight* and isolated photons with p_{T} greater than 50 GeV, and exactly one electron or muon with $p_{\mathrm{T}} > 25$ GeV. Moreover, as required for SR events, the CR events have to satisfy the $\Delta\phi_{\mathrm{min}}(\mathrm{jet}, E_{\mathrm{T}}^{\mathrm{miss}}) > 0.5$ requirement, while to avoid overlaps with the signal region, events are required to have $E_{\mathrm{T}}^{\mathrm{miss}} < 175$ GeV.

In order to reduce the contribution from SM processes other than $W\gamma\gamma$ events, further selections, optimized using MC samples, are applied:

- in order to suppress the $t\bar{t}\gamma$ contribution, the events with more than two selected jets are discarded;
- if the invariant mass of the e-γ selected objects is within 83 GeV $< m_{e\gamma} <$ 97 GeV, the event is discarded in order to reduce the contribution from $Z(\rightarrow ee)\gamma$ events;
- to suppress the $Z\gamma\gamma$ contribution, events with $E_{\mathrm{T}}^{\mathrm{miss}} < 50$ GeV are discarded.

The event selection requirements for the $W\gamma\gamma$ CR are summarized in Table 9.6.

Table 9.7 shows the expected contributions to the $W\gamma\gamma$ control region. The $W\gamma\gamma$ and $Z\gamma\gamma$ contributions are derived from the Monte Carlo samples listed in Sec. 9.1, while the di-photon, electron fake and jet fake contributions are estimated with the data-driven approaches described above. A total of seven events are observed in this CR, of which 1.6 ± 0.6 are expected to arise from sources other than $W\gamma\gamma$ production. Monte Carlo simulation predicts 1.9 ± 0.1 $W\gamma\gamma$ events, leading to a scale factor of 2.9 ± 1.4, assuming no additional contamination of GGM signal events. Correcting the $W\gamma\gamma$ simulation by this factor, a total of 0.17 ± 0.08 $W\gamma\gamma$ events are expected in the signal region. When setting limits on specific signal models, a simultaneous fit to the control region and the signal region is performed, allowing both the signal and $W\gamma\gamma$ contributions to float to their best-fit values. Figure 9.3 shows the distribution of $p_{\mathrm{T}}^{\ell\ell\gamma}$ in the $W\gamma\gamma$ CR.

9.3.4 Combined background estimate

A summary of the estimated background contributions in the SR is presented in Table 9.8. Summing all background contributions, a total of $0.27^{+0.22}_{-0.10}$ Standard Model events are expected in the signal region. Figure 9.4 shows the data and expected background distributions of $E_{\mathrm{T}}^{\mathrm{miss}}$ and m_{eff} in the di-photon sample after the application of requirements of $E_{\mathrm{T}}^{\gamma} > 75$ GeV on each selected photon and of $\Delta\phi_{\mathrm{min}}(\mathrm{jet}, E_{\mathrm{T}}^{\mathrm{miss}}) > 0.5$, but with no requirements yet imposed on $E_{\mathrm{T}}^{\mathrm{miss}}$ and m_{eff}.

9.3.5 Background validation regions

Several *validation regions* (VRs), that have similar kinematic properties to those of the signal region, are explored to check the agreement of the background model with data. The VRs are defined as follows:

- VR1. The first validation region selects a di-photon sample inclusive in m_{eff}. The signal region events contribution is removed by requiring $E_{\mathrm{T}}^{\mathrm{miss}} < 175$ GeV. The full set of requirements is:

Table 9.6: Requirements defining the $W\gamma\gamma$ CR.

$W\gamma\gamma$ CR
2 tight photons with $p_{\mathrm{T}} > 50$ GeV
1 e or μ with $p_{\mathrm{T}} > 25$ GeV
$\Delta\phi_{\mathrm{min}}(\mathrm{jet}, E_{\mathrm{T}}^{\mathrm{miss}}) > 0.5$
$50 < E_{\mathrm{T}}^{\mathrm{miss}} < 175$ GeV
$N(\mathrm{jets}) < 3$
$m_{e\gamma} \notin$ 83–97 GeV

Table 9.7: Expected contributions to the $W\gamma\gamma$ control region. The $W\gamma\gamma$ and $Z\gamma\gamma$ contributions are derived from the Monte Carlo samples listed in Sec. 9.1, while the di-photon, electron fake and jet fake contributions are estimated with the data-driven approaches described above. The table also shows the expected contributions from the two signal focus points, as well as the number of events observed in data. The total expectation can be brought into agreement with the data by scaling the $W\gamma\gamma$ contribution by a factor of 2.9 ± 1.4.

Source	Contribution [Events]
$\gamma\gamma$	0.03 ± 0.02
$\gamma\gamma + \gamma$j	0.8 ± 0.6
$e \to \gamma$ fakes	0.6 ± 0.1
$W\gamma\gamma$	1.85 ± 0.06
$Z\gamma\gamma$	0.19 ± 0.01
Sum	3.47 ± 0.6
$(m_{\tilde{g}}, m_{\tilde{\chi}_1^0}) = (1500\,\text{GeV}, 100\,\text{GeV})$	0.00
$(m_{\tilde{g}}, m_{\tilde{\chi}_1^0}) = (1500\,\text{GeV}, 1300\,\text{GeV})$	0.00
Data	7

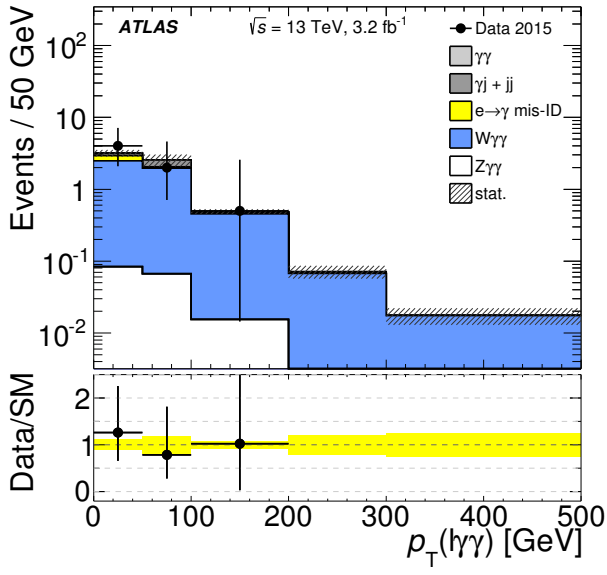

Figure 9.3: The distribution of $p_{\mathrm{T}}^{\ell\ell\gamma}$ in the $W\gamma\gamma$ CR. The expected contributions from SM processes are estimated using a combination of Monte Carlo and data-driven estimates. Uncertainties (shaded bands for MC simulation, error bars for data) are statistical only. The yellow band represents the statistical uncertainty in the data/SM ratio due to the statistics in the model (26).

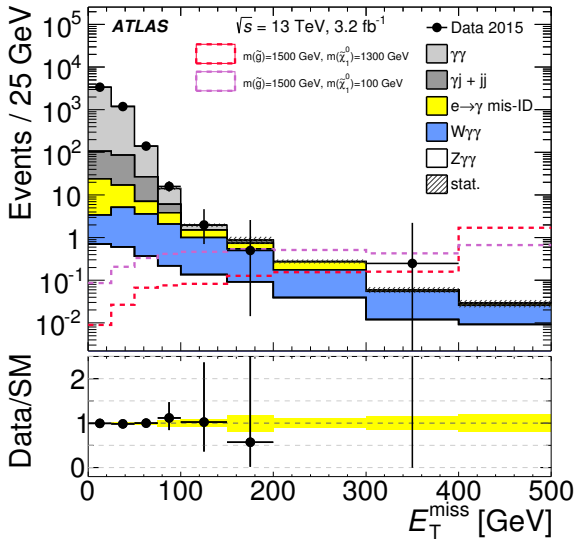

(a) $E_{\mathrm{T}}^{\mathrm{miss}}$

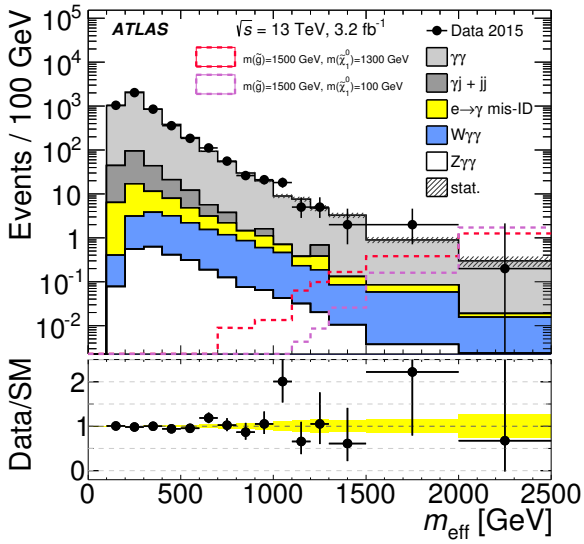

(b) m_{eff}

Figure 9.4: Distributions of $E_{\mathrm{T}}^{\mathrm{miss}}$ (a) and m_{eff} (b) for the di-photon sample after the application of requirements of $E_{\mathrm{T}}^{\gamma} > 75$ GeV on each selected photon and of $\Delta\phi_{\mathrm{min}}(\mathrm{jet}, E_{\mathrm{T}}^{\mathrm{miss}}) > 0.5$, but with no requirements imposed on $E_{\mathrm{T}}^{\mathrm{miss}}$ and m_{eff}. The expected contributions from SM processes are estimated using the combination of Monte Carlo and data-driven estimates discussed in section 9.3. Uncertainties (shaded bands for MC simulation, error bars for data) are statistical only. The yellow band represents the uncertainty in the data/SM ratio that arises from the statisical limitations of the estimates of the various expected sources of SM background. Also shown are the expected contributions from the GGM signal for the two focus points, $(m_{\tilde{g}}, m_{\tilde{\chi}_1^0}) = (1500\,\mathrm{GeV}, 1300\,\mathrm{GeV})$ and $(m_{\tilde{g}}, m_{\tilde{\chi}_1^0}) = (1500\,\mathrm{GeV}, 100\,\mathrm{GeV})$ (26).

Table 9.8: Summary of background estimates, by source, and total combined background, in the signal region. The uncertainties shown include the total statistical plus systematic uncertainty. The Table also shows the expected contributions for the two signal focus points.

Source	Number of events
QCD ($\gamma\gamma$, γj, jj)	$0.05^{+0.20}_{-0.05}$
$e \to \gamma$ fakes	0.03 ± 0.02
$W\gamma\gamma$	0.17 ± 0.08
$Z\gamma\gamma$	0.02 ± 0.02
Sum	$0.27^{+0.22}_{-0.10}$
$(m_{\tilde{g}}, m_{\tilde{\chi}_1^0}) = (1500\,\text{GeV}, 100\,\text{GeV})$	7.0
$(m_{\tilde{g}}, m_{\tilde{\chi}_1^0}) = (1500\,\text{GeV}, 1300\,\text{GeV})$	8.0

  - two tight photons with $E_{\text{T}} > 75$ GeV;
  - $\Delta\phi_{\text{min}}(\text{jet}, E_{\text{T}}^{\text{miss}}) > 0.5$;
  - $E_{\text{T}}^{\text{miss}} < 175$ GeV.

- VR2. The second validation region adds a requirement of $m_{\text{eff}} > 700$ GeV, to highlight the intermediate m_{eff} region. VR2 is defined by the following requirements:
  - two tight photons with $E_{\text{T}} > 75$ GeV;
  - $\Delta\phi_{\text{min}}(\text{jet}, E_{\text{T}}^{\text{miss}}) > 0.5$;
  - $E_{\text{T}}^{\text{miss}} < 175$ GeV;
  - $m_{\text{eff}} > 700$ GeV.

- VR3. The third validation region focuses on the intermediate $E_{\text{T}}^{\text{miss}}$ region. The events in this region are selected requiring:
  - two tight photons with $E_{\text{T}} > 75$ GeV;
  - $\Delta\phi_{\text{min}}(\text{jet}, E_{\text{T}}^{\text{miss}}) > 0.5$;
  - 75 GeV $< E_{\text{T}}^{\text{miss}} < 175$ GeV.

- VR4. The fourth validation region focuses on $\ell\gamma\gamma$ events in a more inclusive selection than the $W\gamma\gamma$ control region discussed in Sec. 9.3.3. This region is selected by requiring:
  - two tight photons with $E_{\text{T}} > 50$ GeV;
  - one and only one selected electron or muon with $p_{\text{T}} > 25$ GeV;

  - $E_{\mathrm{T}}^{\mathrm{miss}} < 175$ GeV.

- VR5. The fifth validation region attempts to enrich a sample of $Z\gamma$ events to check the level of electron-to-photon fakes, but it is rather low count. It is defined by the following requirements:

  - two tight photons with $E_{\mathrm{T}} > 75$ GeV;
  - one and only one selected electron $p_{\mathrm{T}} > 25$ GeV;
  - $E_{\mathrm{T}}^{\mathrm{miss}} < 175$ GeV;
  - the invariant mass of the e-γ pairs must be in the range $83 < m_{e\gamma} < 97$ GeV.

- VR6. The sixth validation region attempts to be a kind of "$N-1$ plot" with respect to the SR. It is defined considering the signal region selection except from no requirements on the $E_{\mathrm{T}}^{\mathrm{miss}}$ event value. Additionally the m_{eff} requirement is relaxed to 1400 GeV to enhance the number of selected events. This region is defined by the following requirements:

  - two tight photons with $E_{\mathrm{T}} > 75$ GeV;
  - $\Delta\phi_{\mathrm{min}}(\mathrm{jet}, E_{\mathrm{T}}^{\mathrm{miss}}) > 0.5$;
  - $m_{\mathrm{eff}} > 1400$ GeV.

  Figure 9.5a shows the VR6 distribution of $E_{\mathrm{T}}^{\mathrm{miss}}$.

- VR7. The seventh validation region is built similarly to VR6, considering all the signal region requirements except from the m_{eff} one. Moreover, the $E_{\mathrm{T}}^{\mathrm{miss}}$ cut is relaxed to 125 GeV. The full set of requirements is:

  - two tight photons with $p_{\mathrm{T}} > 75$ GeV;
  - $\Delta\phi_{\mathrm{min}}(\mathrm{jet}, E_{\mathrm{T}}^{\mathrm{miss}}) > 0.5$;
  - $E_{\mathrm{T}}^{\mathrm{miss}} > 125$ GeV.

  Figure 9.5b shows the VR7 distribution of m_{eff}.

The total number of events from backgrounds compared with the data observed in each validation region is shown in Tables 9.9 and 9.10.

Table 9.9: Summary of background estimates, by source, and total combined background in the validation regions VR1-VR5. The uncertainties shown are statistical only. Also shown are the expected contributions for the two signal focus points.

Source	VR1	VR2	VR3	VR4	VR5
QCD ($\gamma\gamma$, γj, jj)	4702 ± 23	131 ± 4	11.8 ± 1.0	4.1 ± 1.2	0.0 ± 0.0
$e \to \gamma$ fakes	39 ± 1	2.9 ± 0.3	3.0 ± 0.3	8.6 ± 0.5	2.4 ± 0.3
$W\gamma\gamma$	14.6 ± 0.3	3.6 ± 0.1	4.2 ± 0.2	14.5 ± 0.3	0.29 ± 0.04
$Z\gamma\gamma$	2.26 ± 0.05	0.41 ± 0.02	0.59 ± 0.03	1.51 ± 0.03	0.051 ± 0.006
Sum	4757 ± 24	138 ± 4	19.6 ± 1.2	28.7 ± 1.4	2.8 ± 0.3
$(m_{\tilde{g}}, m_{\tilde{\chi}_1^0}) = (1500\,\text{GeV}, 100\,\text{GeV})$	2.5 ± 0.1	9.5 ± 0.2	1.90 ± 0.09	0.37 ± 0.04	0
$(m_{\tilde{g}}, m_{\tilde{\chi}_1^0}) = (1500\,\text{GeV}, 1300\,\text{GeV})$	0.46 ± 0.05	8.7 ± 0.2	0.36 ± 0.04	0	0
Data	4723	146	21	27	6

Table 9.10: Summary of background estimates, by source, and total combined background in the validation regions VR6 and VR7. The uncertainties shown are statistical only. Also shown are the expected contributions from the two signal focus points.

Source	VR6	VR7
QCD ($\gamma\gamma$, γj, jj)	8.8 ± 1.0	0.3 ± 0.3
$e \to \gamma$ fakes	0.21 ± 0.06	1.0 ± 0.2
$W\gamma\gamma$	0.39 ± 0.05	2.4 ± 0.1
$Z\gamma\gamma$	0.040 ± 0.006	0.54 ± 0.02
Sum	9.4 ± 1.0	4.3 ± 0.4
$(m_{\tilde{g}}, m_{\tilde{\chi}_1^0}) = (1500\,\text{GeV}, 100\,\text{GeV})$	9.4 ± 0.1	8.0 ± 0.2
$(m_{\tilde{g}}, m_{\tilde{\chi}_1^0}) = (1500\,\text{GeV}, 1300\,\text{GeV})$	8.3 ± 0.2	8.5 ± 0.2
Data	14	4

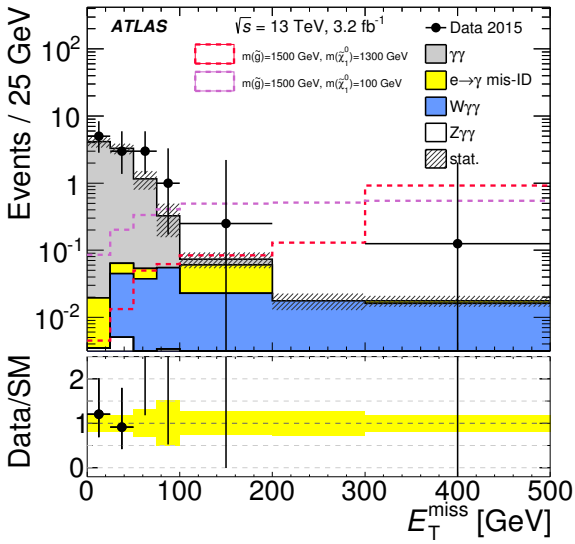

(a) VR6

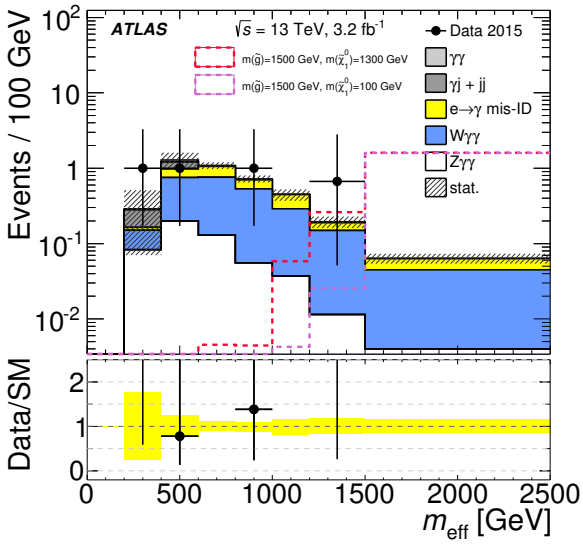

(b) VR7

Figure 9.5: (a) The distribution of $E_{\mathrm{T}}^{\mathrm{miss}}$ in the sixth validation region (VR6) and (b) the distribution of m_{eff} in the seventh validation region (VR7). The expected contributions from SM processes are estimated using the combination of Monte Carlo and data-driven estimates discussed in Sec. 9.3. Uncertainties (shaded bands for MC simulation, error bars for data) are statistical only. The yellow band represents the statistical uncertainty in the data/SM ratio due to the statistics in the model. The Figure also shows the expected contributions from the GGM signal for the two benchmark points, $(m_{\tilde{g}}, m_{\tilde{\chi}_1^0}) = (1500\,\mathrm{GeV}, 100\,\mathrm{GeV})$ and $(m_{\tilde{g}}, m_{\tilde{\chi}_1^0}) = (1500\,\mathrm{GeV}, 100\,\mathrm{GeV})$ (26).

9.4 Signal efficiencies and uncertainties

The acceptances (A) and efficiencies (ε) of the signal region requirements for GGM signal are evaluated using the simulation for each generated value of the gluino and neutralino mass (see Figure 9.6 and Table 9.11). $A \times \varepsilon$ can vary significantly. For example, considering a gluino with mass of 1700 GeV ($A \times \varepsilon$) varies between 14% and 28%, reaching a minimum as the neutralino mass approaches the Z boson mass, and the maximum where the masses of both the gluino and the neutralino states are largest, leading to large amounts of both visible energy and missing transverse momentum that would clearly distinguish signal from background events.

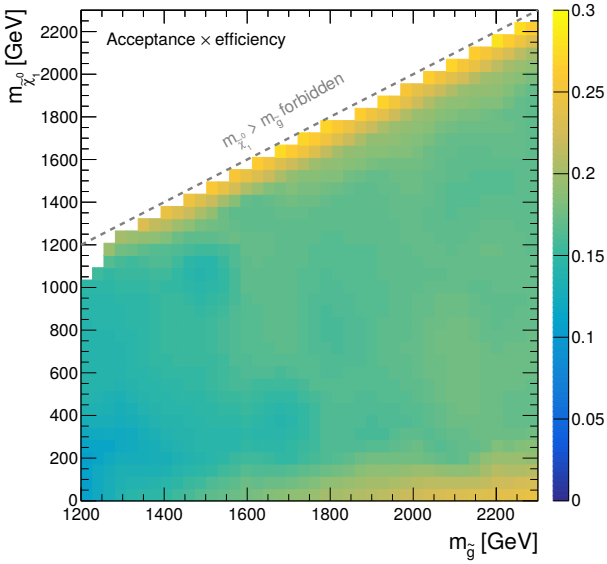

Figure 9.6: Total acceptance × efficiency across the $m_{\tilde{g}}$-$m_{\tilde{\chi}_1^0}$ GGM grid.

Several experimental systematic uncertainties affecting the signal acceptance-times-efficiency have been evaluated and are summarised in Table 9.12.

The integrated luminosity for the 2015 dataset was measured with an uncertainty equal to 2.1% (Sec. 3.2.1).

The uncertainties in the photon energy scale and resolution are evaluated as described in Sec. 6.5. They are propagated to this analysis using the simplified model consisting of a single systematic variation for the energy scale uncertainty and a single systematic variation for the resolution scale uncertainties.

The uncertainty due to the photon identification efficiency is computed by varying the identification efficiency scale factors, obtained from control samples of photons from radiative Z boson decays and from $\gamma + jet$ events and from electrons from $Z \to ee$ (see Sec. 7.1), by $\pm 1\sigma$.

The uncertainties in the jet energy scale and resolution are propagated by varying the jet energies by an amount defined by the differences observed between data and simulation in the transverse momentum balance in multi-jets, γ+jet and Z+jet events.

The uncertainties in the values of whole-event observables, such as $E_{\mathrm{T}}^{\mathrm{miss}}$ and m_{eff},

Table 9.11: Total acceptance × efficiency ($A \times \varepsilon$) for each of the signal models across the $m_{\tilde{g}}$-$m_{\tilde{\chi}_1^0}$ GGM grid.

$m_{\tilde{g}}$ [GeV]	$m_{\tilde{\chi}_1^0}$ [GeV]	$A \times \varepsilon$ [%]	$m_{\tilde{g}}$ [GeV]	$m_{\tilde{\chi}_1^0}$ [GeV]	$A \times \varepsilon$ [%]	$m_{\tilde{g}}$ [GeV]	$m_{\tilde{\chi}_1^0}$ [GeV]	$A \times \varepsilon$ [%]
1200	10	12.27	1700	10	18.65	2100	10	23.28
1200	50	10.31	1700	50	18.82	2100	50	23.04
1200	200	10.47	1700	200	15.06	2100	200	16.69
1200	500	14.23	1700	400	14.06	2100	500	17.74
1200	800	14.16	1700	700	16.76	2100	800	17.84
1200	1000	14.50	1700	1000	16.80	2100	1100	17.01
1200	1100	17.79	1700	1300	16.92	2100	1400	16.46
1200	1150	21.85	1700	1500	18.58	2100	1700	17.10
1200	1190	22.02	1700	1600	23.80	2100	1900	19.42
1300	10	14.07	1700	1650	27.89	2100	2000	24.74
1300	50	14.03	1700	1690	28.44	2100	2050	27.70
1300	300	11.87	1800	10	20.70	2100	2090	28.64
1300	600	14.03	1800	50	20.06	2200	10	23.96
1300	900	14.43	1800	200	16.26	2200	50	23.42
1300	1100	15.34	1800	500	16.45	2200	300	17.37
1300	1200	18.29	1800	800	15.81	2200	600	17.41
1300	1250	20.71	1800	1100	16.35	2200	900	16.77
1300	1290	25.24	1800	1400	16.96	2200	1200	17.34
1400	10	15.26	1800	1600	19.38	2200	1200	17.34
1400	50	14.82	1800	1700	24.87	2200	1500	16.53
1400	200	12.82	1800	1750	26.84	2200	1800	17.52
1400	400	14.07	1800	1790	28.90	2200	2000	20.03
1400	700	15.18	1900	10	20.82	2200	2100	24.74
1400	1000	15.22	1900	50	21.19	2200	2150	28.36
1400	1200	16.89	1900	300	15.82	2200	2190	29.42
1400	1300	21.57	1900	600	16.52	2300	10	24.92
1400	1350	24.66	1900	900	16.51	2300	50	24.52
1400	1390	26.24	1900	1200	16.64	2300	200	19.47
1500	10	17.00	1900	1500	16.95	2300	400	16.90
1500	50	16.63	1900	1700	19.42	2300	700	17.52
1500	200	14.12	1900	1800	24.92	2300	1000	16.95
1500	500	14.87	1900	1850	27.58	2300	1300	16.81
1500	800	15.46	1900	1890	28.46	2300	1600	16.85
1500	1100	13.76	2000	10	21.75	2300	1900	16.59
1500	1300	17.87	2000	50	22.26	2300	2100	19.90
1500	1400	22.34	2000	200	17.98	2300	2200	25.49
1500	1450	26.19	2000	400	16.34	2300	2250	28.32
1500	1490	26.68	2000	700	17.05	2300	2290	29.30
1600	10	17.62	2000	1000	16.82			
1600	50	17.91	2000	1300	17.08			
1600	300	14.46	2000	1600	17.78			
1600	600	16.28	2000	1800	19.54			
1600	900	16.60	2000	1900	25.01			
1600	1200	17.11	2000	1910	24.06			
1600	1400	16.51	2000	1990	29.06			
1600	1500	23.29						
1600	1550	26.19						
1600	1590	27.87						

Table 9.12: Summary of individual and total contributions to the systematic uncertainty of the signal acceptance-times-efficiency. Relative uncertainties are shown in percent, and are averaged over the full range of the ($m_{\tilde{g}}$,$m_{\tilde{\chi}_1^0}$) grid.

Source of uncertainty	Systematic uncertainty
Luminosity	2.1%
Photon identification	3.0%
Photon energy scale	0.2%
Photon energy resolution	0.2%
Jet energy scale	0.4%
Jet energy resolution	0.3%
$E_{\mathrm{T}}^{\mathrm{miss}}$ soft term	$< 0.1\%$
Pile-up uncertainty	1.8%
MC statistics	2.3%
Total experimental uncert.	4.7%

arise from the uncertainties in the energy of the underlying objects from which they are constructed. The uncertainty in the $E_{\mathrm{T}}^{\mathrm{miss}}$ soft term scale contributes negligibly. The uncertainty due to pileup is estimated by varying the mean of the distribution of the number of interactions per bunch crossing overlaid in the simulation by the uncertainties obtained by studying the number of vertices, as a function of the pileup, as well as the results from the measurement of the inelastic cross-section.

An additional source of uncertainty arise from the finite dimension of the generated signal samples. Each strong-production GGM signal point has 10000 generated events, of which 3000 to 1000 pass the signal region selection, resulting in an average relative acceptance uncertainty equal to 2.3% across the gluino-neutralino grid.

Including all the contributions, the quadratic sum of the individual systematic uncertainties is, on average, $\sim 5\%$.

The theoretical uncertanties on the signal cross-sections are listed in Table 9.3. These uncertainties are obtained by following the PDF4LHC recommendations (213). In all signal points, an upper and lower envelope of the cross-sections predictions are defined by the maximum and minimum values estimated from the comparisons of the CTEQ6.6 (217) and the MSTW2008 NLO PDF (218) sets, including both the effects of the PDF and the μ scale uncertainties (and α_s uncertainty for CTEQ6.6):

$$\mathrm{CTEQ}^{\pm} = \sqrt{(PDF^{\pm}_{\mathrm{CTEQ}})^2 + (\mu^{\pm}_{\mathrm{CTEQ}})^2 + (\alpha_s^{\pm})^2}, \tag{9.14}$$

$$\mathrm{MTSW}^{\pm} = \sqrt{(PDF^{\pm}_{\mathrm{MTSW}})^2 + (\mu^{\pm}_{\mathrm{MTSW}})^2}, \tag{9.15}$$

thus the upper (U) and lower (L) variation are defined as:

$$U = max(\mathrm{CTEQ}^{\mathrm{nom}} + \mathrm{CTEQ}^{+}, \mathrm{MTSW}^{\mathrm{nom}} + \mathrm{MTSW}^{+}), \tag{9.16}$$

$$L = min(\mathrm{CTEQ}^{\mathrm{nom}} - \mathrm{CTEQ}^{-}, \mathrm{MTSW}^{\mathrm{nom}} - \mathrm{MTSW}^{-}). \tag{9.17}$$

The nominal value of the cross-section (σ) is taken to be the midpoint of the upper and lower envelopes, while its uncertainty ($\Delta\sigma$) is assigned as the half of the full width of the envelope:

$$\sigma = (U + L)/2, \tag{9.18}$$

$$\Delta\sigma = (U - L)/2. \tag{9.19}$$

9.5 Results

The number of events observed in the SR after the successive application of the selection requirements is shown in Table 9.13, togheter with the expected number of background events arising from SM processes. After applying the full selection, no events are observed in the SR, to be compared to an expectation of $0.27^{+0.22}_{-0.10}$ SM events.

Table 9.13: Number of events observed in the SR in data after the successive application of the selection requirements, as well as the size of the expected SM background.

Requirement	Number of Events
Two photons, $p_{\mathrm{T}}^{\gamma} > 75$	4982
$\Delta\phi_{\mathrm{min}}(\mathrm{jet}, E_{\mathrm{T}}^{\mathrm{miss}}) > 0.5$	4724
$m_{\mathrm{eff}} > 1500$ GeV	1
$E_{\mathrm{T}}^{\mathrm{miss}} > 175$ GeV	0
Expeected SM background	$0.27^{+0.22}_{-0.10}$

9.5.1 Statistical interpretation

The parameter of interest μ, which is the signal strength of the considered model (*i.e.* $\mu = 1$ if the new physics signal has the expected cross-section times branching ratio), is estimated with a maximum likelihood fit to the number of events n_s, observed in the signal region, and n_{CR} observed in the $W\gamma\gamma$ control region.

The likelihood function $L(\mu, \vec{\theta})$ is defined as (see also Sec. 8.7):

$$L(\mu, \vec{\theta}) = \mathrm{Pois}(n_s|\nu_{SR}(\mu, b, \vec{\theta})) \times \mathrm{Pois}(n_{CR}|\nu_{CR}(\mu, b, \vec{\theta})) \times \prod_k G(\theta_k). \tag{9.20}$$

Here $\vec{\theta} = \{\vec{\theta}_{\mathrm{exp.}}, \vec{\theta}_{\mathrm{bkg.}}\}$ is the vector of the nuisance parameters including the contribution from the experimental systematic uncertainties on the signal efficiency ($\vec{\theta}_{\mathrm{exp.}}$), and the uncertainties arising from the background evaluation ($\vec{\theta}_{\mathrm{bkg.}}$); $\nu(\mu, b, \vec{\theta})$ is the expected number of events in the signal region or in the $W\gamma\gamma$ CR given the signal strength μ, in particular it is defined as:

$$\nu(\mu, b, \vec{\theta}) = \mu \times s(\vec{\theta}_{\mathrm{exp.}}) + b(K_{W\gamma\gamma}, \vec{\theta}_{\mathrm{bkg.}}). \tag{9.21}$$

Here $K_{W\gamma\gamma}$ is the normalization factor that fits the $W\gamma\gamma$ events to the events observed in the CR, b is the expected number of SM events, and s is the expected number of signal events. Its central value is obtained as:

$$s = \sigma \times (A \times \varepsilon)(\vec{\theta}_{\mathrm{exp.}}) \times \mathcal{L}(\theta_{\mathrm{lumi}}), \tag{9.22}$$

where, $(A \times \varepsilon)$is the acceptance-times-efficiency given in Table 9.11, and σ is the cross-section of Table 9.3.

The results are obtained with a profiled likelihood ratio (PLR) test statistic (194; 219). The profile likelihood ratio, $\lambda(\mu)$, is built from the likelihood function described in Eq. (9.20), as the ratio between the likelihood maximized with respect to the set of

nuisance parameters ($\vec{\theta}$) for a specified value of the parameter of interest μ, and the likelihood maximized with respect to both the nuisance parameters and the parameter of interest.

$$\lambda(\mu) = \frac{L(\mu, \hat{\hat{\vec{\theta}}}(\mu))}{L(\hat{\mu}, \hat{\vec{\theta}}(\hat{\mu}))}, \tag{9.23}$$

where:

- $\hat{\hat{\vec{\theta}}}$ is the conditional maximum-likelihood (ML) estimator of $\vec{\theta}$, i.e the value of $\vec{\theta}$ that maximizes L for a specified μ;

- $\hat{\mu}$ and $\hat{\vec{\theta}}$ are the ML estimator of the unconditional likelihood.

From the definition of $\lambda(\mu)$ in Eq.(9.23) it follows that $0 \leq \lambda \leq 1$; moreover, $\lambda \sim 1$ implies a good agreement between the data and the hypothesized value of μ. Therefore, $\lambda(\mu)$ is used as test statistic, usually through the derived quantity $t_\mu = -2 \ln \lambda(\mu)$. Thus, higher values of t_μ correspond to an increasing incompatibility between the data and μ hypothesis. The level of disagreement can be quantified by the p-value (Figure 9.7) for the tested μ, which is evaluated as:

$$p_\mu = \int_{t_{\mu,\text{obs}}}^{\infty} f(t_\mu|\mu) dt_\mu, \tag{9.24}$$

where $t_{\mu,\text{obs}}$ is the value of the statistic t_μ observed from the data and $f(t_\mu|\mu)$ represents the expected t_μ distribution under the assumption of a signal strength μ.

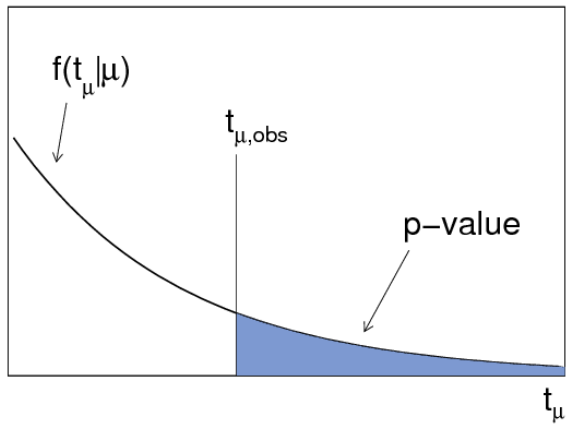

Figure 9.7: Illustration of a p-value obtained from an observed value $t_{\mu,obs}$ of the test statistic t_μ (194).

For $\mu = 0$, the compatibility of the data with the background-only hypothesis is described by the p_0. Rejecting the $\mu = 0$ hypothesis effectively leads to the discovery of

a new signal. The p_0 is computed from the q_0 test statistic, defined as:

$$q_0 = \begin{cases} -2\ln\lambda(0) & \hat{\mu} \geq 0 \\ 0 & \hat{\mu} < 0 \end{cases} = \begin{cases} -2\ln\frac{L(0,\hat{\hat{\theta}}(0))}{L(\hat{\mu},\hat{\hat{\theta}}(\hat{\mu}))} & \hat{\mu} \geq 0 \\ 0 & \hat{\mu} < 0 \end{cases}, \tag{9.25}$$

where the test statistic q_0 assumes a null value for $\hat{\mu} < 0$, because it is assumed that the presence of a new signal can only increase the mean event rate beyond what is expected from the background-only model. The p-value for the null hypothesis is:

$$p_0 = \int_{q_{0,\mathrm{obs}}}^{\infty} f(q_0|0,\hat{\hat{\theta}}(0))dq_0, \tag{9.26}$$

where f is the expected distribution of the test statistics if the same experiment was repeated several times.

The background-only p-value, p_0, is also quoted in terms of the significance Z, that is defined as the number of normal Gaussian standard deviations (σ) above which the mean of the Gaussian has an upper-tail probability equal to p. The relation between p_0 and Z is defined as:

$$Z = \Phi^{-1}(1 - p_0), \tag{9.27}$$

where Φ^{-1} is the quantile, *i.e.* the inverse of cumulative distribution, of the standard Gaussian distribution. Figure 9.8 shows the relation between the significance Z and the p-value.

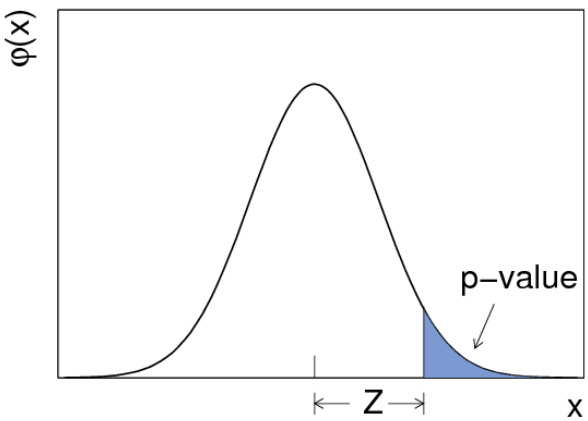

Figure 9.8: The standard Gaussian distribution $\phi(x) = (1/\sqrt{2\pi})\exp(-x^2/2)$, showing the relation between the significance Z and the p-value (194).

In order to set an upper-limit the p-value is computed for several values of μ, until the value corresponding to the fixed threshold α is found: for example $\alpha = 0.05$ to exclude the signal with a confidence level (CL) equal to 95%. The upper limit on μ is therefore the largest μ with $p_\mu \leq \alpha$, while the μ parameters with p_μ above the threshold are excluded with a confidence of $CL = 1 - \alpha$.

More precisely, upper limits on the signal strength parameter μ are set using a modified frequentist (CL_s) (220) method, which instead of the simple p_μ uses:

$$p'_\mu = \frac{p_\mu}{1 - p_b}, \tag{9.28}$$

where

$$p_\mu = \int_{\tilde{q}_{\mu,\mathrm{obs}}}^{\infty} f(\tilde{q}_\mu|\mu, \hat{\hat{\vec{\theta}}}(\mu))d\tilde{q}_\mu, \tag{9.29}$$

$$p_b = 1 - \int_{\tilde{q}_{\mu,\mathrm{obs}}}^{\infty} f(\tilde{q}_\mu|0, \hat{\hat{\vec{\theta}}}(0))d\tilde{q}_\mu. \tag{9.30}$$

The test statistic used for limit setting is $\tilde{q}_\mu$, which differentiates the case of the signal being produced at a rate μ from the case of signal events being produced at a lesser rate $\mu' < \mu$:

$$\tilde{q}_\mu = \begin{cases} -2\ln\tilde{\lambda}(\mu) & \hat{\mu} \leq \mu \\ 0 & \hat{\mu} > \mu \end{cases} = \begin{cases} -2\ln\frac{L(\mu,\hat{\hat{\vec{\theta}}}(\mu))}{L(\hat{\mu},\hat{\vec{\theta}}(\hat{\mu}))} & 0 \leq \hat{\mu} \leq \mu \\ 0 & \hat{\mu} > \mu \\ -2\ln\frac{L(\mu,\hat{\hat{\vec{\theta}}}(\mu))}{L(0,\hat{\hat{\vec{\theta}}}(0))} & \hat{\mu} < 0 \end{cases}. \tag{9.31}$$

The reason for setting $\tilde{q}_\mu = 0$ if $\hat{\mu} > \mu$ is that, when setting an upper limit, data with $\hat{\mu} > \mu$ are disregarded because they represent less compatibility with μ than the data obtained, hence they are not part of the rejection region of the test.

When $\hat{\mu} \leq \mu$, two possible cases are considered. If $\hat{\mu} < 0$, $\hat{\mu}$ is replaced arbitrarily by zero, because $\mu \geqslant 0$ is expected for the signal of a new particle decay, thus a test of negative value would not be significant. If $0 \leq \hat{\mu} \leq \mu$ the test statistic is written in the standard form.

In order to find the p-values, both for exclusion or limit calculation, the sampling distribution $f(q_\mu|\mu)$ for the test statistics are obtained generating toy Monte Carlo pseudo-experiments in which the number of events n and the *global observables*, *i.e.* the values a at which the Gaussian constraint $G(\theta) = G(a|\theta, 1)$ are evaluated (in the nominal model a is set to zero), are all randomized.

9.5.2 Limit setting

Based on the observation of zero events in the SR and the magnitude of the estimated SM background expectation and uncertainty, an upper limit is set on the number of events from any scenario of physics beyond the SM. Assuming that no events due to physical processes beyond those of the SM populate the $\ell\gamma\gamma$ CR used to estimate the $W\gamma\gamma$ background, the observed 95% CL upper limit on the number of non-SM events in the SR is 3.0. Considering the integrated luminosity of 3.2 fb^{-1}, this limit translates into a 95% CL upper limit on the visible cross-section for new physics, defined by the product of cross-section, branching fraction, acceptance and efficiency, of 0.93 fb.

Considering in addition the value and uncertainty of the acceptance-times-efficiency of the selection requirements associated with the SR, as well as the NLO (+NLL) GGM cross-section, for various $(m_{\tilde{g}}, m_{\tilde{\chi}_1^0})$, 95% CL lower limits are set on the mass of the gluino as a function of the mass of the neutralino, in the context of the GGM scenario. Figure 9.9 shows the resulting observed limit on the gluino mass. The observed limits

are exhibited for the nominal SUSY model cross-section expectation, as well as for a SUSY cross-section increased and lowered by one standard deviation of the cross-section systematic uncertainty. Also shown is the expected limit, including its uncertainty range. Because the background expectation is close to zero and no events are observed in data, the expected and observed limits nearly overlap. The observed lower limit on the gluino mass is observed to be roughly independent of neutralino mass, reaching a minimum value of approximately 1650 GeV at a neutralino mass of 250 GeV.

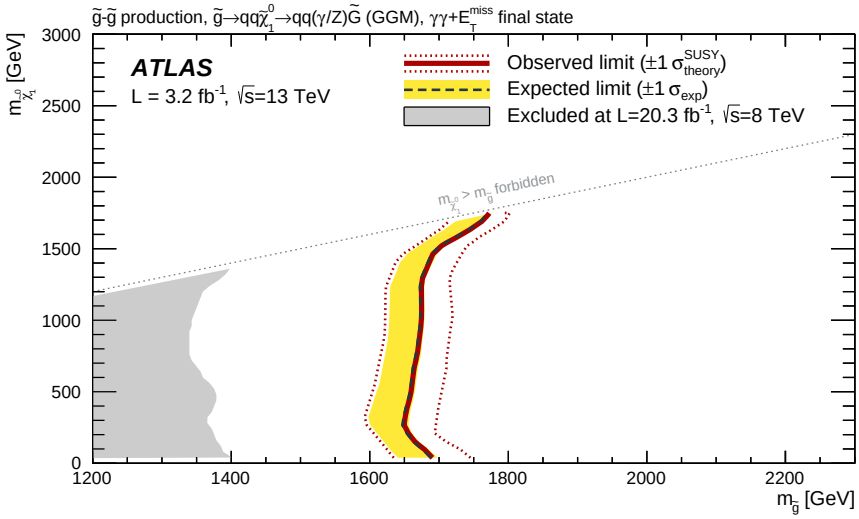

Figure 9.9: Exclusion limits in the neutralino–gluino mass plane at 95% CL. The observed limits are exhibited for the nominal SUSY model cross-section, as well as for a SUSY cross-section increased and lowered by one standard deviation of the cross-section systematic uncertainty. Also shown is the expected limit, as well as the ±1 standard-deviation range of the expected limit, which is asymmetric because of the low count expected. Because the background expectation is close to zero and the observed number of events is zero, the expected and observed limits nearly overlap. The previous limit from ATLAS using 8 TeV data (27) is shown in grey.

9.6 Analysis of the 2015 and 2016 data

The analysis presented in the previous section has been updated exploiting also the data collected during 2016 (29), leading to a total integrated luminosity of 36.1 fb^{-1}. The next paragraphs present the main differences between the newer analysis and the search based on the 2015 data.

9.6.1 Additional model interpretation

Due to the larger number of events available in the 2015–2016 dataset, two additional GGM models characterized by a lower cross-section than the gluino pair production are considered. In the first model (Figure 9.10a), the signal arises from the (electro-weak) production of a degenerate triplet of the $SU(2)$ gauge partner (wino, or $\tilde{W}$) states $\tilde{\chi}_2^0$ and $\tilde{\chi}_1^\pm$, and is dominated by the production of $\tilde{\chi}_1^+\tilde{\chi}_1^-$ and $\tilde{\chi}_2^0\tilde{\chi}_1^\pm$. For the second model, the signal is due to squark pair production as illustraded in Figure 9.10b.

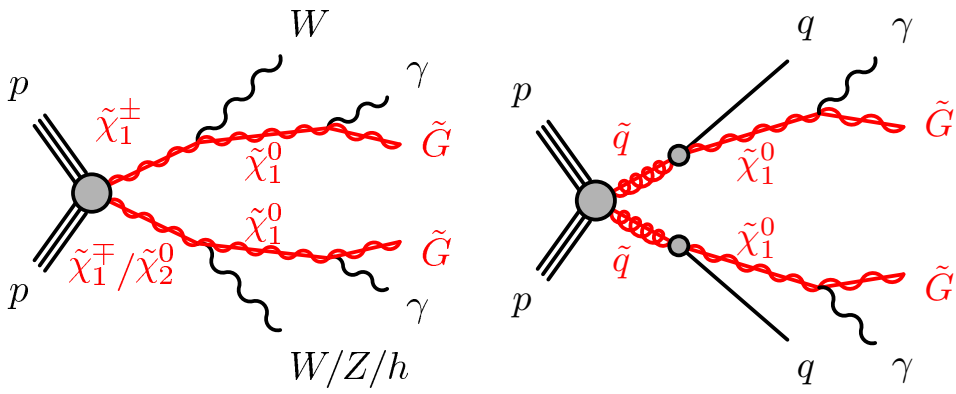

Figure 9.10: Typical production and decay-chain processes for the electro-weak-production (a) and squark-production (b) instances of the GGM model for which the NLSP is a bino-like neutralino.

A total of 104 signal points were generated, with 10000 simulated events each, for the wino-neutralino model, with wino masses ranging in 100 GeV steps from 500 GeV to 1500 GeV, and, for a fixed wino mass, with neutralino masses varying generally in steps of 200 GeV up to the wino mass. In addition, for each value of the wino mass, signal points are generated with neutralino masses of 10 GeV and 50 GeV, and within 10, 50, and 100 GeV of the wino mass. Finally, a set of grid points is included with $m_{\tilde{\chi}_1^0} = m_{\tilde{\chi}_2^0}, m_{\tilde{\chi}_1^\pm} - 200$ GeV for wino masses of 300 and 400 GeV. This grid is depicted graphically in Fig. 9.11a. The typical cross-sections and their uncertainties are summarised in Table 9.14.

For the squark-neutralino model a total of 120 signal points were generated, with 10000 simulated events each, with squark masses ranging in 200 GeV step between 800 GeV and 1200 GeV, and in 100 GeV step between 1200 GeV and 2100 GeV, with neutralino mass varying in steps of 300 GeV up to the squark mass. Just like the other two grids, for each value of the squark mass, signal points are generated with neutralino masses of

10 GeV and 50 GeV, and within 10, 50 and 100 GeV of the gluino mass. This grid is depicted graphically in Fig. 9.11b. The typical cross-section and their uncertainties are summarized in Table 9.15. All squark states are taken to be degenerate in mass, with the exception of the partners of the three right-handed up-type quarks, whose masses are decoupled in order to satisfy GGM sum rules (221).

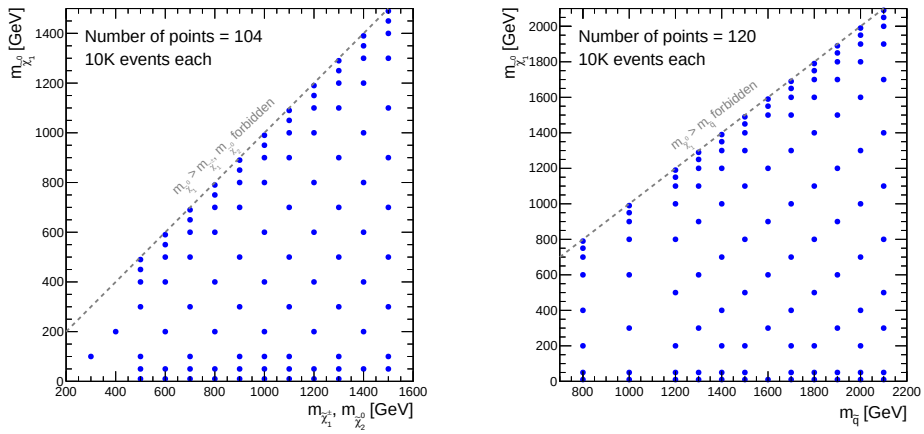

(a) wino-neutralino (b) squark-neutralino

Figure 9.11: Values of the wino and neutralino masses (a) and squark and neutralino masses (b), chosen for the signal event generation and simulation.

9.6.2 Signal region definition

The signal region selection is optimized using four benchmark signal points. Two of the focus points are geared towards strong (gluino) production: one each for low ($m_{\tilde{g}} = 1900$ GeV, $m_{\tilde{\chi}_1^0} = 150$ GeV) and high ($m_{\tilde{g}} = 1900$ GeV,$m_{\tilde{\chi}_1^0} = 1700$ GeV) neutralino mass. The other two focus points are geared towards electro-weak (wino) production: again, one for low ($m_{\tilde{\chi}_2^0}, m_{\tilde{\chi}_1^\pm} = 1000$ GeV, $m_{\tilde{\chi}_1^0} = 100$ GeV) and high ($m_{\tilde{\chi}_2^0}, m_{\tilde{\chi}_1^\pm} = 1000$ GeV, $m_{\tilde{\chi}_1^0} = 800$ GeV) neutralino mass.

Figures 9.12 and 9.13 show the predicted distributions of the leading and subleading photon transverse momentum, m_{eff} and H_{T} respectively, for the four signal focus points as well as for the data and for the background events.

For each mass focus point the optimization of the signal region proceeds as already illustrated in Sec. 9.2. Four independent (but not orthogonal) SRs are identified, two for each production mode, respectively for low and high mass value of the neutralino: $\text{SR}^{\gamma\gamma}_{S-L}$, $\text{SR}^{\gamma\gamma}_{S-H}$ are exploited to test the gluino-neutralino model, while $\text{SR}^{\gamma\gamma}_{W-L}$ and $\text{SR}^{\gamma\gamma}_{W-H}$ are exploited to study the wino-neutralino model. Additionally, the squark-neutralino model is probed using the same signal regions defined for the gluino-neutralino model. The definition of the SR selection requirements is summarised in Table 9.16.

Figures 9.14 and 9.15 show $(A \times \varepsilon)$ across the $m_{\tilde{g}}$-$m_{\tilde{\chi}_1^0}$, $m_{\tilde{q}}$-$m_{\tilde{\chi}_1^0}$ planes for the $\text{SR}^{\gamma\gamma}_{S-L}$ and the $\text{SR}^{\gamma\gamma}_{S-H}$ selections. Figure 9.16 shows the acceptance-times-efficiency across the $m_{\tilde{\chi}_2^0}, m_{\tilde{\chi}_1^\pm}$-$m_{\tilde{\chi}_1^0}$ plane for the $\text{SR}^{\gamma\gamma}_{W-L}$ and $\text{SR}^{\gamma\gamma}_{W-H}$ selections.

Table 9.14: NLO+NLL cross-sections by process, and total cross-section uncertainty, for GGM wino-neutralino signal points.

$m_{\tilde{\chi}_2^0}, m_{\tilde{\chi}_1^\pm}$[GeV]	$\tilde{\chi}_2^0\tilde{\chi}_1^+$[pb]	$\tilde{\chi}_2^0\tilde{\chi}_1^-$[pb]	$\tilde{\chi}_1^+\tilde{\chi}_1^-$[pb]	Total [pb]	Uncertainty (%)
300	2.60×10^2	1.27×10^2	1.90×10^2	5.77×10^2	6.4
400	8.39×10^1	3.71×10^1	5.86×10^1	1.80×10^2	6.3
500	3.29×10^1	1.34×10^1	2.21×10^1	6.84×10^1	6.9
600	1.46×10^1	5.56×10^0	9.50×10^0	2.96×10^1	7.5
700	6.99×10^0	2.52×10^0	4.43×10^0	1.39×10^1	7.5
800	3.54×10^0	1.22×10^0	2.21×10^0	6.97×10^0	7.8
900	1.87×10^0	6.23×10^{-1}	1.15×10^0	3.64×10^0	8.3
1000	1.01×10^0	3.29×10^{-1}	6.22×10^{-1}	1.96×10^0	8.5
1100	5.59×10^{-1}	1.81×10^{-1}	3.43×10^{-1}	1.08×10^0	8.8
1200	3.16×10^{-1}	1.01×10^{-1}	1.96×10^{-1}	6.13×10^{-1}	9.1
1300	1.80×10^{-1}	6.06×10^{-2}	1.16×10^{-1}	3.57×10^{-1}	9.4
1400	1.01×10^{-1}	3.03×10^{-2}	6.87×10^{-2}	2.00×10^{-1}	9.9
1500	5.99×10^{-2}	2.00×10^{-2}	3.96×10^{-2}	1.20×10^{-1}	14

Table 9.15: NLO+NLL cross-sections for squark production excluding stop, and the stop production, and total cross-section, with the uncertainties, for GGM squark-neutralino signal points.

$M_{\tilde{q}}$[GeV]	$\tilde{q}$ pair [fb]	$\widetilde{t}$ pair [fb]	Total [fb]	Uncertainty (%)
800	2.31×10^2	2.88×10^1	2.60×10^2	14
1000	5.00×10^1	6.24×10^0	5.62×10^1	16
1200	1.30×10^1	1.63×10^0	1.47×10^1	18
1300	6.91×10^0	8.64×10^{-1}	7.78×10^0	20
1400	3.77×10^0	4.71×10^{-1}	4.24×10^0	22
1500	2.09×10^0	2.61×10^{-1}	2.35×10^0	24
1600	1.19×10^0	1.48×10^{-1}	1.33×10^0	27
1700	6.76×10^{-1}	8.45×10^{-2}	7.61×10^{-1}	29
1800	3.95×10^{-1}	4.94×10^{-2}	4.44×10^{-1}	31
1900	2.32×10^{-1}	2.89×10^{-2}	2.61×10^{-1}	34
2000	1.37×10^{-1}	1.71×10^{-2}	1.54×10^{-1}	37
2100	8.21×10^{-2}	1.03×10^{-2}	9.23×10^{-2}	40

Table 9.16: Requirements defining the four SRs developed for the di-photon plus $E_{\mathrm{T}}^{\mathrm{miss}}$ signature searches.

Signal Region	$\mathrm{SR}^{\gamma\gamma}_{S-L}$	$\mathrm{SR}^{\gamma\gamma}_{S-H}$	$\mathrm{SR}^{\gamma\gamma}_{W-L}$	$\mathrm{SR}^{\gamma\gamma}_{W-H}$
Number of tight and isolated photons	≥ 2	≥ 2	≥ 2	≥ 2
E_{T}^{γ} [GeV]	> 75	> 75	> 75	> 75
$E_{\mathrm{T}}^{\mathrm{miss}}$ [GeV]	> 150	> 250	> 150	> 250
H_{T} [GeV]	> 2750	> 2000	> 1500	> 1000
$\Delta\phi_{\mathrm{min}}(\mathrm{jet}, E_{\mathrm{T}}^{\mathrm{miss}})$	> 0.5	> 0.5	> 0.5	> 0.5
$\Delta\phi_{\mathrm{min}}(\gamma, E_{\mathrm{T}}^{\mathrm{miss}})$	...	> 0.5	...	> 0.5

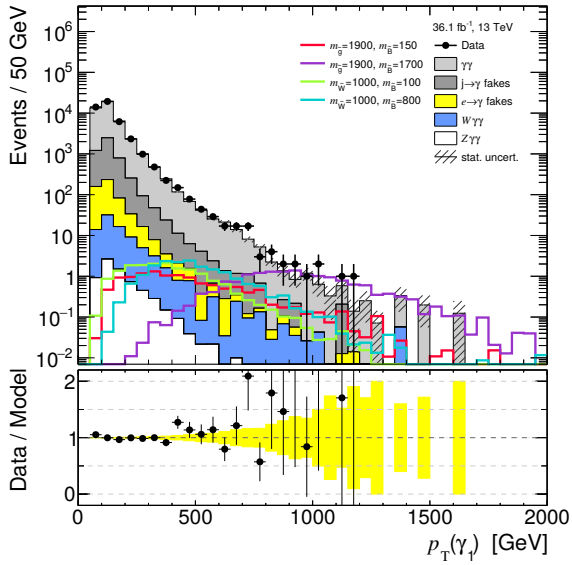

(a) $p_{\mathrm{T}}^{\gamma,1}$

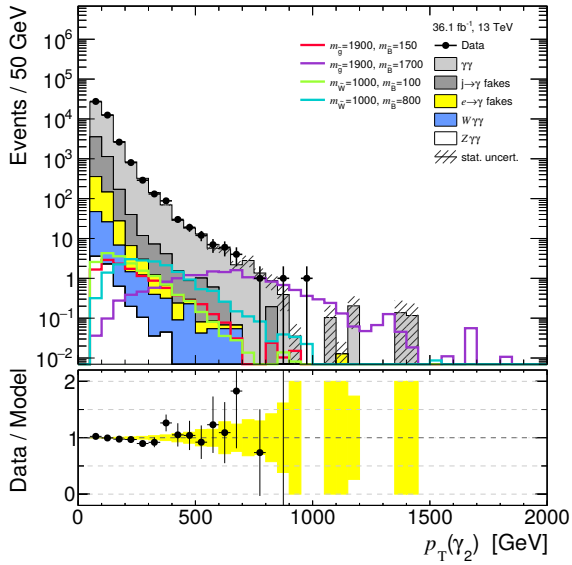

(b) $p_{\mathrm{T}}^{\gamma,2}$

Figure 9.12: Distributions of $p_{\mathrm{T}}^{\gamma,1}$ (a), $p_{\mathrm{T}}^{\gamma,2}$ (b) for the di-photon sample after the application of requirements of $E_{\mathrm{T}}^{\gamma} > 75$ GeV on each selected photon and of $\Delta\phi_{\mathrm{min}}(\mathrm{jet}, E_{\mathrm{T}}^{\mathrm{miss}}) > 0.5$, but with no requirements imposed on $E_{\mathrm{T}}^{\mathrm{miss}}$ and H_{T}. The expected contributions from SM processes are estimated using the combination of Monte Carlo and data-driven estimates discussed in section 9.3. Uncertainties (shaded bands for MC simulation, error bars for data) are statistical only. The yellow band represents the uncertainty in the data/SM ratio that arises from the statistical limitations of the estimates of the various expected sources of SM background. Also shown are the expected contributions from the GGM signal for the four focus points, $(m_{\tilde{g}}, m_{\tilde{\chi}_1^0}) = (1900\,\mathrm{GeV}, 150\,\mathrm{GeV})$, $(m_{\tilde{g}}, m_{\tilde{\chi}_1^0}) = (1900\,\mathrm{GeV}, 1700\,\mathrm{GeV})$, $(m_{\tilde{\chi}_2^0}, m_{\tilde{\chi}_1^\pm}, m_{\tilde{\chi}_1^0}) = (1000\,\mathrm{GeV}, 100\,\mathrm{GeV})$, and $(m_{\tilde{\chi}_2^0}, m_{\tilde{\chi}_1^\pm}, m_{\tilde{\chi}_1^0}) = (1000\,\mathrm{GeV}, 800\,\mathrm{GeV})$.

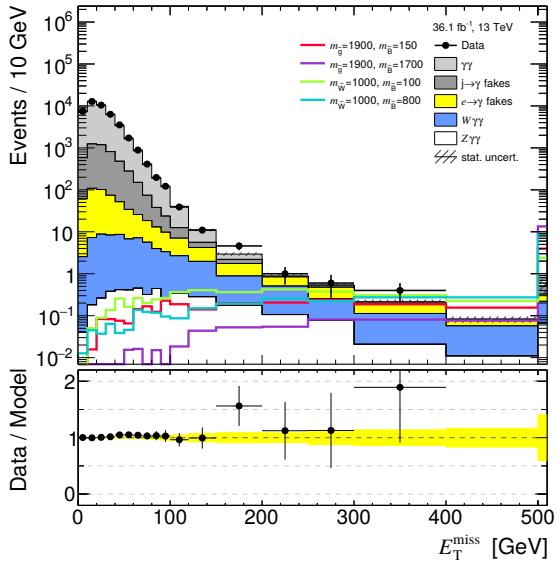

(a) $E_{\mathrm{T}}^{\mathrm{miss}}$

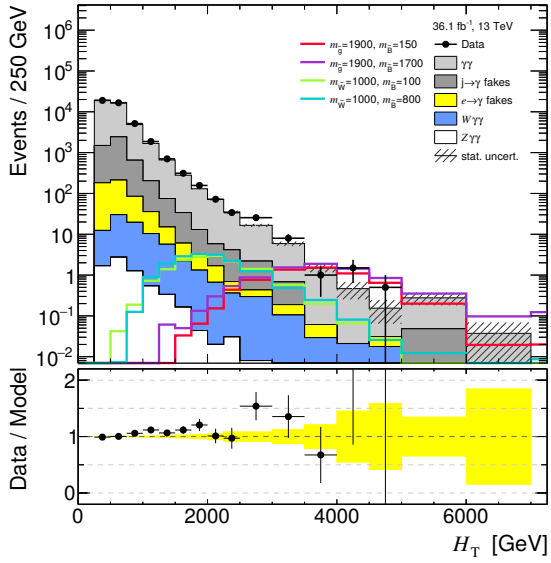

(b) H_{T}

Figure 9.13: Distributions of $E_{\mathrm{T}}^{\mathrm{miss}}$ (a) and H_{T} (b) for the di-photon sample after the application of requirements of $E_{\mathrm{T}}^{\gamma} > 75$ GeV on each selected photon and of $\Delta\phi_{\mathrm{min}}(\mathrm{jet}, E_{\mathrm{T}}^{\mathrm{miss}}) > 0.5$, but with no requirements imposed on $E_{\mathrm{T}}^{\mathrm{miss}}$ and H_{T}. The expected contributions from SM processes are estimated using the combination of Monte Carlo and data-driven estimates discussed in section 9.3. Uncertainties (shaded bands for MC simulation, error bars for data) are statistical only. The yellow band represents the uncertainty in the data/SM ratio that arises from the statistical limitations of the estimates of the various expected sources of SM background. Also shown are the expected contributions from the GGM signal for the four focus points, $(m_{\tilde{g}}, m_{\tilde{\chi}_1^0}) = (1900\,\mathrm{GeV}, 150\,\mathrm{GeV})$, $(m_{\tilde{g}}, m_{\tilde{\chi}_1^0}) = (1900\,\mathrm{GeV}, 1700\,\mathrm{GeV})$, $(m_{\tilde{\chi}_2^0}, m_{\tilde{\chi}_1^\pm}, m_{\tilde{\chi}_1^0}) = (1000\,\mathrm{GeV}, 100\,\mathrm{GeV})$, and $(m_{\tilde{\chi}_2^0}, m_{\tilde{\chi}_1^\pm}, m_{\tilde{\chi}_1^0}) = (1000\,\mathrm{GeV}, 800\,\mathrm{GeV})$.

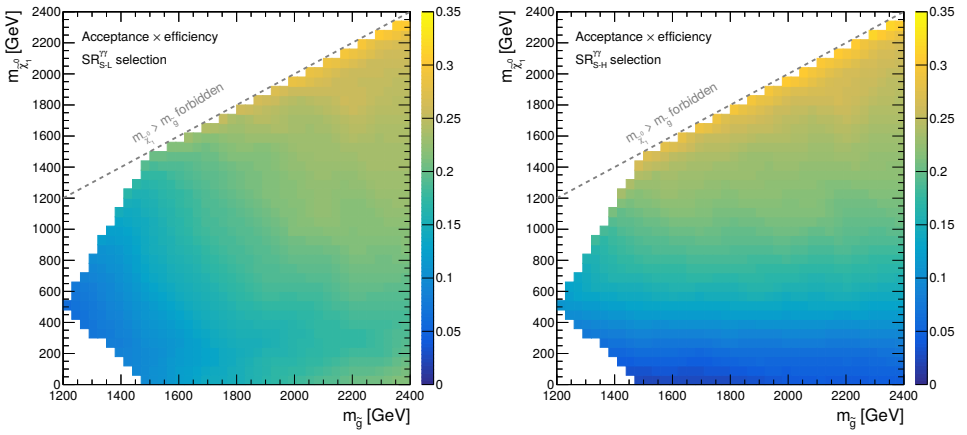

(a) $\mathrm{SR}^{\gamma\gamma}_{S-L}$ (b) $\mathrm{SR}^{\gamma\gamma}_{S-H}$

Figure 9.14: Total acceptance × efficiency across the $m_{\tilde{g}}$-$m_{\tilde{\chi}^0_1}$ GGM grid for the $\mathrm{SR}^{\gamma\gamma}_{S-L}$ (a) and $\mathrm{SR}^{\gamma\gamma}_{S-H}$ (b) signal regions .

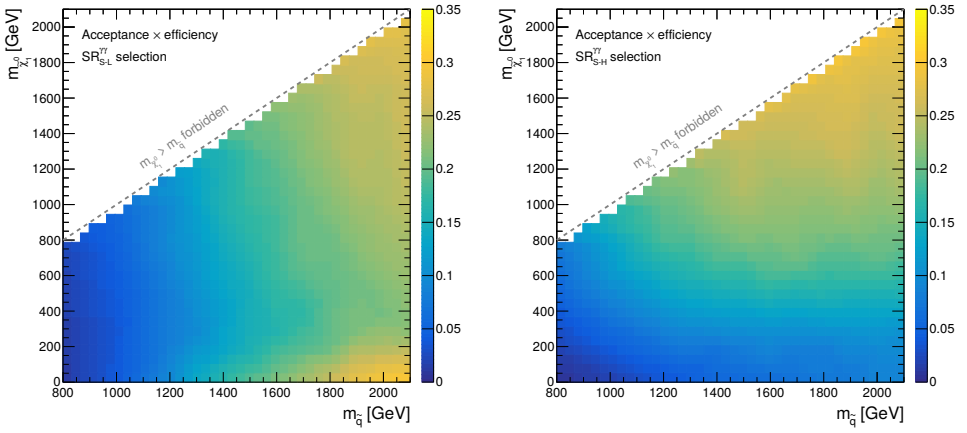

(a) $\mathrm{SR}^{\gamma\gamma}_{S-L}$ (b) $\mathrm{SR}^{\gamma\gamma}_{S-H}$

Figure 9.15: Total acceptance × efficiency across the $m_{\tilde{q}}$-$m_{\tilde{\chi}^0_1}$ GGM grid for the $\mathrm{SR}^{\gamma\gamma}_{S-L}$ (a) and $\mathrm{SR}^{\gamma\gamma}_{S-H}$ (b) signal regions .

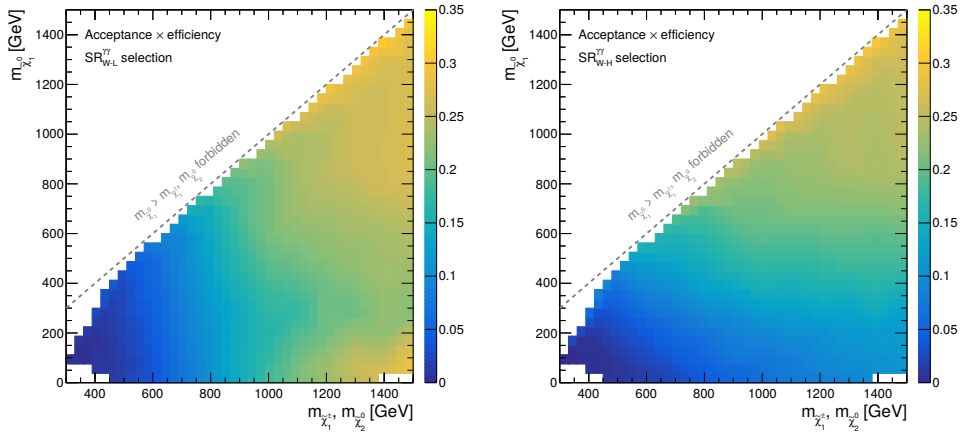

(a) $\mathrm{SR}^{\gamma\gamma}_{W-L}$ (b) $\mathrm{SR}^{\gamma\gamma}_{W-H}$

Figure 9.16: Total acceptance × efficiency across the $m_{\tilde{\chi}^0_2}, m_{\tilde{\chi}^\pm_1}$-$m_{\tilde{\chi}^0_1}$ GGM grid for the $\mathrm{SR}^{\gamma\gamma}_{W-L}$ (a) and $\mathrm{SR}^{\gamma\gamma}_{W-H}$ (b) signal regions .

9.6.3 Background evaluation

The evaluation of the background contributions to the four signal regions is based on the same approach illustrated in Sec. 9.3. Table 9.17 summarizes the number of the expected and the observed events in each signal region. The reliability of the background model is verified by the use of several validation regions. The definitions of these VRs are shown in Table 9.18, together with the expected and observed numbers of events in each region (also shown in Figure 9.17). The background model predictions and the number of observed events are in good agreement in each validation region. Also in the signal regions no significant excess has been found.

Table 9.17: The expected and observed numbers of events for the four signal regions. The quoted errors are the combined statistical and systematic uncertainties (29).

Signal Region	$\mathrm{SR}^{\gamma\gamma}_{S-L}$	$\mathrm{SR}^{\gamma\gamma}_{S-H}$	$\mathrm{SR}^{\gamma\gamma}_{W-L}$	$\mathrm{SR}^{\gamma\gamma}_{W-H}$
$\gamma\gamma$ (QCD)	$0.00^{+0.17}_{-0.00}$	$0.00^{+0.17}_{-0.00}$	$0.15^{+0.17}_{-0.15}$	$0.00^{+0.17}_{-0.00}$
jet $\to \gamma$	$0.19^{+0.21}_{-0.19}$	$0.19^{+0.21}_{-0.19}$	0.93 ± 0.67	$0.19^{+0.21}_{-0.19}$
e $\to \gamma$	0.08 ± 0.04	0.06 ± 0.04	0.88 ± 0.23	0.51 ± 0.15
$(W \to \ell\nu)\gamma\gamma$	0.22 ± 0.14	0.21 ± 0.13	1.55 ± 0.78	1.08 ± 0.56
$(Z \to \nu\nu)\gamma\gamma$	0.01 ± 0.01	0.03 ± 0.02	0.15 ± 0.08	0.27 ± 0.13
Expected background events	$0.50^{+0.30}_{-0.26}$	$0.48^{+0.30}_{-0.25}$	3.67 ± 1.07	$2.05^{+0.65}_{-0.63}$
Observed events	0	0	6	1

Table 9.18: Definition, expected and observed events of the seven validation regions used to confirm background model. The uncertainties on the numbers of expected events are the combined statistical and systematic uncertainties (29).

	E_{T}^{γ} [GeV]	$\Delta\phi_{\mathrm{min}}(\mathrm{jet}, E_{\mathrm{T}}^{\mathrm{miss}})$	N_{lep}	H_{T} [GeV]	$E_{\mathrm{T}}^{\mathrm{miss}}$ [GeV]	N_{exp}	N_{obs}
VR1	> 75	> 0.5	...	...	< 150	43524 ± 4388	43918
VR2	> 75	> 0.5	...	$(1000, 2500)$	< 150	2845 ± 522	3139
VR3	> 75	> 0.5	...	...	$(100, 150)$	112 ± 36	109
VR4	> 50	...	$1e$	< 2000	...	34.5 ± 7.2	38
VR5	> 50	...	1μ	< 2000	...	19.8 ± 7.1	25
VR6	> 75	> 0.5	...	> 1750	...	287 ± 129	336
VR7	> 75	> 0.5	...	...	> 100	139 ± 40	146

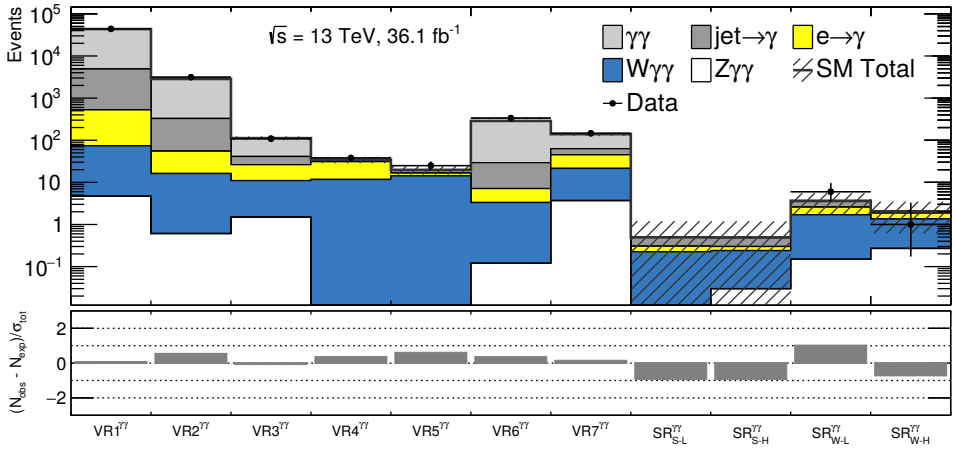

Figure 9.17: Comparisons between expected and observed content of the validation and signal regions. The lower panel shows the pull (difference between observed and expected event counts normalized by the uncertainty) for each region. The uncertainties on the numbers of expected events are the combined statistical and systematic uncertainties.

9.6.4 Results

Since no significant excess is found over the SM expectation upper limits are set on the number of events from any scenario of physics beyond the SM. Assuming that no events due to physical processes beyond those of the SM populate the $\ell\gamma\gamma$ CR used to estimate the $W\gamma\gamma$ background, the observed 95% CL upper limit on the number of non-SM events in the SR is summarised in Table 9.19.

Considering in addition the value and uncertainty of the acceptance-times-efficiency of the selection requirements associated with the SR, as well as the NLO (+NLL) GGM cross-section, for three different production modes investigated considering all possible values of the $\tilde{\chi}_1^0$ mass, 95% CL lower limits of 2150 GeV, 1820 GeV and 1060 GeV are set on the mass of the gluino, squark and wino respectively, as shown by Figures 9.18-9.20.

Table 9.19: Summary of the number of events expected from SM sources ($N_{\text{exp}}^{\text{SM}}$), and the observed number of events (N_{obs}), for each of the four SRs. Also shown are the derived (S_{obs}^{95}) and expected (S_{exp}^{95}) model-independent 95% CL limits on the number of events from non-SM processes, and the observed ($\langle\epsilon\sigma\rangle_{\text{obs}}^{95}$) and expected ($\langle\epsilon\sigma\rangle_{\text{exp}}^{95}$) 95% CL limits on the visible cross-section from non-SM processes. The last column of the table shows the significance Z of the observed excess (if any), and its p-value (p) (29).

Signal Region	N_{obs}	$N_{\text{exp}}^{\text{SM}}$	S_{obs}^{95}	S_{exp}^{95}	$\langle\epsilon\sigma\rangle_{\text{obs}}^{95}$[fb]	$\langle\epsilon\sigma\rangle_{\text{exp}}^{95}$[fb]	Z (p)
$\text{SR}_{S-L}^{\gamma\gamma}$	0	$0.50^{+0.30}_{-0.26}$	3.0	$3.1^{+1.4}_{-0.2}$	0.083	$0.086^{+0.039}_{-0.003}$	0.00 (0.50)
$\text{SR}_{S-H}^{\gamma\gamma}$	0	$0.48^{+0.30}_{-0.25}$	3.0	$3.1^{+1.3}_{-0.1}$	0.083	$0.086^{+0.036}_{-0.003}$	0.00 (0.50)
$\text{SR}_{W-L}^{\gamma\gamma}$	6	3.7 ± 1.1	8.6	$5.8^{+2.8}_{-1.6}$	0.238	$0.161^{+0.078}_{-0.044}$	1.06 (0.14)
$\text{SR}_{W-H}^{\gamma\gamma}$	1	$2.05^{+0.65}_{-0.63}$	3.7	$4.4^{+1.9}_{-1.0}$	0.103	$0.122^{+0.053}_{-0.028}$	0.00 (0.50)

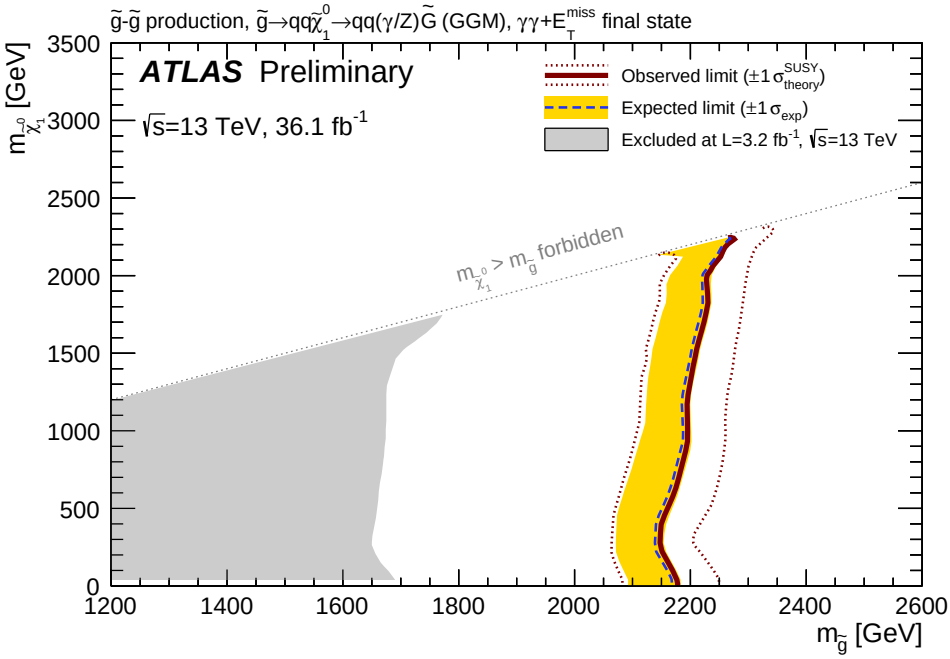

Figure 9.18: Exclusion limits in the neutralino–gluino mass plane at 95% CL, using the combination of the $\text{SR}_{S-H}^{\gamma\gamma}$ analysis and the $\text{SR}_{S-L}^{\gamma\gamma}$ analysis. The observed limits are exhibited for the nominal SUSY model cross-section, as well as for a SUSY cross-section increased and lowered by one standard deviation of the cross-section systematic uncertainty. Also shown is the expected limit, as well as the ± 1 standard-deviation range of the expected limit (29). The previous limit from ATLAS using 13 TeV data and an intengrated luminosity of 3.2 fb^{-1} (see Sec. 9.5.2, (26)) is shown in grey.

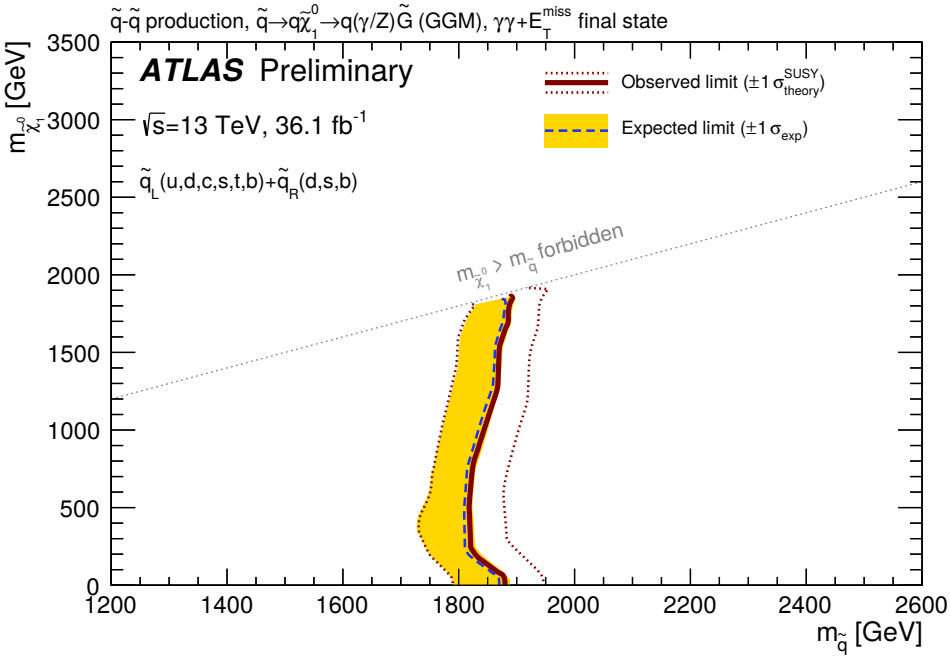

Figure 9.19: Exclusion limits in the neutralino–squarks mass plane at 95% CL, using the combination of the $\mathrm{SR}^{\gamma\gamma}_{S-H}$ analysis and the $\mathrm{SR}^{\gamma\gamma}_{S-L}$ analysis. The observed limits are exhibited for the nominal SUSY model cross-section, as well as for a SUSY cross-section increased and lowered by one standard deviation of the cross-section systematic uncertainty (29).

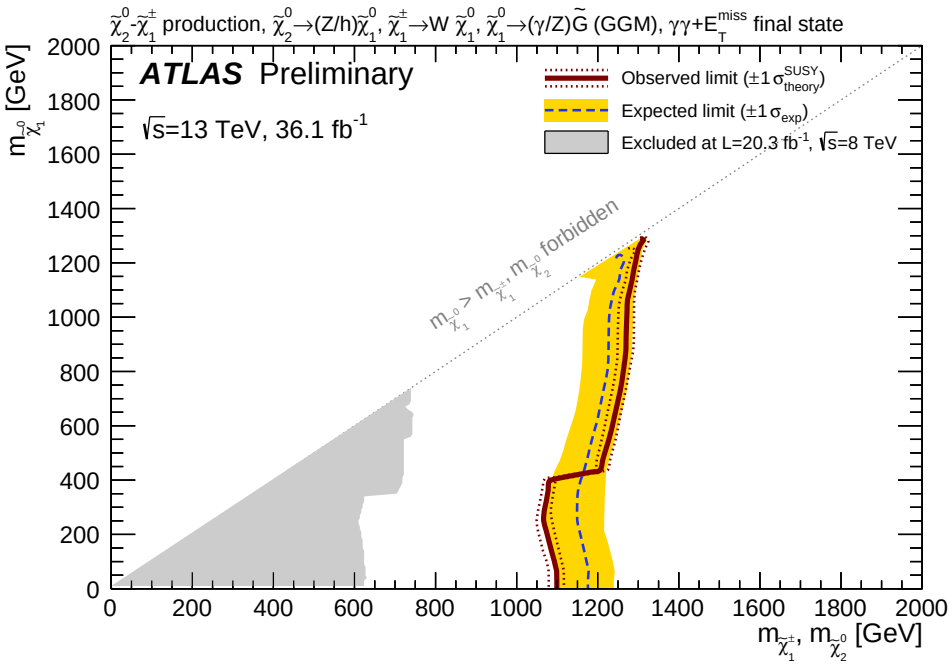

Figure 9.20: Exclusion limits in the neutralino–wino mass plane at 95% CL, using the combination of the $SR^{\gamma\gamma}_{W-H}$analysis and the $SR^{\gamma\gamma}_{W-L}$analysis.. The observed limits are exhibited for the nominal SUSY model cross-section, as well as for a SUSY cross-section increased and lowered by one standard deviation of the cross-section systematic uncertainty. Also shown is the expected limit, as well as the ±1 standard-deviation range of the expected limit.The discontinuity at $m_{\tilde{\chi}_1^0} = \sim 400$ GeV is due to the switch between the use of the $SR^{\gamma\gamma}_{W-L}$ and $SR^{\gamma\gamma}_{W-H}$ analyses, the former of which exhibits a small excess of observed events relative to the expected SM background (29). The previous limit from ATLAS using 8 TeV data (27) is shown in grey.

Conclusion

This thesis presented two different analyses based on the proton-proton collision data collected by the ATLAS detector at $\sqrt{s} = 13$ TeV, corresponding to an integrated luminosity of 36.1 fb^{-1}. The first one is the precision measurement of the Higgs boson mass in the di-photon decay channel, and the second one is the search for the production of supersymmetric particles in a final state containing two photons and missing transverse momentum.

The measured value of the Higgs boson mass is $m_H^{\gamma\gamma} = 125.11 \pm 0.42\,\text{GeV} = 125.11 \pm 0.21(\text{stat}) \pm 0.36(\text{syst})\,\text{GeV}$ (10). This result improves significantly the total uncertainty of the measurement performed by ATLAS exploiting the Run 1 result, $m_H^{\gamma\gamma} = 126.02 \pm 0.51\,\text{GeV} = 126.02 \pm 0.43(\text{stat.}) \pm 0.27(\text{syst.})\,\text{GeV}$ (45), even if it is characterized by a higher systematic uncertainty. The difference between the Run 1 and Run 2 systematic uncertainties accounts for the different level of understanding of the recent 2015 and 2016 data, with respect to 2011 and 2012.

The combination of the $H \to \gamma\gamma$ analysis with a similar analysis in the $H \to ZZ^* \to 4\ell$ (with $\ell = e, \mu$) decay channel is also presented. The combined result is:

$$m_H = 124.98 \pm 0.19\ (\text{stat}) \pm 0.21\ (\text{syst})\ \text{GeV} = 124.98 \pm 0.28\ \text{GeV}.$$

This value in excellent agreement with, and has similar precision to, the value that was measured combining ATLAS and CMS Run 1 data (11).

The second analysis, presented in this manuscript, is the search for production of supersymmetric particles in a final state containing two photons and missing transverse momentum (26). The di-photon final state is predicted by a particular class of Supersymmetry models known as *Gauge-Mediated Supersymmetry Breaking*. In particular, three different models have been considered, where the $\gamma\gamma + E_{\text{T}}^{\text{miss}}$ final state is produced through gluino pair, squark pair, wino pair production in the LHC pp collisions. Since no significant excesses have been found with respect to the Standard Model predictions, lower limits on the sparticle masses are set: $m_{\tilde{g}} > 2150$ GeV, $m_{\tilde{q}} > 1820$ GeV and $m_{\tilde{\chi}_2^0}, m_{\tilde{\chi}_1^\pm} > 1060$ GeV. These limits improve the results obtained using Run 1 data (27) by 750 GeV and 400 GeV for the gluino and the wino mediated models, respectively. A similar analysis has been performed by CMS. Based on a sample of 35.9 $^{-1}$ of pp data accumulated at $\sqrt{s} = 13$ TeV, and assuming a branching fraction of 100% for the photonic decay of the $\tilde{\chi}_1^0$, the CMS collaboration has set 95% lower CL limits of 1.79 TeV and 1.58 TeV for similar models of gluino and squark production and decay, respectively (222).

The thesis presented also the description of several performance studies that are key components of the analysis results. For the Higgs boson mass measurement a study of the photon energy calibration and of the systematic uncertainties that affect the energy measurement has been performed. Using a multivariate regression the energy of the photons is calibrated with an expected linearity and resolution smaller than 0.2% and 1.5%, respectively, for photons with a transverse momentum greater than 50 GeV. In the context of the search for Supersymmetry in the di-photon final state, in order to evaluate the electron-photon background, a measurement of the electron-to-photon fake rate has been performed. The probability that an electron is mis-reconstructed and identified as a photon varies, in data, from 3% to 18% as a function of the pseudorapidity.

Acknowledgements

At the end of my Ph.D., there are a lot of people I want to thank for their precious help and support during these years.

First, I want to thank my supervisors Giovanni and Leonardo. This thesis would not have been completed without them, and it would probably not have started either. Both of them have been (and still are) a great example of what a professional, passionate and hard worker physicist should be.

Thanks to the colleagues of the *SUSY+Photon* team. Among them Bruce deserves a special mention for his dedication to coordinate the di-photon analysis.

The work presented in this manuscript would not have been possible without the contribution and the support of several people from the *HGamma* and the *E/gamma* groups. A special thanks goes to Ruggero for all the inspiring discussions that we had.

Thanks also to the *Liquid Argon* group, which is a clear example of fruitful collaboration between expert physicists and committed young students. I have really enjoyed working with the LAr operation team.

Thanks to the ATLAS groups of Milan and Paris for having welcomed me in the past three years. I am particularly grateful to my Ph.D. colleagues, with whom I shared very nice experiences, both for work and for leisure.

I then want to thank my family and friends. I have always felt you all hold me in high regard, maybe undeservedly. Your warm support has been always important for me.

Last, but not least, I want to thank Cristina, for keeping up with me in the last three years (and the ones before!). You had a very direct experience of pros and cons of a particle physicist's life. I do promise that in the future I will sleep more and disrupt a smaller share of your weekends.

Bibliography

[1] L. Evans and P. Bryant, *LHC Machine*, JINST **3** (2008) S08001.

[2] ATLAS Collaboration, G. Aad et al., *The ATLAS Experiment at the CERN Large Hadron Collider*, JINST **3** (2008) S08003.

[3] CMS Collaboration, S. Chatrchyan et al., *The CMS experiment at the CERN LHC*, JINST **3** (2008) S08004.

[4] ATLAS Collaboration, G. Aad et al., *Observation of a new particle in the search for the Standard Model Higgs boson with the ATLAS detector at the LHC*, Phys.Lett. **B716** (2012) 1–29, arXiv:1207.7214 [hep-ex].

[5] CMS Collaboration, S. Chatrchyan et al., *Observation of a new boson at a mass of 125 GeV with the CMS experiment at the LHC*, Phys.Lett. **B716** (2012) 30–61, arXiv:1207.7235 [hep-ex].

[6] P. W. Higgs, *Broken symmetries, massless particles and gauge fields*, Phys.Lett. **12** (1964) 132–133.

[7] F. Englert and R. Brout, *Broken Symmetry and the Mass of Gauge Vector Mesons*, Phys.Rev.Lett. **13** (1964) 321–323.

[8] G. Guralnik, C. Hagen, and T. Kibble, *Global Conservation Laws and Massless Particles*, Phys.Rev.Lett. **13** (1964) 585–587.

[9] ATLAS Collaboration Collaboration, *Measurements of Higgs boson properties in the diphoton decay channel with 36.1 fb^1 pp collision data at the center-of-mass energy of 13 TeV with the ATLAS detector*, Tech. Rep. ATLAS-CONF-2017-045, CERN, Geneva, Jul, 2017. https://cds.cern.ch/record/2273852.

[10] ATLAS Collaboration, M. Aaboud et al., *Measurement of the Higgs boson mass in the $H \to ZZ^* \to 4\ell$ and $H \to \gamma\gamma$ channels with $\sqrt{s}$=13TeV pp collisions using the ATLAS detector*, Tech. Rep. ATLAS-CONF-2017-046, CERN, Geneva, Jul, 2017. http://cds.cern.ch/record/2273853.

[11] ATLAS, CMS Collaboration, G. Aad et al., *Combined Measurement of the Higgs Boson Mass in pp Collisions at $\sqrt{s} = 7$ and 8 TeV with the ATLAS and CMS Experiments*, Phys. Rev. Lett. **114** (2015) 191803, arXiv:1503.07589 [hep-ex].

[12] Y. A. Golfand and E. P. Likhtman, *Extension of the Algebra of Poincare Group Generators and Violation of p Invariance*, JETP Lett. **13** (1971) 323–326.

[13] A. Neveu and J. H. Schwarz, *Factorizable dual model of pions*, Nucl. Phys. **B31** (1971) 86–112.

[14] A. Neveu and J. H. Schwarz, *Quark Model of Dual Pions*, Phys. Rev. **D4** (1971) 1109–1111.

[15] P. Ramond, *Dual Theory for Free Fermions*, Phys. Rev. **D3** (1971) 2415–2418.

[16] D. V. Volkov and V. P. Akulov, *Is the Neutrino a Goldstone Particle?*, Phys. Lett. **B46** (1973) 109–110.

[17] J. Wess and B. Zumino, *A Lagrangian Model Invariant Under Supergauge Transformations*, Phys. Lett. **B49** (1974) 52.

[18] J. Wess and B. Zumino, *Supergauge Transformations in Four-Dimensions*, Nucl. Phys. **B70** (1974) 39–50.

[19] L. Alvarez-Gaume, M. Claudson, and M. Wise, *Low-Energy Supersymmetry*, Nucl. Phys. **B207** (1982) 96.

[20] M. Dine, W. Fischler, and M. Srednicki, *Supersymmetric technicolor*, Nucl. Phys. **B189** (1981) 575.

[21] S. Dimopoulos and S. Raby, *Supercolor*, Nucl. Phys. **B192** (1981) 353.

[22] C. R. Nappi and B. A. Ovrut, *Supersymmetric extension of the $SU(3)\times SU(2)\times U(1)$ Model*, Phys. Lett. **B113** (1982) 175.

[23] M. Dine and A. Nelson, *Dynamical supersymmetry breaking at low-energies*, Phys. Rev. **D48** (1993) 1277, `hep-ph/9303230`.

[24] M. Dine, A. Nelson, and Y. Shirman, *Low-energy dynamical supersymmetry breaking simplified*, Phys. Rev. **D51** (1995) 1362, `hep-ph/9408384`.

[25] M. Dine, A. Nelson, Y.Nir, and Y. Shirman, *New tools for low-energy dynamical supersymmetry breaking*, Phys. Rev. **D53** (1996) 2658, `hep-ph/9507378`.

[26] ATLAS Collaboration, M. Aaboud et al., *Search for supersymmetry in a final state containing two photons and missing transverse momentum in $\sqrt{s}$ = 13 TeV pp collisions at the LHC using the ATLAS detector*, Eur. Phys. J. **C76** no. 9, (2016) 517, `arXiv:1606.09150 [hep-ex]`.

[27] ATLAS Collaboration, *Search for photonic signatures of gauge-mediated supersymmetry in 8 TeV pp collisions with the ATLAS detector*, Phys. Rev. D **92** (2015) 072001, `arXiv:1507.05493 [hep-ex]`.

[28] ATLAS Collaboration Collaboration, *Electron and photon energy calibration with the ATLAS detector using data collected in 2015 at $\sqrt{s} = 13$* TeV, Tech. Rep. ATL-PHYS-PUB-2016-015, CERN, Geneva, Aug, 2016. `https://cds.cern.ch/record/2203514`.

[29] ATLAS Collaboration, M. Aaboud et al., *Search for photonic signatures of gauge-mediated supersymmetry in 13 TeV pp collisions with the ATLAS detector.*, Tech. Rep. ATLAS-CONF-2017-080, CERN, Geneva, Dec, 2017. `https://atlas.web.cern.ch/Atlas/GROUPS/PHYSICS/CONFNOTES/ATLAS-CONF-2017-080/ATLAS-CONF-2017-080.pdf`.

[30] ATLAS Collaboration, M. Aaboud et al., *Search for new phenomena in high-mass diphoton final states using 37 fb^{-1} of proton–proton collisions collected at $\sqrt{s} = 13$ TeV with the ATLAS detector*, Submitted to: Phys. Lett. (2017), `arXiv:1707.04147 [hep-ex]`.

[31] ATLAS Collaboration, M. Aaboud et al., *Search for resonances in diphoton events at $\sqrt{s}$=13 TeV with the ATLAS detector*, JHEP **09** (2016) 001, `arXiv:1606.03833 [hep-ex]`.

[32] ATLAS Collaboration, M. Aaboud et al., *Search for heavy resonances decaying to a Z boson and a photon in pp collisions at $\sqrt{s} = 13$ TeV with the ATLAS detector*, Phys. Lett. **B764** (2017) 11–30, `arXiv:1607.06363 [hep-ex]`.

[33] Wikipedia, "Fundamental interactions."

http://en.wikipedia.org/wiki/Fundamental_interaction.

[34] Particle Data Group Collaboration, C. Patrignani et al., *Review of Particle Physics*, Chin. Phys. **C40** no. 10, (2016) 100001.

[35] M. E. Peskin and D. V. Schroeder, *An Introduction to Quantum Field Theory*. Westview Press, 1995.

[36] J. Goldstone, A. Salam, and S. Weinberg, *Broken Symmetries*, Phys. Rev. **127** (1962) 965–970.

[37] MuLan Collaboration, D. M. Webber et al., *Measurement of the Positive Muon Lifetime and Determination of the Fermi Constant to Part-per-Million Precision*, Phys. Rev. Lett. **106** (2011) 041803, arXiv:1010.0991 [hep-ex]. [Phys. Rev. Lett.106,079901(2011)].

[38] A. Djouadi, *The Anatomy of electro-weak symmetry breaking. I: The Higgs boson in the standard model*, Phys.Rept. **457** (2008) 1–216, arXiv:hep-ph/0503172 [hep-ph].

[39] T. Hambye and K. Riesselmann, *Matching conditions and Higgs mass upper bounds revisited*, Phys. Rev. **D55** (1997) 7255–7262, arXiv:hep-ph/9610272 [hep-ph].

[40] ATLAS, CMS Collaboration, G. Aad et al., *Measurements of the Higgs boson production and decay rates and constraints on its couplings from a combined ATLAS and CMS analysis of the LHC pp collision data at $\sqrt{s} = 7$ and 8 TeV*, JHEP **08** (2016) 045, arXiv:1606.02266 [hep-ex].

[41] LHC Higgs Cross Section Working Group Collaboration, D. de Florian et al., *Handbook of LHC Higgs Cross Sections: 4. Deciphering the Nature of the Higgs Sector*, arXiv:1610.07922 [hep-ph].

[42] LHC Higgs Cross Section Working Group Collaboration, J. R. Andersen et al., *Handbook of LHC Higgs Cross Sections: 3. Higgs Properties*, arXiv:1307.1347 [hep-ph].

[43] H. M. Georgi, S. L. Glashow, M. E. Machacek, and D. V. Nanopoulos, *Higgs Bosons from Two Gluon Annihilation in Proton Proton Collisions*, Phys. Rev. Lett. **40** (1978) 692.

[44] C. Anastasiou, C. Duhr, F. Dulat, E. Furlan, T. Gehrmann, F. Herzog, A. Lazopoulos, and B. Mistlberger, *High precision determination of the gluon fusion Higgs boson cross-section at the LHC*, JHEP **05** (2016) 058, arXiv:1602.00695 [hep-ph].

[45] ATLAS Collaboration, G. Aad et al., *Measurement of the Higgs boson mass from the $H \to \gamma\gamma$ and $H \to ZZ^* \to 4\ell$ channels with the ATLAS detector using 25 fb^{-1} of pp collision data*, Phys. Rev. **D90** no. 5, (2014) 052004, arXiv:1406.3827 [hep-ex].

[46] ATLAS Collaboration, G. Aad et al., *Measurements of Higgs boson production and couplings in the four-lepton channel in pp collisions at center-of-mass energies of 7 and 8 TeV with the ATLAS detector*, Phys. Rev. **D91** no. 1, (2015) 012006, arXiv:1408.5191 [hep-ex].

[47] CMS Collaboration, V. Khachatryan et al., *Observation of the diphoton decay of the Higgs boson and measurement of its properties*, Eur. Phys. J. **C74** no. 10, (2014) 3076, arXiv:1407.0558 [hep-ex].

[48] CMS Collaboration, S. Chatrchyan et al., *Measurement of the properties of a Higgs boson in the four-lepton final state*, Phys. Rev. **D89** no. 9, (2014) 092007,

arXiv:1312.5353 [hep-ex].

[49] ATLAS Collaboration, G. Aad et al., *Measurement of Higgs boson production in the diphoton decay channel in pp collisions at center-of-mass energies of 7 and 8 TeV with the ATLAS detector*, Phys. Rev. **D90** no. 11, (2014) 112015, arXiv:1408.7084 [hep-ex].

[50] ATLAS Collaboration, G. Aad et al., *Observation and measurement of Higgs boson decays to WW* with the ATLAS detector*, Phys. Rev. **D92** no. 1, (2015) 012006, arXiv:1412.2641 [hep-ex].

[51] ATLAS Collaboration, G. Aad et al., *Study of (W/Z)H production and Higgs boson couplings using $H \to WW^*$ decays with the ATLAS detector*, JHEP **08** (2015) 137, arXiv:1506.06641 [hep-ex].

[52] CMS Collaboration, S. Chatrchyan et al., *Measurement of Higgs boson production and properties in the WW decay channel with leptonic final states*, JHEP **01** (2014) 096, arXiv:1312.1129 [hep-ex].

[53] ATLAS Collaboration, G. Aad et al., *Evidence for the Higgs-boson Yukawa coupling to tau leptons with the ATLAS detector*, JHEP **04** (2015) 117, arXiv:1501.04943 [hep-ex].

[54] CMS Collaboration, S. Chatrchyan et al., *Evidence for the 125 GeV Higgs boson decaying to a pair of τ leptons*, JHEP **05** (2014) 104, arXiv:1401.5041 [hep-ex].

[55] ATLAS Collaboration, G. Aad et al., *Search for the $b\bar{b}$ decay of the Standard Model Higgs boson in associated $(W/Z)H$ production with the ATLAS detector*, JHEP **01** (2015) 069, arXiv:1409.6212 [hep-ex].

[56] CMS Collaboration, S. Chatrchyan et al., *Search for the standard model Higgs boson produced in association with a W or a Z boson and decaying to bottom quarks*, Phys. Rev. **D89** no. 1, (2014) 012003, arXiv:1310.3687 [hep-ex].

[57] L. D. Landau, *On the angular momentum of a system of two photons*, Dokl. Akad. Nauk Ser. Fiz. **60** no. 2, (1948) 207–209.

[58] C.-N. Yang, *Selection Rules for the Dematerialization of a Particle Into Two Photons*, Phys. Rev. **77** (1950) 242–245.

[59] ATLAS Collaboration, G. Aad et al., *Study of the spin and parity of the Higgs boson in diboson decays with the ATLAS detector*, Eur. Phys. J. **C75** no. 10, (2015) 476, arXiv:1506.05669 [hep-ex]. [Erratum: Eur. Phys. J.C76,no.3,152(2016)].

[60] ATLAS Collaboration, G. Aad et al., *Determination of spin and parity of the Higgs boson in the $WW^* \to e\nu\mu\nu$ decay channel with the ATLAS detector*, Eur. Phys. J. **C75** no. 5, (2015) 231, arXiv:1503.03643 [hep-ex].

[61] J. C. Collins and D. E. Soper, *Angular Distribution of Dileptons in High-Energy Hadron Collisions*, Phys. Rev. **D16** (1977) 2219.

[62] CMS Collaboration, V. Khachatryan et al., *Constraints on the spin-parity and anomalous HVV couplings of the Higgs boson in proton collisions at 7 and 8 TeV*, Phys. Rev. **D92** no. 1, (2015) 012004, arXiv:1411.3441 [hep-ex].

[63] ATLAS Collaboration, M. Aaboud et al., *Evidence for the $H \to b\bar{b}$ decay with the ATLAS detector*, arXiv:1708.03299 [hep-ex].

[64] CMS Collaboration Collaboration, *Evidence for the decay of the Higgs Boson to Bottom Quarks*, Tech. Rep. CMS-PAS-HIG-16-044, CERN, Geneva, 2017. https://cds.cern.ch/record/2278170.

[65] S. P. A summary of the SUSY model can be found in: Martin, *A Supersymmetry*

Primer, hep-ph/9709356, 1997.

[66] J. Terning, *Modern supersymmetry: Dynamics and duality*. 2006.

[67] M. Lisanti, *Lectures on Dark Matter Physics*, pp. , 399–446. 2017. arXiv:1603.03797 [hep-ph]. https://inspirehep.net/record/1427360/files/arXiv:1603.03797.pdf.

[68] Planck Collaboration, P. A. R. Ade et al., *Planck 2015 results. XIII. Cosmological parameters*, Astron. Astrophys. **594** (2016) A13, arXiv:1502.01589 [astro-ph.CO].

[69] R. Haag, J. T. Lopuszanski, and M. Sohnius, *All Possible Generators of Supersymmetries of the s Matrix*, Nucl. Phys. **B88** (1975) 257.

[70] S. R. Coleman and J. Mandula, *All Possible Symmetries of the S Matrix*, Phys. Rev. **159** (1967) 1251–1256.

[71] Super-Kamiokande Collaboration, K. Abe et al., *Search for proton decay via $p \to e^+\pi^0$ and $p \to \mu^+\pi^0$ in 0.31megaton·years exposure of the Super-Kamiokande water Cherenkov detector*, Phys. Rev. **D95** no. 1, (2017) 012004, arXiv:1610.03597 [hep-ex].

[72] L. Girardello and M. T. Grisaru, *Soft Breaking of Supersymmetry*, Nucl. Phys. **B194** (1982) 65.

[73] P. Draper and H. Rzehak, *A Review of Higgs Mass Calculations in Supersymmetric Models*, Phys. Rept. **619** (2016) 1–24, arXiv:1601.01890 [hep-ph].

[74] P. Bechtle, T. Plehn, and C. Sander, *Supersymmetry*, pp. , 421–462. 2015. arXiv:1506.03091 [hep-ex]. https://inspirehep.net/record/1375491/files/arXiv:1506.03091.pdf.

[75] F. Alonso and M. T. Dova, *Búsqueda de Supersimetría en eventos con un fotón, jets y energía faltante con el detector ATLAS*, Feb, 2016. https://cds.cern.ch/record/2147473. Presented 28 Mar 2016.

[76] ATLAS Collaboration, G. Aad et al., *Search for nonpointing and delayed photons in the diphoton and missing transverse momentum final state in 8 TeV pp collisions at the LHC using the ATLAS detector*, Phys. Rev. **D90** no. 11, (2014) 112005, arXiv:1409.5542 [hep-ex].

[77] CMS Collaboration, *Search for supersymmetry with photons in pp collisions at $\sqrt{s}$ = 8 TeV*, Phys. Rev. D **92** (2015) 072006, arXiv:1507.02898 [hep-ex].

[78] J. Alwall, P. Schuster, and N. Toro, *Simplified Models for a First Characterization of New Physics at the LHC*, Phys. Rev. **D79** (2009) 075020, arXiv:0810.3921 [hep-ph].

[79] W. Beenakker, R. Hopker, and M. Spira, *PROSPINO: A program for the Production of Supersymmetric Particles In Next-to-leading Order QCD, hep-ph/9611232*, 1996.

[80] J. D. Jackson, *Classical Electrodynamics*. Wiley, first ed., 1962.

[81] L. A. Harland-Lang, A. D. Martin, P. Motylinski, and R. S. Thorne, *Parton distributions in the LHC era: MMHT 2014 PDFs*, Eur. Phys. J. **C75** no. 5, (2015) 204, arXiv:1412.3989 [hep-ph].

[82] R. Bruce, C. Bracco, R. De Maria, M. Giovannozzi, A. Mereghetti, D. Mirarchi, S. Redaelli, E. Quaranta, and B. Salvachua, *Reaching record-low * at the CERN Large Hadron Collider using a novel scheme of collimator settings and optics*, Nucl. Instrum. Meth. **A848** (2017) 19–30.

[83] "Website of ATLAS Public Luminosity Results." https://twiki.cern.ch/twiki/bin/view/AtlasPublic/LuminosityPublicResultsRun2.

[84] ATLAS Collaboration, M. Aaboud et al., *Luminosity determination in pp collisions at $\sqrt{s}$ = 8 TeV using the ATLAS detector at the LHC*, Eur. Phys. J. **C76** no. 12, (2016) 653, arXiv:1608.03953 [hep-ex].

[85] P. Jenni, M. Nordberg, M. Nessi, and K. Jon-And, *ATLAS Forward Detectors for Measurement of Elastic Scattering and Luminosity*,.

[86] S. van der Meer, *Calibration of the effective beam height in the ISR*, Tech. Rep. CERN-ISR-PO-68-31. ISR-PO-68-31, CERN, Geneva, 1968. https://cds.cern.ch/record/296752.

[87] ATLAS Collaboration, G. Ucchielli, *LUCID Upgrade for ATLAS Luminosity Measurement in Run II*, Tech. Rep. ATL-FWD-PROC-2016-001, CERN, Geneva, Oct, 2016. https://cds.cern.ch/record/2227284.

[88] F. Marcastel, *CERN's Accelerator Complex. La chaîne des accélérateurs du CERN*,. https://cds.cern.ch/record/1621583. General Photo.

[89] D. Boussard and T. P. R. Linnecar, *The LHC Superconducting RF System*, Tech. Rep. LHC-Project-Report-316. CERN-LHC-Project-Report-316, CERN, Geneva, Dec, 1999. https://cds.cern.ch/record/410377.

[90] A. Team, "Diagram of an LHC dipole magnet. Schéma d'un aimant dipôle du LHC." Jun, 1999.

[91] J.-L. Caron, "LHC quadrupole cross section.." AC Collection. Legacy of AC. Pictures from 1992 to 2002., May, 1998.

[92] M. Kramer and F. J. P. Soler, *Large Hadron Collider Phenomenology*. SUSSP Publications and Institute of Physics Publishing, 2004.

[93] LHCb Collaboration, J. Alves, A. Augusto et al., *The LHCb Detector at the LHC*, JINST **3** (2008) S08005.

[94] ALICE Collaboration, K. Aamodt et al., *The ALICE experiment at the CERN LHC*, JINST **3** (2008) S08002.

[95] TOTEM Collaboration, G. e. a. Anelli, *The TOTEM Experiment at the CERN Large Hadron Collider*, J. Instrum. **3** (2008) S08007.

[96] LHCf Collaboration, O. Adriani et al., *The LHCf detector at the CERN Large Hadron Collider*, JINST **3** (2008) S08006.

[97] "ATLAS EXPERIMENT." http://atlas.ch/.

[98] ATLAS Collaboration Collaboration, *ATLAS central solenoid: Technical Design Report*. Technical Design Report ATLAS. CERN, Geneva, 1997. https://cds.cern.ch/record/331067. Electronic version not available.

[99] ATLAS Collaboration, *ATLAS barrel toroid: Technical design report*,.

[100] ATLAS Collaboration, *ATLAS endcap toroids: Technical design report*,.

[101] ATLAS Collaboration, G. Aad et al., *The ATLAS Inner Detector commissioning and calibration*, Eur. Phys. J. **C70** (2010) 787–821, arXiv:1004.5293 [physics.ins-det].

[102] ATLAS Collaboration, M. S. Alam et al., *ATLAS pixel detector: Technical design report*,.

[103] ATLAS Collaboration, M. Capeans, G. Darbo, K. Einsweiller, M. Elsing, T. Flick, M. Garcia-Sciveres, C. Gemme, H. Pernegger, O. Rohne, and R. Vuillermet, *ATLAS Insertable B-Layer Technical Design Report*,.

[104] K. Potamianos, *The upgraded Pixel detector and the commissioning of the Inner*

Detector tracking of the ATLAS experiment for Run-2 at the Large Hadron Collider, PoS **EPS-HEP2015** (2015) 261, arXiv:1608.07850 [physics.ins-det].

[105] A. Abdesselam et al., *The barrel modules of the ATLAS semiconductor tracker*, Nucl. Instrum. Meth. **A568** (2006) 642–671.

[106] ATLAS Collaboration, A. Abdesselam et al., *The ATLAS semiconductor tracker end-cap module*, Nucl. Instrum. Meth. **A575** (2007) 353–389.

[107] ATLAS TRT Collaboration, E. Abat et al., *The ATLAS TRT barrel detector*, JINST **3** (2008) P02014.

[108] E. Abat et al., *The ATLAS TRT end-cap detectors*, JINST **3** (2008) P10003.

[109] *The Expected Performance of the ATLAS Inner Detector*, Tech. Rep. ATL-PHYS-PUB-2009-002. ATL-COM-PHYS-2008-105, CERN, Geneva, Aug, 2008. http://cds.cern.ch/record/1118445.

[110] ATLAS Collaboration Collaboration, *Particle Identification Performance of the ATLAS Transition Radiation Tracker*, Tech. Rep. ATLAS-CONF-2011-128, CERN, Geneva, Sep, 2011. https://cds.cern.ch/record/1383793.

[111] ATLAS Collaboration, *ATLAS liquid argon calorimeter: Technical design report*,.

[112] ATLAS Collaboration, G. Aad et al., *Readiness of the ATLAS Liquid Argon Calorimeter for LHC Collisions*, Eur. Phys. J. **C70** (2010) 723–753, arXiv:0912.2642 [physics.ins-det].

[113] ATLAS Collaboration, G. Aad et al., *Drift Time Measurement in the ATLAS Liquid Argon Electromagnetic Calorimeter using Cosmic Muons*, Eur. Phys. J. **C70** (2010) 755–785, arXiv:1002.4189 [physics.ins-det].

[114] H. Abreu et al., *Performance of the electronic readout of the ATLAS liquid argon calorimeters*, JINST **5** (2010) P09003.

[115] W. E. Cleland and E. G. Stern, *Signal processing considerations for liquid ionization calorimeters in a high rate environment*, Nucl. Instrum. Meth. **A338** no. 2-3, (1994) 467–497.

[116] ATLAS Collaboration, *ATLAS tile calorimeter: Technical design report*,.

[117] ATLAS Collaboration, G. Aad et al., *Readiness of the ATLAS Tile Calorimeter for LHC collisions*, Eur. Phys. J. **C70** (2010) 1193–1236, arXiv:1007.5423 [physics.ins-det].

[118] ATLAS Liquid Argon HEC Collaboration, B. Dowler et al., *Performance of the ATLAS hadronic end-cap calorimeter in beam tests*, Nucl. Instrum. Meth. **A482** (2002) 94–124.

[119] A. Artamonov et al., *The ATLAS forward calorimeters*, JINST **3** (2008) P02010.

[120] ATLAS Collaboration, *ATLAS muon spectrometer: Technical design report*,.

[121] ATLAS Collaboration, *ATLAS first level trigger: Technical design report*,.

[122] ATLAS Collaboration, *ATLAS high-level trigger, data acquisition and controls: Technical design report*,.

[123] ATLAS Collaboration, M. Aaboud et al., *Performance of the ATLAS Trigger System in 2015*, Eur. Phys. J. **C77** no. 5, (2017) 317, arXiv:1611.09661 [hep-ex].

[124] "ATLAS Trigger Operation Public Results." https://twiki.cern.ch/twiki/bin/view/AtlasPublic/TriggerOperationPublicResults.

[125] *Expected electron performance in the ATLAS experiment*, Tech. Rep. ATL-PHYS-PUB-2011-006, CERN, Geneva, Apr, 2011.

[126] *Expected photon performance in the ATLAS experiment*, Tech. Rep. ATL-PHYS-PUB-2011-007, CERN, Geneva, Apr, 2011.

[127] W. Lampl, S. Laplace, D. Lelas, P. Loch, H. Ma, S. Menke, S. Rajagopalan, D. Rousseau, S. Snyder, and G. Unal, *Calorimeter clustering algorithms: Description and performance*,.

[128] ATLAS Collaboration, ATLAS Collaboration, *Electron efficiency measurements with the ATLAS detector using 2012 LHC proton-proton collision data*, Eur. Phys. J. **C77** no. 3, (2017) 195, arXiv:1612.01456 [hep-ex].

[129] ATLAS Collaboration Collaboration, *Electron efficiency measurements with the ATLAS detector using the 2015 LHC proton-proton collision data*, Tech. Rep. ATLAS-CONF-2016-024, CERN, Geneva, Jun, 2016. https://cds.cern.ch/record/2157687.

[130] ATLAS Collaboration, *Improved electron reconstruction in ATLAS using the Gaussian Sum Filter-based model for bremsstrahlung*, Tech. Rep. ATLAS-CONF-2012-047, CERN, Geneva, May, 2012.

[131] ATLAS Collaboration, M. Aaboud et al., *Measurement of the photon identification efficiencies with the ATLAS detector using LHC Run-1 data*, Eur. Phys. J. **C76** no. 12, (2016) 666, arXiv:1606.01813 [hep-ex].

[132] https://twiki.cern.ch/twiki/bin/view/AtlasPublic/ElectronGammaPublicCollisionResults.

[133] ATLAS Collaboration, G. Aad et al., *Topological cell clustering in the ATLAS calorimeters and its performance in LHC Run 1*, Eur. Phys. J. **C77** (2017) 490, arXiv:1603.02934 [hep-ex].

[134] ATLAS Collaboration, G. Aad et al., *Muon reconstruction performance of the ATLAS detector in proton–proton collision data at $\sqrt{s}$ =13 TeV*, Eur. Phys. J. **C76** no. 5, (2016) 292, arXiv:1603.05598 [hep-ex].

[135] M. Cacciari, G. P. Salam, and G. Soyez, *The Anti-k(t) jet clustering algorithm*, JHEP **04** (2008) 063, arXiv:0802.1189 [hep-ph].

[136] ATLAS Collaboration, M. Aaboud et al., *Jet energy scale measurements and their systematic uncertainties in proton-proton collisions at $\sqrt{s} = 13$ TeV with the ATLAS detector*, Phys. Rev. **D96** no. 7, (2017) 072002, arXiv:1703.09665 [hep-ex].

[137] *Pile-up subtraction and suppression for jets in ATLAS*, Tech. Rep. ATLAS-CONF-2013-083, CERN, Geneva, Aug, 2013. https://cds.cern.ch/record/1570994.

[138] *Jet Calibration and Systematic Uncertainties for Jets Reconstructed in the ATLAS Detector at $\sqrt{s} = 13$ TeV*, Tech. Rep. ATL-PHYS-PUB-2015-015, CERN, Geneva, Jul, 2015. https://cds.cern.ch/record/2037613.

[139] *Tagging and suppression of pileup jets with the ATLAS detector*, Tech. Rep. ATLAS-CONF-2014-018, CERN, Geneva, May, 2014. https://cds.cern.ch/record/1700870.

[140] ATLAS Collaboration, G. Aad et al., *Performance of algorithms that reconstruct missing transverse momentum in $\sqrt{s} = 8$ TeV proton-proton collisions in the ATLAS detector*, Eur. Phys. J. **C77** no. 4, (2017) 241, arXiv:1609.09324 [hep-ex].

[141] *Performance of missing transverse momentum reconstruction for the ATLAS detector in the first proton-proton collisions at at $\sqrt{s}$= 13 TeV*, Tech. Rep.

ATL-PHYS-PUB-2015-027, CERN, Geneva, Jul, 2015. https://cds.cern.ch/record/2037904.

[142] R. Turra, C. Meroni, and M. Fanti, *Energy calibration and observation of the Higgs boson in the diphoton decay with the ATLAS experiment*, Jan, 2013. https://cds.cern.ch/record/1517442. Presented 18 Feb 2013.

[143] ATLAS Collaboration, G. Aad et al., *Electron and photon energy calibration with the ATLAS detector using LHC Run 1 data*, Eur. Phys. J. **C74** no. 10, (2014) 3071, arXiv:1407.5063 [hep-ex].

[144] ATLAS Collaboration, M. Aharrouche, C. Adam-Bourdarios, M. Aleksa, D. Banfi, D. Benchekroun, et al., *Measurement of the response of the ATLAS liquid argon barrel calorimeter to electrons at the 2004 combined test-beam*, Nucl.Instrum.Meth. **A614** no. 3, (2010) 400–432.

[145] L. Courneyea, D. Dannheim, M. Delmastro, S. Elles, M. Gouighri, L. Iconomidou-Fayard, I. Koletsou, W. Lampl, Z. Liang, L. March, P. Strizenec, F. Tarrade, R. Ueno, M. Vincter, Z. Weng, and H. Zhang, *Computation and validation of the electronic calibration constants for the ATLAS Liquid Argon Calorimeters*, Tech. Rep. ATL-LARG-INT-2010-007, CERN, Geneva, 7, 2010.

[146] J. Quinlan, *Simplifying decision trees*, International journal of man-machine studies **27** no. 3, (1987) 221–234.

[147] L. Breiman, J. Friedman, and R. Olshen, *Classification and regression trees*. Chapman & Hall, New York, NY, 1984.

[148] A. Hoecker, P. Speckmayer, J. Stelzer, J. Therhaag, E. von Toerne, and H. Voss, *TMVA: Toolkit for Multivariate Data Analysis*, PoS **ACAT** (2007) 040, arXiv:physics/0703039. http://tmva.sourceforge.net/.

[149] GEANT4 Collaboration, S. Agostinelli et al., *GEANT4: A Simulation toolkit*, Nucl. Instrum. Meth. **A506** (2003) 250–303.

[150] J. Allison et al., *Geant4 developments and applications*, IEEE Trans. Nucl. Sci. **53** (2006) 270.

[151] D. Thain, T. Tannenbaum, and M. Livny, *Distributed computing in practice: the Condor experience.*, Concurrency - Practice and Experience **17** no. 2-4, (2005) 323–356.

[152] M. Aaboud et al. tech. rep.

[153] K. J. Anderson, L. Batkova, M. Cavalli-Sforza, T. Carli, M. Cascella, T. Davidek, T. Del Prete, T. Djobava, A. Dotti, R. Febbraro, N. Gollub, H. Hakobyan, A. Henriques, M. H. Hurwitz, A. Isaev, I. Jen-La Plante, A. Karyukhin, H. Khandanyan, J. Khramov, Y. Kulchitsky, M. Makouski, M. Mosidze, A. Myagkov, J. E. Pilcher, L. Pribyl, M. Rullgard, C. Santoni, N. Shalanda, A. Solodkov, O. Solovyanov, J. Starchenko, P. Stavina, M. Simonyan, R. Teuscher, P. Tsiareshka, E. Vichou, V. Vinogradov, I. Vivarelli, M. Volpi, and T. Zenis, *Calibration of ATLAS Tile Calorimeter at Electromagnetic Scale*, Tech. Rep. ATL-TILECAL-PUB-2009-001. ATL-COM-TILECAL-2008-016, CERN, Geneva, Nov, 2008. https://cds.cern.ch/record/1139228.

[154] ATLAS Collaboration Collaboration, C. Fischer, *Study of TileCal scintillators irradiation using the Minimum Bias integrators*, Tech. Rep. ATL-TILECAL-PROC-2016-006, CERN, Geneva, Jun, 2016. https://cds.cern.ch/record/2160267.

[155] *Expected photon performance in the ATLAS experiment*, Tech. Rep.

ATL-PHYS-PUB-2011-007, CERN, Geneva, Apr, 2011. http://cds.cern.ch/record/1345329.

[156] ATLAS Collaboration Collaboration, *Photon identification in 2015 ATLAS data*, Tech. Rep. ATL-PHYS-PUB-2016-014, CERN, Geneva, Aug, 2016. http://cds.cern.ch/record/2203125.

[157] A. G. Zecchinelli, L. Carminati, T. Lari, and S. Manzoni, *Search for Supersymmetry in the di-photon plus missing transvers momentum final state with the ATLAS detector in $\sqrt{s} = 13$ TeV pp collision*, Apr, 2016.

[158] CMS Collaboration, V. Khachatryan et al., *Precise determination of the mass of the Higgs boson and tests of compatibility of its couplings with the standard model predictions using proton collisions at 7 and 8 TeV*, Eur. Phys. J. **C75** no. 5, (2015) 212, arXiv:1412.8662 [hep-ex].

[159] ATLAS Collaboration, G. Aad et al., *The ATLAS Simulation Infrastructure*, Eur.Phys.J. **C70** (2010) 823–874, arXiv:1005.4568 [physics.ins-det].

[160] A. Djouadi, J. Kalinowski, and M. Spira, *HDECAY: A Program for Higgs boson decays in the standard model and its supersymmetric extension*, Comput. Phys. Commun. **108** (1998) 56–74, arXiv:hep-ph/9704448 [hep-ph].

[161] A. Bredenstein, A. Denner, S. Dittmaier, and M. M. Weber, *Radiative corrections to the semileptonic and hadronic Higgs-boson decays H —¿ W W / Z Z —¿ 4 fermions*, JHEP **02** (2007) 080, arXiv:hep-ph/0611234 [hep-ph].

[162] A. Bredenstein, A. Denner, S. Dittmaier, and M. M. Weber, *Precise predictions for the Higgs-boson decay $H \to WW/ZZ \to 4$ leptons*, Phys. Rev. D **74** (2006) 013004, arXiv:hep-ph/0604011 [hep-ph].

[163] A. Bredenstein, A. Denner, S. Dittmaier, and M. M. Weber, *Precision calculations for the Higgs decays H —¿ ZZ/WW —¿ 4 leptons*, Nucl. Phys. Proc. Suppl. **160** (2006) 131–135, arXiv:hep-ph/0607060 [hep-ph]. [,131(2006)].

[164] S. Alioli, P. Nason, C. Oleari, and E. Re, *NLO Higgs boson production via gluon fusion matched with shower in POWHEG*, JHEP **04** (2009) 002, arXiv:0812.0578 [hep-ph].

[165] K. Hamilton, P. Nason, E. Re, and G. Zanderighi, *NNLOPS simulation of Higgs boson production*, JHEP **10** (2013) 222, arXiv:1309.0017 [hep-ph].

[166] J. Butterworth et al., *PDF4LHC recommendations for LHC Run II*, J. Phys. G **43** (2016) 023001, arXiv:1510.03865 [hep-ph].

[167] T. Sjostrand, S. Mrenna, and P. Z. Skands, *A Brief Introduction to PYTHIA 8.1*, Comput. Phys. Commun. **178** (2008) 852–867, arXiv:0710.3820 [hep-ph].

[168] C. Anastasiou, C. Duhr, F. Dulat, F. Herzog, and B. Mistlberger, *Higgs Boson Gluon-Fusion Production in QCD at Three Loops*, Phys. Rev. Lett. **114** (2015) 212001, arXiv:1503.06056 [hep-ph].

[169] S. Actis, G. Passarino, C. Sturm, and S. Uccirati, *NLO electroweak corrections to Higgs boson production at hadron colliders*, Phys. Lett. B **670** (2008) 12–17, arXiv:0809.1301 [hep-ph].

[170] C. Anastasiou, R. Boughezal, and F. Petriello, *Mixed QCD-electroweak corrections to Higgs boson production in gluon fusion*, JHEP **04** (2009) 003, arXiv:0811.3458 [hep-ph].

[171] P. Nason, *A New method for combining NLO QCD with shower Monte Carlo algorithms*, JHEP **11** (2004) 040, arXiv:hep-ph/0409146 [hep-ph].

[172] S. Frixione, P. Nason, and C. Oleari, *Matching NLO QCD computations with*

Parton Shower simulations: the POWHEG method, JHEP **11** (2007) 070, arXiv:0709.2092 [hep-ph].

[173] S. Alioli, P. Nason, C. Oleari, and E. Re, *A general framework for implementing NLO calculations in shower Monte Carlo programs: the POWHEG BOX*, JHEP **06** (2010) 043, arXiv:1002.2581 [hep-ph].

[174] P. Nason and C. Oleari, *NLO Higgs boson production via vector-boson fusion matched with shower in POWHEG*, JHEP **02** (2010) 037, arXiv:0911.5299 [hep-ph].

[175] M. Ciccolini, A. Denner, and S. Dittmaier, *Strong and electroweak corrections to the production of Higgs + 2jets via weak interactions at the LHC*, Phys. Rev. Lett. **99** (2007) 161803, arXiv:0707.0381 [hep-ph].

[176] M. Ciccolini, A. Denner, and S. Dittmaier, *Electroweak and QCD corrections to Higgs production via vector-boson fusion at the LHC*, Phys. Rev. D **77** (2008) 013002, arXiv:0710.4749 [hep-ph].

[177] K. Arnold, M. Bahr, G. Bozzi, F. Campanario, C. Englert, et al., *VBFNLO: A Parton level Monte Carlo for processes with electroweak bosons*, Comput. Phys. Commun. **180** (2009) 1661–1670, arXiv:0811.4559 [hep-ph].

[178] P. Bolzoni, F. Maltoni, S.-O. Moch, and M. Zaro, *Higgs production via vector-boson fusion at NNLO in QCD*, Phys. Rev. Lett. **105** (2010) 011801, arXiv:1003.4451 [hep-ph].

[179] O. Brein, A. Djouadi, and R. Harlander, *NNLO QCD corrections to the Higgs-strahlung processes at hadron colliders*, Phys. Lett. B **579** (2004) 149–156, arXiv:hep-ph/0307206 [hep-ph].

[180] L. Altenkamp, S. Dittmaier, R. V. Harlander, H. Rzehak, and T. J. E. Zirke, *Gluon-induced Higgs-strahlung at next-to-leading order QCD*, JHEP **02** (2013) 078, arXiv:1211.5015 [hep-ph].

[181] M. Ciccolini, S. Dittmaier, and M. Krämer, *Electroweak radiative corrections to associated WH and ZH production at hadron colliders*, Phys. Rev. D **68** (2003) 073003, arXiv:hep-ph/0306234 [hep-ph].

[182] J. Alwall, R. Frederix, S. Frixione, V. Hirschi, F. Maltoni, O. Mattelaer, H. S. Shao, T. Stelzer, P. Torrielli, and M. Zaro, *The automated computation of tree-level and next-to-leading order differential cross sections, and their matching to parton shower simulations*, JHEP **07** (2014) 079, arXiv:1405.0301 [hep-ph].

[183] NNPDF Collaboration (R. D. Ball et al), *Parton distributions for the LHC Run II*, JHEP **04** (2015) 040, arXiv:1410.8849 [hep-ph].

[184] *ATLAS Run 1 Pythia8 tunes*, Tech. Rep. ATL-PHYS-PUB-2014-021, CERN, Geneva, Nov, 2014. https://cds.cern.ch/record/1966419.

[185] W. Beenakker, S. Dittmaier, M. Krämer, B. Plumper, M. Spira, et al., *NLO QCD corrections to $t\bar{t}H$ production in hadron collisions*, Nucl. Phys. B **653** (2003) 151–203, arXiv:hep-ph/0211352 [hep-ph].

[186] S. Dawson, C. Jackson, L. Orr, L. Reina, and D. Wackeroth, *Associated Higgs production with top quarks at the large hadron collider: NLO QCD corrections*, Phys. Rev. D **68** (2003) 034022, arXiv:hep-ph/0305087 [hep-ph].

[187] Y. Zhang, W.-G. Ma, R.-Y. Zhang, C. Chen, and L. Guo, *QCD NLO and EW NLO corrections to $t\bar{t}H$ production with top quark decays at hadron collider*, Phys. Lett. **B738** (2014) 1–5, arXiv:1407.1110 [hep-ph].

[188] S. Frixione, V. Hirschi, D. Pagani, H. S. Shao, and M. Zaro, *Electroweak and QCD*

corrections to top-pair hadroproduction in association with heavy bosons, JHEP **06** (2015) 184, arXiv:1504.03446 [hep-ph].

[189] T. Gleisberg, S. Hoeche, F. Krauss, M. Schonherr, S. Schumann, F. Siegert, and J. Winter, *Event generation with SHERPA 1.1*, JHEP **02** (2009) 007, arXiv:0811.4622 [hep-ph].

[190] T. HSG1 Group, *Selection for H-gt;gammagamma analysis supporting note, for Moriond 2013*, Tech. Rep. ATL-COM-PHYS-2013-093, CERN, Geneva, Jan, 2013. https://cds.cern.ch/record/1510141.

[191] B. Lenzi and D. Delgove, *Selection of the diphoton production vertex using multivariate techniques for $H \to \gamma\gamma$ and other analyses*, Tech. Rep. ATL-COM-PHYS-2015-1321, CERN, Geneva, Oct, 2015. https://cds.cern.ch/record/2062239.

[192] J. R. Andersen et al., *Les Houches 2015: Physics at TeV Colliders Standard Model Working Group Report*, in *9th Les Houches Workshop on Physics at TeV Colliders (PhysTeV 2015) Les Houches, France, June 1-19, 2015*. 2016. arXiv:1605.04692 [hep-ph]. http://lss.fnal.gov/archive/2016/conf/fermilab-conf-16-175-ppd-t.pdf.

[193] N. Lorenzo Martinez and R. Turra, *Mass measurement in the $H \to \gamma\gamma$ channel: Supporting documentation for the Mass Paper*, Tech. Rep. ATL-COM-PHYS-2014-018, CERN, Geneva, Jan, 2014. https://cds.cern.ch/record/1642851.

[194] G. Cowan, K. Cranmer, E. Gross, and O. Vitells, *Asymptotic formulae for likelihood-based tests of new physics*, Eur.Phys.J. **C71** (2011) 1554, arXiv:1007.1727 [physics.data-an].

[195] ATLAS Collaboration, G. Aad et al., *Measurement of the inclusive isolated prompt photon cross section in pp collisions at $\sqrt{s} = 7$ TeV with the ATLAS detector*, Phys. Rev. **D83** (2011) 052005, arXiv:1012.4389 [hep-ex].

[196] ATLAS Collaboration, G. Aad et al., *Measurement of the isolated di-photon cross-section in pp collisions at $\sqrt{s} = 7$ TeV with the ATLAS detector*, Phys. Rev. **D85** (2012) 012003, arXiv:1107.0581 [hep-ex].

[197] ATLAS Collaboration, G. Aad et al., *Combined search for the Standard Model Higgs boson in pp collisions at $\sqrt{s} = 7$ TeV with the ATLAS detector*, Phys. Rev. **D86** (2012) 032003, arXiv:1207.0319 [hep-ex].

[198] H.-L. Lai, M. Guzzi, J. Huston, Z. Li, P. M. Nadolsky, et al., *New parton distributions for collider physics*, Phys. Rev. D **82** (2010) 074024, arXiv:1007.2241 [hep-ph].

[199] S. Schumann and F. Krauss, *A Parton shower algorithm based on Catani-Seymour dipole factorisation*, JHEP **03** (2008) 038, arXiv:0709.1027 [hep-ph].

[200] S. Hoeche, F. Krauss, S. Schumann, and F. Siegert, *QCD matrix elements and truncated showers*, JHEP **05** (2009) 053, arXiv:0903.1219 [hep-ph].

[201] S. Frixione, *Isolated photons in perturbative QCD*, Phys. Lett. **B429** (1998) 369–374, arXiv:hep-ph/9801442 [hep-ph].

[202] A. Djouadi, J.-L. Kneur, and G. Moultaka, *SuSpect: A Fortran code for the supersymmetric and Higgs particle spectrum in the MSSM*, Comput.Phys.Commun. **176** (2007) 426–455, arXiv:hep-ph/0211331 [hep-ph].

[203] M. Muhlleitner, A. Djouadi, and Y. Mambrini, *SDECAY: A Fortran code for the decays of the supersymmetric particles in the MSSM*, Comput.Phys.Commun. **168**

(2005) 46–70, arXiv:hep-ph/0311167 [hep-ph].

[204] A. Djouadi, M. Muhlleitner, and M. Spira, *Decays of supersymmetric particles: The Program SUSY-HIT (SUspect-SdecaY-Hdecay-InTerface)*, Acta Phys. Polon. **B 38** (2007) 635, arXiv:hep-ph/0609292 [hep-ph].

[205] M. Bahr et al., *Herwig++ Physics and Manual*, Eur. Phys. J. C **58** (2008) 639–707, arXiv:0803.0883 [hep-ph].

[206] J. Pumplin et al., *New Generation of Parton Distributions with Uncertainties from Global QCD Analysis*, JHEP **12** (2002) 0207, arXiv:hep-ph/0201195v3.

[207] E. Richter-Was, D. Froidevaux, and L. Poggioli, *ATLFAST 2.0 a fast simulation package for ATLAS*, Tech. Rep. ATL-PHYS-98-131, CERN, Geneva, Nov, 1998. https://cds.cern.ch/record/683751.

[208] W. Beenakker, R. Hopker, M. Spira, and P. Zerwas, *Squark and gluino production at hadron colliders*, Nucl.Phys. **B492** (1997) 51–103, arXiv:hep-ph/9610490 [hep-ph].

[209] A. Kulesza and L. Motyka, *Threshold resummation for squark-antisquark and gluino- pair production at the LHC*, Phys. Rev. Lett. **102** (2009) 111802, arXiv:0807.2405 [hep-ph].

[210] A. Kulesza and L. Motyka, *Soft gluon resummation for the production of gluino-gluino and squark-antisquark pairs at the LHC*, Phys. Rev. **D80** (2009) 095004, arXiv:0905.4749 [hep-ph].

[211] W. Beenakker et al., *Soft-gluon resummation for squark and gluino hadroproduction*, JHEP **12** (2009) 041, arXiv:0909.4418 [hep-ph].

[212] W. Beenakker et al., *Squark and gluino hadroproduction*, Int. J. Mod. Phys. **A26** (2011) 2637–2664, arXiv:1105.1110 [hep-ph].

[213] M. Botje, J. Butterworth, A. Cooper-Sarkar, A. de Roeck, J. Feltesse, et al., *The PDF4LHC Working Group Interim Recommendations*, arXiv:1101.0538 [hep-ph].

[214] G. Cowan, *Discovery sensitivity for a counting experiment with background uncertainty*, tech. rep., Royal Holloway, London. http://www.pp.rhul.ac.uk/~cowan/stat/medsig/medsigNote.pdf.

[215] ATLAS Collaboration, G. Aad et al., *Measurements of $Z\gamma$ and $Z\gamma\gamma$ production in pp collisions at $\sqrt{s} = 8$ TeV with the ATLAS detector*, Phys. Rev. **D93** no. 11, (2016) 112002, arXiv:1604.05232 [hep-ex].

[216] G. Bozzi, F. Campanario, M. Rauch, and D. Zeppenfeld, *$W\gamma\gamma$ production with leptonic decays at NLO QCD*, Phys. Rev. **D83** (2011) 114035, arXiv:1103.4613 [hep-ph].

[217] P. M. Nadolsky et al., *Implications of CTEQ global analysis for collider observables*, Phys. Rev. **D78** (2008) 013004, arXiv:0802.0007 [hep-ph].

[218] A. Martin, W. Stirling, R. Thorne, and G. Watt, *Parton distributions for the LHC*, Eur.Phys.J. **C63** (2009) 189–285, arXiv:0901.0002 [hep-ph].

[219] K. Cranmer, *Practical Statistics for the LHC*, pp. , 267–308. 2015. arXiv:1503.07622 [physics.data-an]. https://inspirehep.net/record/1356277/files/arXiv:1503.07622.pdf. [,247(2015)].

[220] A. L. Read, *Presentation of search results: The CL(s) technique*, J.Phys. **G28** (2002) 2693–2704.

[221] P. Meade, N. Seiberg, and D. Shih, *General Gauge Mediation*, Prog. Theor. Phys.

Suppl. **177** (2009) 143–158, arXiv:0801.3278 [hep-ph].

[222] CMS Collaboration, A. M. Sirunyan et al., *Search for supersymmetry in events with at least one photon, missing transverse momentum, and large transverse event activity in proton-proton collisions at sqrt(s) = 13 TeV*, arXiv:1707.06193 [hep-ex].